UNIVERSITÉ CATHOLIQUE DE LOUVAIN
Faculty of Sciences
Institute of Condensed Matter and Nanosciences

SYNTHESIS STRATEGIES TOWARDS NEW HETEROMETALLIC AND FUNCTIONALIZED MOFS

Doctoral dissertation submitted for the degree of
Ph.D. in Sciences

Timothy Steenhaut
Louvain-la-Neuve
2021

JURY COMPOSITION

President

Prof. Yann Garcia (UCLouvain)

Jury Members

Prof. Michel Devillers (UCLouvain)

Prof. Alexandru Vlad (UCLouvain)

Prof. Johan Wouters (UNamur)

Prof. Christian Serre (ENS)

Supervisors

Prof. Sophie Hermans (UCLouvain)

Prof. Yaroslav Filinchuk (UCLouvain)

Table of Contents

Acknowledgements

Je tiens tout d'abord à remercier mes promoteurs qui m'ont accepté dans leur labo et accompagné tout au long de ces années de thèse et de bien vouloir encore me supporter à l'avenir. Merci Sophie pour m'avoir apporté la rigueur nécessaire à tout bon scientifique et pour votre bienveillance. Grace à vous j'ai progressé, non seulement en chimie mais aussi dans d'autres domaines (psychologie…). Thank you Yaroslav for the good mood, the good food, and your ever-lasting availability for a good chat.

Je tiens également à remercier les professeurs Christian Serre, Johan Wouters, Michel Devillers, Alexandru Vlad et Yann Garcia pour avoir accepté de faire partie de mon jury de thèse pour la discussion constructive durant la soutenance privée ainsi que d'avoir permis d'améliorer considérablement la qualité du manuscrit.

Également un grand merci aussi au prof. Olivier Riant, mon co-promoteur de mémoire, pour sa lettre de recommandation qui m'a permis d'obtenir le FRIA.

Koen, je vais écrire ceci en français (omdat ik goed genoeg weet dat je liever Frans dan Nederlands praat met mij) : merci pour tout, tu as été comme mon encadrant de thèse, toujours là pour m'aider quand nécessaire.

Un tout grand merci à mes mémorants, Nicolas, (le futur Dr.) Séraphin (son amour pour le titane) et Robin (aka. Robijntje, surtout garde la pêche !) et aussi à mon « demi mémorant » Iago, grâce à qui le temps a filé, on a bien rigolé (aussi un peu beaucoup travaillé). Merci aussi à mes stagiaires (IPL et autres), et tout particulièrement Ousam et Florent. Vous avez tous considérablement contribué aux résultats présentés dans ce manuscrit (ainsi qu'à ceux qui ne s'y trouvent pas).

Je tiens également à remercier tous les membres des groupes de recherche de Sophie (pizza party !) et de Yaroslav. Merci à Véronique d'avoir été là depuis le début (partenaire de galère, courage). Merci à

Nathalie dlT (the golden lady), Julien, Maïté, Tommy pour m'avoir aidé dans mes analyses. Merci également à Nathalie B., Nadzeya, Samuel, Antonin, Louise, Sarah et Yang. Thank you also Igor, Xiao, Ting and Jian. Pour la super ambiance au B1 je tiens également à remercier l'équipe de Tom & co et plus particulièrement Xavier, Michael, J-B, Vanessa (les anciens), Gaby, Carole, Chloé, Camila, Joséphine, Guillaume, Oleksii, Lisa, Max (the next generation) ainsi qu'Aurore et Claire.

Un énorme merci à Jean-François, pour tous les aspects techniques et scientifiques, et pour tout le reste (ce serait bien trop long à énumérer… et à caractère confidentiel).

Gabriella, grazie per tutte le misurazioni NMR speciali e le lunghe discussioni.

Merci Jessica pour les longues discussions et les (très) nombreuses commandes.

Merci au PAT pour le support administratif (surtout quand on s'y perd) et technique, ainsi que les conversations annexes : Jacqueline, Céline, François D., Pierre, Delphine, Laurent, Axel et François B…

Merci aussi à toute l'équipe des TP complémentaires avec qui j'ai pu travailler durant ces 5 dernières années : le prof. Benjamin Elias, Pascale, Alain, Simon, François…

Je remercie également mes collaborateurs de l'UNamur pour la RMN du solide : grazie Luca and Carmela, et de la KULeuven : Grazie Giacomo for the « collaboration ».

Merci également à ma famille pour le soutien durant toutes ces années d'études (promis, un jour je quitterai la maison).

Merci, Thank you, Dank u, Grazie, Gracias, Спасибо !

Abstract

This thesis is dedicated to new, doped and functionalized MOFs, with potential use in catalysis, gas storage and adsorption from solution. The main efforts were focused on the (sustainable) synthesis and characterization of those materials.

A new green aqueous strategy for obtaining MIL-100(Fe) through the use of alkali trimesate salts, which were all thoroughly characterized and whose structures have been solved by X-ray diffraction, has been developed. The MOF's formation mechanism has been investigated and a Fe_3BTC_2 (BTC^{3-} = benzene-1,3,5-tricarboxylate) intermediate isolated as single crystals, allowed to elucidate its structure. Furthermore, the influence of carboxylate salts as crystallization modulators has been investigated and the obtained materials were shown to be efficient in the removal of Au^{3+} from aqueous solutions.

This new synthetic strategy was further developed to allow incorporation of second metal. Bimetallic MIL-100(Fe,M) MOFs were successfully obtained with transitions, *p*-bloc and rare-earth elements as doping metals in a one-pot fashion. The amount of incorporated doping metal could be controlled and it was demonstrated that metals in the +III oxidation state were incorporated preferentially into the framework over iron, that was in turn preferentially incorporated over metals in the +II oxidation state. A PXRD-based determination method for the amount of doping metals in the MOFs was also developed and its efficiency compared to classical ICP and AAS methods.

The functionalization of mono- and bimetallic Al- and Fe-based MIL-100 MOFs with ethylenediamine (EN) was investigated. It was shown that only Al-containing MOFs could withstand contact with EN in toluene. Upon functionalization with ethylenediamine, MIL-100(Al), obtained with hierarchized porosity through a new synthetic approach, showed improved affinity for CO_2 in the low pressure range. Furthermore, this EN@MIL-100(Al) material contains both Brønsted acidic and basic functions. The free amines of the functionalized MOF

could be efficiently post-functionalized by a fluorescent BODIPY probe and the functions inside the large mesoporous cages of the MOF could specifically react with ninhydrin thanks to size selectivity of the pore windows. Al-containing MOFs also showed an unexpected increase in CO_2 sorption at high pressures (> 20 bar), which is likely due to insertion in the Al-O-H bonds to form carbonic acid species.

More sustainable strategies towards the synthesis of MOFs were further investigated for the rare-earth based MOF-76 series. Those MOFs could be obtained in ethanol as only solvent, in the absence of the commonly used toxic DMF. We evidenced an effect of the size of the rare-earth metal on the size of the obtained particles, as well as on the possibility to perform the synthesis, which only succeeds for the larger and smaller lanthanides (and lanthanum), but not for the intermediate ones. The synthesis mechanism has also been investigated for MOF-76(La), showing that partial esterification of the linker is responsible for quite low yields, although the unreacted materials can be recycled. We also evidenced an effect of the size of the rare-earth on the water stability, which increases with decreasing radius of the metal. The water stability could also be increased by substitution of the trimesate linker by 2-aminotrimesate, which in addition adds blue fluorescence to the frameworks. Xenon adsorption in MOF-76(La) was also investigated by *in situ* PXRD, revealing an interesting structural transformation.

The synthesis of MOFs with the mtn topology containing Ti^{3+} was also addressed, by using $TiCl_3(THF)_3$ obtained from $(TiCl_3)_3AlCl_3$ as cheap precursor. NH_2-MIL-101(Ti^{III}) was successfully obtained as the first Ti^{3+}-based MOF with this topology containing functionalities on its linkers. Other MOFs with the same topology could not be obtained by the same procedure, while substituting 2-aminoterephthalate by other types of linkers. Elemental and solution state NMR analyses enabled to determine that the clusters of the MOF contain chloride as charge balancing anion, and strongly bound DMF molecules that can be partly decoordinated. Once activated under appropriate conditions,

as determined by *in situ* PXRD, the MOF displays enhanced affinity for H_2 compared to the previously described MIL-101(Ti).

Finally, the introduction of structural defects into the model MOF HKUST-1, obtained by salt-assisted mechanochemical methods and different post-synthetic treatments, has been investigated. It was shown, by combination of multiple characterization methods, that treatment with methanol induced the creation of Cu^I defects, whereas treatment with ethanol created defects in the form of free –COOH functions. Synthesis of the same MOF using liquid-assisted grinding resulted in a MOF with a very low amount of structural defects, even compared to solvothermally obtained single crystals, which contained a low amount of Cu^I defects. It was shown that carboxylic acid defects have a negative impact on CO_2 sorption and catalytic cyclopropanation, whereas the presence of Cu^I defects was able to partly counteract the poisoning effect on catalysis. Overall, defect-free HKUST-1 obtained from liquid-assisted grinding seems to be the best material for catalytic cyclopropanation; the solvothermally obtained large crystals with small amounts of Cu^I defects showed the highest CO_2 gravimetric uptake.

Although MOFs are becoming more and more popular, and despite industrial applications timidly emerging, control on the synthesis of those materials remains challenging. The work presented in this thesis mainly aims at improving the sustainable production of MOFs containing trimesate linkers, with well-characterized structures, as well as at the introduction of new types of active sites, under the form of second (“exotic”) metals, amine functions and defects, by easy to implement synthetic approaches. Those materials may find use in multiple applications, such as catalysis and gas sorption.

Abbreviations

AAS	**A**tomic **A**bsorption **S**pectroscopy
ATR	**A**ttenuated **T**otal **R**eflectance
BTC^{3-}	**B**enzene-1,3,5-**t**ri**c**arboxylate
DSC	**D**ifferential **S**canning **C**alorimetry
ESRF	**E**uropean **S**ynchrotron **R**adiation **F**acility
FTIR	**F**ourier **T**ransform **I**nfrared **S**pectroscopy
HPLC	**H**igh-**P**erformance **L**iquid **C**hromatography
ICP-OES	**I**nductively **C**oupled **P**lasma – **O**ptical **E**mission **S**pectroscopy
IR	**I**nfra**r**ed
MIL	**M**atériaux de l'**I**nstitut **L**avoisier
MOF	**M**etal-**O**rganic **F**ramework
N/A	**N**ot **A**vailable
NMR	**N**uclear **M**agnetic **R**esonance
PCT	**P**ressure-**C**omposition isotherms
PXRD	**P**owder **X**-**R**ay **D**iffraction
SCXRD	**S**ingle **C**rystal **X**-**R**ay **D**iffraction
SNBL	**S**wiss-**N**orwegian **B**eam**l**ines
S-PXRD	**S**ynchrotron **P**owder **X**-**R**ay **D**iffraction
TGA	**T**hermal **G**ravimetric **A**nalysis
VT-PXRD	**V**ariable-**T**emperature **P**owder **X**-**R**ay **D**iffraction
XPS	**X**-ray **P**hotoelectron **S**pectroscopy
XRD	**X**-**R**ay **D**iffraction

CHAPTER I

State of the Art

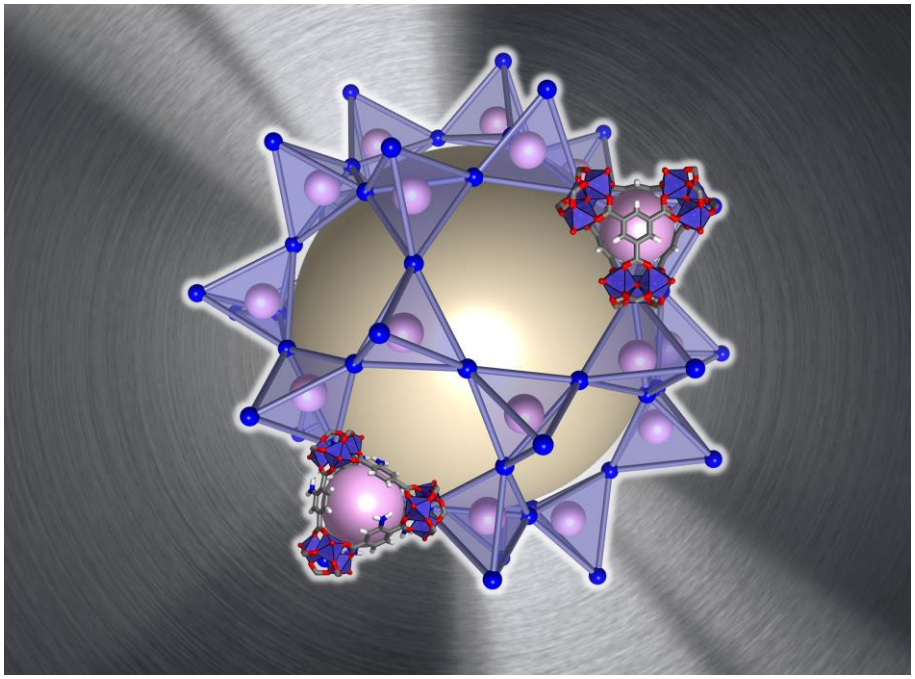

Chapter I - Introduction

1. State of the Art

1.1. Metal-organic frameworks

Metal-organic frameworks (MOFs) are defined as coordination polymers with an open framework containing potential voids.[1] Such frameworks are formed by the combination of metal centres or clusters, which are sometimes called *secondary building units* (SBUs),[2] and, usually rigid, bridging ligands, called *linkers*. Those materials are most of the time crystalline, and can possess permanent porosity. For those reasons, MOFs have great potential in many fields such as sorption of toxic molecules, ions [3,4,5,6] or greenhouse gases,[7,8,9] energy storage and conversion,[10,11,12,13,14] drug delivery,[15,16] sensing applications,[17,18] *etc*.

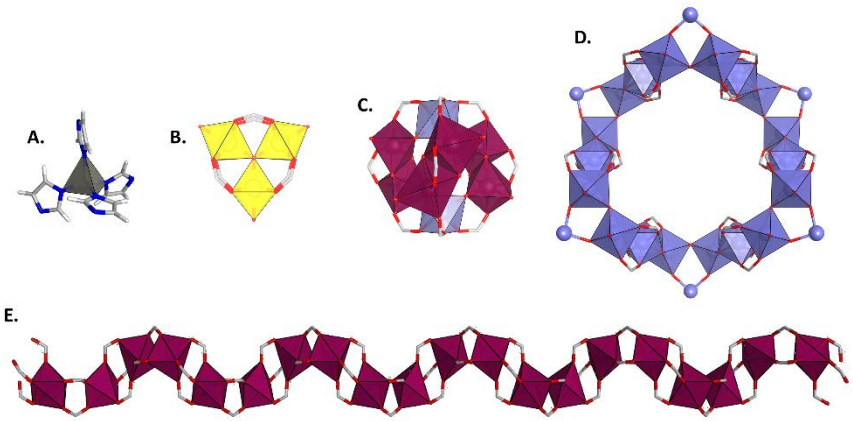

Figure I-1. Illustration of the variability of types of metal centers and clusters that can be found in MOFs: isolated metal centers ((**A.**) ZIF-8), clusters ((**B.**) MIL-100 and MIL-101, (**C.**) MIL-110 and (**D.**) MIL-96) and infinite chains ((**E.**) MOF-76). Polyhedra represent metal centers, part of linkers are represented with carbon, oxygen, nitrogen and hydrogen in grey, red, blue and white respectively.

The metal centers can be either isolated metal cations, small or large cluster units, or can even be infinite chains (Figure I-1).[19] Furthermore, MOFs can be mono-, bi-, or multimetallic with up to 10 different metals in the same structure.[20,21] The organic linkers generally

have at least two coordinating functions that serve as struts bridging between the metal centers or clusters of the MOF to construct the framework. Those linkers can be bidimensionnal (e.g. terephthalate, trimesate, imidazolate, etc.) or tridimensional (e.g. 1,3,5,7-adamantanetetracarboxylate) (Figure I-2).[22] A MOF material can be built from one or several types of different linkers, leading to a quasi-infinite variety of possible structures.[23] The obtained frameworks can have different topologies and manifest different types of porous networks, with either channels or spherical shapes, or combinations of several types of interconnected pores that can lead to very complex networks (Figure I-3).[24]

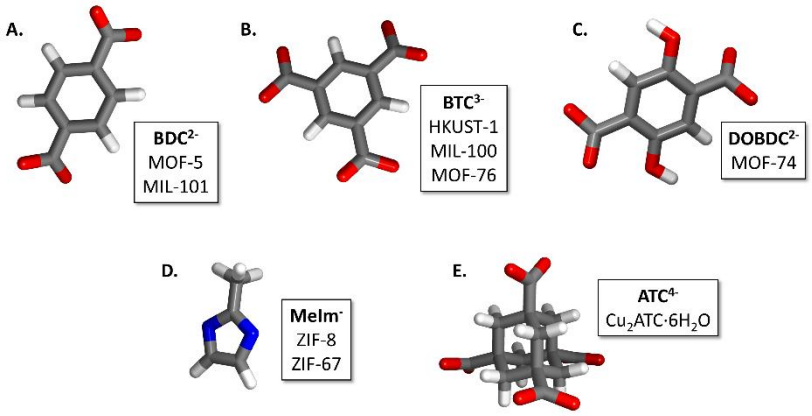

Figure I-2. Example of bidimensionnal ((**A.**) terephthalate (BDC^{2-}), (**B.**) trimesate (BTC^{3-}), (**C.**) dihydroxyterephthalate ($DOBDC^{2-}$) and (**D.**) methylimidazolate) and tridimensional ((**E**) 1,3,5,7-adamantanetetracarboxylate (ATC^{4-})) linkers that can be used for the synthesis of MOFs, with some examples of representative porous MOFs for each.

The availability of the pores for practical applications not only depends on the respective size of the pores composing the network, but also on the pore opening (i.e. pore windows, or apertures), which can be much smaller than the pore itself.[25] For this reason, it is possible to obtain mesoporous frameworks having only microporous windows (e.g. MIL-100 and MIL-101, see below).

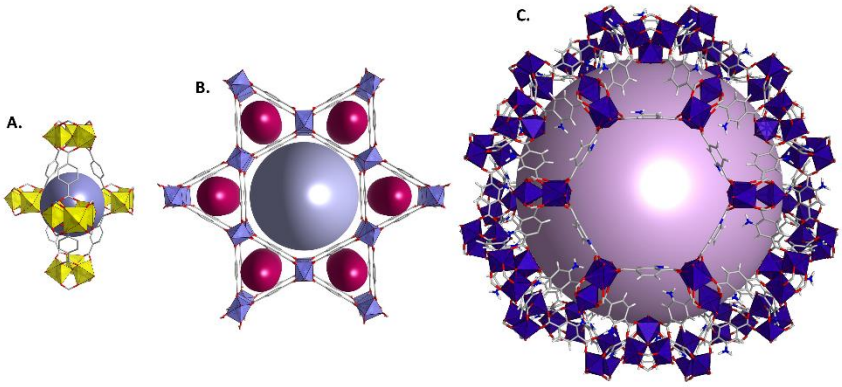

Figure I-3. Illustration of the types of pores that can be present in MOFs. (**A.**) small spherical pores in MOF-235, (**B.**) two types of porous channels in MIL-96 and (**C.**) mesoporous spherical pores in MIL-101. Tetrahedrons represent metals centers; carbon, oxygen, nitrogen and hydrogen are represented in grey, red, blue and white respectively.

An important consideration in MOF design, especially when building structures with very large pores, is the possibility to use extended linkers. Indeed, it has been demonstrated that some isotopological frameworks with increasing pore size can be obtained when using linkers with identical denticity and coordinating moieties but having an extended backbone (Figure I-4). An early example of this principle has been shown with MOF-5 derivatives.[26] This principle has since been applied to various other MOFs, including extended members of the MIL-100 and MIL-101 family.[27] However, when using extended linkers to increase the size of the cavities inside MOFs, interpenetration of the formed frameworks often occurs (Figure I-4), leading to loss of available pore volume and surface area.[28]

Compared to other porous materials, such as zeolites and carbon materials, MOFs present the advantage of enabling a virtually infinite variety of metal and linker combinations. Furthermore, their well-defined crystal structure enables to build custom-made materials for every type of application, with tunable pores bearing given

functionalities at well-located positions. Such specific sites can in theory be designed for interaction with very specific molecules, similarly to the interaction of substrates in enzymatic pockets. However, as their discovery is quite recent compared to other porous materials that are used for industrial applications for ages, their implementation in practical applications is only emerging at this point.

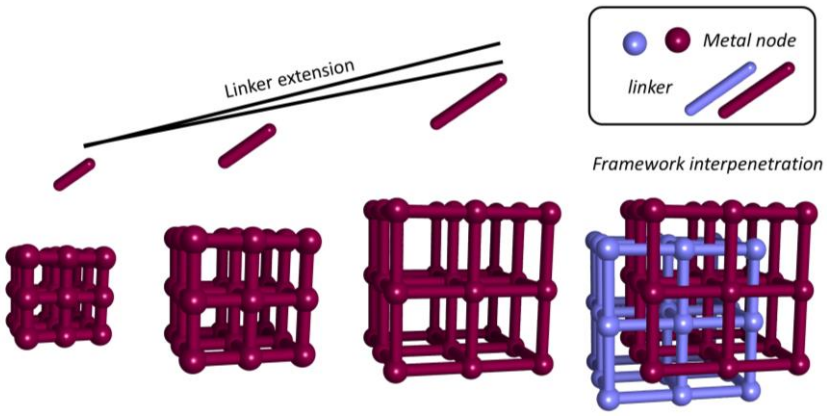

Figure I-4. Illustration of linker extension and interpenetration of MOFs that can occur during the synthesis of MOFs with extended linkers.

1.1.1. Stability

When considering applications involving harsh conditions, the stability of MOF materials is of outermost importance. Indeed, under practical conditions the materials can be exposed to solvents, steam, heat, *etc*.).[29] Stability tests are often performed by assessing material's crystallinity through PXRD and evaluating whether its porosity is maintained by using nitrogen physisorption analysis before and after exposure to the required conditions.[30,31]

The first discovered frameworks (also known at the time as coordination polymers) were generally composed of rather weakly bound metals and linkers, or very flexible linkers, resulting in structures that easily collapsed. This is directly related to the fact that the formation of weaker bonds is reversible and thus facilitates

crystallization and the discovery of new crystalline structures. However, over the years new MOFs presenting better stability, based on strongly interacting and more rigid building units, have been developed to overcome practical limitations imposed by the stability issues.[29]

The stability of MOF structures is often directly related to the strength of Lewis acid/base interactions between metal and linker moieties. It can generally be stated that the interaction between hard acids and hard bases, or between soft acids and soft bases, according to the HSAB (Hard and Soft Acids and Bases) theory of Pearson, are rather strong.[29] According to this principle, MOFs based on the combination of high-valency metals and oxygenated linkers such as carboxylates often lead to the formation of rather stable structures, which are therefore more suitable for applications under harsh conditions. For the same reasons, good stability is also observed for MOFs based on low-valency metals and azolate linkers. The main difference between both types of MOFs is that the ones based on carboxylates and high-valency metals present a higher stability in acidic media, whereas low-valency metal-azolate MOFs are more stable in basic media. This can be explained by the strong interactions between high-valency metals and hydroxide species and the pK_a of the linkers, giving paths to the decomposition of the MOFs in the respective media.

1.1.2. Activation

As MOFs are often used in applications requiring access to the framework's pores, it is essential to be able to empty those cavities first. Indeed, the synthesis methods used to obtain MOF materials often result in the pores being filled with residual unreacted materials (e.g. protonated linkers or metal salts) and solvents. The procedures allowing the removal of trapped materials from the porous network in MOFs are commonly called "*activation*".[32]

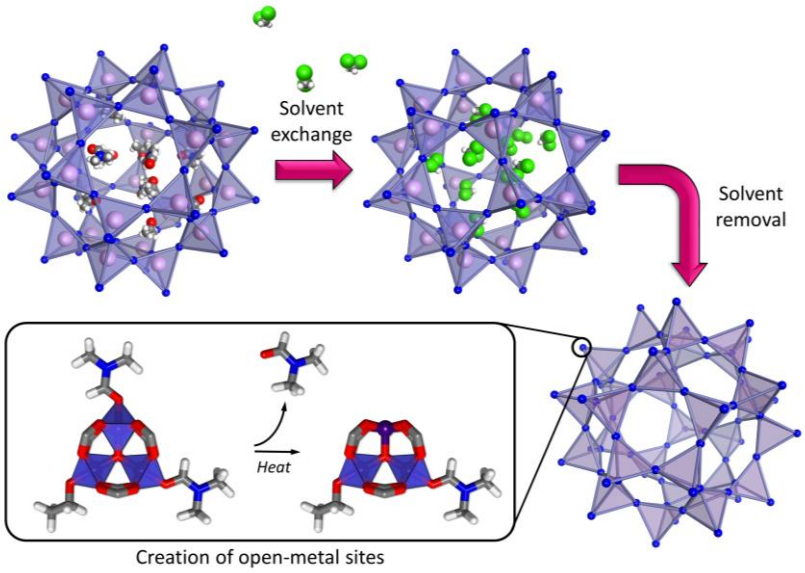

Figure I-5. Scheme of a typical MOF activation procedure: exchange of solvent inside pores by a lower surface tension solvent, evacuation of the solvent under vacuum to empty pores, and (inset) creation of open-metal sites by removal of coordinated solvents (example of MIL-101(Ti^{III})).[33]

Unreacted materials are often removed by thorough washing in appropriate solvents that are able to dissolve the species occupying the pores, without dissolving the MOF. The solvent molecules that remain in the MOF's pores upon washing are subsequently removed by heating under vacuum or at ambient pressure (Figure I-5).[34] The use of supercritical CO_2 to exchange solvents allows avoiding capillary forces that normally apply on the pore walls during the evacuation of solvent molecules and is therefore very useful when working with rather fragile frameworks.[35] Avoiding capillary forces during MOF activation can also be achieved by freeze-drying methods.[32] Similarly, capillary forces can be lowered by exchanging the solvents in the pores for those having lower surface tension, followed by thermal treatment. More recently, it has been reported that MOFs (among which MIL-101(Fe)-NH_2) can be photothermally activated by simple irradiation with a UV light source, generating the heat required to remove the trapped solvents even without applying vacuum.[36]

Interestingly, some MOFs enable the creation of so-called *open-metal sites* (OMSs), or *coordinatively unsaturated sites* (CUSs, aslo known as open-metal sites) that can be achieved by the removal of solvent molecules coordinated on the metal sites (Figure I-5).[37] This is generally performed by thermal treatment, often under vacuum, sometimes after solvent exchange if the coordinated solvents have too high boiling points to be removed by direct heating (e.g. exchange of DMF for methanol).[34] Such solvent exchange is classically performed over several days, eventually under reflux or higher temperature (under autogenous pressure) or by Soxhlet extraction. However, recent studies about solvents exchange kinetics in MOFs show that this process often occurs over much shorter durations and at lower temperatures than the ones that are sometimes routinely used,[38] enabling to envisage greener activation strategies. The presence of CUSs is useful mainly for applications in catalysis[39,40] and gas sorption or separation[41] as those can function as active sites for interacting with substrate molecules. It is worth mentioning that only a small fraction of the plethora of MOFs described in the literature possesses potential open-metal sites, however the enormous potential of CUSs makes the MOFs possessing them amongst the most widely studied ones (i.e. MIL-101, MIL-100, HKUST-1, MOF-74 *etc.*).[37]

The choice of the applied activation procedure depends on the stability and the nature of the MOF and its building blocks, and the solubility of the unreacted materials remaining in the pores. Structural integrity should be verified after this process to ensure that no degradation of the framework occurred, and the efficiency of the activation process should be evaluated by nitrogen physisorption analysis.[34]

1.1.3. Defects

MOFs, although being crystalline most of the time, usually contain various amounts of structural defects. The latter can originate from their synthesis or can be introduced post-synthetically and can be present in different forms. Defects can roughly be grouped in missing-linker and

missing-metal defects.[42] In all cases, the framework must achieve charge neutrality. Therefore, when missing linker defects are present, anions, often under the form of hydroxides or oxides, complete the coordination environment of the metals, and vice versa.[43] Such defects can be present in the bulk of the material, and are always present at the surface, where they can hinder diffusion processes into the material.[44]

The presence and nature of structural defects in MOFs is often difficult to assess and requires a combination of various analytical techniques probing the coordination of linkers and metals, as well as the metal oxidation states.[45] The presence of defects also leads to new properties of the MOF materials that are not predicted based on the average crystal structure. Such properties can either be bad for the material's performance, but sometimes defects can enhance gas sorption or catalytic properties,[46,47] for example by the creation of new coordination vacancies. Therefore, defect-engineering in MOF materials is a current area of research.[48] Addition of defects in MOFs can often be performed by adding modulators in the reaction media. Modulators are chemical species that enter in competition with the linker for coordination to the metal, and are often monocarboxylic acids. Those species can then take the place of some of the linkers to create missing-linker defects.[49] Defects can also be introduced in MOFs by variation of the engaged stoichiometry between reactants during the synthesis.[50]

1.2. MOF syntheses

1.2.1. Classical synthesis pathways

The early discovery of MOFs was mainly based on the use of solvothermal methods, in which metal precursors and linkers are dissolved in an appropriate solvent, followed by generally prolonged heating enabling crystallization of the MOFs.[51] The choice of solvent is generally performed based on the solubility of the precursors, which explains that *N*,*N*-dimethylformamide (DMF) or similar solvents such as diethylformamide (DEF) are routinely used, as they easily dissolve

both organic and inorganic species.[52] Heating is often performed at temperatures well above the boiling point of the solvent, requiring the use of high-pressure autoclaves. The solvothermal approach often allows obtaining products in a form of single-crystals, which facilitates their structural analysis. However, this method is quite energy demanding and the reaction often proceeds in a "black box" manner and mostly relies on good luck to obtain the desired framework, as many parameters such as temperature, reaction time, the presence of crystallization modulators, the concentration of reactants, the type of solvent, *etc*. have a determining impact on the resulting MOF. Therefore, high-throughput screening methods have been developed to facilitate the investigation of the impact of reaction parameters on the obtained MOFs. These high-throughput methods generally rely on the use of custom-made multi-well autoclaves, allowing performing dozens of syntheses with variations in the composition of the reaction medium in parallel.[53]

Solvothermal methods require high temperatures and pressures, making *in situ* investigations is quite complicated, and therefore the formation mechanism of MOFs under those conditions remains quite enigmatic. For some systems however, the mechanisms could be studied by dedicated methods. This is for example the case of the formation of NH_2-MIL-101(Al), which could be studied by *in situ* PXRD,[54] and of MIL-100(Al), for which the crystal growth was be monitored by NMR (^{1}H and ^{27}Al nuclei), by using dedicated equipment that withstands high pressures and temperatures.[55]

To favour slow crystallization of a porous structure instead of rapid precipitation of an amorphous solid, slow release of one of the reactive species in the reaction medium can be an alternative to classical solvothermal methods. Based on this, electrochemical methods, involving a dissolution of a metallic electrode to slowly release the metal cations have been developed, and later were industrialized for the production of HKUST-1, as an example.[56] Another strategy involves the use of preformed metals clusters, enabling to avoid the cluster

formation step during the synthesis and thus avoiding the formation of other types of (undesirable) SBUs that could lead to the formation of other topologies.[57]

1.2.2. Green methodologies

Different methods exist to render synthetic protocols for MOFs and other chemicals more environmentally friendly. Such methodologies are responding to the twelve principles of *green chemistry* (see Figure I-6), which aim at reducing or eliminating the generation of hazardous and polluting substances and rendering processes more energy-efficient.[58]

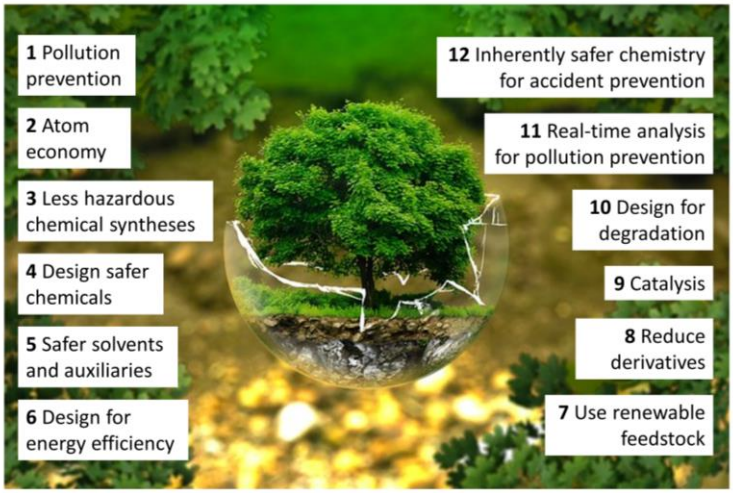

Figure I-6. The 12 principles of green chemistry.

Mechanochemistry can be used for making the synthesis of MOFs greener. Indeed, this strategy involves grinding solid reactants together for enabling the formation of the framework. This allows using less (in the case of liquid-assisted grinding) or no solvents (for dry milling) for the synthesis of MOFs.[59] However, as the reaction if often incomplete, removal of unreacted materials from the obtained MOF requires thorough washing procedures to empty their pores. Furthermore, mechanochemical processes consume significant amounts of energy, and as mechanical stresses are involved, the porosity of materials is not

always guaranteed, as the formed MOFs can be destroyed during the grinding process.[60] Furthermore, mechanical stresses can also lead to the presence of more defects in the structure than when using conventional synthetic strategies.[61]

Solvothermal reactions can be performed using energy more efficiently for heating by using microwave technology. Indeed, using microwaves allows to heat the reaction mixture much faster than with conventional heating.[62] Furthermore, as heating is achieved much faster, the synthesis of MOFs under microwave irradiation can proceed several orders of magnitude faster than when using conventional methods.[63]

To make MOF production more energy efficient, lowering the reaction temperatures is the most efficient way. If a reaction can be performed at room temperature, production costs are drastically lowered compared to demanding solvothermal processes.[64] Furthermore, this involves that reactions can be performed under ambient pressure, removing the need for high-pressure reactors. However, concerning MOF synthesis strategies, reducing the heat will not only play on kinetics and slow down the reaction, but it will also change the solvent's chemistry, leading to amorphous materials or completely different topologies.[65] Obtaining a given MOF at lower reactions temperatures is however possible, but often involves the need for changing the complete reaction system, including the solvent system and/or the used reactants.[66]

The most straightforward method to render MOF production processes more sustainable is to use greener chemicals. This involves the use of less polluting and toxic solvents, avoiding the classical DMF or DEF and replacing them by greener alternatives.[67] Recently, alternatives to such high-boiling point polar solvents, such as the bio-based solvent Cyrene® (dihydrolevoglucosenone), were demonstrated in synthesis of MOFs.[68] However, such solvents are still very expensive compared to common ones. The greenest of all solvents alternatives is the use of water, as it is non-toxic, non-flammable and renewable.

Alcohols can also be regarded as green solvents.[69] However, as solvents participate in coordination processes, and thus in the MOF formation mechanism, switching from one solvent system to another for the synthesis of a given MOF is not always straightforward and needs experimental development. Switching to greener solvents (e.g. water, alcohols, *etc.*) for the washing of unreacted materials and activation of the formed MOF materials is also part of the improvement of synthetic strategies. However, some solvents might as well dissolve the MOF itself, and attention must thus be paid to the framework stability in the solvent used for the washing procedures as well.

Using greener precursors is also a useful strategy for greener MOF synthetic procedures. This can be performed for example by choosing metal salts with benign anions (i.e. acetates, sulfates, oxides or hydroxides) instead of chlorides or nitrates which are not environmentally friendly.[70] Using linker salts instead of protonated acids also improves the green aspect of MOF production processes.[71] The use of renewable bio-based linkers for the synthesis of MOFs is also another strategy to improve the sustainability of MOF production, however this alternative will inevitably lead to the formation of other framework structures.[70]

1.2.3. Functionalities and post-functionalization strategies

As they contain both metal centres and organic linkers, MOFs are very tuneable in nature. Their properties can be for example be modulated by varying the size and charge of the metal, which will have an impact on the interaction strength with respective guest molecules, generally according to the HSAB principle.[72]

The presence of organic linkers is also a valuable tool to add functionalities into MOFs. The most straightforward example is the addition of amine functions that do not participate in the coordination network on aromatic rings of linkers.[73] Such amine functions can be

added for example for their basicity, introducing possibility to interact with acidic guest molecules.[74]

Although the principle of changing metals and adding linker functionalities in MOFs seems a straightforward method to modulate the properties of a given framework, doing so by direct synthesis is often quite tricky.[75] Indeed, each metal possesses its particular chemistry and interactions with solvent molecules, as well as differences in coordination numbers and propensity to form either clusters or isolated metal centres.[76] The same problem arises when functionalities are added on linkers, especially when such functionalities can participate in coordination with metals (e.g. amines, alcohols, carboxylates, *etc*.).[77]

To solve this problem, post-synthetic modification (PSM) strategies have been developed. Instead of directly adding the desired metals or functionalities in the reaction medium from which the MOF crystallizes, these methods rely on the modification of pre-formed MOFs to add particular functions in a subsequent step.[75,77]

Metals can be added through post-synthetic exchange, by soaking the MOF into a solution containing a salt of the new metal to incorporate into the framework, allowing exchange with the metal centres of the preformed structure. Such exchange can be partial, leading to bimetallic MOFs, or total.[78] The exchange efficiency depends on the nature of both the metal in the preformed MOF and of the metal that needs to be incorporated, with most efficient exchanges occurring when the newly formed bonds between metal centres and linker are of increasing strength.[79] However, such metal exchange is not always efficient, and sometimes leads to structural transformation of the template framework.[80] Furthermore, exchanging metals in preformed MOFs is not the most economical and environmentally friendly synthetic approach, as it often needs an excess of metal to reach full exchange, and inevitably leads to metal waste.

Functionalities can be added on linkers as well, through the use of classical organic transformation reactions (Figure I-7). For example,

when using linker derivatives with amine functions that cannot be added through direct synthesis due to the coordinating interactions of the amine with the metal, nitro derivatives, which are less coordinating, can be used, or can be introduced post-synthetically by nitration. The nitro function of the resulting framework can subsequently be reduced into amines (Figure I-7, A. and B.).[81]

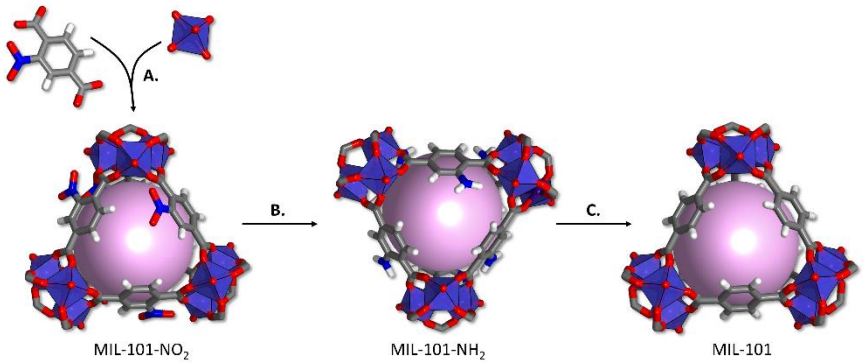

Figure I-7. Strategies to incorporate or remove functionalities on the linkers of MOFs : (**A.**) direct synthesis from functionalized linker, (**B.**) by post-synthetic organic transformations of linker functionalities and (**C.**) defunctionalization.

On the opposite, MOFs that can only directly be synthesized with functionalized linkers can be de-functionalized to achieve the non-functionalized MOF. This is for example the case of NH_2-MIL-101(Al), which can be synthesized directly from 2-aminoterephthalic acid as linker source, whereas its non-functionalized counterpart, MIL-101(Al) cannot be directly synthesized from terephthalic acid (Figure I-7, C.).[82] However, elimination of the amine functions in NH_2-MIL-101(Al) can be performed by reaction with *tert*-butyl nitrite to form a diazo derivative that can be reduced by heating in methanol, leading to the unfunctionalized MIL-101(Al).[83]

Such post-functionalization strategies of linker functionalities on MOFs are quite versatile. However, the main drawback is that such strategies can only be applied with frameworks that are stable enough to withstand the organic reaction conditions.[30]

1.3. Applications

Thanks to their tuneable pores and open-metal sites, MOFs can be used for many applications (Figure I-8). Those range from gas sorption, extraction of various molecules, drug release, sensing, to biomedical (drug delivery) and catalysis. The main applications that are covered in this thesis are described in the following paragraphs.

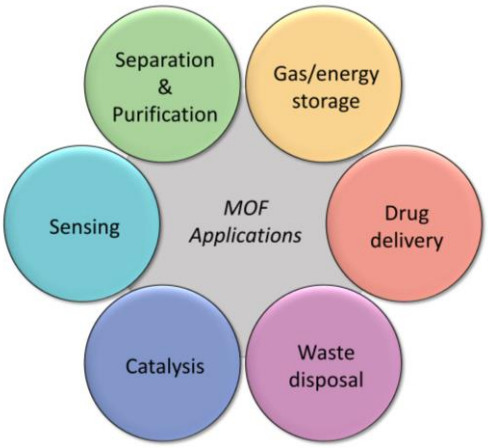

Figure I-8. Main applications of MOF materials.

1.3.1. Catalysis

MOFs are ideal candidates for heterogeneous catalysis, which is a key technology for organic chemistry and the chemical industry, not only because of their adjustable porosity but also because the nearly infinite possible combinations of metal nodes and organic linkers that allow modulating the catalytic activity of the material.[84] This, in combination with the structural uniformity of well-defined single-site catalytic centres in the framework, distinguishes MOFs from other porous heterogeneous catalysts, such as porous organic polymers or activated carbon and even allows bridging the gap between homogeneous and heterogeneous catalysts.[85] In the past, MOFs were known to be thermally unstable and to decompose in water and therefore considered bad candidates as catalysts in most usual reaction conditions.[86] However, recently much improvement has been achieved

in the design of more stable MOFs, as stated above, opening new doors for such type of applications.

The use of high valence metals in MOFs can also have a positive effect on their catalytic activity, as they are hard Lewis acids that can also create Brønsted acidic sites by polarisation of O-H bonds.[87] It is known that the activity arising from the metal centres, namely Lewis and/or Brønsted acidity, is not only due to coordinatively unsaturated sites inherent to the MOF's crystal structure, but can also be induced by the presence of defects.[88]

The catalytic activity of MOFs is not limited to acidity. One of the other activities that can be added to MOFs is exactly the opposite: basicity. This can be done by adding functionalities on the linkers, such as amine groups.[89] This basic activity can be combined with the acidity of CUSs, thus leading to bifunctional acid-base catalysts.[90] Such catalysts cannot be obtained directly by assembly of acids and bases because of the neutralisation of both species in solution. The right choice of metal centre or the use of special linkers (*e.g.* linkers containing an active complex) may also render MOFs able to perform oxidation or reduction reactions.[91] Finally, chiral ligands can also be added in MOFs to induce enantioselective catalysis.[92] It should be noted that catalytic reactions can happen either in the bulk porous network of the MOF, or at its surface. Distinction between both phenomena can be done through means of modelization of reaction kinetics.[93]

1.3.2. Gas sorption and separation

One of the key applications for MOFs concerns gas separation and storage, because they might greatly reduce operations costs compared to existing technologies. Indeed, concerning gas separation the most widely used technology is based on cryogenic distillation.[94] MOFs can separate gases by acting as sieves, by adapting the pore size according to the size of the gas molecules, enabling the smaller ones to pass through the framework whereas larger molecules cannot enter the pore system.[95] Other than this size-specific separation, different active sites can be added to the MOFs to generate interactions between the

framework and the gas molecules. Such sites can for example be CUSs, which can coordinate to the lone pairs of some gases (e.g. NH_3, SO_2, CO_2, *etc.*).[96,97]

When targeting applications, the composition of a gas phase must be seriously considered. Those are complex mixtures that include for example water vapour, which is a major constituent of industrial fumes, from which the elimination of carbon dioxide is a major concern.[31] Indeed, the capture materials must not only be able to withstand exposure to such constituents, but must also be able to interact specifically with the target gas molecule. Therefore, open-metal sites for example are not the best solution for removing CO_2 in industrial exhausts, as those sites will have the tendency to coordinate much more strongly with water molecules.[98]

When it comes to selective adsorption of CO_2, separation based on size-selectivity is a suitable option, as this gas has a relatively small kinetic diameter (3.3 Å vs. 3.64 Å for N_2). For capture of carbon dioxide, specific functions can also be added to the linkers of MOFs, such as amines, which provide basic sites that are able to interact with acidic gases such as CO_2.[99] Such functionalization can even lead to the formation of carbamic acid and carbamate species upon interaction of CO_2 with the MOF (*i.e.* chemisorption).[100] Instead of adding amine functions on the linkers, affinity of the framework for CO_2 can also be increased through functionalization of the metal sites with ethylenediamine or other polyamines that can coordinatively attach to the MOF while exposing the other amino function for interaction with carbon dioxide.[101] Interaction for CO_2 can also be enhanced by other functions such as open nitrogen sites (e;g. triazoles and tetrazoles), alkyl, hydroxyl or carboxylic acid groups, or by the use of phosphonate or sulfonate linkers that both enhance the stability of the frameworks towards water, hence improving their ability for CO_2 capture related applications.[102] Is should be noted that under low pressure, the adsorption capacity towards CO_2 is mainly dominated by the heat of adsorption (*i.e.* improved by the presence of favorable adsorption sites,

either CUSs or linker functionalities), while at higher pressures the surface area of the MOF becomes the dominating factor.[102] Unfortunately, it is difficult to assess which MOFs present the highest CO_2 uptake as different studies are often performed under very different conditions, not allowing for direct comparisons, as CO_2 adsorption is greatly temperature-dependent.[103] This is also a major concern, as most MOF materials are studied for this purpose at relatively low temperatures (usually up to 30°C), while industrial applications often require a stability towards hot exhaust gases, greatly exceeding those temperatures. Recently, a zinc-based MOF, named CALF-20 (Calgary Framework), possessing very good selectivity towards CO_2 and a very high stability towards steam and wet acid gases has been described.[104] This MOF is synthesized through a scalable procedure from cheap commercially available linkers (triazole and oxalate) in water and methanol. Owing to its interesting properties, this MOF has been implemented for pilot-scale post-combustion capture of CO_2 in a cement plant, demonstrating that MOFs can efficiently be implemented for this purpose.[105,106]

Gas storage is also of interest for energy purposes. This mainly concerns the storage of hydrogen (but also methane), as it possesses a high energy density and releases only water upon oxidation and is therefore considered as a green energy alternative.[107] However, hydrogen is also an explosive gas for which storage is nowadays mainly performed in high-pressure vessels. Suitable MOFs are able to adsorb quite a lot of hydrogen (up to 10 wt.% or 40 g H_2/L at 100 bar and 77 K) under softer conditions.[108] Practically, a container filled with an appropriate MOF material can store more hydrogen under similar temperature and pressure conditions than an empty container, or the same amount under lower pressure and/or higher temperature. This mainly occurs thank to the interaction between the H_2 molecules and the MOF's surface, hydrogen sorption in porous (non-functionalized) materials being roughly a linear function of surface area.[109] However, it is known that the interaction with some types of metal sites in materials used for hydrogen sorption are favourable (i.e. Cr^{2+} and

Ti^{3+}).[110,111] Therefore, designing MOFs with suitable types of CUSs is of interest in the development of hydrogen storage technologies.[112]

1.3.3. Adsorption from solutions

MOFs are also useful for separation of species in solution, which are of importance in various applications such as the removal of pollutants from drinking water,[113,114] or even the recovery of precious metals from seawater for example.[115] Similarly to adsorption of gases, several active sites can be exploited in MOFs for adsorption from solutions. For organic molecules, those include interactions of the molecules by coordination with the MOF's metal centres, as well as interactions with the organic linkers of the MOFs, for example by π-π interactions when aromatic systems are involved, or through interaction with linker functionalities.[116] For metals, interactions can involve coordination with specific functionalities of the linker (amines, hydroxyls, thiols etc.).[117,118] Another way to remove metals from solution is by reduction to the metallic state to trap metal (nano)particles inside the MOF, using redox active sites present in the MOF.[115]

1.4. Towards industrialization of MOFs

1.4.1. General considerations

With some scarce exceptions (like noble metal- or lanthanide-based MOFs), the most expensive raw material to synthesize MOFs is the linker source.[119] Furthermore, linkers are often derived from non-renewable resources (petrochemistry). Lowering the cost and enhancing the sustainability of linker syntheses can be performed in several ways. One convenient way that gains more and more interest is by using renewable linkers, like amino acids. Another manner is by using widely available linkers that are produced on large scale, mainly for the production of other chemicals, or by recycling from waste (e.g. terephthalate, that is used to make polyterephthalate, that can be decomposed back to serve as raw material for MOF synthesis).[120] The design of custom linkers for MOFs to achieve a desired topology

however usually requires linker molecules that are sometimes not even commercial, driving up their production cost.

When considering large-scale production, the availability, price and recyclability of solvents must also be taken into account, as well as their toxicity and eventual flammability, as they will be used in large amounts.[119] Lab-scale production processes often involve solvents that cause problems for scale-up because of their dangerousness. Ideally, syntheses should be performed using as low amounts as solvent as possible and the solvent of choice is water, especially with transition of industrial processes to greener pathways. Indeed, water is widely available, at a negligible cost and is non-toxic and does not have flammability issues. Further attention must also be paid to the recycling of the solvents, which can drive up production costs depending on the energy required (e.g. more volatile solvents can be recycled by distillation, whereas non-volatile solvents require more energy or different recycling processes).

Particular attention must also be paid to the choice of the metal source for the syntheses. Ideally, oxides, carbonates, acetates or sulfate salts should be used as they do not possess corrosive properties that are inherent to chlorides or explosiveness inherent to nitrates for example.[121] Given that most large-scale reactors are made of stainless steel, avoiding corrosiveness of reactants is of major concern. Furthermore, the price of the metal source should be taken into account. Some metal salts are waste produced on large scale from other industrial processes and could thus serve as widely available cheap sources for MOF production processes. Iron sulfate is an example, as it is produced as a waste material from the steel industry.

Although nano-sized MOF materials can easily be processed in the lab (i.e. through centrifugation), this is not the case for large-scale processing. In the latter case, particle size is a major concern as too small particles can be a problem for processability, create toxicity issues as workers can inhale dust, that is also responsible for explosion hazard. For those reasons, ideal particle size should be in the micrometer range

or above. Shaping of MOFs and their introduction into composite materials, as this enables their use in other forms than powders, is also crucial for their commercialization and application in MOF-based devices.[122]

1.4.2. MOF manufacturing companies

Table I-1. Main companies commercializing MOFs or MOF-related technologies.

Company	Head office
BASF	Germany
Advanced Materials Center Dresden	Germany
SiKÉMIA	France
NovoMOF	Switzerland
Promethean particles	UK
MOF Technologies	Ireland
MOFapps	Norway
ProfMOF	Norway
Sigma-Aldrich	USA
Strem chemicals	USA
Framergy	USA
Mosaic Materials	USA
NuMat	USA
MOFgen Ltd.	UK
Chemsoon	China

Over the past decades, the main industrial manufacturer of MOF materials has been BASF, that has pioneered the large-scale production and manufacturing of a dozen of MOFs, including Basolite® C300 and Basolite ® F300 (better known as HKUST-1 and MIL-100(Fe)). Those MOFs are produced through patented processes and are available for

researchers through chemical distributor (i.e. Sigma-Aldrich). However, those materials remain very expensive (i.e. about 4000 € for 500 g of Basolite ® F300 via Sigma Aldrich) and their textural properties measured in the lab are often quite different from the ones claimed by the manufacturer.[123]

Recent advances in MOF production, coupled with the many applications that they enable, led to the emergence of several MOF-related spin-out companies over the last years. Those are either focused on the development of a given application, relying on a specific MOF, commercialize a small catalogue of MOFs, or produce them on demand. Table I-1 summarizes the main companies that manufacture MOFs and/or develop MOF-related applications and the location of their head office.

1.5. Structural description of the MOFs covered in this Thesis

The different Chapters of this thesis all deal with a particular type of MOF, each having a different degree of structural complexity. Each type of MOF is described in the following paragraphs.

1.5.1. HKUST-1

HKUST-1 is one of the first MOFs that has been discovered, its first description dating back to 1999.[124] It was discovered at the Hong-Kong University of Science and Technology, where its name comes from. This MOF is based on simple bimetallic clusters being surrounded by four bridging carboxylates, leading to the formation of paddlewheel units. The carboxylates come from the commercially available trimesate, or benzene-1,3,5-tricarboxylate, linker. The network formed by the interconnection of cluster units by the linkers leads to the formation of three types of spherical pores (Figure I-9). Interestingly, the paddlewheel clusters are similar to that of copper(II) acetate, and not surprisingly the first MOF of this topology that was obtained was the monometallic copper derivative, HKUST-1(Cu). Later on, other monometallic derivatives have been obtained, based on various metals that either also have acetates with similar paddlewheel

structures (Cr^{II}, Mo^{II}),[125,126] or based on metals that do not exist as acetates with comparable structure ($Fe^{II,III}$, Ni^{II}, Zn^{II}, $Ru^{II,III}$, Mn^{II}, Fe^{II}, Co^{II}).[127,128,129,130,131] Later on, bimetallic and even trimetallic HKUST-1 derivatives have been obtained, incorporating several of the above-mentioned metals, and even including noble metals such as Rh or Pd.[132,133,134]

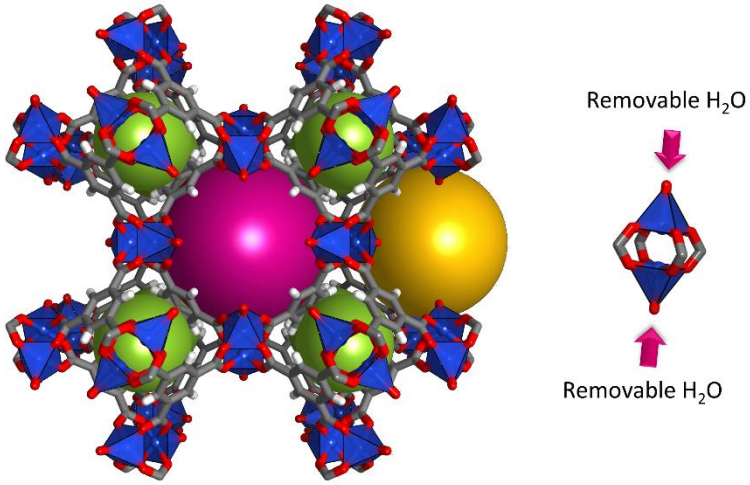

Figure I-9. Structure of HKUST-1 with three types of pores (represented by pink, green and orange spheres), with detail of paddlewheel cluster unit with removable solvent molecules. Metal centers are represented by blue tetrahedral, carbon, oxygen and hydrogen are represented in grey, red and white respectively.

When all metal centres of HKUST-1 are in the +II oxidation state, each individual metallic site can in theory be desolvated through thermal activation, leading to the creation of two open-metal sites per paddlewheel unit (Figure I-9). Those open-metal sites are key to the many explored applications of this type of MOF, as it enables interaction with guest molecules.[97] As HKUST-1 is based on, usually, low-valent metal centres in the +II oxidation state and carboxylate linkers, having weak acid/hard base interaction according to the HSAB principle, HKUST-1 is not particularly stable, especially in the presence of moisture.[98] However, as one of the first discovered MOFs, it has the advantage of having been widely studied, enabling to use this MOF as

"model" for extensive studies facilitated by existing knowledge, and which is also facilitated by the rather simple structure of the framework.

1.5.2. MOF-76

First discovered as its terbium analogue by Yaghi *et al.* in 2005, MOF-76 is a rare-earth based MOF, built of infinite rod-shaped SBUs, interconnected by trimesate linkers (Figure I-10).[76] MOF-76 presents open channels, structural flexibility upon heating and solvent removal and high thermal stability up to about 600°C.[135,136,137] Each metal centre is surrounded by six oxygen atoms from the trimesate linkers. However, as lanthanide ions can have very high coordination numbers (usually comprised between 8 to 9, but possible up to 12, depending on the size of the lanthanide and the nature of ligands),[138] the remaining coordination sites, that are occupied by solvent molecules after synthesis, can be activated to create multiple CUSs.

MOF-76 is mostly obtained from solvothermal reaction, involving the use of DMF, or mixtures of this solvent with water and/or ethanol, with or without crystallization modulators.[139] It has also been demonstrated that particle shape and size can be controlled by modulating the synthesis parameters, for example by using crystallization modulators.[140] MOF-76 derivatives have been reported with a wide variety of metals, through the whole series of stable lanthanides (excluding promethium) and with lanthanum and yttrium as other rare-earth elements.[137,141] Due to the nature of those metals, derivatives made from, or doped with, Eu and Tb present respectively red and green fluorescence under UV irradiation, typical of complexes of those lanthanides. Multimetallic derivatives can be used for producing white light emission through control of the amount of each metal in the structure.[142] As some species have a quenching effect on the luminescence of this MOF, it can also be used for selective detection in solution (e.g. sensing of U^{VI}, antiobiotics, DMF, acetone, ethanol *etc.*).[143,144,139] The presence of lanthanides is also useful for exploiting the magnetic properties of those elements, MOF-76(Gd) for example presents a magnetocaloric effect depending on the solvation state of the

MOF.[145] Recently, it has been shown that the electrical resistivity of MOF-76(Nd) is sensitive to humidity level and this MOF can thus be used as a sensor.[146] However, it is noticeable that there is a lack of information in the literature about the stability of MOF-76 derivatives towards water, and the structural integrity of the MOF after exposure to humidity has not been assessed. As most MOFs, MOF-76 derivatives have also been studied for adsorption of various gases, such as CH_4, CO_2, N_2 and H_2.[135,146]

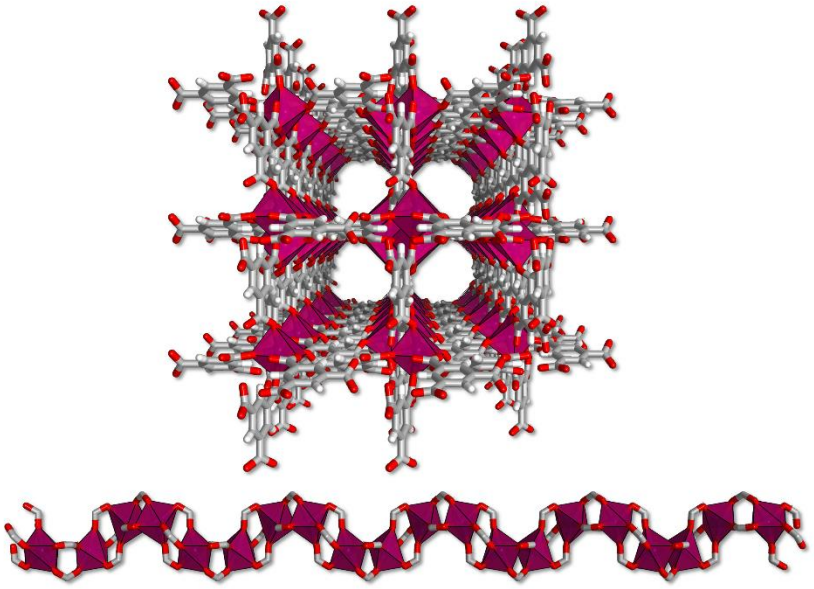

Figure I-10. Structure of MOF-76 with detail of (upper) pore channels and (lower) infinite rod-shaped SBUs. Rare-earth atoms are represented by purple polyhedra, carbon, oxygen and hydrogen atoms are represented in grey, read and white, respectively.

1.5.3. MOFs with the mtn topology: MIL-100 and MIL-101

In this thesis, two Chapters are dedicated to a particular MOF, namely MIL-100, and one section will be dedicated to its analogue, MIL-101. MIL-100 and MIL-101 are two isotopological MOFs that were discovered in 2004 and 2005, respectively, by Férey et al. at the *Institut Lavoisier*, where the names of those MOFs come from (MIL =

Matériaux de l'Institut Lavoisier, or *Materials from Institute Lavoisier*).[147,148] Those two MOFs are amongst the most widely studied ones to date owing to their remarkable properties, which highly depend on the metals composing them but having very large surface areas and high porosity as constant features. Furthermore, those MOFs are built from the commercially available trimesic acid (benzene-1,3,5-tricarboxylic acid = H_3BTC) and terephthalic acid (H_2BDC) linkers, for MIL-100 and MIL-101 respectively, which is useful regarding perspectives in practical production and applications.

MIL-100 and MIL-101 are based on carboxylate bridged trimeric μ_3-O centred SBUs, having C_{3v} symmetry, of the general formula $M_3(\mu_3\text{-}O)(O_2CR)_6X_3$ (Figure I-11, A.). M_3 represents the three octahedral metal centres of the SBU, which can be homo- or heterometallic. X stands for solvent molecules or anionic charge-balancing species, or a combination thereof, present at the apical position of each metal centre. Six RCO_2^- moieties coming from the linkers of the MOF complete the SBU by bridging two adjacent metal centres. Those SBUs are particularly interesting in the design of MOFs because they usually comprise metals having rather high oxidation states (Cr^{3+}, Fe^{3+}, Al^{3+}, Sc^{3+}, Ti^{4+}, *etc*.),[149] responsible for strong bonds interconnecting the linkers and the SBUs, leading to the formation of robust MOFs. Indeed, to achieve neutrality, the total charge of the metals in the cluster must at least compensate the charge of the central $\mu_3\text{-}O^{2-}$ units as well as that of the six bridging carboxylate moieties (8 negative charges). For this, at least one of the metal centres must have the +III oxidation state and the two others must at least be +II. Higher oxidation states of the metals composing the framework are of course possible, as the apical ligands can be neutral solvent molecules, and thus allow the generation of CUSs by activation,[150,151] or charged species having one (e.g. halides or hydroxyl ions), or two (e.g. oxide ions) negative charges, or any combination thereof. This allows in theory the incorporation of virtually any kind of positively charged metal centre into the cluster moieties, except the ones that are in the +I oxidation

state, therefore excluding alkali metals and low-valent transition or p-block metals (e.g. Cu^{+} or Tl^{+}).

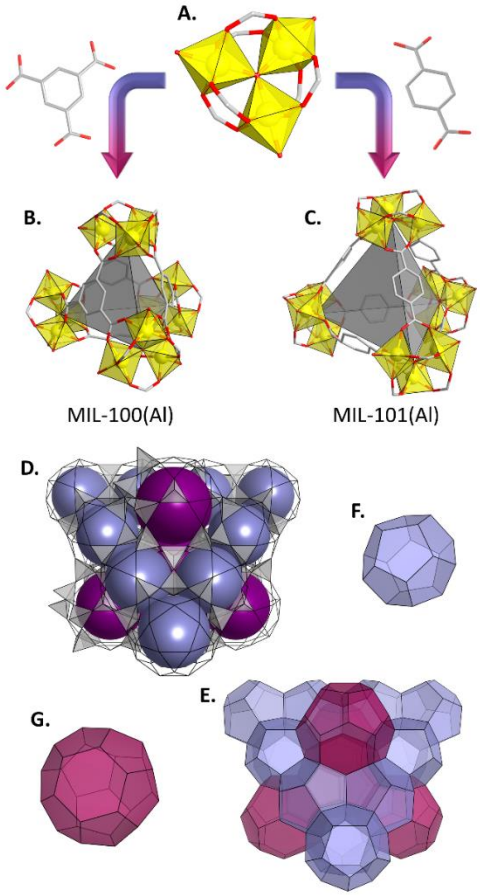

Figure I-11. Structure of (**A.**) the $M_3(\mu_3\text{-}O)X_3(O_2CR)_6$ clusters and the supertetrahedra formed with (**B.**) trimesate and (**C.**) terephthalate linkers (color code: red = oxygen, grey = carbon, yellow = M, hydrogens are omitted for clarity). The interconnection of supertetrahedra (grey tetraedra) (**D.**) forms the framework of the MIL-100 and MIL-101 MOFs with large (purple) and small (blue violet) mesopores in the mtn topology (**E.**). Details showing the pentagonal windows of the (**F.**) small mesopores and pentagonal and hexagonal windows of the (**G.**) large mesopores.

The interconnection of four metal SBUs in MIL-100 and MIL-101 by BTC^{3-} or BDC^{2-} leads to the formation of supertetrahedra of which the metal clusters form the vertexes and the linkers form either the faces, for MIL-100, or the edges, for MIL-101 (Figure I-11, B. and C.).

The assembly of those microporous supertetrahedra allows the formation of the framework, in a *mtn* topology (the same as the commercial zeolite socony Mobil Thirty-Nine, ZSM-39[152]). This framework is composed of two types of interconnected mesoporous cages having microporous hexagonal and pentagonal windows (Figure I-11, D. – G.). The size of those cages is larger for MIL-101 than for MIL-100, and depends somewhat of the metal centres present in the framework. They are approximately of 24Å and 29Å for MIL-100(Cr) and 27Å and 34Å for MIL-101(Cr).[153] Nitrogen sorption experiments reveal that those compounds have type I isotherms, typical of microporous materials.[154] However, those MOFs are most of the time regarded as mesoporous because of the diameter of their cages which is accurately determined by X-ray diffraction,[155,156,157,158] even if they do not exhibit the type IV isotherm typical of mesoporous materials. Sometimes they are even considered as hierarchical frameworks because micropores are present inside the supertetrahedra.[159]

Although MIL-100 MOFs exist with many different metals, this thesis will focus on their iron and aluminium-based versions, as well as bimetallic iron-based derivatives, because Fe and Al are abundant, non-toxic and lightweight metals. For this reason, only the known synthesis methods of MIL-100(Al), MIL-100(Fe) and bimetallic MIL-100 MOFs will be discussed below, as the synthesis methods can usually not be transposed easily to another metal.

MIL-100(Al) was first obtained as a highly porous (S_{BET} = 2152 m^2g^{-1}) yellow powder, by hydrothermal reaction of $Al(NO_3)_3 \cdot 9H_2O$, HNO_3 and trimethyl-1,3,5-trimesate as linker source at 210°C for 3 to 4h.[160] Tedious control of the pH was crucial for this synthesis as it had to be set precisely at values between 0.5 and 0.7, lower pH values leading to the formation of MIL-110(Al) and longer reaction times yielding MIL-96(Al), two other types of Al-BTC MOFs. On the contrary to MIL-100(Cr) and MIL-100(Fe), which could only be obtained as crystalline powders, very small single crystals of this MOF could be obtained and the structure was solved by microdiffraction

using synchrotron radiation, leading to the first structural characterization of a MIL-100 MOF by this technique, despite the Fe and Cr derivatives were discovered earlier. *In situ* NMR and *ex-situ* XRD and SEM studies were performed in another work to get insight into the reaction mechanism responsible for the MOF's formation.[55] It was shown that MIL-100(Al) is the kinetic product, whereas MIL-96(Al), another Al-BTC trimesate MOF, is the thermodynamic one. The kinetic nature of MIL-100(Al) and the thermodynamic nature of MIL-96(Al) were corroborated by other studies,[161,162,163] and it was shown that fast heating methods, such as microwave irradiation, enable isolation of thermodynamically unstable MOFs such as MIL-100(Al) more easily and much more rapidly than through conventional heating. However, all these synthetic procedures need tedious control of the reaction parameters as MIL-96(Al) and/or MIL-110(Al) often form if small modifications are applied to the procedure. Moreover, it has recently been shown that adding some acetic acid in the reaction mixture allows the formation of cluster deficiencies in the MOF, as evidenced by TGA.[164]

Alternative synthesis procedures have been developed since then (Table I-2), some of them having only small differences with the initial one. Trimesic acid can also be used instead of trimethyl-1,3,5-trimesate as cheaper source of linker. One way to achieve this is by generating the ester *in situ* during the synthesis by addition of methyl or ethyl containing molecules, typically methanol, ethanol, *N*,*N*-dimethylformamide (DMF) or *N*,*N*-diethylformamide (DEF), into an aqueous reaction mixture composed of aluminium nitrate, HNO_3 and H_3BTC.[165] Heating this mixture at 200°C leads to the formation of MIL-100(Al) with BET surface areas up to 1920 $m^2.g^{-1}$ over a 4h period of time. Control of pH (ideally at pH = 1.6 when DMF is used), as well as controlling the nature and stoichiometry of the used methyl or ethyl containing molecules, is crucial for the outcomes of the synthesis. The use of cetyltrimethylammonium bromide (CTAB) as surfactant in the synthesis of aluminium trimesate MOFs has also been studied at lower synthesis temperatures (120°C) in water/ethanol mixtures by using

trimesic acid as linker source, with the purpose to obtain MOFs with hierarchical pore structure.[166] In this case, MIL-100(Al) with a BET surface area of 1550 m^2g^{-1} could be selectively obtained. Higher concentrations of water in the medium led to the formation of MIL-96(Al) as secondary phase and lower pH values to MIL-110(Al). It has also been reported that MIL-100(Al) could be selectively obtained through microwave irradiation of an aqueous suspension of aluminium nitrate and trimesic acid in the presence of an inducing agent.[167] Different inducing agents were tested and it was shown that aluminophosphate molecular sieves, SAPO-11 and SAPO-34, as well as Al-, Ni- and Co-based phosphates were efficient for selective synthesis of MIL-100(Al), whereas molecular sieves that do not contain phosphate moieties (i.e. ZSM-5, MCM-41 or SBA-15) were not able to play this role. In the absence of any inducing agents, MIL-96(Al) was formed as single phase. MIL-100(Al) can also be obtained in the form of a gel through reaction of $Al(NO_3)_3 \cdot 9H_2O$ with trimesic acid in an ethanol solution at 120°C.[168] The obtained gel can then be transformed into an aerogel by drying under air, or into a xerogel by using a supercritical CO_2 drying process.

MIL-100(Fe) is classically obtained through solvo- or hydrothermal synthesis, using nitric and/or hydrofluoric acid as crystallization modulators, with metallic iron or an iron salt as metal source and trimesic acid as linker source.[169] Although a few attempts were made to render the synthesis of this MOF more sustainable, noticeably through mechanochemical means in the absence of HF,[170] the largest improvement has been its synthesis in aqueous solution at room temperature.[171] This synthesis is performed by reaction of a solution containing $FeCl_2$ and a mixture of trimesic acid and sodium hydroxide in the presence of air. However, in presence of an excess of NaOH, the resulting MIL-100(Fe) contains Fe_3O_4 particles as secondary phase.[172]

Table I-2. Different synthesis pathways to obtain MIL-100(Al) and BET surface areas of the obtained MOFs.

S_{BET} ($m^2.g^{-1}$)	Reactants and conditions	Ref.
2152	$Al(NO_3)_3{\cdot}9H_2O$, HNO_3, Me_3BTC, water, 210°C, 3 to 4 h	[160]
1056	$Al(NO_3)_3{\cdot}9H_2O$, H_3BTC, water, MW (210°C), 1 min	[161]
1701	$Al(NO_3)_3{\cdot}9H_2O$, HNO_3, Me_3BTC, water, MW (200°C, 1200 W), 83 min	[162]
300	$Al(NO_3)_3{\cdot}9H_2O$, HNO_3, H_3BTC, water, MW (210°C), 30 min	[163]
2400	$Al(NO_3)_3{\cdot}9H_2O$, HNO_3, Me_3BTC, water, MW (210°C), 30 min	[163]
1482	$Al(NO_3)_3{\cdot}9H_2O$, HNO_3, Me_3BTC, water, 210°C, 3 days	[173]
1920	$Al(NO_3)_3{\cdot}9H_2O$, HNO_3, H_3BTC, water, DMF (210°C), 4 h	[165]
1550 - 1970	$Al(NO_3)_3{\cdot}9H_2O$, H_3BTC, water, cetyltrimethylammonium bromide, EtOH, 120°C, 12 h	[166]
1534 - 1576	$Al(NO_3)_3{\cdot}9H_2O$, H_3BTC, water, inducing agent (insoluble phosphate), MW (190°C, 300 W), 10 min	[167]
1761 - 1795	$Al(NO_3)_3{\cdot}9H_2O$, H_3BTC, ethanol, 120°C, 1h	[168]
920	$Al(NO_3)_3{\cdot}9H_2O$, H_3BTC, ethanol, 120°C, 1h	[174]
1670	$Al(NO_3)_3{\cdot}9H_2O$, H_3BTC, water, MW (1200 W), 5 min	[175]

Concerning bimetallic MIL-100(M_1,M_2) MOFs, few examples exist in the literature, and most MOFs were synthesized by solvothermal methods that mostly involve the use of aggressive acids like HNO_3 or HF as modulators. In some cases, the second metal was introduced by post-synthetic exchange, adding a second step in the synthesis.

Upon thermal activation, only one out of three aluminium atoms per trimer can be coordinatively unsaturated in MIL-100(Al), as shown by quantitative ^{1}H and ^{27}Al NMR experiments, leading to a pentacoordinated Al center (Figure I-12).[176] In the case of MIL-100(Fe), at least two of the three Fe atoms are in the +III oxidation state, whereas the third one can be in the +III or +II oxidation state. The oxidation state of the iron depends partly on the synthesis procedure and the nature of the iron precursors, but reduction can also occur upon activation under heat and vacuum, leading to the creation of CUSs on the metal centers of the clusters (Figure I-12).[177]

Table I-3. Mono- and bimetallic MIL-100(M_1,M_2) MOFs described in the literature to this date, their synthesis methods and applications.

M_1	M_2	Synthesis method	Application	Ref
Cr, V or Sc	-	Solvothermal	CO_2 adsorption	178
Sc	Al, Cr or Fe	Hydrothermal and solvothermal	Friedel-Crafts, oxidation and tandem catalysis	179
Al, Cr, Sc or V	-	Solvothermal	Catalytic tetrahydropyranylation	180
V, Al, Fe or Cr	-	Solvothermal	Catalytic condensation of glycerol with acetone	181
Al, Cr, Fe, In, Sc or V	-	Solvothermal	Prins condensation of β-pinene and formaldehyde	182
Fe	Mn	Hydrothermal (with HF)	Catalytic reduction of NO_x by NH_3	183
Sc	Ti	Solvothermal, post-synthetic exchange; high valence metal metathesis and oxidation	Photodegradation of methylene blue	184
Ti	-	Solvothermal	Photocatalysis	185
Fe	Ni	Hydrothermal, HNO_3 assisted	Prins reaction of β-pinene and paraformaldehyde	186
Ti	Fe, Ni, Co, Zn	Metal exchange on bimetallic MUV-10(Ca,Ti)	-	80
Ti	Fe, Ni, Co	Solvothermal	Hydrolysis catalysts for nerve agents simulants	187

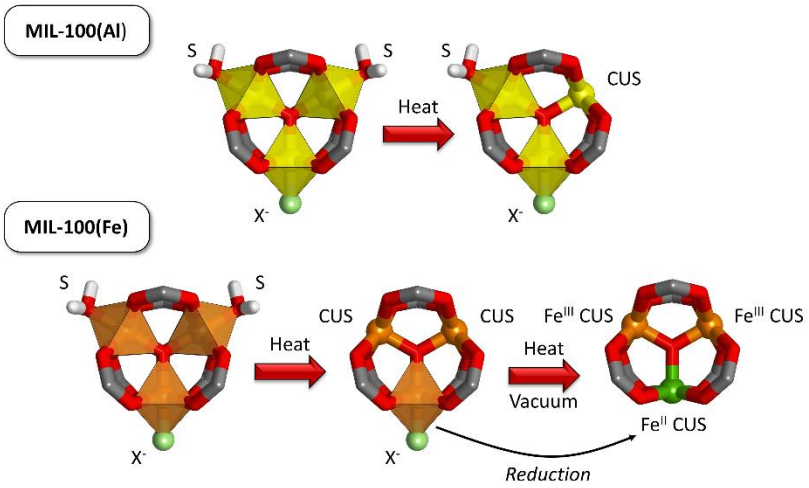

Figure I-12. Activation and creation of CUSs on MIL-100(Al) (upper) and MIL-100(Fe) (lower). Octahedral Al and Fe^{III} sites are represented by yellow and orange octahedra respectively, Al, Fe^{III} and Fe^{II} CUSs are represented by yellow, orange and dark green spheres, respectively. Charge balancing anions (X^-: OH^-, Cl^- or F^-, depending on synthesis conditions) are represented by light green spheres, solvent molecules (S) are represented by water. Carbon, oxygen and hydrogen atoms are respectively represented in grey, red and white.

2. Characterization methods

MOFs are particularly complex materials for which assessing their composition, structure and properties requires a wide variety of techniques. Their structural determination is mainly performed through X-ray diffraction techniques, complemented by spectroscopic characterizations. The properties of MOFs are determined by various experimental techniques; nevertheless, the determination of textural properties by means of physisorption analysis remains one of the routinely used techniques, independently from the target application.

2.1. X-Ray diffraction

Determination of the spatial arrangement of atoms in MOFs is of outermost importance to understand their complex architectures. Provided that the studied MOFs are crystalline in nature,[188] this is usually achieved by the use of X-ray diffraction.

2.1.1. Single crystal X-ray diffraction (SCXRD)

The most straightforward method to determine the structure of MOFs is by using single-crystal X-ray diffraction (SCXRD). However, this method has a few limitations, the most obvious one being the need of large enough single crystals. Indeed, some MOFs, especially the most stable ones based on hard Lewis acid/base interactions, often form very fine powders,[189,190] or only very small crystals whose size is not sufficient for SCXRD analysis in most laboratories. The analysis of very small crystals can however be performed by diffraction using small beams, which is accessible at most synchrotron facilities.[191]

2.1.2. Laboratory and synchrotron powder diffraction (PXRD)

As many MOFs are often obtained as very fine powders, powder X-ray diffraction (PXRD) is therefore often used for the structural characterization of MOFs. Powder diffraction data is collected as only one pattern for each sample, projecting all spatial information of the reciprocal space in a single "image", making indexing difficult, as well as structure determination and refinement. Solving new structures through PXRD is very challenging, and requires special competences.[189]

However, as diffraction patterns are structure dependent, PXRD can be used routinely for comparison of new compounds with known ones by search and match or "fingerprinting".[192] Indeed, two MOFs having the same topology and cell parameters will have similar peak positions, although their relative intensities can vary because of differences in pore filling.[193] This is very useful for determination of the structure of metal-doped, as well as functionalized MOFs that are isomorphous to previously described frameworks, even when high structural complexity is involved (for example with MIL-100 or MIL-101 frameworks).[194] It must however be noted that for measuring neat diffraction patterns of structures with large cell parameters, which mainly diffract at very low angles, some precautions must be taken for

the measurements. Indeed, low angles on PXRD patterns are often masked by the beam-stop of the diffractometer, the purpose of which is to stop the direct beam before it hits the detector.

This is particularly the case for MIL-100 or MIL-101 MOFs, having very large unit cells giving rise to main diffraction peaks at low diffraction angles. Since our main diffractometers are equipped with molybdenum sources, which are more suitable for X-ray analysis in transmission mode, we had to optimize significantly the beam-stop as well as increase its distance to the sample.

For more demanding analyses, synchrotron powder X-ray diffraction (S-PXRD) is often used.[195] Thanks to the much higher X-ray intensity and beam quality, and reduced instrumental line broadening, very high quality diffraction data are obtained, along with very short measurements times, enabling experiments that are not possible using conventional laboratory diffractometers.[196]

As mentioned above, the main limitation of SCXRD is the availability and quality (as well as size) of single crystals. Powder diffraction, on the other hand, is sensitive to texture (preferred orientation) that can be taken into account of and of so-called poor powder average, in case we characterize a mixture of fine and coarse crystalline particles. To avoid these issues, special precautions should be taken, including the use of area detectors and multiple measurements on similar samples. The *in-situ* experiments, on the contrary, are showing differences induced by external stimuli, such as guest entrance, and thus can be exploited more consistently using data series. The systems studied in this thesis contain very large pores, and did not produce single crystals. Thus, we were limited to phase identification mostly, as well as comparison of samples before and after different treatments.

2.2. Thermal analysis

2.2.1. Thermal gravimetric analysis and differential scanning calorimetry

Knowledge about the thermal stability and desolvation behaviour of MOFs is crucial when considering applications. Therefore, thermal gravimetric analysis (TGA) can be used to determine those properties.

Weight losses of the sample can be attributed either to solvent release, a decomposition or a reaction within the sample.[197] Solvent release, which is often the first event observed during TGA of MOFs, results in a weight loss proportional to the solvent content of the material, at temperatures near the boiling point of the solvent. Sometimes, however, this can happen at (much) higher temperatures due to (strong) interactions between the solvent molecules and the framework, e.g. coordination to the metal center.[197] Decomposition of the framework is best observed by performing the analysis using air or oxygen as working gas, as this results in burning of the organic linker and its complete transformation into gaseous molecules (for structures with common organic linkers containing C, O, N, S and H atoms). From this weight loss, the metal/linker ratio of the structure can often be determined, as the residual weight after calcination is made up by metal oxides.[198] In some cases, a weight increase can be observed due to reaction with, or adsorption of, the working gas.[199]

Since weight losses are sometimes difficult to attribute to a given thermal event by the use of TGA alone, this method is nowadays commonly coupled to differential thermal analysis (DTA) or differential scanning calorimetry (DSC).[200] This allows distinguishing between endo- and exothermic effects and facilitates attribution of the weight losses observed by TGA, as energy needs to be provided to the solvent molecules for allowing their evaporation, resulting in endothermic peaks on the DSC curve, and decomposition often releases energy, which is given by exothermic peaks during DSC analysis, to give a few examples.[201] Furthermore, DSC allows observing thermal

events that do not result in weight loss or gain, such as melting or phase transitions for example.[200]

The problem of this combination of techniques is that they inherently characterize the bulk samples, including the amorphous phases. The experimental error of TGA is approximately 1 wt. %, while the errors are typically larger for DSC. Mass spectrometry is sometimes coupled to TGA/DSC in order to analyse the nature of the volatile products forming upon decomposition, but these analyses are typically only qualitative.

2.2.2. Variable temperature diffraction

Although TGA/DSC measurements allow determining the temperature at which the MOF linkers are destroyed, this temperature might be different from the one at which the actual decomposition of the MOF occurs.[202] Indeed, thermal treatment can cause the framework to collapse at temperatures well below the decomposition temperature determined by the more classical thermal analyses.[150] Therefore, variable temperature powder diffraction is of outermost importance in the determination of the real thermal stability window of the framework.

Furthermore, MOFs can undergo structural changes during heating. This can be due, for example, by the contraction of the pores when guest molecules are desorbed or by phase transitions.[136] Thermodiffractometry is also a valuable tool for studying temperature-dependent structural changes of other types of chemicals, for example hydrated salts, whose structures change upon desolvation triggered by rise in temperature.[203]

The main difficulty of this technique lies in the necessity to find a compromise between the angular resolution of the diffraction data and the time resolution for the measurement. Fast measurements usually are possible with low resolution instruments based on large area detectors.

2.3. Vibrational spectroscopies

2.3.1. Fourier-transform infrared spectroscopy (FTIR)

Fourier-transform infrared spectroscopy (FTIR) is an efficient method to check the quality of synthesized MOFs. Indeed, experimental spectra can routinely be compared to reported ones.[150] More interestingly, FTIR can be used to determine whether a MOF has been efficiently activated, as solvents peaks are often visible for as-synthesized materials, and should disappear completely only upon removal of all adsorbed and coordinated solvent molecules.[204] Furthermore, FTIR is also efficient at the detection of structural defects within complex structures, which are sometimes overlooked by PXRD analysis.[205] Such structural defects can for example appear as stretchings of free carboxylic acids, which are not fully coordinated.[206] In this aspect, FTIR is complementary to TGA that enables determining the metal/linker ratio. Furthermore, specific functions added into MOFs, upon, for example, post-functionalization, are often visible on FTIR spectra.[207] The main limitations of this technique is that several signals on the FTIR spectra can be overlapping, and some functionalities could thus not be detected efficiently. Also, the characteristic peaks are not at all characteristic to a particular MOF but to various chemical groups, while the fingerprint region is difficult to interpret and thus requires a good reproducibility to be merely used for identification.

The main problem of vibrational methods is their sensitivity to local structure mainly, and spectra obscuring by impurities, solvents, atmosphere components. The advantage can be seen in the sensitivity to the amorphous phases.

2.4. Nuclear magnetic resonance (NMR)

2.4.1. Solution state NMR

Solution-state NMR analysis can be efficiently used to detect organic species in MOFs upon digestion of samples.[150] For this purpose, the sample must first be dissolved. This can be done either in acidic

media, allowing reprotonation of the organic linker, which must then be dissolved in an appropriate organic solvent, for example by addition of DMSO.[208] The MOF can also be dissolved in a basic aqueous medium, allowing transformation of the linker into a water-soluble salt.[209] Importantly, for NMR analysis it is recommended to remove any species that could interfere with the measurement, which requires a clear sample without any paramagnetic species.[210] For MOFs containing paramagnetic species, those must first be eliminated, for example by precipitation (e.g. removing Fe by precipitation into hydroxides followed by filtration) or by changing the paramagnetic species into a non-paramagnetic ones that can remain in the solution (e.g. oxidation of Ti^{3+} into Ti^{4+}). The obtained data from digested MOF samples might be used to determine the ratio between linkers, when considering MOFs with multiple linkers,[211] or to determine the solvent content, either in physisorbed or in coordinated state. This technique can be particularly useful for determining the presence of organic charge-balancing anions that are not observable by PXRD analysis due to the complexity of the considered structure.[33] Furthermore, it can be used for determining the presence of any coordinated species, resulting for example from a post-synthetic functionalization.[212] The advantage of this method compared to FTIR, is that it allows not only the detection of organic species, but also their quantification, by comparing integral values.[213] This quantification can be done either by ratios of integrals of the various species present inside the MOF (e.g. integrals of linkers and solvent molecules), or by the use of an internal standard that is added after dissolution of the MOF.[214] The main drawback of this method is that some species deteriorate in highly concentrated acids or bases, especially under heating sometimes required for the dissolution of MOFs. This is for example the case of DMF, which can be adsorbed inside the MOF, and can be decomposed by acids or bases into volatile dimethylamine and formic acid or formate, depending on the conditions used for dissolution.[215] Therefore, it might be useful to measure reference spectra of individual compounds (linkers, solvents, etc.) that underwent similar dissolution conditions as the MOF, as this enables

easier interpretation of the resulting spectra. The NMR techniques are very sensitive to ^{1}H, this may present an issue to interpret all the peaks from protic impurities even when they account for less than 1% of the sample.

Furthermore, liquid-state NMR can be used for monitoring reactions happening in solutions, enabling the study of the formation mechanism of MOFs. This has for example been implemented for the study of Al-based MOFs, such as NH_2-MIL-101(Al) which contains several NMR active nuclei, some of which give intense signals (i.e. ^{1}H, ^{27}Al, and also ^{13}C).[216] The number of studies related to understanding the formation of MOFs by solution state NMR is however limited as MOFs are often obtained under harsh solvothermal conditions.[217] Therefore, special equipment, including specially designed high-pressure NMR tubes and spectrometer equipped with a probe that can heat to the required temperatures for the reaction to proceed (often > 100°C) must be used to enable such investigations.[218]

2.4.2. Solid-state NMR

Solid-state NMR is also a very valuable tool for the determination of organic species present in MOFs. It has the advantage of probing the species that are present in the solid materials directly, avoiding the need to destroy the sample before analysis, and therefore giving a more representative view of the composition of the framework.[219] Furthermore, solid-state NMR allows probing the coordination environment of the metals composing the MOF,[220] which is not possible upon dissolution, enabling the monitoring of different processes in MOFs, such as activation.[221] However, solid-state NMR gives spectra with significant line broadening compared to its liquid-state counterpart, which renders interpretation and quantification more difficult.[222] Also, as the entire sample is probed, it is not possible to remove paramagnetic species if those are present, and the analysis can thus be hindered. Considering the requirement of fast spinning, the in-situ experiments are difficult to do with solid-state NMR, and the peaks are always much broader than in solution.

2.5. Elemental analyses and metal content determination

Elemental analysis and spectroscopic metal content determination methods can be useful in some cases for the determination of a MOF's structure, especially in the case of complex frameworks for which diffraction methods are limited due to structural complexity and a lack of single crystals. Elemental CHN(S) analysis consists in burning the sample and allow the formed gases to pass over a catalyst to enable complete oxidation into CO_2, H_2O, NO_2 and SO_2 to determine the C, H, N and S contents.[223]

Inductively-coupled plasma (ICP) coupled with optical emission spectroscopy (OES), as well as atomic absorption spectroscopy (AAS) can be used to determine the quantity of metal in a sample.[224] One of the advantages of ICP-OES in comparison with AAS is that less sample is needed for the analysis (detection limit down to ppt or less vs. ppb). Furthermore, fewer interferences can occur, allowing the use of mixed standard solutions for establishing the calibration curves, whereas the second techniques needs a different series of standard solutions for analysing the content of each metal.[225]

Other elements, such as halogens, can also be determined by elemental analysis. The Schöninger flask method for example allows to determine F, Cl, Br and I contents in a sample.[226] To do so, the sample is burnt in a flask containing a solution of NaOH and pure oxygen. The released gases are then adsorbed into the solution and the halogen content can be determined by suitable titration or ion chromatography.[227]

When highly porous MOFs are considered, the solvent content in their pores may vary a lot depending on the humidity conditions.[31] As the above-mentioned methods give a quantification in weight fractions, it is important that the samples are weighed under strictly identical conditions to enable comparing the results. Therefore, the synthesized MOFs should be dried and their mass should not vary when exposed to air before sampling. Alternatively, the samples may be activated and aliquots for analysis may be weighed in a glovebox to avoid uptake of

humidity before weighing. Although the above methods enable to give valuable information about the samples composition, such as the quantity of linkers and or/solvents and more generally the chemical formula of MOFs, they are all destructive.

X-Ray photoelectron spectroscopy (XPS) can also be used for elemental content analysis. In addition, the oxidation states of the elements from the sample can also be determined. However, it must be stressed out that XPS only probes the surface of the sample (down to ~5 nm depth), which might be completely different from the bulk composition. This method is thus sensitive to the surface and the defects it contains. Furthermore, the analysis is performed by X-rays under vacuum, which is prone to induce metal reduction. Results from XPS analyses must thus be taken with great care, as they are not representative of the bulk composition and the obtained information may be due to damage induced on the sample by the experimental conditions of the technique itself.

2.6. Gas sorption

As the porosity and accessibility of the pores of MOFs is at the basis of many of their applications (i.e. gas sorption, separation, catalysis, etc.), the characterization of those properties is of outermost importance. This is performed by adsorption of gases, under either low or high pressures or temperatures.

2.6.1. Nitrogen physisorption

Nitrogen physisorption is the most routinely employed method for the determination of the textural properties of porous materials in general.[154] This method consists in analysing the solid by low-pressure adsorption of nitrogen at cryogenic temperatures (-196 °C). Analysis of the sample starts under high vacuum, and the sample is then exposed to increasing pressures of nitrogen, which adsorbs onto the solid's surface, followed by desorption. The quantity of gas adsorbed is then plotted against the pressure to obtain (physi)sorption isotherms comprising an adsorption and a desorption branch, which can either be fully reversible

or display hysteretic behaviour. The analysis of those sorption isotherms allows, based on their shape and by the use of various equations relying on physical considerations, to determine textural information such as surface area and pore size distribution.[154] Nowadays, the software of physisorption analysers automatically performs all the mathematical treatment of the data. The most commonly used mathematical models for determining surface areas, which are expressed in m^2/g of activated material, are the Brunauer-Emmett-Teller (BET)[228] and Langmuir[229] models, which take into account multilayer, and single-layer adsorption of nitrogen, respectively, whereas the Barrett-Joyner-Halenda (BJH)[230] model is often used to determine the pore-size distribution. However, each mathematical model has been developed for a specific type of material, and MOFs possess such a wide structural diversity that none of those models can be used for determining really representative values of surface area for all MOFs. Those models are thus essentially used for comparing the textural properties of different MOFs, rather than determining exact values (although the BET method gives quite accurate estimates of MOF surface areas), which can be more accurately determined by theoretical simulations based on the knowledge of the framework's structure.[231] Other gasses than nitrogen can also be used for physisorption analysis. Those include the use of carbon dioxide, for textural determination of materials with pore openings that are smaller than the kinetic diameter of nitrogen,[232] krypton for the analysis of materials with small surface areas,[154] or hydrogen that enables to better visualize progressive filling of different sized micropores.[233]

The BET surface is taken as a reference to the method that became standard in the characterization of porous materials. It is not necessarily giving the exact value of the pore surface but rather collates with it, the main advantage being the easiness of repeating the characterization under very similar conditions (i.e. in other labs). The errors on the surface area can easily be of the order of 10%, despite the statistical estimates of the method usually indicating much higher precision. The

weighting errors are also non-negligible. The larger samples give more reliable results, but require longer time for reaching equilibrium at each point, making these experiments even longer.

2.6.2. Pressure-composition isotherms (PCT)

The analysis of the sorption properties of materials for a given gas and application (energy storage, carbon capture, etc.) are often assessed by PCT analysis.[234] This is achieved by the volumetric method using a Sieverts apparatus.[235] This technique has the advantage of using wide temperature and pressure windows. MOFs are also activated under vacuum by heating prior to analysis.[236] The isotherms are often given as *excess uptakes* (i.e. the total quantity of gas that is adsorbed by the material, which is the excess quantity compared to an empty container; the volume calibrations are made by helium pycnometry, assuming this light gas does not physisorb on MOFs) versus the pressure of the gas used for the analysis.[237] This method allows for measuring gas sorption properties with virtually any gas at pressures up to 200 bar within large temperature ranges, going from cryogenic temperatures (using liquid nitrogen or liquid argon) to temperatures exceeding 200°C (using an heating mantle).[238] Using two isotherms spanning over a wide pressure range allows to extract isosteric heats of adsorption as a function of loading, by applying the Clausius-Clapeyron equation.[239]

The main problem of this technique is the necessity to do complex volume and temperature calibrations, practically for each sample, using helium pycnometry. Small leaks may be confused with an uptake with slow kinetics, thus these measurements require care and time. The experimental errors are measured in micromoles of the adsorbed gas, therefore the relative amounts with regard to the sample depend much on the absolute uptake amounts (i.e. the errors are smaller for big uptakes).

2.6.3. Gravimetric methods

Gas sorption in porous materials can also be assessed by means of gravimetric methods. Gravimetric gas sorption under high pressures

can be assessed through specialized equipment containing a magnetic suspension balance and a sample holder confined in a high-pressure setup.[240] Measurement of gas sorption up to the ambient pressure can be realized by using a classical thermogravimetric analyser.[241] To assess the gas sorption, the sample must first be activated, which can be done quite easily in a TGA system by simple heating. As using vacuum in a thermogravimetric analyser is a bit more tricky, although not impossible to realize,[242] activation under vacuum can be performed *ex situ* and loading of the activated sample in the TGA machine can be done without contact to ambient air, provided the TGA is housed in a glovebox. TGA systems are particularly useful to probe the reversibility of gas sorption, by periodically switching the working gas from an inert and non-adsorptive species (e.g. He) to the gas for which sorption should be probed (e.g. CO_2, O_2, C_3H_8 etc.).[197] The obtained values from such an analysis are given in wt.% and can easily be converted to other units. This method is particularly suited for adsorption of "heavy" gases such as CO_2, CH_4, etc. although precautions must be taken when working with flammable gases.[243] As adsorption of lighter gases will result in smaller changes in sample weight upon adsorption, the relative error on the obtained values will be increased. Using TGA methods, it is also possible to measure complete isotherms up to the atmospheric pressure, by working with controlled mixtures of the gas to be adsorbed and of an inert gas.[244] Adsorption isotherms, reversibility and cyclability tests can be obtained at any desired temperature using the oven/cooling of the TGA system,[245] even going down well below 0°C. The main limitations concerning temperature arise when cooling heavy gases such as Ar or CO_2, which results in unwanted buoyancy effects for which corrections cannot be applied below a certain temperature.

3. Aims and structure of the Thesis

This thesis aims at developing efficient and reproducible methodologies for the synthesis of new and modified MOFs that can find applications in catalysis and gas storage, applying the principles of green chemistry wherever possible. Metal doping strategies, as well as post-synthetic functionalization and defect engineering are used to modify and improve the performances of various MOF materials.

The main part of this thesis will be dedicated to the green aqueous synthesis of MIL-100(Fe) and its bimetallic derivatives. Among remarkably stable MOFs, MIL-100 derivatives show quite interesting properties,[246] like high surface areas up to more than 2000 m^2/g, thermal stability and resistance to solvents.[247] MIL-100(Fe) was chosen as template material given the high natural abundance, low cost and non-toxic nature of iron. Furthermore, iron centers in MIL-100(Fe) have been shown to be active in catalysis and gas sorption.[248,249,250] It was shown that adding a doping metal into the structure can impressively improve some properties of MOFs and MIL-100 in particular.[251,20,252,253] However, until now, very few combinations of template and doping metals were investigated and all those materials were synthesized by solvothermal methods that mostly involve the use of HNO_3 or HF as modulators, which can present a danger when used on large scale. In some cases, the second metal was introduced by post-synthetic exchange, adding a second step in the synthesis. Moreover, the possibility of mixing metals with large differences of ionic radii in the MIL-100 structure has not been investigated yet. Thus, the main aim of this work was to develop an easy and if possible green synthesis route of MIL-100, allowing in particular to extend these series towards various metal and ligand substitutions.

The first part of the results (Chapter II) is dedicated to the development of a synthesis strategy for obtaining pristine monometallic MIL-100(Fe) from alkali trimesates as linker source and water as solvent. As MOF formation mechanisms were not much studied in the

literature, particular attention has been paid to understanding of the influence of reaction parameters and isolation of reaction intermediates.

In the second part of results (Chapter III) our goal is to introduce a wide range of metal substitutions into the Fe-based MIL-100, serving as a low-cost templating structure, based on the improved preparative strategy developed in the previous Chapter. We investigate the possibility to control the amount of doping metal in the structure and to incorporate new metals, some with large ionic radii,[254] such as cadmium and lanthanides, to evaluate the limits of the developed synthetic method.

Chapter IV is dedicated to the post-synthetic functionalization of monometallic and bimetallic aluminum and iron-based MIL-100 MOFs with ethylenediamine on their open-metal sites. Ethylenediamine is a cheap molecule that is able to anchor itself to metal sites by one of its amine functions, while leaving the other available. The latter can be used for post-functionalization and for carbon dioxide capture. This methodology has previously been explored in the literature with the stable MIL-100(Cr).[255] However, chromium is a metal of concern because of its toxicity, and therefore we have implemented this methodology with iron and aluminum. Furthermore, aluminum is a lightweight metal, allowing to envisage applications where gravimetric considerations are of importance.

The chemistry of the MOF-76 series, based on rare-earths and the trimesate linker, is covered in Chapter V. As the commonly employed synthesis method to obtain these MOFs systematically employs DMF as solvent, we focused our attention on the possibility of obtaining this MOF in ethanol as more sustainable solvent. Furthermore, the stability of MOF-76 members towards water has been investigated throughout the lanthanide series. We also investigated the influence of the presence of an amine function on the trimesate linker on the properties of this MOF.

Our interest in the synthesis of MOFs with the mtn topology has been explored further with the aim to incorporate Ti^{3+} in MIL-100 and

MIL-101 derivatives by direct synthesis (Chapter VI). Indeed, although Ti^{3+} can be regarded as a useful active site for hydrogen storage, there are only very few reports with MOFs containing this species. Therefore, we explored new synthetic pathways to obtain such MOFs.

Finally, the use of ball-milling for the green synthesis of HKUST-1 has been explored (Chapter VII). Mechanochemistry can be considered as a green process due to the reduced use of solvents, however it involves significant impacts that tend to destroy the MOFs already upon its formation or to create defect structures. Our attention has therefore been focussed on the defects induced in this framework by ball-milling. The importance of post-synthetic treatments and incorporation of mesopores has also been studied and the influence of the obtained defects on the ability of the framework to catalyse cyclopropanation reactions has been investigated.

This thesis is focussed mainly on the development of new and more sustainable synthesis and functionalization approaches of interesting MOFs with open-metal sites based on the commercially available trimesate linker, as well as their characterisation. The results described in this Thesis are summarized in Chapter VIII, put along with perspectives regarding the obtained materials. This is followed by an Appendix. As the present thesis discusses a large amount of experimental results, part of the appendices (that were published as research articles) are not included in the manuscript but can be found on the Internet as electronic supplementary information. A complete table of the appendices, which mainly contain results of PXRD, TGA, FTIR, NMR and gas sorption analyses, as well as the references to access material published elsewhere, can be found at the beginning of the Appendices section.

CHAPTER II

Alkali Trimesates for green Synthesis of MIL-100(Fe)

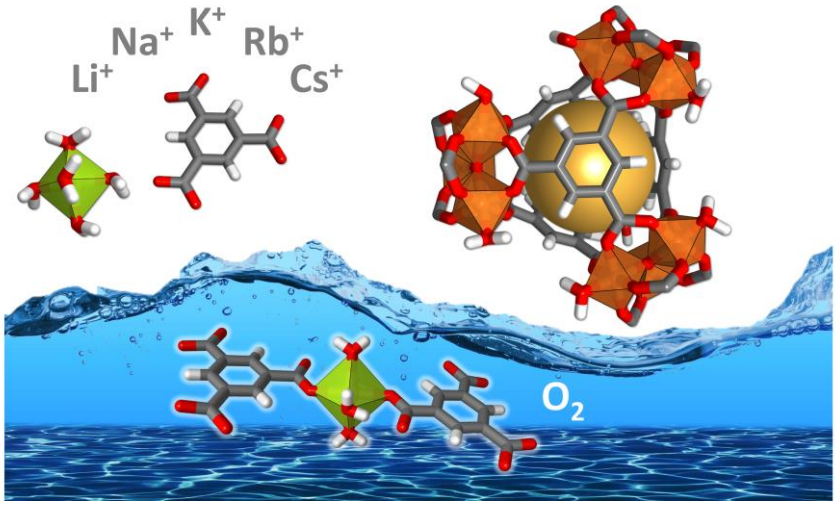

This Chapter is partly inspired by the following publication:

Steenhaut, T.; Hermans, S.; Filinchuk, Y. *Green synthesis of a large series of bimetallic MIL-100(Fe) MOFs*, New Journal of Chemistry, **2020**, *44*, 3847-3855, doi: 10.1039/d0nj00257g.

Chapter II - Alkali Trimesates for green Synthesis of MIL-100(Fe)

1. Abstract

This chapter focuses on the synthesis and characterization of alkali trimesates (M_3BTC, M = Li, Na, K, Rb and Cs), the water soluble precursors to MIL-100(Fe). These salts are all obtained through rapid synthesis at ambient temperature using water and ethanol as solvents, that can be regarded as a "green" process. The hydration states of the salts were characterized by thermal gravimetric analysis and their structures determined by single crystal XRD and variable-temperature PXRD experiments. A well-controlled synthesis of high-quality MIL-100(Fe) using these salts as precursors will be presented in the next Chapters of this thesis. Here, the formation mechanism of MIL-100(Fe) from those precursors in water has been studied, as well as the role of different parameters of synthesis. Finally, a MOF obtained in this way is compared to its analogue obtained by a classical solvothermal approach regarding the adsorption of Au^{3+} from aqueous solutions.

2. Introduction

It was shown MIL-100(Fe) can be obtained in mild conditions by mixing solutions of iron (II) chloride and trimesic acid (H_3BTC) deprotonated with NaOH in a basic environment.[171,256] We quickly found that this procedure is reproducible and scalable but does not allow incorporating any doping metal by simply adding a second salt along with $FeCl_2$. Inspired by an earlier work on other MOFs,[257] we modified the reported procedure by using alkali salts of trimesic acid, $M_3BTC{\cdot}xH_2O$, in slightly acidic environment, after prior determination of their hydration states by TGA and variable-temperature PXRD. We also used iron (II) sulphate as iron source instead of the corresponding chloride because of its lower cost and better suitability for industrial

needs as it does not present the corrosion issues occurring in the presence of chloride ions.[121]

To gain a better understanding of the synthetic process, we systematically varied several reaction parameters, such as the nature of the alkali ion, the oxidizing agent used to convert $Fe^{(II)}$ to $Fe^{(III)}$ and the solvent. We also isolated the reaction intermediate and identified its structure thanks to single crystal XRD.

Finally, we studied the influence of various carboxylate salts as crystallization modulators in the applied synthesis procedure. As functionalized MIL-100(Fe) obtained by a classical solvothermal approach has previously been proven useful for efficient recovery of Au^{3+} from aqueous solution, providing a possibility to envisage gold extraction from sea water,[115] we investigated the possibility of using the MOF obtained by our methodology to do the same. Surprisingly, the redox properties of our MOF seems to enable performing this process very efficiently even without any functionalization of the MOF.

3. Materials and Methods

Chemicals

Trimesic acid (98%) was purchased from Acros Organics. Denaturated ethanol (Technisolv, 99%), diethyl ether (GPR Rectapur), sodium hydroxide pellets and hexane (HiPerSolv, CHROMANORM) were purchased from VWR Chemicals. Lithium hydroxide monohydrate (>= 99.0%) was purchased from Fluka. Potassium hydroxide (reagent grade, 90%, flakes) was purchased from Sigma-Aldrich. Rubidium hydroxide hydrate (99%) and cesium hydroxide (99.9%) were purchased from Alfa Aesar. Iron sulphate (technical grade) was supplied from Forever products. Bromine (99.6%, for analysis) and hydrogen peroxides (35 wt. % in solution in water stabilized) were purchased from Acros Organics. Iodine (sublimed) was purchased from Merck.

All chemicals were used as received except iron sulphate, which was purified by heating a saturated aqueous solution (close to the

boiling point) in the presence of iron metal and sulphuric acid for one hour. The obtained hot solution was filtered and allowed to cool. Ethanol was added to the solution to crystallize the iron sulphate, which was isolated by filtration on a glass frit. The purifier $FeSO_4$ heptahydrate was washed with ethanol and dried under vacuum (using a Schlenk line).

Synthesis of MIL-100(Fe) in basic conditions (old procedure)

H_3BTC (1.42 g) and NaOH (0.80 g) were added to 125 ml of deionized water and the solution was sonicated until all the H_3BTC was dissolved (pH = 12). A second solution was made by dissolving 2.25 g of $FeSO_4 \cdot 7H_2O$ in 125 ml of water (pH = 4.87). Both solutions were mixed and allowed to react in the presence of air (in a 500 ml erlenmeyer flask, 500 rpm agitation) for 15 hours. Immediately after addition, the measured pH was 7.25, and the obtained precipitate dark green, then the colour turned to orange upon oxidation. The precipitate was separated from the supernatant liquid by centrifugation and washed using 3 x 50 ml of deionized water and 3 x 50 ml of denatured ethanol. The obtained solid was then dried using a rotary evaporator at 70°C and once the powder was dry, the evaporation flask was allowed to cool under vacuum, using a Schlenk line.

Synthesis of MIL-100(Fe) in acidic conditions (new procedure)

Na_3BTC trihydrate was obtained by adding 1 eq. of H_3BTC to 3 eqs. NaOH in a minimum amount of water. The obtained solution was filtered to remove any unreacted trimesic acid. Ethanol was added to the filtrate to precipitate the sodium trimesate. The obtained compound was washed with ethanol to remove any unreacted NaOH (the pH was tested using a paper indicator) and then with diethylether. The obtained white fluffy very light powder was then dried in a large beaker in an oven at 45°C overnight. ^1H NMR (300.1 MHz, D_2O) δ 8.42 (s, 3H). ^{13}C NMR (75.76 MHz, D_2O) δ 174.75, 136.53, 131.43. TGA weight loss upon dehydration: exp. 17.8 %, calc. 16.4 %.

1.86 g of Na_3BTC trihydrate was dissolved in 125 ml of deionized water. A second solution was made by dissolving 2.25 g of $FeSO_4 \cdot 7H_2O$ in 125 ml of water (pH = 4.87). Both solutions were mixed together and allowed to react in the presence of air (in a 500 ml erlenmeyer flask, 500 rpm agitation) for 15 hours. Immediately after addition, the measured pH was 6.08, and a yellow precipitate appeared slowly, then the colour turned to orange upon oxidation. The precipitate was separated from the supernatant liquid by centrifugation and washed using 3 x 50 ml of deionized water and 3 x 50 ml of denaturated ethanol. The obtained solid was then dried using a rotary evaporator at 70°C and once the powder was dry, the evaporation flask was allowed to cool under vacuum, using a Schlenk line.

Growth of Fe^{II} intermediate single crystals

A solution of $FeSO_4$ and a solution of Li_3BTC were prepared in water that was degassed through argon bubbling. Subsequently, a first layer of the $FeSO_4$ solution was introduced in an NMR tube under a flux of argon, followed by a layer of degassed water and a layer of the Li_3BTC solution (each layer corresponding to a filling level of approximately 3 cm in the NMR tube). The NMR tube was then sealed. After several days, yellow single crystals of the intermediate, suitable for single crystal X-ray analysis, were obtained.

Synthesis of MIL-100(Fe)-Br

1.86 g of Na_3BTC trihydrate was dissolved in 125 ml of deionized water. A second solution was made by dissolving 2.25 g of $FeSO_4 \cdot 7H_2O$ in 125 ml of water. Both solutions were degassed by argon bubbling and introduced together in an Erlenmeyer flask containing an empty test tube. Once both solutions were introduced, 2 mL of liquid bromine was quickly introduced in the test tube through the septum, by help of a syringe and needle. The reaction mixture was then stirred continuously for two hours, under a stream of argon. The obtained product was filtered on a nylon membrane and washed with water and ethanol, followed by drying under air.

Synthesis of MIL-100(Fe)-Cl

MIL-100(Fe)-Cl obtained through scaling-up of a reported synthesis procedure.[115] In brief, 11.34 g of $FeCl_3$ and 3.92 g of trimesic acid were added in a 210 mL Teflon lined autoclave together with 140 mL of demineralized water. The autoclave was sealed and the mixture was heated to 130°C for 3 days. The solid was recovered through centrifugation and washed with methanol. Finally, the sample was dried under vacuum at room temperature.

TGA/DSC measurements under air and nitrogen were recorded on a Mettler-Toledo TGA/DSC 3+ STAR^e system. Gas flows of 100 ml min^{-1} and heating rates of 10 °C min^{-1} were used.

Single crystal X-ray diffraction data were recorded at the Swiss-Norwegian beamlines (SNBL) at the European Synchrotron Radiation Facility (ESRF, Grenoble) at a wavelength of 0.68683 Å or 0.79800 Å using a Pilatus 2M detector. Data was collected for two different orientations of each crystal.

Variable-temperature synchrotron powder X-ray diffraction (VT-S-PXRD) patterns of samples were recorded at the Swiss-Norwegian beamlines (SNBL) at the European Synchrotron Radiation Facility (ESRF, Grenoble) at a wavelength of 0.68683 Å or 0.79800 Å using a Pilatus 2M detector. The samples were loaded into glass capillaries of 0.5 mm diameter. For temperature dependent measurements, a calibrated heating gas blower was used and the samples were heated from room temperature to 500 °C.

Variable-temperature Raman spectra were measured using a Bruker RFS 100/S spectrometer equipped with a 1064 nm laser of 100 mW. Heating of the samples was performed *in situ* using a home-made device.

Fourier transform infrared (FTIR) spectra were recorded in the range of 4000-370 cm^{-1} with a resolution of 4 cm^{-1} using a Bruker Alpha spectrometer equipped with a Platinum ATR module (diamond crystal) housed in an MBraun argon-filled glovebox.

Lab PXRD analyses were performed using a MAR345 image plate detector and an Incoatec Microfocus Source^{HIGHBRILLIANCE} (IμS^{HIGHBRILLIANCE}) Mo ELM47 operating at 50 kV and 1000 µA. The samples were exposed to X-rays for 5 minutes during which the capillary with the sample was rotated by 180°. Diffraction data was integrated by the Fit2D software (using data from a 0.1 mm diameter capillary filled with LaB_6 as calibrant). Alternatively, PXRD measurements were collected on a STOE STADI P Combi diffractometer using $CuK_{\alpha 1}$ radiation (40 kV, 40 mA) (graphite primary monochromator). The diffracted beam was recorded on a DECTRIS MYTHEN 1K strip detector. Samples were loaded in 0.7 mm diameter capillaries, aligned to the geometric center of the diffractometer and measured in transmission, with independent 2-theta movement.

Nitrogen physisorption measurements at 77 K were performed on a Micromeritics ASAP 2020 instrument. All samples were degassed at 200 °C during 10 h prior to analysis.

ICP and Schöninger flask analyses were performed by Medac Ltd.

4. Results and Discussion

4.1. Synthesis of alkali trimesates

Alkali trimesates were simply obtained by stepwise addition of a stoichiometric amount of solid trimesic acid to a concentrated aqueous solution of the corresponding alkali hydroxide (MOH), with help of ultrasonication or magnetic stirring to speed up the process, according to the following equation:

$$3\ MOH_{(aq.)} + H_3BTC \rightarrow M_3BTC_{(aq.)} + 3\ H_2O$$

Ethanol was then added to the yellowish solutions containing the water soluble salts to precipitate them. The solids were recovered by filtration, washed with ethanol, air-dried and then further dried at 45°C in an oven. The choice of ethanol for the washing was justified by the solubility of both the alkali hydroxides and trimesic acid in this solvent, allowing the removal of any traces of remaining reactants.

Alternatively, diethyl ether could be used for the last washing to speed up the drying of products, but rendering the process less “green”.

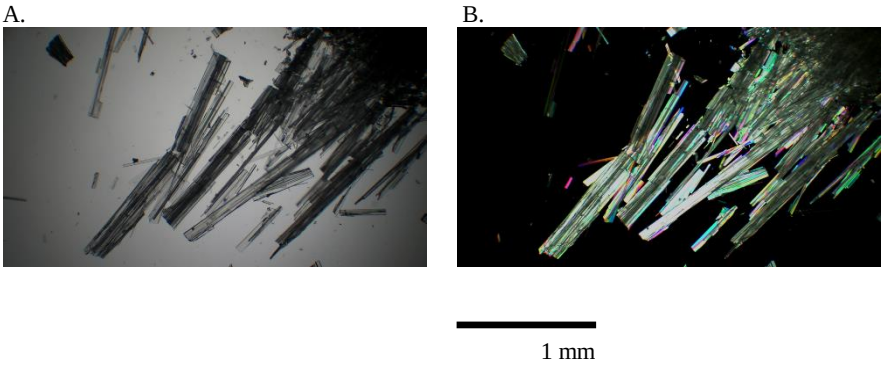

Figure II-1. Optical micrographs of $(Na_3BTC)_4 \cdot 21H_2O$ crystals. (A.) Transmission and (B.) crossed polarizers.

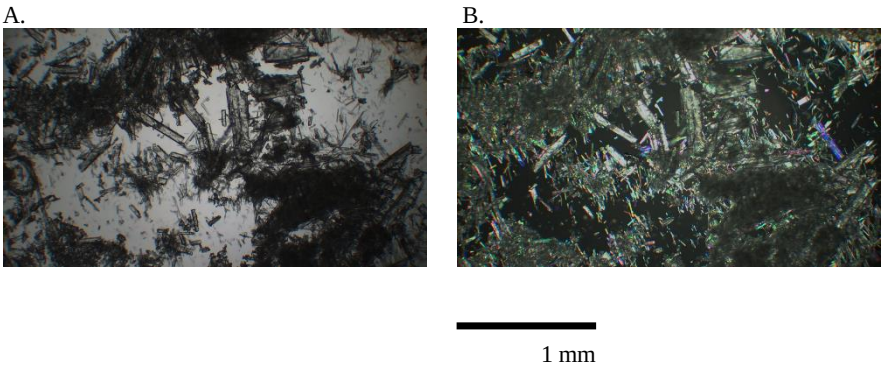

Figure II-2. Optical micrographs of $(K_3BTC) \cdot 2H_2O$ crystals. (A.) Transmission and (B.) crossed polarizers.

In order to enable characterization by single crystal X-ray diffraction (SCXRD), a small quantity of each sample was dissolved in water in a small vial, and ethanol was gently deposited with a pipette, taking care of not mixing the two phases. The vials were then placed in a refrigerator (+ 4 °C) for one or two days, yielding single crystals suitable for SCXRD characterization. Micrographs of the crystals obtained for the sodium and potassium salts are shown in Figure II-1 and Figure II-2.

4.2. Determination of hydration states of alkali trimesates

Table II-1. Formulas of alkali trimesate hydrates at different temperatures determined by TGA under air.

Alkali metal	Hydrate formula	Transition temperature (air) (°C)	Weight loss (calculated) (%)	Weight loss (experimental) (%)
Li	$Li_3BTC·H_2O$	> 100	-	-
	$Li_3BTC·⅔H_2O$	> 250	2.57	2.97
	Li_3BTC	> 300	7.32	7.41
Na	$Na_3BTC·3H_2O$	-	-	-
	Na_3BTC	> 150	16.36	17.76
K	$K_3BTC·2H_2O$	-	-	-
	K_3BTC	> 150	9.99	10.09
Rb	$Rb_3BTC·2H_2O$	-	-	-
	Rb_3BTC	> 100	7.21	7.35
Cs	$Cs_3BTC·5H_2O$	-	-	-
	$Cs_3BTC·2H_2O$	> 50	5.61	5.39
	Cs_3BTC	> 100	12.94	13.84

Prior to further use, the hydration state of the obtained salts was determined by thermogravimetric analysis (TGA) under air and nitrogen atmospheres (Fig. S II-1 to Fig. S II-5). Those analyses allowed determining that a monohydrate was obtained for lithium, a trihydrate was obtained for sodium and dihydrates were obtained for potassium and rubidium. For cesium trimesate, the dihydrate was likely also obtained after the initial drying at 45°C. However, TGA analysis indicated the presence of either trihydrate or pentahydrate, which are dehydrated to $Cs_3BTC·2H_2O$ at temperatures close to 45°C. As both TGA analyses were performed on the same batch, and samples were introduced upon different residence times in (moist) air on the sample automatic changer of the thermogravimetric analyzer, we deduced that the dihydrate is quite hygroscopic under ambient conditions, leading to higher hydrates upon prolonged contact with air moisture. Nearly all samples could be completely dehydrated by heating under air at temperatures between 150 and 200°C, except for $LiBTC_3·H_2O$, for which the anhydrous state could only be obtained after heating to 300°C, showing exceptionally strong bonding to the water molecule,

likely due to the polarizing power of Li. The hydration states of the alkali trimesates, as well as the dehydration temperatures determined by TGA under air and nitrogen are summarized in Table II-1 and Table II-2, respectively.

Table II-2. Formulas of alkali trimesate hydrates at different temperatures determined by TGA under nitrogen.

Alkali metal	Hydrate formula	Transition temperature (air) (°C)	Weight loss (calculated) (%)	Weight loss (experimental) (%)
Li	$Li_3BTC·H_2O$	> 100	-	-
	$Li_3BTC·⅔H_2O$	> 250	2.57	2.69
	Li_3BTC	> 300	7.32	6.81
Na	$Na_3BTC·3H_2O$	-	-	-
	$Na_3BTC·H_2O$	> 150	11.54	11.43
	Na_3BTC	> 250	16.36	16.05
K	$K_3BTC·2H_2O$	-	-	-
	K_3BTC	> 200	9.99	9.94
Rb	$Rb_3BTC·2H_2O$	-	-	-
	Rb_3BTC	> 100	7.21	7.26
Cs	$Cs_3BTC·3H_2O$	-	-	-
	$Cs_3BTC·2H_2O$	> 50	2.58	3.1
	Cs_3BTC	> 100	8.19	8.49

The transition temperatures from one hydration state to another are globally very similar under air and nitrogen atmospheres. Noticeable, the monohydrate of the sodium salt can be observed only under nitrogen atmosphere but does not appear under air. The dehydration of the salts could also be evidenced by *in situ* Raman spectroscopy for Li, Na and Rb salts (Fig. S II-6 to Fig. S II-8).

To further confirm the hydration state, gain a better understanding of the obtained salts, and determining whether any of them possesses porosity, their structure was solved from single crystal and variable-temperature synchrotron powder X-ray diffraction (VT-SPXRD). The obtained structures all confirmed the hydration states determined by TGA at each temperature. Single crystals were generally available only for higher hydration states, the crystallites becoming smaller upon dehydration. The crystal structures of $(Na_3BTC)_4(H_2O)_{21}$ and

$Na_3BTC{\cdot}3H_2O$ are shown in Figure II-3 and Figure II-4 as examples. The structural formulas, as well as the cell parameters are given in Table II-3. Unfortunately, none of the obtained structures showed the presence of pores.

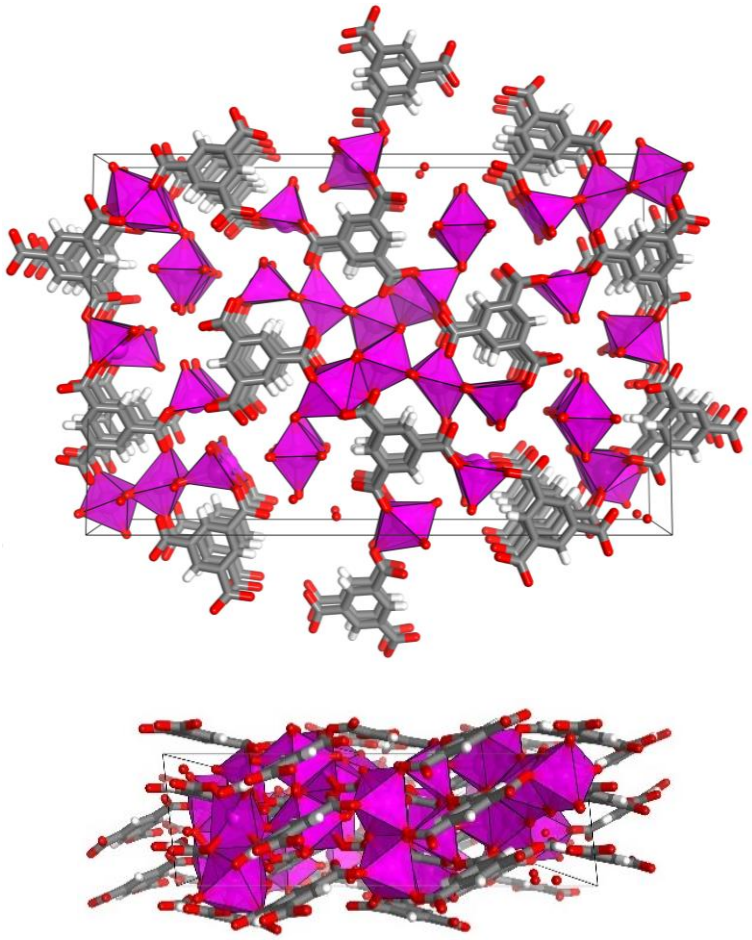

Figure II-3. Crystal structure of $(Na_3BTC)_4(H_2O)_{21}$ solved from single crystal XRD. Na, C, O and H are represented in pink, grey, red and white respectively.

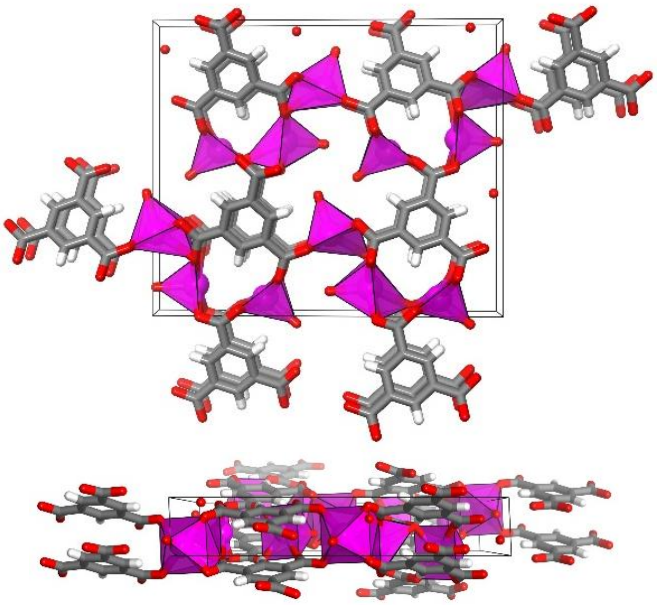

Figure II-4. Crystal structure of $Na_3BTC{\cdot}3H_2O$ solved from synchrotron PXRD. Na, C, O and H are represented in pink, grey, red and white respectively.

Table II-3. Structure formulas, space groups and cell parameters of the alkali trimesates solved from SC-XRD and PXRD.

Metal	Structure formula		Space group	Cell parameters, Å and °						
	Single crystal	PXRD		*a*	*b*	*c*	α	β	γ	Cell V, Å^3
Li	$Li_3BTC(H_2O)_5$		*Pbca*	13.3228	7.0898	27.8938	90	90	90	2634.71
		$Li_3BTC(H_2O)$	*P*-1	7.36	8.0331	9.4245	107.03	108.48	104.88	466.223
		Li_3BTC	*Pnna*	6.81238	9.12654	14.0363	90	90	90	872.686
Na	$(Na_3BTC)_4(H_2O)_{21}$		$P2_1/c$	7.0854	34.1474	22.4793	90	96.055	90	872.686
	$Na_3BTC(H_2O)_3$	$Na_3BTC(H_2O)_3$	$P2_1$	3.3978	16.7133	19.8334	90	92.559	90	1125.2
		Na_3BTC	$Pbc2_1$	3.508	17.0384	15.3911	90	90	90	919.94
K		$K_3BTC(H_2O)_2$	$P2_1/c$	16.6338	10.5726	7.67695	90	99.411	90	1331.93
		K_3BTC	*Pmma*	16.329	7.5888	9.312	90	90	90	1154
Rb	$(Rb_3BTC)_3(H_2O)_{16}$		$P2_1$	10.3978	19.7884	12.0343	90	99.512	90	2442.1
		$Rb_3BTC(H_2O)_2$	$C2/c$	10.0855	19.3037	14.1292	90	91.387	90	2749.97
Cs		$Cs_3BTC(H_2O)$	$C2/c$	10.5175	19.9045	14.5659	90	90.698	90	3049.06
		Cs_3BTC	$P2_12_12$	17.7972	17.7972	4.42517	90	90	90	1559.14

4.3. Synthesis of MIL-100(Fe) from alkali trimesates

The synthesis of MIL-100(Fe) in aqueous media at room temperature is possible both in slightly acidic and in slightly basic conditions. While the reaction product is MIL-100(Fe) in both cases, the reaction mechanisms and the intermediates appear to be very different, and as we will show in the next Chapter, an effective metal substitution is possible only in the acidic conditions.

In the known synthesis procedures, a mixture of trimesic acid and NaOH typically shows high pH of about 12.[171,256] Upon the addition of $FeSO_4$ solution, a dark green precipitate forms immediately and the pH drops to 7.25. The precipitate turns to orange after a few minutes due to the Fe^{2+} oxidation by air (Figure II-5, B).

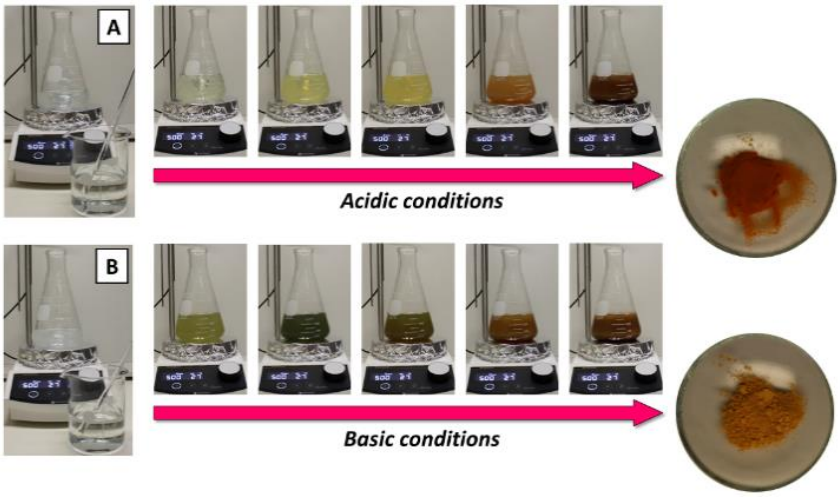

Figure II-5. Solutions before mixing (left), colour change during the reaction (middle) and the final product on a watch glass (right) for the synthesis of MIL-100(Fe) in (A) acidic and (B) basic conditions. The differences in coloration of the precipitates during the reaction indicate the existence of different reaction intermediates.

Our new procedure uses a solution of an alkali trimesate, whose syntheses are described above, showing a practically neutral pH (7.07 for the salt). An addition of $FeSO_4$ solution yields initially a colourless transparent solution with pH 6.08, which slowly produces a yellow

precipitate turning to orange upon oxidation by air (Figure II-5, A). The appearance and the colour of the obtained MIL-100(Fe) powders are significantly different as well as the specific surface areas and pore size distributions, despite the samples displaying the same crystal structure by PXRD (Fig. S II-9 and Fig. S II-10). Although the isolation of alkali salts, which are not commercially available, adds a supplementary step in the synthetic procedure of MIL-100(Fe), using the salts as precursors allows better control over the pH of the reaction mixture and enhances the reproducibility of the synthesis.

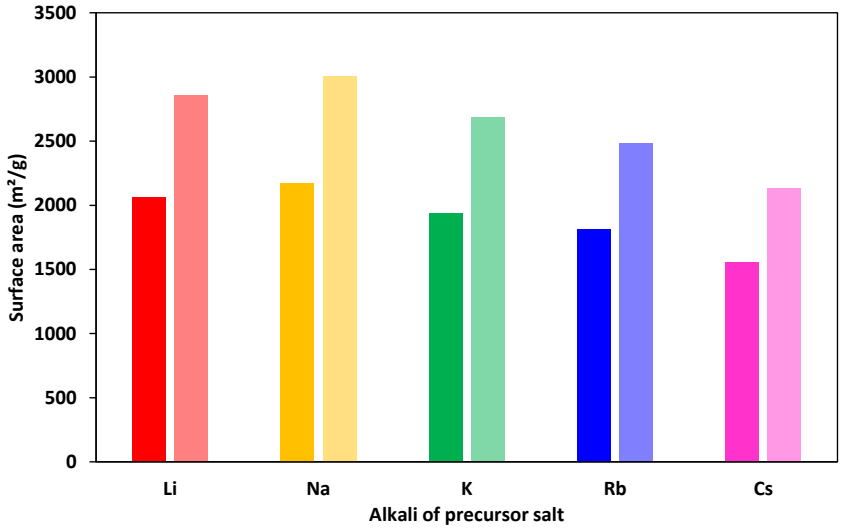

Figure II-6. BET (dark colors) and Langmuir (light colors) surface areas of MIL-100(Fe) samples obtained from different alkali trimesate precursor salts.

In order to determine the importance of the nature of the alkali cation, the same synthetic procedure was applied with the Li, Na, K, Rb and Cs salts of trimesic acid. The products isolated after 4 hours of the reaction showed an identical appearance, as all final products were obtained as orange powders. PXRD analysis of the products (Fig. S II-11) further showed that MIL-100(Fe) was obtained starting from all alkali metal salts. The nature of the alkali trimesate impacts the accessible surface areas of the resulting MIL-100(Fe) samples (Figure II-6 and Table. S II-1). The MOF obtained from the sodium salt,

MIL-100(Fe)-Na, possesses a BET surface area of 2173 $m^2.g^{-1}$, which is about 10% higher than for MIL-100(Fe)-Li and MIL-100(Fe)-K, having surface areas of respectively 2060 and 1935 $m^2.g^{-1}$. Those values are all close to the reported theoretical surface area of 2000 $m^2.g^{-1}$ for MIL-100 MOFs,[258] although the slightly higher surface of MIL-100(Fe)-Na could be due to the presence of structural defects. The surface area then decreases with increasing alkali metal radius (S_{BET} = 1813 and 1553 m^2/g for Rb and Cs, respectively). Although the sample obtained from Na_3BTC shows the highest surface area, all samples have a relatively good porosity, indicating that the alkali ion only slightly affects the MOF formation.

The space time yield was determined to be 34 and 8 $kg/m^3/day$ for the synthesis with sodium trimesate as precursor upon 220 min and 24h of reaction, respectively. The total yield however increased with reaction time (1.28 and 1.99 g for 250 mL of reaction mixture).

4.4. Investigation of the MIL-100(Fe) synthesis mechanism

In an attempt to get a better understanding of the role of oxygen in the formation mechanism of MIL-100(Fe) under the aforementioned green synthesis conditions, a few more experiments have been performed. The first experiment consisted of growing single crystals from the iron sulfate and alkali trimesate precursors in degassed water under an inert atmosphere (see the experimental part for details). The structure of the crystal obtained from the lithium trimesate precursor has been solved from single crystal XRD (Figure II-7). The obtained intermediate, which is isostructural to previously reported Co and Ni analogues (CSD Refcodes EBUNAR and NIHGAM), did not contain the alkali metal, but only isolated iron cations in the +II oxidation state, trimesate linker and water molecules. The iron atoms all have octahedral coordination, and are either bridging two carboxylate units of different trimesates, with four water molecules completing the coordination sphere, or are coordinated to one carboxylate unit with five water molecules completing the coordination. The crystal structure also contains two non-coordinated water molecules in the asymmetric unit.

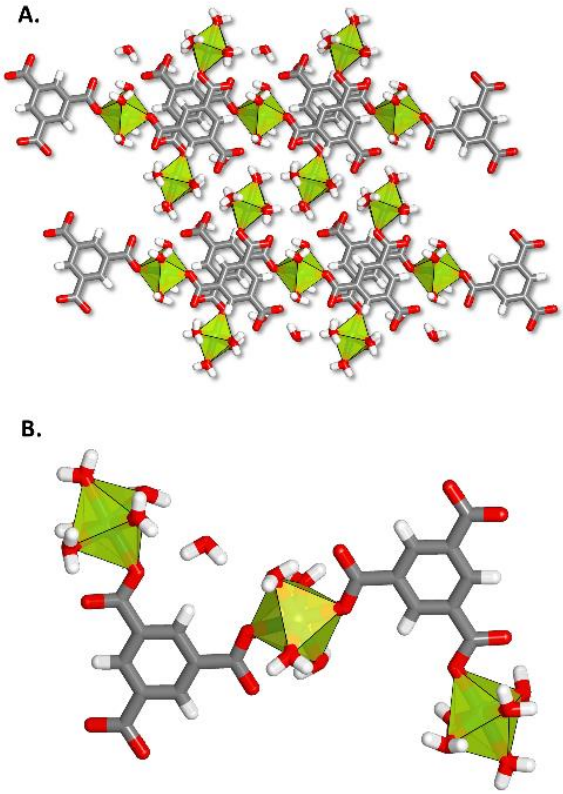

Figure II-7. (A.) Structure of the isolated $Fe_3BTC_2 \cdot 16H_2O$ intermediate, with (B.) the focus on the asymmetric unit.

The obtained intermediate was isolated by filtration under inert atmosphere. When stirred in water in the presence of air, this intermediate formed diffraction-pure MIL-100(Fe), showing that neither the presence of the alkali metals, nor the the sulfate ions from the $FeSO_4$ precursor played a significant role in the formation of the final MOF.

To assess whether the presence of water and oxygen are crucial for the formation of MIL-100(Fe) from the obtained Fe(II) intermediate, oxidation attempts were performed using different solvents and oxidants, and the resulting products were analyzed by means of PXRD (Fig. S II-12). Oxidation in 20 mL of degassed water was performed on 100 mg of the isolated intermediate with either 0.25 mL of liquid Br_2 or

1 mL of 35 wt. % H_2O_2. After 10 minutes of reaction, the solids were separated by filtration and analyzed by PXRD. The powders after the oxidation changed the colour to orange-to-red (compared to the yellow of the Fe_3BTC_2 intermediate), indicating that iron has been oxidized. Surprisingly, none of the obtained products showed diffraction peaks corresponding to MIL-100(Fe). Similar powder patterns were obtained when oxidation was attempted with Br_2 in hexane as solvent, or when oxidation was attempted by heating with solid iodine (0.25 g, excess iodine was removed by sublimation). The similarities between the PXRD patterns resulting from oxidation by the above procedures and the pattern of the Fe_3BTC_2 intermediate indicate that iron undergoes oxidation without any important structural change, likely accompanied by substitution of water molecules by OH^- and/or Br^- or I^-. When oxidation is performed in dry state with elemental bromine (0.25 mL, excess Br_2 was removed by heating), no clear diffraction pattern is obtained due to important fluorescence of X-rays on the sample, suggesting an inclusion of bromine in the sample. Similarly, when the Fe_3BTC_2 intermediate is stirred in ethanol in the presence of air for several hours, the PXRD pattern of the compound (Fig S II-13) remains unchanged, indicating that water is crucial for the transformation of the Fe(II) intermediate into MIL-100(Fe).

To determine whether the formation of the Fe_3BTC_2 intermediate is the step of MIL-100(Fe) synthesis, further oxidation tests were performed on a mixture of degassed water, Na_3BTC and $FeSO_4$ under argon. Bromine was added as oxidant during those tests under two different forms: by direct addition of bromine water, or by slow diffusion of bromine vapor. The direct addition resulted in immediate precipitation of an amorphous product (PXRD not shown), whereas the slow diffusion of bromine under the form of vapor led to the formation of MIL-100(Fe) (named MIL-100(Fe)-Br hereunder), as demonstrated by PXRD (Figure II-8). The reaction of bromine vapor with water leads to the slow formation of dissolved oxygen and HBr, through the following equation (1):

$$2\ H_2O + 2\ Br_2 \rightleftharpoons 4\ HBr + O_2 \quad (1)$$

In the presence of bromine vapor, the reaction thus likely proceeds by the formation of Fe_3BTC_2 that is slowly oxidized by the oxygen released in the reaction between water and bromine vapor. Noticeably, the peaks on the PXRD pattern of MIL-100(Fe)-Br are broadened compared to the ones of MIL-100(Fe) obtained by oxidation in water in the presence of air. This indicates the presence of either smaller crystallites or more defects in the structure. This could be explained by the slower incorporation of O_2 in the reaction mixture when stirring in a mixture of Br_2/Ar instead of air, leading to faster nucleation and crystal growth of MIL-100(Fe)-Br than MIL-100(Fe). Finally, combination of ICP and Schöninger flask analysis shows that about 11% of the clusters of MIL-100(Fe)-Br contain bromide anions (13.8 wt. % Fe and 0.73 wt. % Br; Br/Fe molar ratio = 0.037).

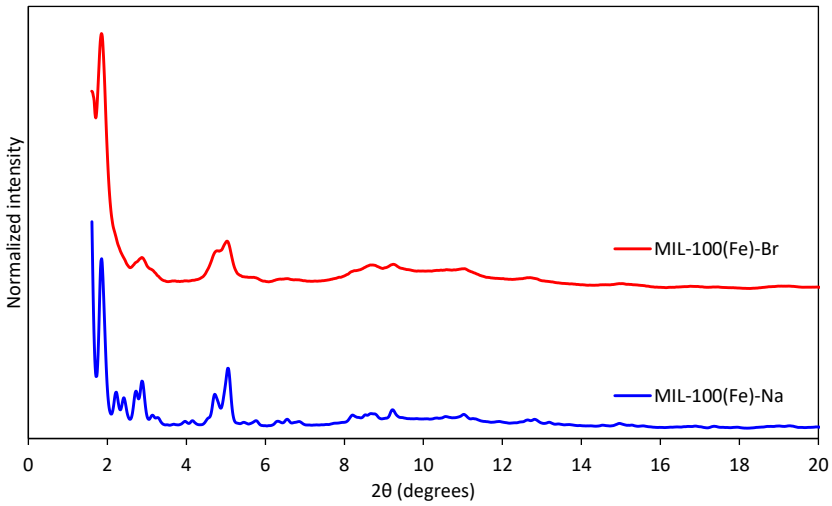

Figure II-8. PXRD patterns of MIL-100(Fe) samples obtained from sodium trimesate as precursor with air (MIL-100(Fe)-Na) and bromine vapor (MIL-100(Fe)-Br) as oxidants.

From the above experiments, we can state that the overall reaction of the synthesis of MIL-100(Fe) proceeds in two separate steps. At first, iron (II) trimesate precipitates, followed by oxidation by O_2 in the

presence of water, leading to the desired MIL-100(Fe) structure (equations 2 and 3).

$$3\ Fe^{2+} + 2\ BTC^{3-} + x\ H_2O \rightarrow Fe_3BTC_2{\cdot}xH_2O \quad (2)$$

$$4\ Fe_3BTC_2{\cdot}xH_2O + 3\ O_2 \rightarrow 4\ Fe_3O(OH)(H_2O)_2BTC_2 + (4x\text{-}10)\ H_2O \quad (3)$$

4.5. Influence of crystallization modulators and Au^{III} sorption in resulting MIL-100(Fe) MOFs

The influence of different crystallization modulators on the textural and gold sorption properties of MIL-100(Fe) obtained through our green synthesis procedure was investigated. A total of four different types of sodium carboxylate modulators was investigated, in order to test the influence of different functional groups, with the carboxylate functions of the modulator accounting for 10% of total carboxylate functions added during the synthesis, the remaining 90% being the ones of the trimesate linkers. Pyromellitate (Pyr, Figure II-9, **A.**) was employed to evaluate the possibility to incorporate mismatched carboxylic acids, *tert*-butyl benzoate (*t*BuBenz, Figure II-9, **B.**) was employed to investigate the influence of bulky hydrophobic functionalities whereas thiodiglycolate (Thio, Figure II-9, **C.**) and 2-aminocaproate (Capr, Figure II-9, **D.**) were employed to evaluate the impact of aliphatic molecules bearing hydrophilic functionalities on the synthesis.

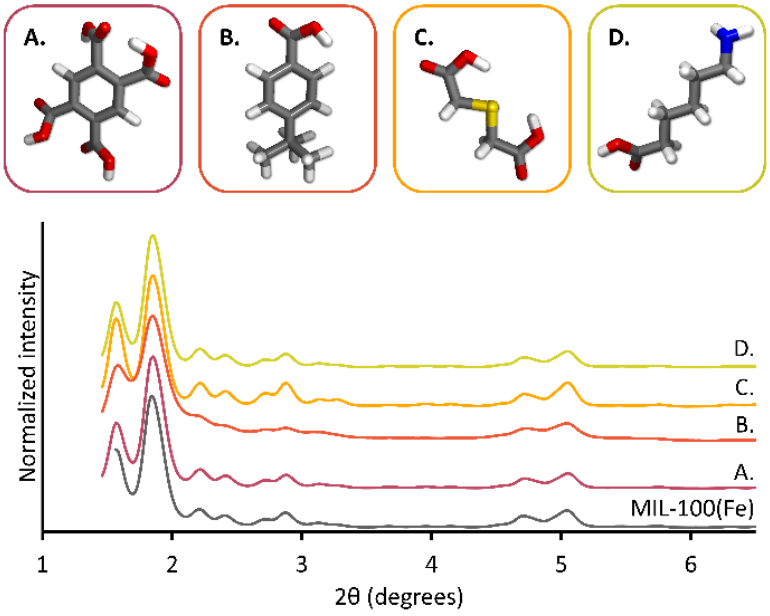

Figure II-9. Molecular structure of tested modulators for the green synthesis of MIL-100(Fe), together with PXRD patterns of MIL-100(Fe) reference sample and the MIL-100(Fe)-modulator samples obtained in presence of: (A.) pyromellitate, (B.) *tert*-butyl benzoate, (C.) thiodiglycolate and (D.) 2-aminocaproate.

From PXRD (Figure II-9), it appears that the synthesis in the presence of all four modulators yielded crystalline MIL-100(Fe). However, in the case of *tert*-butyl benzoate (Figure II-9, **B**), the powder pattern of the obtained MIL-100(Fe)-*t*BuBenz presented significant peak broadening, indicating that the obtained material either possessed a large amount of defective sites, or that very small crystallites were obtained. The patterns of MIL-100(Fe)-Pyr, MIL-100(Fe)-Thio and MIL-100(Fe)-Capr all had peak widths similar to that of MIL-100(Fe) obtained in the absence of any modulator.

To evaluate whether the used modulators are incorporated in the materials, or if they remain in solution after synthesis, the materials were digested in NaOD, dissolving the linkers as sodium salts and eliminating the paramagnetic iron species as insoluble oxides and/or hydroxides. The obtained solutions were subsequently filtered and analyzed by solution ^{1}H-NMR to evaluate the ratio of modulator to trimesate. From this analysis, the incorporation efficiency, that reflects the modulator/BTC^{3-} ratio in the MOF compared to the engaged ratio for the synthesis, could be determined. Note that as some of the linker can still remain unreacted in the solution upon the MOF formation (i.e. incomplete reaction), this incorporation efficiency can theoretically exceed 100% if the modulator is incorporated preferentially over BTC^{3-}. The results of this determination, shown in Table II-4, evidence that the modulator was incorporated in the case of the aromatic linkers, whereas the aliphatic thiodiglycolate and 2-aminocaproate were not incorporated into the materials. Pyromellitate was incorporated with an efficiency of only 57 %, which could be explained by the mismatch of one carboxylate function of the modulator, and *t*Bu benzoate was incorporated with a much better efficiency, of 119 %. The preferable incorporation of *t*Bu benzoate compared to trimesate cannot be explained by more efficient coordination, since the modulator only has one carboxylate function compared to three for the trimesate linkers. However, the bulky nature of the *t*-butyl function does not allow the modulator to leave the pores of the MOF once they are formed, whereas the smaller trimesate can diffuse through the framework after its formation, likely explaining why so much *t*Bu benzoate is incorporated into the MOF.

The textural properties of the different materials were evaluated by nitrogen physisorption experiments (Fig. S II-14). As expected by the presence of the bulky *tert*-butyl functions in the MOF, MIL-100(Fe)-*t*BuBenz possesses a highly reduced surface area (613 $m^2.g^{-1}$) compared to the MOF obtained without modulator. The low surface area, together with the presence of supplementary peaks on the FTIR spectrum compared to the other MIL-100(Fe) materials (Fig. S

II-15) further supports the presence of an important amount of defects inside this material, as already expected from the peak broadening on the PXRD pattern. MIL-100(Fe)-Pyr and MIL-100(Fe)-Thio possess BET surface areas typical for MIL-100(Fe) MOFs, of respectively 1780 and 1646 $m^2.g^{-1}$. Surprisingly, MIL-100(Fe)-Capr possesses the highest surface area of all this MOFs series, exceeding 2400 $m^2.g^{-1}$. This result indicates that the use of 10% 2-aminocaproate during the green synthesis of MIL-100(Fe) allows for efficient modulation of the crystallization, leading to a high quality material. It should be noted that none of those three latter materials have supplementary signals on the FTIR spectra compared to the one of MIL-100(Fe) obtained without modulator (Fig. S II-15), even if MIL-100(Fe)-Pyr has some modulator remaining in the final material, as shown by solution ^{1}H-NMR of the digested MOF.

Table II-4. Ratios of modulator and BTC^{3-} linker in the MOFs obtained in the presence of various modulators as determined by ^{1}H-NMR of samples digested in NaOD, with corresponding incorporation efficiency of the modulator and calculated BET surface areas of the samples.

Material	**Modulator**	**Modulator / BTC^{3-}**	**Incorporation efficiency**	**BET surface area**
		(%)	(%)	($m^2.g^{-1}$)
MIL-100(Fe)-Na	-	-	-	2173
MIL-100(Fe)-Pyr	Pyromellitate	4.3 / 95.7	57	1780
MIL-100(Fe)-*t*BuBenz	*t*Butyl-benzoate	35.6 / 64.4	119	613
MIL-100(Fe)-Thio	Thiodiglycolate	0 / 100	0	1646
MIL-100(Fe)-Capr	2-aminocaproate	0 / 100	0	2401
MIL-100(Fe)-Cl	-	-	-	1822

The materials obtained by modulator-mediated synthesis, as well as pristine MIL-100(Fe) obtained by the green synthesis method, were investigated for their ability to recover Au^{III} from aqueous solutions. Indeed, only one previous study has been dedicated to the use of MIL-100(Fe) for recovering this particular metal.[115] This previous

study was performed using a MIL-100(Fe) MOF obtained through conventional solvothermal synthesis in DMF from an Fe^{3+} precursor, as well as some MIL-100(Fe) samples with incorporated polymers in their pores.

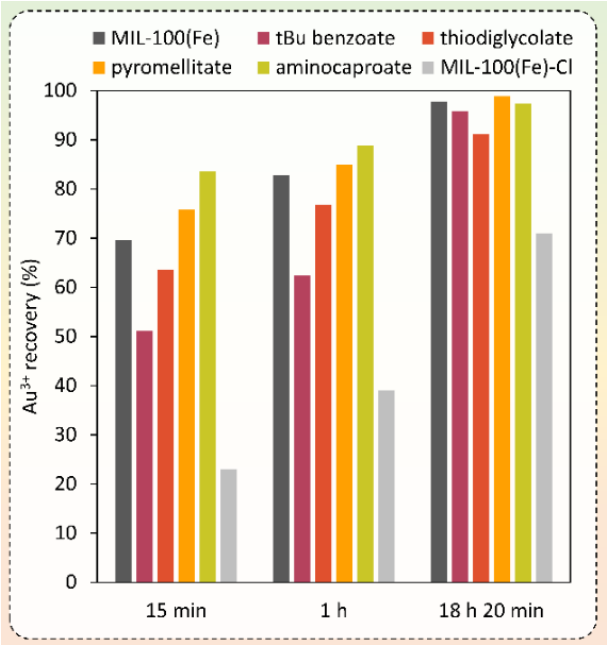

Figure II-10. Au^{III} recovery from a 50 ppm $KAuCl_4$ solution upon different contact times (15 min, 1 h and 18 h 20 min) for the MIL-100(Fe) samples obtained with different crystallization modulators and the MIL-100(Fe)-Cl sample reproduced from the literature.

In our experiments, 10 mg of oven dried MOF material was used to recover gold from 10 mL of a 50 ppm aqueous Au^{III} solution (as a solution of $KAuCl_4$ in water) under continuous shaking. Interestingly, atomic absorption spectroscopy (AAS) of the supernatant solutions showed that all the MIL-100(Fe) materials obtained through the synthesis in water performed quite well in Au^{III} removal, with between 91 and 99% efficiency after 1100 min (18 h 20 min) of contact time (Figure II-10). The speed of the uptake however is dependent on the material, and roughly increases with increasing surface area of the considered MOF.

To get some insight into the removal mechanism of Au^{III} from solution of the various MOF materials obtained through the green synthesis method, we recovered the solids after 1100 min of exposure to the Au^{III} solution and analyzed the obtained powders by PXRD (Fig. S II-16). Interestingly, all the materials revealed the presence of metallic Au^0 in the MOF, indicating that the Au^{III} has been reduced during the process. Surprisingly, it has been reported that the conventional solvothermally obtained MIL-100(Fe) in its pristine state did not reduce Au^{III} and possesses lower Au^{III} removal performances than its composites with polymers inside the pores.[115] To verify this statement, we reproduced the experiment with a MOF obtained according to the reported synthetic procedure (see Experimental part), which is called MIL-100(Fe)-Cl here. It presented a quite high surface area (Table 4). From the results of the Au^{III} adsorption test, it clearly appears that the sample obtained through conventional solvothermal synthesis in DMF does not allow as good gold recovery as the MIL-100(Fe) samples obtained through our green synthesis procedure (Figure II-10) and PXRD reveals only negligible traces of Au^0 in this sample (Fig. S II-16).

To explain the difference between MIL-100(Fe) obtained under green aqueous conditions and solvothermal synthesis in DMF, we analyzed the cluster structure of the compounds. As stated above, the MOF obtained in water possesses hydroxyl moieties to ensure the charge neutrality on the MOF's clusters (Figure II-11). However, we were able to determine, by combination of ICP-OES and Cl analysis, that one chloride anion is present on each cluster for the MOF obtained in DMF (Figure II-11, inset, see Table S II-2). The nature of the counter-ion is thus likely to be the reason why the two materials perform so differently during Au^{III} sorption experiments. Furthermore, the "green" MOFs were obtained from an Fe^{2+} precursor, which can result in part of the iron being in the +II oxidation state in the final compound. Also, the presence of hydroxide counter-ions facilitate the redox shift between Fe^{2+} and Fe^{3+} in the materials, since Fe^{3+} can easily be reduced

in the MOF by assistance of a weakly acidic medium transforming OH^- into water by protonation (Figure II-11).

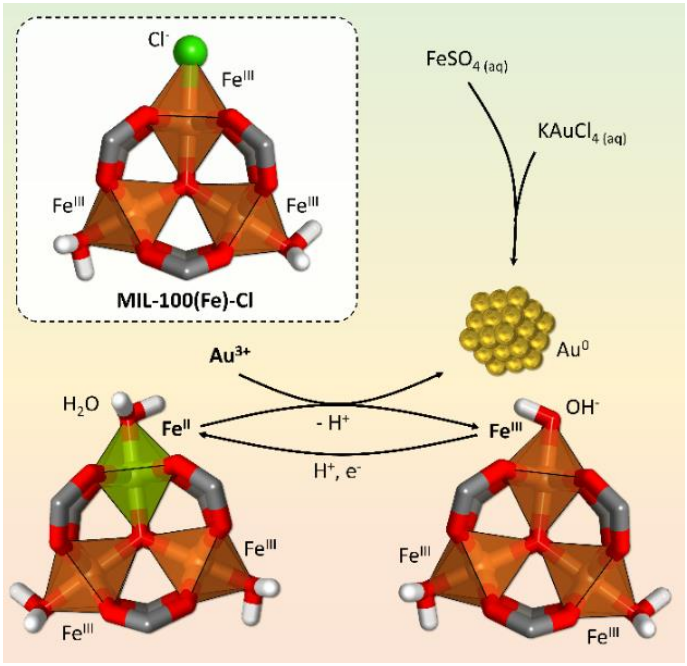

Figure II-11. Proposed reduction mechanism of Au^{III} into Au^0 on Fe^{II} in the clusters of hydroxyl-containing MIL-100(Fe) obtained by the green synthesis (three clusters are needed to reduce one Au^{III}), and reduction of $KAuCl_4$ by $FeSO_4$ to demonstrate that Fe^{II} reduces Au^{III} into metallic gold. Upper left inset: $Fe_3^{III}(\mu_3\text{-}O)Cl(O_2CR)_6$ cluster that does not contain Fe^{II} for Au^{III} reduction in MIL-100(Fe)-Cl. Color code: orange octahedra = Fe^{III}; green octahedra = Fe^{II}; grey = C; red = O; white = H; green sphere = Cl; gold = Au^0.

This same reduction process in MIL-100(Fe)-Cl would require a much stronger acid to transform the chloride anion into HCl. The reduction of Au^{III} in the MOF can thus be explained by the presence of Fe^{2+}, which enables reduction of the gold, assisted by simultaneous reversible oxidation of iron in the clusters. This hypothesis was further supported by mixing a solution containing $FeSO_4$ with a solution containing $KAuCl_4$, leading to reduction and precipitation of metallic gold, as shown by PXRD of the obtained precipitate (Fig. S II-17), demonstrating that Fe^{2+} is sufficiently reducing to trigger this reaction.

We hypothesize that the reduction of Au^{III} by the Fe^{II} sites in the clusters occurs through an inner sphere redox mechanism by a bridging chloride from the $[AuCl_4]^-$ species in solution, forming Au-Cl-Fe bonds during electron transfer.

6. Conclusions

The green synthesis of MIL-100(Fe) in water has been improved through the use of alkali trimesate salts as precursors. The salts of all alkali metals in their different hydration forms have been synthesized and characterized by means of TGA and Raman spectroscopy, and their structures solved by synchrotron single crystal and PXRD. The use of sodium trimesate as precursor afforded MIL-100(Fe) with the largest surface area. It was shown that the reaction between Fe^{2+} and the trimesate salts in aqueous medium proceeds through the formation of an Fe_3BTC_2 intermediate, whose structure was solved by single-crystal XRD. Both water and air oxygen were shown to be necessary for the reaction to proceed, as other tested solvents and/or oxidants were not able to transform the intermediate into MIL-100(Fe). Space-time yields up to 34 kg/m³/day were obtained through our new procedure. Furthermore, this synthesis is based on the use of cheap $FeSO_4$ as metal source, which is suitable for industrialization, as it does not cause corrosion to reactors unlike chlorides or nitrates. As water is the only solvent used and no heating is required, the main cost for the production of MIL-100(Fe) through this new procedure is the one of the linker. Carboxylates as crystallization modulators were used to modify the textural properties of MIL-100(Fe). When aromatic carboxylates are used, the modulator was partly incorporated into the MOF's structure, whereas aliphatic carboxylates were not. The green MIL-100(Fe) materials showed improved Au^{III} adsorption performances compared to a solvothermally obtained sample, increasing with the MOF surface area. The nature of the charge balancing anion is likely the reason for the difference in the observed results: the clusters in the MOF obtained through our green synthesis strategy contains hydroxide anions and efficiently reduces Au^{III} to the metallic state, whereas the

solvothermally obtained sample contains chloride anions and does not reduce Au^{III}.

CHAPTER III

Bimetallic transition, p-bloc and lanthanide MIL-100(Fe,M) MOFs

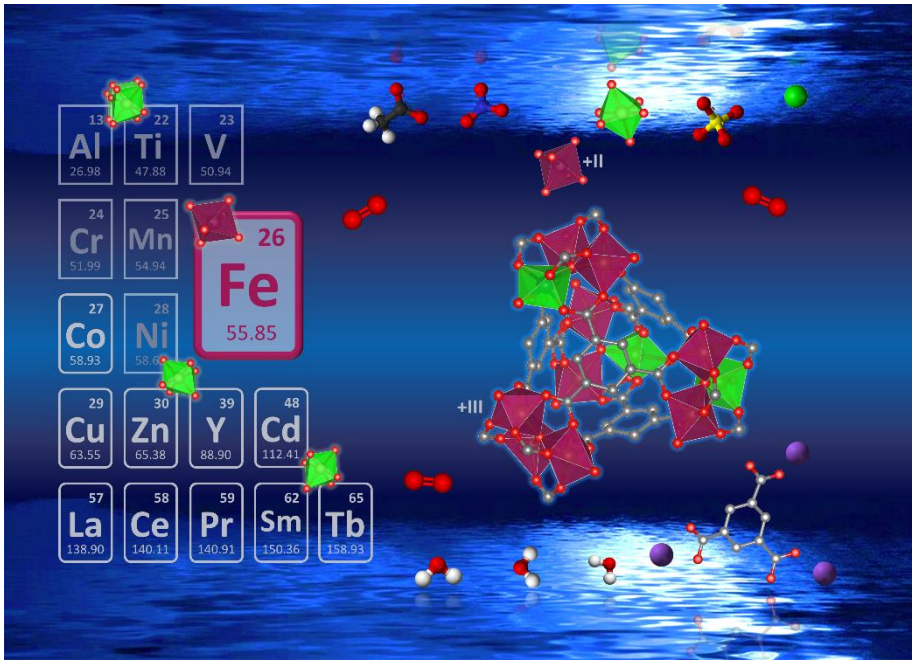

This Chapter is inspired by the following publication:

Steenhaut, T.; Hermans, S.; Filinchuk, Y. *Green synthesis of a large series of bimetallic MIL-100(Fe,M) MOFs*, New Journal of Chemistry, **2020**, *44*, 3847-3855, doi: 10.1039/d0nj00257g / journal back cover.

Chapter III - Bimetallic transition, *p*-bloc and lanthanide MIL-100(Fe,M) MOFs

1. Abstract

This section deals with the synthesis of bimetallic MIL-100(Fe,M) MOFs containing first and second row transition metals, aluminium as *p*-bloc metal and lanthanides. The synthetic method is based on the use of the alkali trimesates presented in the previous chapter and different reaction parameters are investigated through the use of cobalt as model metal. The synthetic procedure is then extended to the incorporation of Al, Ti, V, Cr, Mn, Ni, Cu, Zn and Cd. We also investigate the specific case of lanthanides, which possess a different chemistry than main group metals and have very large ionic radii compared to the iron of the template MOF.

We demonstrate that we can control the amount of doping metal in the structure and that transition and main group metals with large ionic radii, such as cadmium(II), can also be incorporated into the structure, as well as some lanthanides. Finally, we present a new convenient way to determine the percentage of a doping metal in complex MOFs by PXRD.

2. Introduction

Iron centers in MIL-100(Fe) have been shown active in catalysis and gas sorption.[248,249,250] It was shown that adding a doping metal into the structure can impressively improve some properties of MOFs and of MIL-100 in particular.[251,20,252,253] However, until now, very few combinations of template and doping metals were investigated and all those materials were synthesized by solvothermal methods that mostly involve the use of HNO_3 or HF as modulators, leading to hazardous scale-up. In some cases, the second metal was introduced by post-synthetic exchange, adding a second step in the synthesis. Moreover, the possibility of mixing metals with large differences of ionic radii in the MIL-100 structure has not been investigated yet.

Our goal is to introduce a wide range of metal substitutions into the Fe-based MIL-100, serving as a low-cost templating structure; iron having the advantages of being very abundant, cheap and non-toxic. Addition of water-soluble metal salts in the reaction mixture of our new synthetic procedure presented in the previous Chapter allowed us to incorporate many metals in +II, +III and +IV oxidation states to afford bimetallic MIL-100(Fe,M) MOFs through a green single-step synthesis.

3. Materials and Methods

Chemicals

Trimesic acid (98%) and sulphuric acid (96%) were purchased from Acros Organics. Denaturated ethanol (Technisolv, 99%) and hydrochloric acid (37%) were purchased from VWR Chemicals. Iron sulphate (technical grade) was supplied from Forever products. Cobalt (II) sulphate heptahydrate (99+%) was purchased from Janssen Chimica. Copper (II) chloride dihydrate was purchased from Riedel-deHaën. Cadmium nitrate hexahydrate (99.9%), aluminium chloride (99.9%), vanadium(III) chloride (97%) and titanium(III) chloride (99.999%) were purchased from Sigma-Aldrich. Cobalt(II) chloride hexahydrate (98%) was purchased from Fluka. Nickel(II) chloride hexahydrate (98%) and potassium dichromate (99.8%) were purchased from Merck. Manganese(II) chloride (98%) was purchased from Aldrich. Zinc chloride (98%) was purchased from Alfa Aesar. Lanthanum(III) carbonate was purchased from K&K laboratories, Inc. Praseodymium(III,IV) oxide (99.9%) was prurchased from Acros. Neodymium(III) oxide (Nd_2O_3/TREO: min. 99.9%), europium(III) oxide (Eu_2O_3/TREO: min. 99.99%), erbium(III) oxide (Er_2O_3/TREO: min. 99.9%) and ytterbium(III) oxide (Yb_2O_3/TREO: min. 99.9%) were purchased from Strategic Elements. Samarium(III) oxide (99.9%) was purchased from Koch-Light Laboratories Ltd. Cerium(III) acetate hydrate (99.9%) and terbium(III) nitrate hexahydrate (99.999%) were purchased from Aldrich.

All chemicals were used as received except from iron sulphate, which was purified by heating a saturated aqueous solution (close to the boiling point) in the presence of iron metal and sulphuric acid for one hour. The obtained hot solution was filtered and allowed to cool. Ethanol was added to the solution to crystallize the iron sulphate, which was isolated by filtration on a glass frit. The purifier $FeSO_4$ heptahydrate was washed with ethanol and dried under vacuum (using a Schlenk line).

Synthesis of $CrCl_3$ hexahydrate

Chromium(III) chloride was synthesized by gently adding 20 mL of methanol to 5.92 g of $K_2Cr_2O_7$ dissolved in 17 mL of concentrated (37%) HCl. This reaction was carried out in a very large Erlenmeyer flask placed in an ice bath (the reaction is very exothermic). The obtained dark green solution was then boiled to dryness and the obtained green solid was washed with ethanol and ether followed by drying under vacuum. FTIR: 3526 cm^{-1} (sharp), 2986 cm^{-1} (broad), 1584 cm^{-1}, 888 cm^{-1}, 722 cm^{-1}, 612 cm^{-1}, 494 cm^{-1}, 408 cm^{-1}. The spectrum corresponds to reference data.[259]

Synthesis of MIL-100(Fe,M) in acidic conditions

The syntheses of the doped MIL-100(Fe,M) MOFs were realized following the identical procedure to that described in the previous Chapter, starting from $Na_3BTC{\cdot}3H_2O$. The only difference being that the iron sulphate was replaced by a mixture of $FeSO_4{\cdot}7H_2O$ and another metal salt in different ratios. Table S III-2 A lists the used salts and their respective quantities. The pH and the colours of the different precipitates is also given in Table S III-2 B.

Synthesis of lanthanide chlorides

To 3 eq. of concentrated (37%) aqueous HCl was added 1 eq. Ln in the form of the corresponding oxide or carbonate. The oxide was reacted with the acid until a clear solution was obtained (applying heating where needed). Then excess acetone was added to remove the excess water and the organic and aqueous layers were shaken

vigorously. The organic layer was then eliminated by decantation. This operation was repeated until a solid started to precipitate in the aqueous layer. The solid was then filtered using a glass frit and acetone was used to wash the resulting crystals. The salt was then dried under vacuum (using a Schlenk line) and stored in a desiccator.

Synchrotron powder X-ray diffraction (S-PXRD) patterns of MIL-100(Fe,M) samples were recorded at the Swiss-Norwegian beamlines (SNBL) at the European Synchrotron Radiation Facility (ESRF, Grenoble) at a wavelength of 0.68683 Å or 0.79800 Å using a Pilatus 2M detector. The samples were loaded into glass capillaries of 0.5 mm diameter. For temperature dependent measurements, a calibrated heating gas blower was used and the samples were heated from room temperature to 500 °C.

ATR-FTIR spectra were recorded in the range of 4000-370 cm^{-1} with a resolution of 4 cm^{-1} using a Bruker Alpha spectrometer equipped with a Platinum ATR module (diamond crystal) housed in an MBraun argon-filled glovebox.

Nitrogen physisorption measurements at 77 K were performed on a Micromeritics ASAP 2020 instrument. All samples were degassed at 200 °C during 10 h prior to analysis.

XPS analyses were carried out with a SSI-X-probe (SSX 100/206) photoelectron spectrometer from Surface Science Instruments, equipped with a monochromatized microfocus Al X-Ray source. The samples were prepared by sticking on a double-face adhesive tape mounted onto small brass sample holders that were placed on an insulating ceramic carousel (Macor). An electron flood gun combined with a nickel grid were used to avoid charge effects. The CasaXPS software (Casa Software Ltd) was used to perform the data treatment.

ICP-AES measurements were performed after sample calcination at 500 °C followed by digestion in aqua regia. An ICAP-6500 apparatus from ThermoFisher Scientific was used to carry out the analyses.

For **AAS**, samples were digested in aqua regia followed by filtration to remove the reprotonated H_3BTC. AAS measurements were performed using a PerkinElmer 3110 atomic absorption spectrometer. Fe Fe and Co analysis, an oxidizing air-acetylene flame was used to atomize the samples. Intensitron^{TM} hollow cathode lamps (PerkinElmer) were used for the measurements (pure Co cathode for cobalt determination and mixed FeNiCu lamp for Fe determination).

Lab **PXRD** analyses of calcined MIL-100(Fe,M) samples were performed using a MAR345 diffractometer with X-rays generated by a Rigaku UltraX 18S X-ray generator (molybdenum anode, 0.71073 Å), with a monochromated beam (Xenocs FOX 3D mirror).

TGA/DSC measurements under air and nitrogen were recorded on a Mettler-Toledo TGA/DSC 3+ STAR^e system. Gas flows of 100 ml min^{-1} and heating rates of 10 °C min^{-1} were used.

4. Results and Discussion

4.1. Incorporation of Co in MIL-100(Fe)

To investigate the possibility of synthesizing mixed-metal MIL-100(Fe,M) compounds in aqueous media, we decided to first test M = cobalt. Indeed, Fe and Co are the closets neighbours in the Periodic Table and both possess a (relatively) stable +II oxidation state, which makes Co^{2+} a particularly suitable candidate for developing the synthesis method. MIL-100(Fe,Co) was obtained by mixing a solution of iron(II) and cobalt(II) sulphates with a solution of $Na_3BTC{\cdot}3H_2O$ in air. This mixture allowed the reaction to proceed in an acidic media and consequently allowed the incorporation of the second metal. PXRD patterns show a single phase MIL-100(Fe,Co) (Fig. S III-3) whatever the Fe/Co ratio (in the 5-35 mol% Co range). The ATR-IR spectra are all very similar to the undoped MIL-100(Fe) MOF (Fig. S III-4). The incorporation of Co into the structure was confirmed and quantified by inductively coupled plasma-optical emission spectroscopy (ICP-OES) (see Figure III-1). It should be noted that using NaOH and H_3BTC instead of purified sodium trimesate results in the presence of secondary

phases due to the basic pH of the linker solution. The formation of metal-BTC intermediates containing $Fe^{(II)}$ and $Co^{(II)}$ that are subsequently oxidized into MIL-100(Fe,Co) can explain why the incorporation only succeeds in acidic media, whereas in basic media it is prevented by the formation of hydroxide species. Indeed, in the slightly acidic medium used for the successful synthesis, we were able to isolate the $Fe_3BTC_2 \cdot 12H_2O$ intermediate, as well as its Co analogue (Fig. S III-5).

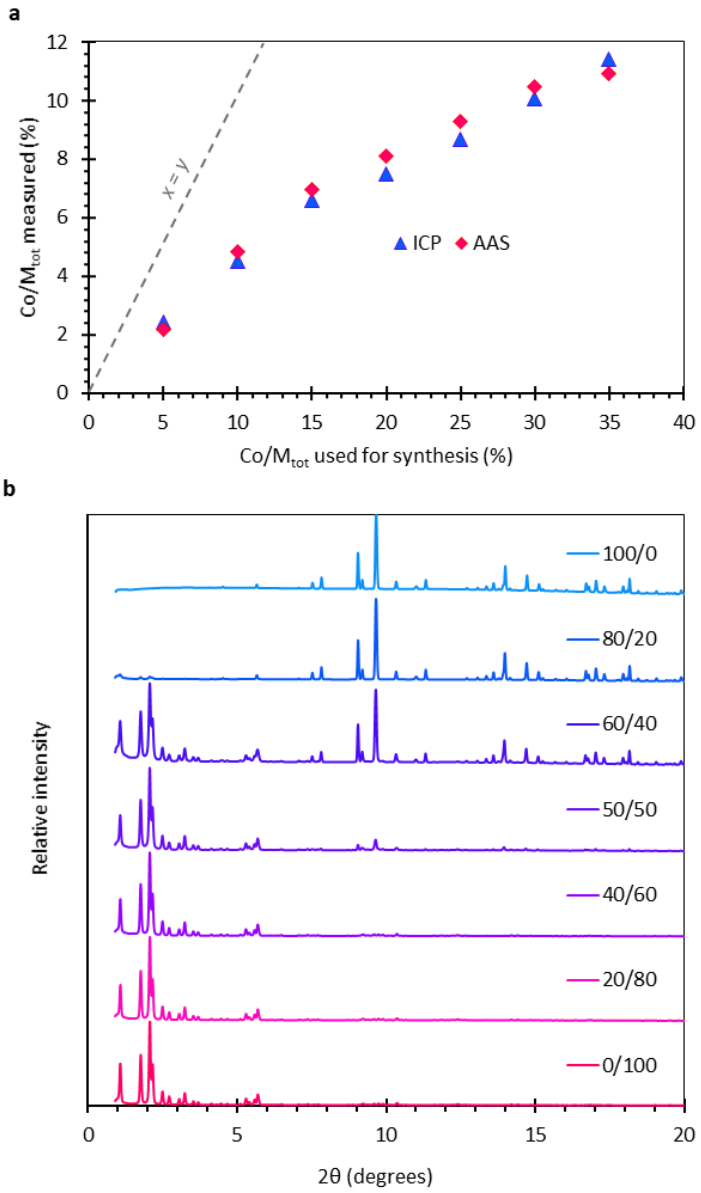

Figure III-1. (a) Incorporated quantity of cobalt into MIL-100(Fe) in function of the quantity used for the synthesis. Indicated percentages correspond to mol%). (b) PXRD patterns of compounds obtained using different Co/Fe ratios for the synthesis, showing pure MIL-100 phase for Co/Fe = 0/100 to 40/60 and the apparition of a second crystalline phase (a non-porous $M^{II}_3BTC_2$ hydrate) for higher Co/Fe ratios.

4.2. Variation of the amount of incorporated Co

In order to verify whether we can control the amount of incorporated doping metal, we varied the starting ratio of Fe(II) and Co(II) in the synthesis solution. The reaction time (4 h), the volume of the reaction mixture and the stirring rate were kept constant to ensure that the oxidation would proceed in the same manner. The obtained MIL-100(Fe,Co) samples were calcined and digested in aqua regia followed by ICP-OES measurements. The Co/M_{tot} ratios in the obtained MOFs were plotted against the Co/M_{tot} ratios used for the synthesis (Figure III-1, a). A clear trend is observed: the amount of cobalt incorporated into the structure increases with the engaged ratio. However, there is a limit to the amount of Co that can be incorporated into the structure. When the used Co/M_{tot} ratios is higher than 40 mol%, a second crystalline phase is present in the powder diffraction patterns (Figure III-1, b). When the reaction time is increased, the amount of incorporated Co also increases. For instance, when 20 mol% of Co is used, ICP-OES shows in the resulting MIL-100(Fe,Co) a Co/M_{tot} value of 7.9 mol% after 4 h while it is 11 mol% after 24 h of reaction. For comparison purposes, we performed a post-synthetic exchange by soaking pure MIL-100(Fe) into a concentrated aqueous solution of Co^{2+}. This led to a compound with very poor substitution compared to the direct synthesis, as shown by ICP (for more details see Annexes).

4.3. Incorporation of other transition and *p*-block metals

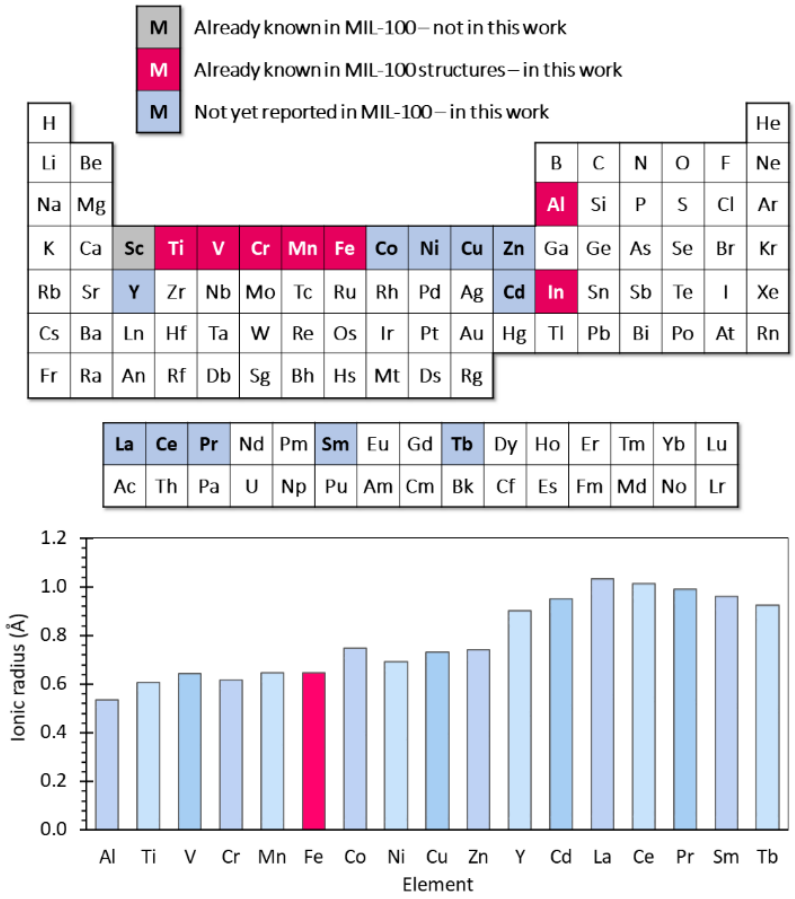

Figure III-2. Ionic radii of iron and some of the doping metals that were incorporated in MIL-100(Fe,M) in this work (lower part) and their position in the periodic table (upper part). The presented ionic radii are for coordination state VI with the most probable oxidation state (+III low spin for Fe, +II for Co, Ni, Cu, Zn and Cd, +III for Al, V, Cr, Mn, Y, La, Ce, Pr, Sm and Pr and +IV for Ti) according to the revised values reported by Shannon and Prewitt.[260]

A large variety of other doping metals was used to evaluate the limits of our synthesis strategy. One would expect that at a certain size of the doping element a substitution will not occur. For this reason, we investigated the incorporation of several transition and p-block metals with a particular attention on the differences in size and the possible

oxidation states of the doping element. Due to their specific reactivities, the case of lanthanides as doping metals is covered in a separate section (see section 4.7).

To our surprise, all the doping ions that can be solubilized in water substituted well into MIL-100(Fe), despite some large differences in ionic radii with Fe(III), see Figure III-2. However, a few elements are not suitable for incorporation into MIL-100(Fe) by our synthetic procedure. This is the case of Pb^{2+} that precipitates in the presence of the SO_4^{2-} ions of the iron(II) sulphate precursor, or of Bi^{3+} that undergoes oxolation in water. S-PXRD patterns (Fig. S III-6) and ATR-IR spectra (Fig. S III-7) of the different samples showed that they are all single phase, isostructural and that all the tested metals can be incorporated into the structure. The M_{dopant}/M_{tot} ratios obtained after 16 h reaction using 20 mol% of doping metal were determined by ICP-OES (Table S III-1) and appear to be significant (7.5 to 29.9 mol%) but dependent on the nature of the used metals. Comparison of the ICP-OES and XPS (Table S III-1) results shows that the bulk and surface contents with a given doping metal are not always identical. This could be due to a preferential incorporation of either the doping metal (M) of template metal (Fe) and the subsequent variation of the relative concentrations of the metals in solution during the crystal growth. Metals that are preferentially incorporated are then more concentrated in the core of the crystal than on its surface. This theory is supported for the +II and +III doping metals that do not undergo oxidation neither reduction during the incorporation process. Indeed, the iron, being oxidized from +II to +III during the formation of the MOF, is incorporated preferentially over +II metals (Co^{2+}, Ni^{2+}, Zn^{2+} and Cd^{2+}) but not over +III metals (Al^{3+}, Cr^{3+} and lanthanides). However, when the doping metal undergoes redox during the incorporation (*i.e.* Cu, Ti and V), more complex processes are at work, as shown in Figure III-3. When plotting the M_{dopant}/M_{tot} surface (XPS determined) vs. bulk (ICP determined) concentrations, clear cut regions of the preferential substitutions appear with respect to the oxidation states of the doping metal, as shown in Figure III-3, which suggests satisfactory

rationalization of the obtained results and potentially a predictive power for the incorporation of other metals.

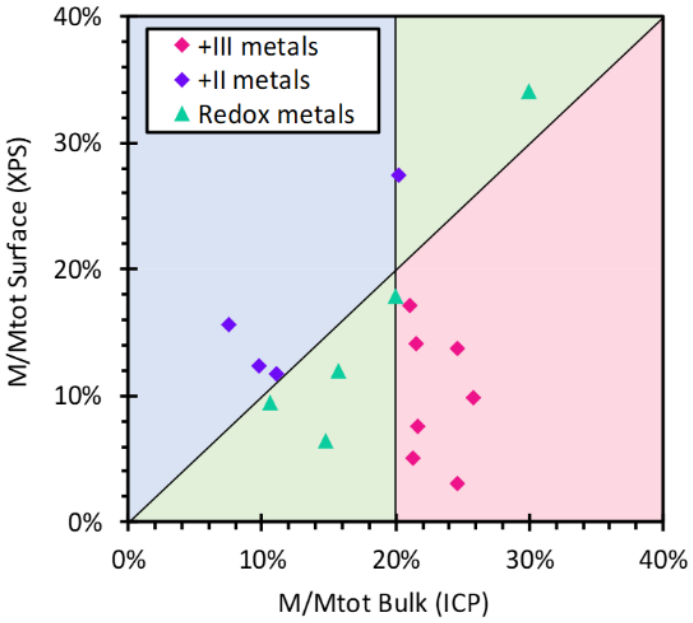

Figure III-3. Illustration of the preferential incorporation process. Metals in the +III oxidation state are incorporated preferentially over iron in MIL-100(Fe,M), leading to higher bulk than surface concentrations of M. Similarly, Fe is incorporated preferentially over +II metals. The blue and pink areas of the graph indicate the zones expected for preferential incorporation of Fe over M and of M over Fe respectively. The doping metals undergoing redox during the formation of the MOF are all located in the green areas, indicating the existence of more complex processes during the incorporation of those metals. The M/Fe ratio used for all syntheses was 20/80. Indicated percentages correspond to mol%.

4.4. Materials porosities

Before nitrogen sorption experiments, all materials were activated by heating under vacuum at 200 °C for 10 hours. Importantly, all the obtained materials sustained this activation step without collapsing of the structures. The BET surface areas of the MIL-100(Fe,M) materials were high for most doping metals (Fig. S III-8). Nearly all the obtained compounds show nitrogen adsorption-desorption curves with a very similar shape; of the I(a) type according to the IUPAC classification of

physisorption isotherms,[154] characteristic of purely microporous materials (Fig. S III-8). However, for M = Cr, the surface area is significantly lower than with other first-row transitions metals. Second-row transition metals show smaller, although still large, surface areas (S_{BET} = 1462 m^2 g^{-1} for M = Cd). Importantly, MIL-100(Fe,M) with doping metals having typical oxidation state +II, namely Ni, Co and Zn, show about 10% higher surface areas than MIL-100(Fe), likely due to the improved dehydration of the metal sites, see Scheme III-1. The surface area of the nickel-doped MOF (2274 m^2 g^{-1}) is significantly larger than the one of MIL-100(Fe,Ni) materials previously reported (1525-1570 m^2 g^{-1}).[186]

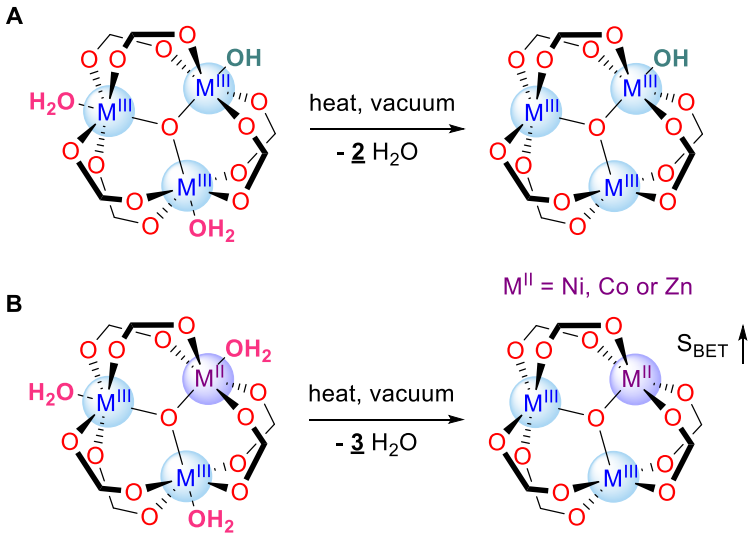

Scheme III-1. (A) Only two water molecules can be desorbed from Fe_2M^{III}-μ_3-oxo clusters whereas (B) three water molecules can be desorbed from Fe_2M^{II}-μ_3-oxo clusters, leading to more higher surface areas.

Interestingly, the MIL-100(Fe,M) samples with M = Ti, Cu, Al and V show a slight hysteresis in their sorption-desorption curves. S-PXRD patterns of those three last compounds also show peak broadening as compared to the other materials. These observations suggest the presence of mesopores, defects and/or intergrain porosities into the materials.

4.5. Thermal behaviour

The thermal stability of the obtained compounds was evaluated by TGA measurements under both nitrogen and air (Fig. S III-11 and Figure III-4). All the compounds, with the notable exception of MIL-100(Fe,Cu) show very similar decompositions temperatures under nitrogen (around 420 °C), as well as under air (around 355 °C). The presence of copper in MIL-100(Fe,Cu) has an important effect on the thermal stability of the compound as the decomposition temperature drops from ~355 °C to 327 °C under air and from ~420°C to 354 °C under nitrogen.

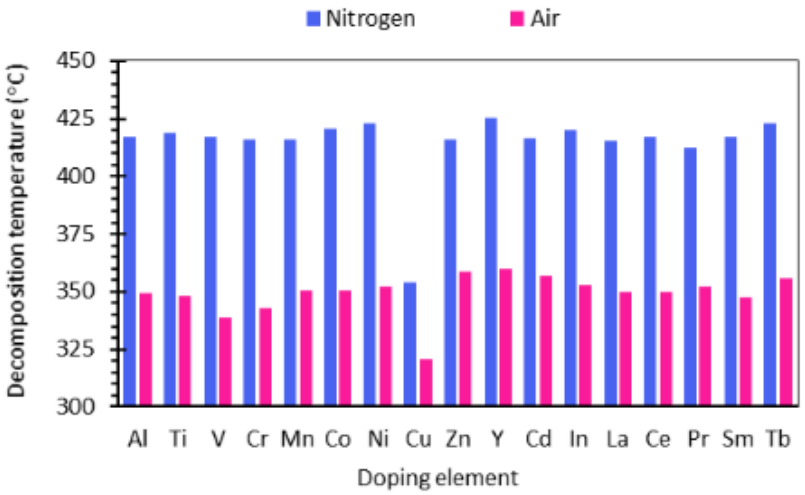

Figure III-4. Decomposition temperature of the MIL-100(Fe,M) compounds determined by TGA under air and nitrogen.

Heating the samples at a rate of 10 K min^{-1} did not allow to get rid of all the coordinated solvent molecules before the decomposition, even if this last event occurs at temperatures above 400 °C under nitrogen (354 °C in the case of MIL-100(Fe,Cu)). This can be explained by the strong bonds formed between the coordinated solvent molecules and the metal centres.

4.6. Determination of oxidation states

XPS was used to determine the oxidation states of the incorporated doping metals (Fig. S III-12 and Table III-1, p.119). The analysis revealed that oxidation states depend highly on the nature of the doping metal, ranging from +I to +V. The incorporation of metals with the oxidation states +II, +III and +IV can easily be accommodated by varying the nature of the oxygenated ligand on the doping metal site (Figure III-5, upper part). If we consider that only one doping metal atom is present in each M_3-μ_3-oxo cluster (*i.e.* Fe_2M-μ_3-oxo clusters) at the maximum, and that the iron centres are in the +III oxidation state, then M(II) does not need any counter ion. Similarly, M(II) is balanced by OH^- (the presence of Cl^- or SO_4^{2-} was not detected by XPS) and M(IV) is balanced by μ_1-O^{2-} ions.

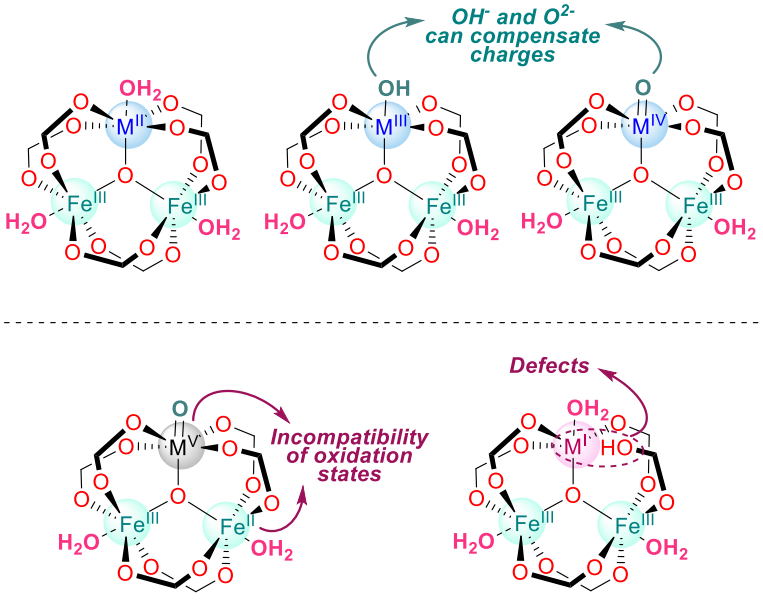

Figure III-5. Illustration of neutral Fe_2M-μ_3-oxo clusters that can be formed with M in oxidation states +II, +III and +IV with charge balance by OH^- or O^{2-} units (upper part) and problems arising in the charge balance in the presence of doping metals in the +I or +V oxidation states.

On the other hand, the presence of Cu(I), that is detected in MIL-100(Fe,Cu), cannot be explained by a perfect cluster structure. It

is likely that in this case defects are present in significant amounts in the cluster or in the framework structure (Figure III-5, lower part). This nicely correlates with the hysteresis observed on the nitrogen sorption isotherm, peaks broadening in the diffraction patterns, as well as the lower thermal stability of MIL-100(Fe,Cu). For MIL-100(Fe,V), V^{5+} was detected along with V(IV) and V(III). The +V oxidation state of the doping metal is also incompatible with a perfect cluster structure (unless one of the iron atoms is present in the +II oxidation state, but this again is incompatible with the strong oxidizing power of V^{5+}). Defects around the V^{5+} centres must therefore be considered in this case too, correlated again with the hysteresis observed on the nitrogen sorption isotherm of MIL-100(Fe,V) and peak broadening in the diffraction profiles.

Table III-1. Oxidation states of doping metals in MIL-100(Fe,M) MOFs doped with different transition (Ti, V, Cr, Mn, Co, Ni, Cu, Zn and Cd) and main group (Al) metals.

Sample name	Oxidation state of doping metal detected by XPS				
	+I	+II	+III	+IV	+V
MIL-100(Fe,Al)	⊘	⊘	✓	⊘	⊘
MIL-100(Fe,Ti)	⊘	⊘	⊘	✓	⊘
MIL-100(Fe,V)	⊘	⊘	✓	✓	✓
MIL-100(Fe,Cr)	⊘	⊘	✓	⊘	⊘
MIL-100(Fe,Mn)	⊘	✓	₿	₿	⊘
MIL-100(Fe,Co)	⊘	✓	⊘	⊘	⊘
MIL-100(Fe,Ni)	⊘	✓	⊘	⊘	⊘
MIL-100(Fe,Cu)	✓	✓	⊘	⊘	⊘
MIL-100(Fe,Zn)	⊘	✓	⊘	⊘	⊘
MIL-100(Fe,Cd)	⊘	✓	⊘	⊘	⊘

✓ The oxidation state has been identified;
✓ The oxidation state has been identified in minor proportions;
⊘ The oxidation state has not been detected;
₿ The oxidation state could not be excluded nor demonstrated by XPS.

4.7. Incorporation of lanthanides and secondary phases

We investigated the possibility of introducing lanthanides (and rare earth metals in general) in MIL-100(Fe). Those metals possess much larger ionic radii and much higher coordination numbers than transition and *p*-bloc metals. Because of this, it might, at first sight, seem difficult to introduce them into the clusters composing MIL-100 MOFs. However, the large ionic radius and high coordination numbers might lead to improved performances of the resulting bimetallic MIL-100(Fe,Ln) materials. Indeed, it they are introduced successfully, only 5 coordination sites around the lanthanide centres will be occupied by unremovable ligands, namely the central μ_3-oxo and the four carboxylate linkers (Figure III-6).

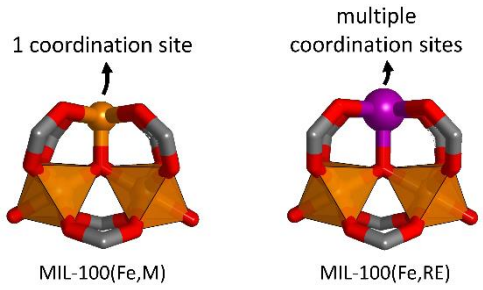

Figure III-6. Scheme of coordination around the secondary metal in MIL-100(Fe,M) (left) and MIL-100(Fe,Ln).(right). Five coordination sites are occupied by the μ_3-oxo and carboxylate ligands, the other coordination sites can, in theory, be decoordinated upon activation, leading to larger CUSs for MIL-100(Fe,Ln) around the lanthanide (or rare earth) metal as it possesses a larger ionic radius and higher coordination numbers.

Upon synthesis, the other coordination positions will be occupied by solvent molecules. On the contrary to transition and *p*-bloc metals, more than one coordination site should be available for coordination with solvent molecules (as the coordination numbers of lanthanides are usually comprised between 8 and 9, but can exceed this number). Therefore, upon activation of those materials, MIL-100(Fe,Ln) should possess much larger CUSs around the lanthanide centres. Furthermore,

exchange kinetics of ligands on lanthanides are quite fast, and the newly introduced CUSs could therefore be very useful in (Lewis acid) catalysis.

A first attempt to obtain lanthanide-containing MIL-100(Fe,Ln) MOFs was performed by using the same procedure as the one described above for introducing transition and main group metals, by engaging 20 mol% of a lanthanide metal (added as water soluble chloride), being either La, Ce, Pr, Sm or Tb. Although the obtained compounds all possess high surface areas and metal doping contents > 20 mol% (Table III-2), nearly all the samples showed a secondary phase on their PXRD patterns (Fig. S III-9).

Table III-2. Bulk and surface doping contents of lanthanides in MIL-100(Fe,Ln) and BET surface areas of the materials obtained by magnetic stirring, reacting for 16 h and engaging 20 mol% of doping lanthanide.

Sample name	Bulk doping metal content (ICP) (mol%)	Surface doping metal content (XPS) (mol%)	S_{BET} ($m^2\ g^{-1}$)
MIL-100(Fe)	-	-	2012
MIL-100(Fe,Y)	25.7	9.8	1350
MIL-100(Fe,La)	21.0	17.1	1137
MIL-100(Fe,Ce)	29.9	34.1	788
MIL-100(Fe,Pr)	24.5	13.7	942
MIL-100(Fe,Sm)	24.5	3.0	1445
MIL-100(Fe,Tb)	21.2	5.1	1419

Variable temperature synchrotron PXRD revealed that this secondary phase disappears upon heating, at a temperature that decreases with decreasing ionic radius of the lanthanides ion (Fig. S III-9). This secondary phase did not reappear after cooling down of the samples, but it did after rehydration of the sample, as was exemplified by PXRD measurements on MIL-100(Fe,Pr) (Fig. S III-9). The secondary phase was identified as being a hydrate with the formula

$LnBTC(H_2O)_6$, having a diffraction pattern identical to the simulation from the structure in the CCDC database (Refcode: KEBSOA). Only MIL-100(Fe,Tb), which contained the smallest of all lanthanides explored in this first attempt, showed a single phase in its as-synthesized form. An attempt to obtain MIL-100(Y), containing yttrium as a rare earth ion having similar properties to heavy (small) lanthanides, also resulted in the presence of a secondary (unidentified) phase on the PXRD pattern.

XPS spectra of the samples showed that, as expected, all lanthanides were incorporated in the +III oxidation states, except for Ce, which is present in both +III and +IV oxidations states (Fig. S III-12). Furthermore, the samples of MIL-100(Fe,Ln) with Ln = La, Pr and Sm showed the presence of sodium on their external surface, as revealed by the XPS survey spectra (Fig. S III-10). ICP-OES analysis further confirmed the presence of sodium in those samples (Fig. S III-10).

An attempt to obtain MIL-100(Fe,Ln) MOFs with a larger variety of lanthanides, starting from solutions containing a lower Ln content, of 10 mol%, was performed in parallel with Ln = La, Ce, Pr, Nd, Sm, Eu, Er and Yb, by stirring on an orbital shaker. However, after 16 h of reaction, all the samples also showed a secondary phase on the PXRD pattern (Figure III-7). Insufficient oxidation due to too gentle stirring could explain those results, and therefore another attempt was made by switching back to magnetic stirring. This second attempt allowed obtaining a single phase MIL-100(Fe,Ln) MOF only for Ln = Eu (Figure III-8). To ensure that the absence of a secondary phase was not due to amorphous LnBTC hydrates that undergo a crystalline to amorphous phase transition upon drying, some of the MOFs were wetted with a drop of water for a second PXRD analysis, showing no appearance of additional diffraction peaks (data not shown).

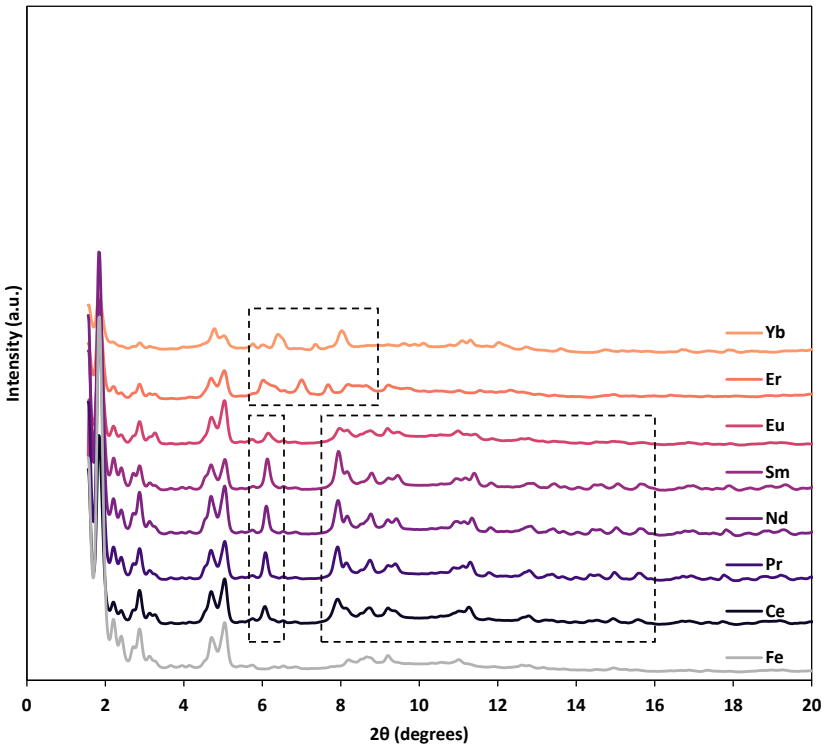

Figure III-7. PXRD patterns of MIL-100(Fe,Ln) samples obtained using 10% of Ln as doping metal, with orbital shaking, together with MIL-100(Fe) reference sample. Diffraction peaks of secondary phases are framed.

It is noticeable that with at least 10 mol% of engaged lanthanides, only Eu, Tb and Er seem to allow for obtaining single phase MIL-100(Fe,Ln) MOFs. Those lanthanides are all located in the middle of the lanthanide series. On the one hand, larger (lighter) lanthanides, such as La, Ce, Pr, Nd and Sm all show the presence of an isostructural secondary phase, $LnBTC(H_2O)_6$. This hydrated structure possesses lanthanide centres that are nine-coordinated, and are a consequence of the large ionic radius of the light lanthanides, that tend to adopt high coordination numbers, explaining the difficulty to insert them in MIL-100(Fe,Ln). On the other hand, heavier (smaller) lanthanides, which are here represented by Yb and Er as the only examples, seems to be difficult to insert in MIL-100(Fe,Yb) and MIL-100(Fe,Er) for some other unexplained reason.

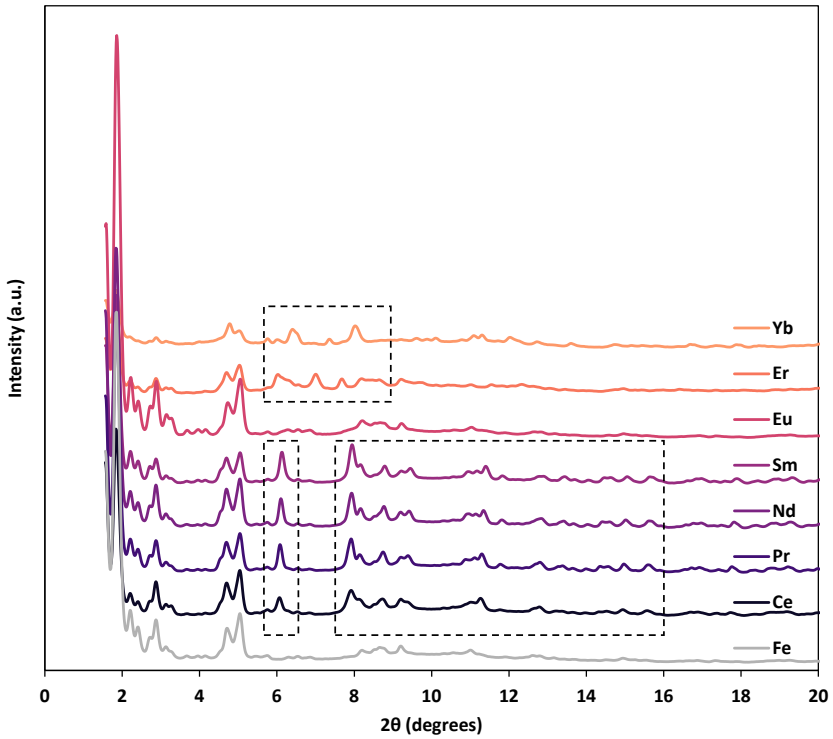

Figure III-8. PXRD patterns of MIL-100(Fe,Ln) samples obtained using 10% of Ln as doping metal, with magnetic stirring at 500 rpm, along with MIL-100(Fe) reference sample. Diffraction peaks of secondary phases are framed. Only Eu-containing sample was obtained as a single phase.

Because of its position in approximatively the middle of the lanthanide series and of its interesting properties, different samples of europium-doped MIL-100(Fe,Eu) were synthesized with different doping ratios, having up to 1/6 of the metal content being Eu, which corresponds to one Eu atom for every two clusters on average. PXRD patterns of the obtained samples present a single MIL-100 phase (Figure III-9). FTIR spectra of the obtained MOFs show some differences with the spectrum of un-doped MIL-100(Fe), mainly in the region of the C=O stretching, influenced by the nature of the metals composing the clusters (1500-1600 cm^{-1}) (Figure III-10). Those are explained by the large difference in size between iron and europium, resulting in significant changes in vibrations of the metal-O bonds.

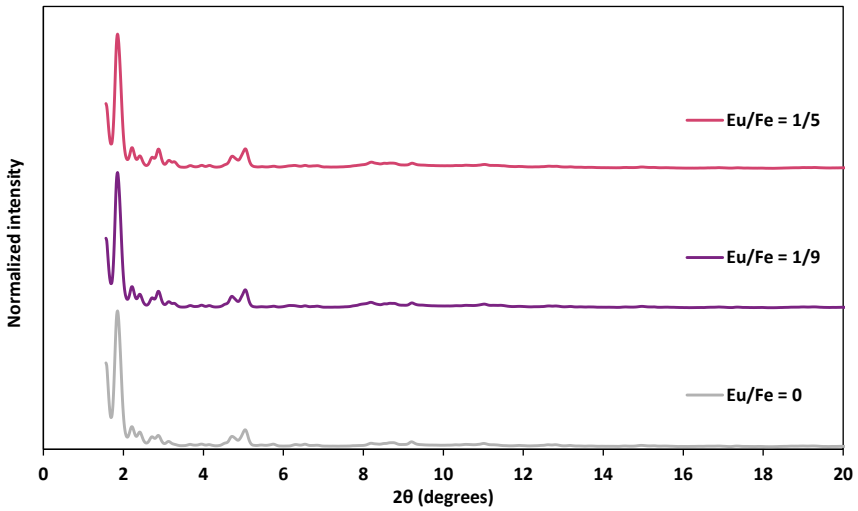

Figure III-9. PXRD patterns of phase-pure MIL-100(Fe,Eu) obtained with different Eu/Fe ratios (0; 1/9 and 1/5).

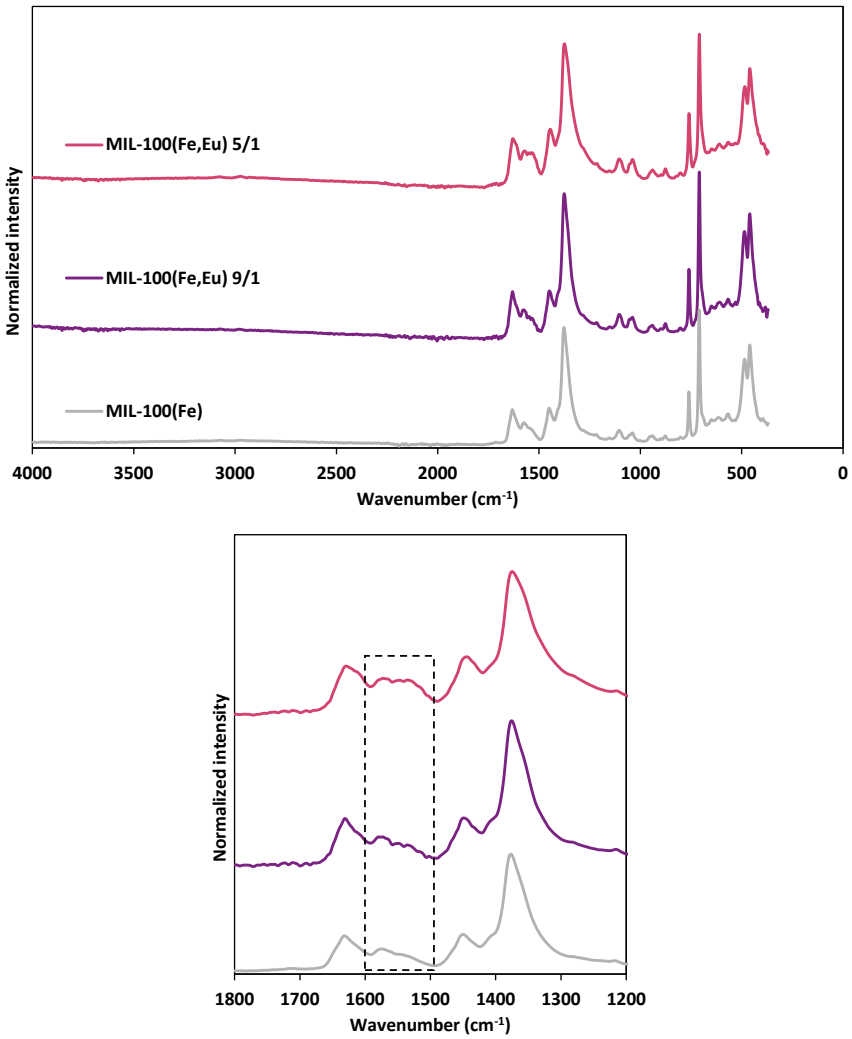

Figure III-10. FTIR spectra of phase-pure MIL-100(Fe,Eu) obtained with different Eu/Fe ratios (0; 1/9 and 1/5), with enlargement of the carboxylate region (lower figure).

ICP-OES was applied to determine the europium content in each MOF. As expected, the incorporation of the lanthanide was slightly above the engaged ratio (see Table III-3). An attempt to synthesize a sample with a higher Eu content, by engaging 33% of Eu (one Eu atom per cluster on average), resulted in the appearance of an amorphous EuBTC hydrate as secondary phase (Figure III-11). This secondary phase is present even when the reaction time is increased to 13 days

(Figure III-11), indicating that it is the quantity of Eu engaged for the synthesis that is the limiting factor and not the reaction time.

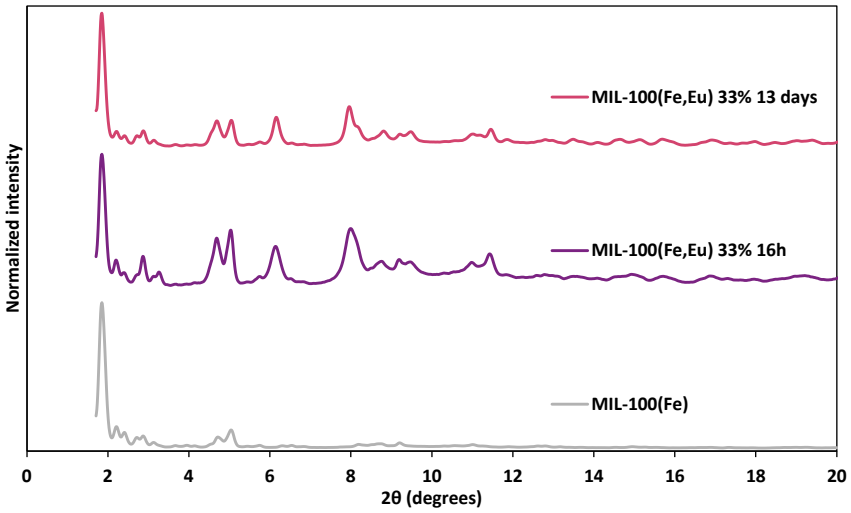

Figure III-11. PXRD patterns of impure MIL-100(Fe,Eu) sample obtained with Eu/Fe ratios of ½ after 16h and 13 days of reaction, with MIL-100(Fe) reference sample.

Table III-3. ICP-OES determined Eu/M_{tot} ratios and BET surface areas of single phase MIL-100(Fe,Eu) samples, along with the ones of un-doped MIL-100(Fe).

Sample name	Eu/M_{tot} (ICP-OES) (%)	S_{BET} ($m^2\ g^{-1}$)	S_{BET} ($m^2\ mmol^{-1}$)
MIL-100(Fe)	-	2173	1301
MIL-100(Fe,Eu) 10%	10.7	N/A	N/A
MIL-100(Fe,Eu) 17%	18.8	1222	978

4.8. Using PXRD for doping metal quantification

Finally, a methodological development made in the course of this work deserves a discussion. The most usual methods for dosing the metals in MOFs, and more specifically bimetallic MOFs, include ICP and Atomic Absorption Spectroscopy (AAS). However, these methods

need digestion of the sample and a dilution prior to analysis. Also, a standard curve must be established for both methods. Moreover, a different hollow cathode lamp must be used for quantifying each different metal by AAS. For this reason, it would be convenient to have a valid method for simultaneously determining the metal content and the M_{dopant}/M_{tot} ratio without need for sample digestion and dilution. PXRD would be a convenient way to determine this by Rietveld refinement as most laboratories working on MOFs have access to this method. However, the complex structure of MIL-100(Fe,M) compounds and the difficulty to attain complete removal of solvents and guests from the pores does not allow to accomplish metal content determination using this method directly on the MIL-100 compounds. However, we tested a strategy that consists in calcination of the samples in air followed by measuring the PXRD pattern of the resulting oxides (Fig. S III-13) and subsequent Rietveld refinement, allowing determining M_{dopant}/M_{tot}. Here we show that this determination is quite accurate in the specific cases where two oxides having different crystal structures are obtained. For example, calcination of MIL-100(Fe,Co) leads to a mixture of Fe_2O_3 and $CoFe_2O_4$. Once Rietveld refinement is performed and the weight fraction of Fe_2O_3 and $CoFe_2O_4$ are determined, the metal ratio can easily be calculated (see Annexes). This method does not apply in case of solid solutions from or isostructural oxides with similar cell dimensions are obtained. For example, MIL-100(Fe,Cr) is oxidized into $(Fe,Cr)_2O_3$, Rietveld refinement is thus of no use for metal quantification. When the main and the doping metals have a large difference in number of electrons (*i.e.* Al and Fe) or when absorption coefficients are too high, the method also gives uncertain results (although absorption correction in Rietveld refinement can be applied to some extent). The main advantage of this method is that the analysis can be coupled to TGA measurements, by measuring a PXRD pattern of the combustion residue. Characterization by TGA and by ICP (or AAS) measurements *via* conventional methods would require the destruction of a larger amount of sample than the method we propose. The precision of our method was tested against ICP and

AAS for MIL-100(Fe,Co) and against ICP for MIL-100(Fe,M) (M = Cr, Co, Ni, Cu and Zn), showing its validity (see Fig. S III-13).

5. Conclusions

In this Chapter, we developed a green and easy method for synthesizing bimetallic MIL-100(Fe,M) compounds at room temperature in water, avoiding energy demanding solvothermal processes and avoiding the use of strong mineral acids, all these conditions are good prerequisites for an easy scale up. This synthesis is performed in a single step, and therefore is less time-consuming and more efficient than post-synthetic exchange approaches. We showed that the incorporation of doping metals is only possible at pH values below 7 and that $Na_3BTC{\cdot}3H_2O$ is a useful linker source. Importantly, we demonstrated that the amount of the incorporated doping metal can be tuned in a controlled manner. Metals in the +I as well as +V oxidation states were incorporated as dopants into the structure of MIL-100(Fe) for the first time. We showed that large differences between the ionic radius of the doping and the templating metals does not lead to phase segregation. We also showed that the incorporation of Cu(I) drastically lowers the thermal stability of MIL-100(Fe,Cu) and that the incorporation of V, Al and Ti induces the formation of mesopores. Finally, we developed a PXRD-based method that can be combined with TGA to easily access the metal ratios in complex mixed-metal MOFs with less sample required than for the currently used ICP and AAS based methods.

The obtained MIL-100(Fe,M) compounds could serve in fields like gas sorption and catalysis. On the one hand, the presence of metals in the +II oxidation state can strongly influence the sorption of some gases through the increased amount of open-metal sites in the materials, or could serve in redox catalysis. On the other hand, the presence of high oxidation state metals could serve as efficient Lewis acid sites for catalysis.

CHAPTER IV

Functionalization of mono- and bimetallic MIL-100(Al,Fe) MOFs by ethylenediamine: post-functionalization, Brønsted acido-basicity and unusual CO_2 sorption behavior

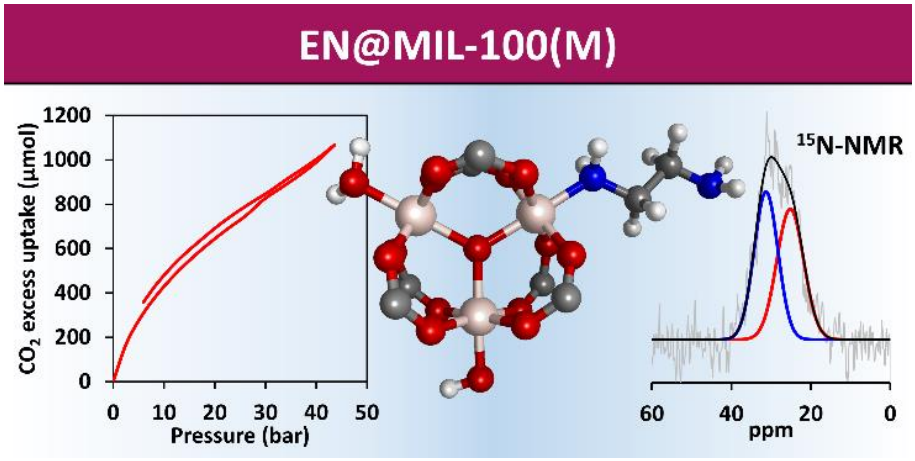

This Chapter is inspired by the following publication:

Steenhaut, T.; Fusaro, L.; Robeyns, K.; Lacour S.; Li, X.; Mahy, J. G.; Louppe V.; Grégoire, N.; Barozzino-Consiglio, G.; Statsyns J.-F.; Aprile C.; Filinchuk Y.; Hermans, S. *Functionalization of mono- and bimetallic MIL-100(Al,Fe) MOFs by ethylenediamine: postfunctionalization, Brønsted acido-basicity, and unusual CO_2 sorption behaviour*, Inorg. Chem., **2021**, *60*, 21, 16666-16677, doi: 10.1021/acs.inorgchem.1c02568

Chapter IV - Functionalization of mono- and bimetallic MIL-100(Al,Fe) MOFs by ethylenediamine: post-functionalization, Brønsted acido-basicity and unusual CO_2 sorption behavior

1. Abstract

The metal sites of MIL-100(Fe), MIL-100(Fe,Al), and MIL-100(Al) metal−organic frameworks (MOFs) were decorated with ethylenediamine (EN). Interestingly, the Al-containing MOFs presented hierarchized porosity, and their structural integrity was maintained upon functionalization. Solution and solid-state NMR confirmed the grafting efficiency in the case of MIL-100(Al) and the presence of a free amine group. It was shown that MIL-100(Al) can be functionalized by only one EN molecule in each trimeric Al_3O cluster unit, whereas the other two aluminum sites are occupied by a hydroxyl and a water molecule. The $-NH_2$ sites of the grafted ethylenediamine can be used for further postfunctionalization through amine chemistry and are responsible for the basicity of the functionalized material as well as increased affinity for CO_2. Furthermore, the presence of coordinated water molecules on the Al-MOF is responsible for simultaneous Brønsted acidity. Finally, the Al-containing MOFs show an unusual carbon dioxide sorption mechanism at high pressures that distinguishes those materials from their iron and chromium counterparts and is suspected to be due to the presence of polarized Al−OH bonds.

2. Introduction

To improve sorption of CO_2 and other guest molecules in MOFs (or in other porous materials such as mesoporous silica),[261] functionalization of those materials with basic functions,[262] and more specifically amines,[263] is very efficient. Such functions are also very valuable tools for post-functionalization purposes relying on the rich

chemistry of amines,[264] as well as for base-promoted catalysis.[265] The incorporation of amines is usually carried out by using modified linkers to build the MOF. However, amine-bearing linkers are often more expensive. One alternative is to functionalize metal sites in MOFs with cheap ethylenediamine (EN)[266,267,268,269,270] or other polyamines,[271] which use one -NH_2 site as anchor to the MOF's structure, leaving a second pendant amine site available. In addition to anchor functionalities to the MOF, the functionalization of the CUSs with amines can also increase the stability towards water.[272,273] The chromium-based MIL-100(Cr) is a MOF that has shown great promise in this perspective.[255,274,275] However, this chromium-based MOF is not likely to be used in large-scale industrial applications due to environmental and health concerns.[276] This is because of strong regulations concerning chromium, which is highly hazardous in its +VI oxidation state.[277] Nevertheless, the MIL-100 structure remains very interesting for functionalization purposes because its large pores (25 and 29 Å diameter) allow for introducing functional units while still maintaining high surface areas.[147,278] For this reason, we investigated the possibility to functionalize MIL-100(Al) and MIL-100(Fe), which are based on widely available (and thus cheap) and less problematic metals, as well as their bimetallic counterpart MIL-100(Fe,Al). Furthermore, because it is based on the lightest metal that can commonly attain the +III oxidation state, MIL-100(Al) is more promising for gravimetric gas sorption applications owing to its lower density.

3. Experimental

A. Instruments

Powder diffraction data were collected on a STOE STADI P Combi diffractometer using either MoKα radiation (50 kV, 40 mA) or CuK_α radiation (40 kV, 40 mA) (graphite primary monochromator). The diffracted beam was recorded on a DECTRIS MYTHEN 1K strip detector. Samples were loaded in 0.7 mm diameter capillaries, aligned

to the geometric center of the diffractometer and measured in transmission, with independent 2-theta movement.

Infrared spectra were recorded in the 4000-370 cm^{-1} range on a Bruker Alpha spectrometer equipped with a Platinum ATR module (diamond crystal) housed in an argon-filled glovebox.

TGA measurements of the MOFs were performed on a Mettler Toledo TGA/DSC^{3+} system equipped with a sample robot. The air flow was of 100 ml/min. An initial isotherm at 27°C was applied during 15 minutes before heating the sample up to 900°C at a rate of 10 K/min. TGA-MS was done by coupling a ThermoStarTM GSD 301 T mass spectrometer to the outlet of the TGA oven.

Nitrogen sorption isotherms were measured at 77 K using a Micromeritics ASAP2020 equipment. All samples were activated at 200°C or 150°C (depending on the sample) under dynamic vacuum for 10 h prior to analysis.

TEM images were obtained on an LEO 922 Omega Energy Filter Transmission Electron Microscope operating at 120 kV. The samples were suspended in ethanol and a drop of the suspension was deposited on a holey carbon film supported on a copper grid (Holey Carbon Film 300 Mesh Cu, Electron Microscopy Sciences), which was dried overnight at room temperature, before introduction in the microscope.

Solution-state ^{1}H NMR spectra were recorded at room temperature (296 K) on a Bruker Avance II 300 spectrometer operating at 300.1 MHz. Experiments were run under TopSpin program (3.2 version, Bruker) using a BBFO {^{1}H, X} probehead equipped with a z-gradient coil. ^{1}H chemical shifts are reported in parts per million (ppm) and referenced to the residual signal of DMSO-d_5 (δ 2.50 ppm). Samples were prepared by putting an appropriate amount of solid in a glass test tube equipped with a ground glass joint. For activation, a glass stopcock, connected to a vacuum supply (via a Schlenk line), was adapted on the test tube and heating was applied using an oil bath. About 0.5 ml D_2SO_4 was then added to the sample by using a glass

pipette, followed by an appropriate amount (enough to obtain a clear solution after heating) of DMSO-d_6. The test tube was then sealed with a glass stopper and the mixture was heated using a heat gun until a clear solution was obtained (in case of difficult solubilization, some DMSO-d_6 was added and the mixture was heated again to obtain a clear solution). The solution was then cooled and transferred into a 5 mm thin-walled precision NMR sample tube for analysis. Note: The added volume of DMSO-d_6 is variable depending on the sample to dissolve. The total quantity needed to achieve complete dissolution is dependent on the nature of the sample (portions of ~0.5 ml were added until a clear solution was obtained). This results in variable D_2SO_4/DMSO ratios for each analyzed sample and in slight shifts of peak positions in the ^{1}H NMR spectra but does not affect the quantification of the EN/H_3BTC ratio.

Solid-state ^{13}C and ^{15}N Cross-Polarization (CP) Magic Angle Spinning (MAS) NMR spectra were acquired at room temperature, on a Bruker Avance-500 NMR spectrometer operating at 11.7 T (125.8 MHz for 13C and 50.6 MHz for ^{15}N) and equipped with a 4 mm CP-MAS Bruker probe. ^{13}C CP-MAS spectra were recorded using a contact time of 2 ms, a spinning rate of 10 KHz, relaxation delay of 5 s and 1000 scans. ^{15}N CP-MAS spectrum was recorded using a contact time of 2 ms, a spinning rate of 8 KHz, relaxation delay of 10 s and 92000 scans. The processing comprised exponential multiplication of the free induction decay with a line broadening factor of 10 Hz, zero filling prior to Fourier transform, phase, and baseline corrections. Chemical shifts scales were referenced externally to solid adamantane (^{13}C: 38.68 ppm) and ammonium chloride (^{15}N: 39.3 ppm).[279,280] Solid-state ^{27}Al MAS NMR spectra were acquired at room temperature, on a 400 MHz Varian VNMRS spectrometer operating at 9.4 T (104.2 MHz for ^{27}Al) and equipped with a 4 mm Chemagnetics T3 probe. MAS spectra were recorded using a spinning rate of 8 kHz. Processing comprised manual baseline correction. Chemical shifts were referenced externally to aluminum nitrate in H_2O (^{27}Al: 0.0 ppm). Note: The MIL-100(Al) sample that was used for solid-state NMR investigations was first

activated and then rehydrated by prolonged exposure to air for several days.

Solid-state UV-vis measurements of bromothymol blue impregnated samples were performed on a Shimadzu UV-3600 Plus UV-Vis-NIR spectrometer equipped with a Harrick single-beam Praying Mantis Diffuse Reflectance collection system. A Spectralon® Diffuse Reflectance Standard was used to measure the background spectra.

Solution-state UV-vis measurements of the ninhydrin tests were collected on a 1700 UV/visible spectrophotometer from Shimadzu.

Volumetric carbon dioxide sorption experiments were performed on an IMI-HTP Sievert's apparatus from Hiden Isochema. For the experiments, about 100 mg of sample was used and activated under vacuum at 100°C or 200°C before sorption experiments. The excess uptake values were converted to mmol/g of dry sample based on the sample's weight after activation.

Gravimetric cyclic sorption experiments were performed on a Mettler Toledo TGA/DSC^{3+} system. For each experiment, the sample was activated in situ in the thermogravimetric analyzer by heating (10 K/min) to 100°C (2h isotherm) and cooling back to 25°C (10 K/min) and maintaining this temperature for 90 min, all those operations being performed under helium (100 ml/min). The adsorption/desorption cycles were realized by switching gas fluxes every 60 min from helium (100 ml/min) to carbon dioxide (100 ml/min) and vice-versa at a constant temperature of 25°C.

Elemental analyses (ICP and CHN) were performed by Medac Ltd. (UK).

Gravimetric CO_2 low pressure sorption isotherms were performed using a Netzsch STA 449 F3 TGA instrument equipped with a stainless steel oven hosted in an argon-filled glovebox. The sample was subjected to a constant gas flux of 100 mL.min^{-1} of an Ar/CO_2 mixture with an increasing proportion of CO_2 every 30 minutes (0%, 5%, 10%,

15%, 20%, 25%, 30%, 40%, 50%, 60%, 70% and 80%) under a constant temperature of 27°C. The adsorption was followed by 90 minutes desorption under a flux of 100 mL of argon. The mass increase at equilibrium after 30 min of exposure to each gas mixture of a given composition was plotted against the partial pressure of CO_2 to obtain the corresponding adsorption isotherm. The samples were degassed at 100°C under vacuum *ex-situ* before the experiments and transferred to the glovebox without contacting air.

B. Chemicals

Trimesic acid (98%), heptane (99%), thiophosgene (85%), iodomethane (99%, stabilized), dry ether (99.5%, extra dry), triethylamine (99%) and toluene (99.85%, Extra Dry, AcroSeal®) were purchased from Acros Organics. Denatured ethanol (Technisolv, 99%), dimethylformamide (HiPerSolv, CHROMANORM), methanol (HiPerSolv, CHROMANORM), DCM (HiPerSolv, CHROMANORM), pentane (HiPerSolv, CHROMANORM), hexane (HiPerSolv, CHROMANORM), sodium hydroxide pellets, HCl 37% (AnalaR, NORMAPUR) and ninhydrin (AnalaR, NORMAPUR® ACS, Reag. Ph. Eur., for analysis) were purchased from VWR Chemicals. D_2SO_4 and DMSO-d_6 were purchased from Euriso-top. Ethylenediamine (>99.5%), boron trifluoride diethyletherate, aluminum chloride (98%) and hexylamine (99%) were purchased from Merck. Bromothymol blue was purchased from Alfa Aesar. All chemicals were used as received.

C. Synthetic procedures

Gram scale synthesis of MIL-100(Al) !! Caution !! This synthesis employs large amounts of chemicals, therefore precautions must be taken. This is especially the case for the dissolution of aluminum chloride in water, which is extremely exothermic and may release hydrogen chloride. Therefore, this dissolution must be performed under an efficient fumehood using good quality borosilicate, thick-walled, glassware. Water must be poured as quickly as possible on $AlCl_3$ to avoid overheating. This step causes impressive and excessive fuming.

Preparation of solution A: 31.5 g of trimesic acid were dissolved in 3 L of denatured ethanol in a 4 L Erlenmeyer flask. The flask was shaken until all the acid was completely dissolved. Stepwise addition of the acid and sonication are recommended for avoiding the formation of aggregates and speeding up the process. Once a clear solution was obtained, 3.15 ml of concentrated hydrochloric acid were added and the mixture was homogenized by shaking. *Preparation of solution B:* 17.25 g of $AlCl_3$ were added in a dry 4 L Erlenmeyer flask. 3 L of demineralized water was added through a large glass funnel, the first 1000 ml were added as fast as possible (!! Exothermic reaction !!). The mixture was homogenized, followed by the addition of 35.0 ml of DMF. The flask was shaken to obtain a homogeneous mixture. *Preparation of the MOF:* Solutions A and B were mixed together in a 10 L polyethylene can. The can was closed with a screw cap and thoroughly shaken to obtain a homogeneous mixture. The mixture was then poured in glass bottles (10 bottles of 500 ml capacity each containing 400 ml of the reaction mixture, and 1 bottle of 2.5 L capacity containing 2000 ml of the mixture). All the bottles were placed into an oven at 83°C for 6 days. The white precipitate was centrifuged at 6000 rpm and washed with water (3 times) and ethanol (3 times). The powder was then suspended in a minimum amount of ethanol and the suspension was evaporated under reduced pressure at 70°C using a rotary evaporator.

Small-scale syntheses of Al-BTC MOFs: Solutions A and B were prepared as described above (in smaller volumes). 200 ml of each solution were then mixed together in 500 ml screw-capped glass bottles. The bottles were sealed and placed in an oven at 80°C for a given amount of time (4, 5, 6, 8, 11 or 15 days). The white precipitate was centrifuged at 4000 rpm and washed with water (3 times) and ethanol (3 times). The powder was then suspended in a minimum amount of ethanol and the liquid was evaporated under reduced pressure at 70°C using a rotary evaporator. !!! Note that the rotation speed during the centrifugation is lower than for the large-scale synthesis (the speed for the large-scale synthesis was increased in order to recover more material). This has two consequences on the obtained product: 1. More

material is recovered when using higher speed (the supernatants are not clear solutions, but have an aspect similar to milk); 2. The size distribution of the particles changes when higher speeds are used; this can be seen by broadening of the PXRD peaks and on the BJH pore size distribution of the materials. The presence of very small (nano)-particles is in agreement with the aspect of the supernatants.

Synthesis of bimetallic MIL-100(Fe,Al) MOF: The synthesis was adapted from a procedure described previously by us,[281] by using a 8/2 starting molar ratio of Fe/Al and setting the reaction time to 10h instead of 16h, allowing the incorporation of a higher amount of Al compared to Fe (leading to a Fe/Al ratio of 2/1 in the final material).

Functionalization with ethylenediamine: The following procedure was adapted from an earlier report describing the synthesis of EN@MIL-100(Cr).[274] 1.2 g of as-synthesized MIL-100 were introduced into a 250 ml three-neck flask equipped with a condenser, a rubber septum and a glass stopcock. The MOF was heated at 200°C under vacuum (using the glass stopcock connected to a Schlenk line) overnight for activation. The flask was subsequently allowed to cool down under vacuum and the stopcock was closed. Then, 120 ml of anhydrous toluene were added by using a syringe. Once the toluene was added, the flask was backfilled with argon. Note: adding the toluene when the flask is under vacuum allows to wet the MOF powder so that it does not fly up in the flask when the volume is backfilled with argon. The suspension was stirred to disperse the MOF and 0.10 ml of ethylenediamine were added by syringe. The stopcock was closed again and an argon filled balloon was added at the top of the condenser. The mixture was then refluxed for 12h. After cooling down the flask, the mixture was centrifuged and the toluene supernatant discarded. The solid was then washed 3 times with *n*-hexane and 2 times with *n*-pentane. The obtained solid was then dried, while still being in the (open) centrifugation tubes, in an oven under air at 45°C during 3 hours to afford a powder of the functionalized MOF (white powder for

EN@MIL-100(Al); brown powders for EN@MIL-100(Fe) and EN@MIL-100(Fe,Al)).

Synthesis of the 8-thiomethyl-BODIPY fluorescent dye: The BODIPY dye was synthesized according to a reported three-step procedure,[282] with small modifications. In brief, a solution of freshly distilled pyrrole (4.2 ml in 90 ml of dry ether) was added dropwise to a thiophosgene solution (2.3 ml in 80 ml of dry toluene) in an ice bath (0°C) under argon by using a syringe. After complete addition, the solution was stirred for 30 minutes. The reaction was then quenched by addition of 100 ml of a 10 mol% NaOH solution in water/methanol (10:90 v/v), followed by one hour of stirring at room temperature. The solvent was then removed in vacuo and the resulting crude product was purified on a short silica pad by using a heptane/DCM (1:3 v/v) mixture containing 1% triethylamine. Only the bright orange fraction was collected and the solvents evaporated in vacuo, yielding red crystals of high purity of Bis-(1H-pyrrol-2-yl)-methione. ^{1}H-NMR (CDCl3, 300 MHz, 293K): δ 7.80 (2H, m), 7.42 (2H, m), 6.53-6.54 (2H, m), 2.91 (3H,s)). 0.45g of the obtained product was subsequently dissolved in 7.4 ml of DCM under argon atmosphere, followed by the addition of 2.9 ml of methyl iodide. The mixture was stirred for 26h at room temperature and the solvent was evaporated in vacuo. The obtained crude 2-[Methylsulfanyl-(1H-pyrrol-2-yl)-methylene]-2H-pyrrolium iodide was used for the last step of the synthesis without further purification or analysis. 0.88 g of the obtained product was dissolved in 19 ml of DCM under argon atmosphere, followed by the addition of 2 ml of triethylamine and subsequent stirring at room temperature for 40 min. Then, 1.63 ml of $BF_3{\cdot}Et_2O$ was added and the mixture stirred further for 24h. Solvents were removed in vacuo and the obtained crude product was dissolved in some DCM. The product was purified by chromatography on silica by subsequently using heptane/DCM/triethylamine mixtures with various solvents ratios (100:10:1.1 → 100:100:2 → 50:100:1.5). A second purification, consisting in washing in water and extraction in toluene allowed to

obtain high purity 8-(Thiomethyl)4,4-difluoro-4-bora-3a,4a-diaza-sindacene (BODIPY).

Post-functionalization with BODIPY dye: 50 mg of as-synthesized (non-activated) MOF sample were soaked in 15 ml of a solution of the BODIPY probe in dichloromethane (1 mg in 100 ml) and stirred for 10 minutes before being filtered and washed with dichloromethane on a PTFE filtration membrane (pore size 0.45 µm). The BODIPY functionalized samples were finally air dried.

D. Ninhydrin and bromothymol blue tests

Ninhydrin test: First, a solution of $5 \cdot 10^{-3}$ M of ninhydrin in ethanol was prepared. Then, a calibration plot was determined with hexylamine as a standard primary amine. A specific amount of hexylamine solution (between $5 \cdot 10^{-5}$ and $8.3 \cdot 10^{-4}$ M) was mixed with ninhydrin for 2h at 65°C, then cooled for 15 min at room temperature. The primary amine peak appears at 580 nm (blue coloration). Suspensions of 0.5 g/L of activated MOFs (recovered after BET analysis) were prepared in ethanol and dispersed for 5 min under ultrasonic treatment. Then, 2 mL of these suspensions were mixed with 1 mL of the ninhydrin solution for 2 h under 65°C and cooled at room temperature for 15 min. The samples were centrifuged at 15,000 RPM for 30 min. Then, the UV-vis spectra of the supernatants were measured with the spectrophotometer and the concentration of primary amine was estimated thanks to absorbance measured at 580 nm and the calibration plot.

Acidity determination by adsorption of bromothymol blue: A transparent solution of bromothymol blue in toluene was prepared (50 mg in 100 ml) and about 10 ml of this solution was added to 50-100 mg of the solid to be analyzed (non-activated MOF or reference sample) in a test tube. The solution was stirred with a glass rod until the sample was colored (about 1 min). Then the solid was decanted, toluene was removed by using a pipette and the sample was washed twice with *n*-hexane and once with *n*-pentane, followed by drying in a vacuum oven at 60°C for about 30 min. The diffuse reflectance spectra of the obtained samples were then measured.

4. Results and Discussion

4.1. Collapse of MIL-100(Fe) upon contact with ethylenediamine

Our first attempt concerned the functionalization with ethylenediamine of MIL-100(Fe), which was obtained using a previously described method[281]. To do so, the synthesized MOF was first activated by heating under vacuum at 200°C to remove physisorbed and coordinated solvent molecules, and was then refluxed under argon in toluene in the presence of EN. However, the powder X-ray diffraction (PXRD) pattern of MIL-100(Fe) after this treatment revealed that the compound had completely lost its crystallinity, becoming amorphous (see ESI, Fig. S IV-1). Significant changes were also observed in the FTIR spectrum of MIL-100(Fe) after the reaction with EN (see ESI, Fig. S IV-2). This shows that MIL-100(Fe) cannot be functionalized with ethylenediamine without collapsing using toluene as solvent, unlike the more robust MIL-100(Cr), which possesses an well-known framework stability thanks to the kinetic inertness of Cr^{3+} complexes.[255,274] Coordinating solvents that can compete with ethylenediamine, like ethanol, have however been reported to allow the functionalization of this MOF with EN[283] or other amines[284] with at least partial retention of the crystal structure. The lower stability of MIL-100(Fe) compared to its Cr-analogue can be explained by the fact that it, and Fe-complexes in general, possesses kinetic lability of the linkers bound to Fe, and because Fe^{3+} can be reduced to Fe^{2+} which forms weaker bonds with carboxylate linkers.

4.2. Optimized synthesis of MIL-100(Al)

Regarding MIL-100(Al), most reports on the synthesis of this particular MOF use hydro- or solvothermal processes involving high reaction temperatures requiring autoclaves.[166,167,165] We thus attempted an approach using a lower temperature, set at 80°C. We obtained the Al-based MOF by mixing an ethanol solution containing trimesic acid and some HCl with an aqueous solution of $AlCl_3$ containing some DMF

(see Experimental section for details). The obtained mixture was incubated in closed screw-capped glass bottles in an oven at 80°C and the resulting white precipitates were washed with water and ethanol and collected by centrifugation followed by drying under vacuum.

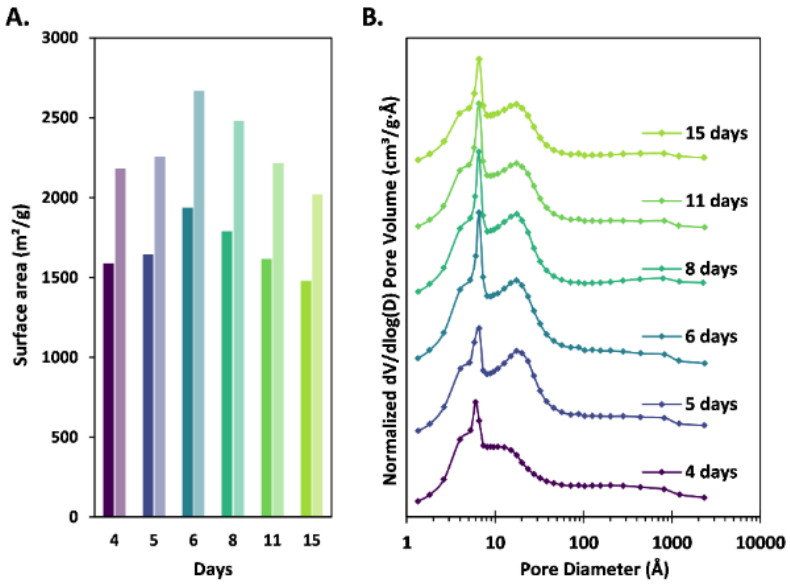

Figure IV-1. **A.** Evolution of the Brunauer-Emmett-Teller (dark colors) and Langmuir (light colors) surface areas of Al-BTC MOF samples obtained after different reaction times. Both BET and Langmuir values are given, as those are the most commonly reported textural data in the literature for MOFs. **B.** Evolution of the Barrett-Joyner-Halenda pore size distribution of Al-BTC MOF samples obtained after different reaction times.

Nitrogen sorption experiments were performed on MOF samples obtained after different incubation times to evaluate their specific surface area by the Brunauer-Emmett-Teller (BET) and Langmuir methods (Figure IV-1, **A**) as well as their Barrett-Joyner-Halenda (BJH) pore size distribution (Figure IV-1, **B**). From the obtained results, it is clear that a maximum in surface area is obtained after 6 days of reaction (S_{BET} = 1937 m²/g); longer reaction times leading to a continuous decrease of surface areas. Overall, all the MOF samples obtained have quite large surface areas compared with the ones of other reported

syntheses (see Table S IV-3): between 1479 and 1937 m²/g (BET), or 2019 and 2667 m²/g (Langmuir) (Figure IV-1, **A**).

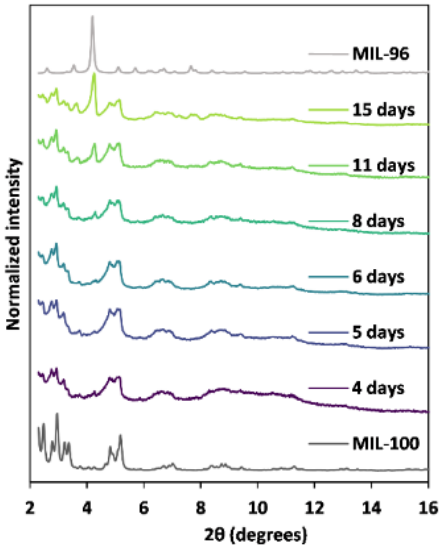

Figure IV-2. PXRD patterns of Al-BTC MOF samples obtained after different reaction times, along with simulated patterns of MIL-100 and MIL-96 for comparison (wavelength: 1.5406 Å).

To determine why the evolution of the surface area went through a maximum, powder X-ray diffraction (PXRD) patterns of all samples were measured after activation by heating under vacuum at 200°C for 10 hours (Figure IV-2). The MOFs obtained after 4, 5 and 6 days of reaction time show the presence of a pure MIL-100 phase whereas the samples isolated after longer reaction times also contain MIL-96 as a secondary phase. Therefore, the samples obtained during this optimization step were named "Al-BTC" as they are not all phase pure. MIL-96 is another Al-BTC MOF having lower surface area than MIL-100,[285,286] thus explaining why it decreases after 6 days of reaction. The formation of MIL-96 upon longer reaction times can be explained by its better thermodynamic stability.[167] The presence of unreacted trimesic acid in the pores of the compounds, which is commonly encountered when other preparation methods are used, can

be excluded according to the FTIR spectra of the different samples (Figure IV-3 and Fig. S IV-3), as the characteristic bands of C=O (1720 cm^{-1}) and C–O (1349 and 1273 cm^{-1}) stretching of free H_3BTC are not present.[221] The increase of surface area between 4 to 6 days of reaction is presumably due to the slow formation and crystallization of MIL-100, leading to the highest quality MIL-100(Al) sample after 6 days.

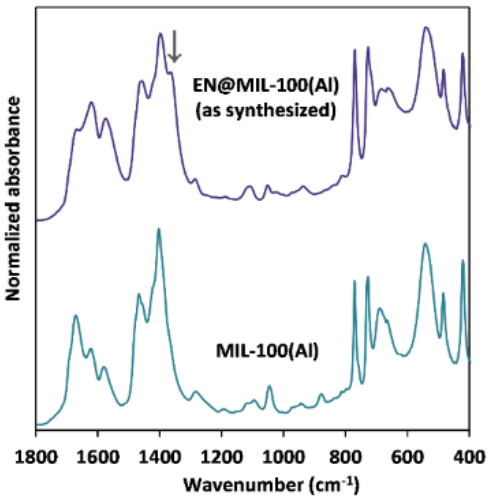

Figure IV-3. FTIR spectra of as-synthesized MIL-100(Al) and EN@MIL-100(Al) MOFs, the arrow indicates the peak corresponding to the C–N stretch of ethylenediamine.

To our delight, the BJH pore size distribution plots show the presence of not only micropores in the materials, but also small mesopores with a diameter of around 20 Å (Figure IV-1, **B**). The presence of such mesopores would not be expected based on the crystal structures of MIL-100 or MIL-96, which are both microporous and should give rise to a type I isotherm. Furthermore, the nitrogen sorption isotherms displayed a hysteresis (see ESI, Fig. S IV-4 and Fig. S IV-5), which is not what would be expected for microporous compounds. The mesoporous nature of those cavities is furthermore indicated by the shape of the hysteresis, intermediate of the H2(b) and H5 types according to IUPAC classification, which are both typical of the presence of mesopores in the material.[154] This led to the conclusion that

the obtained materials possess hierarchized porosity. This is a useful textural feature because large pores are of interest to keep large surface areas upon functionalization of MOFs, and hierarchized solids allow faster diffusion of guest molecules through the porous framework.[287] The analysis of the BJH plots shows that there is also an optimum of the pore size distribution after 6 days of reaction. Moreover, the presence of a second hysteresis in the adsorption isotherms at partial pressures close to unity with a characteristic shape of a H3 type according to IUPAC is typical of non-rigid aggregates of plate-like particles. Transmission electron microscopy (TEM) imaging shows that the obtained solid is indeed composed of such aggregates (Fig. S IV-10).

Given the interesting textural properties of the obtained MIL-100(Al) MOF, we decided to investigate the possibility to scale-up the synthesis as the yield was quite low. For this purpose, several liters of precursor solution were prepared (see Experimental section for the detailed procedure) and the MOF was successfully obtained at gram scale by applying the optimized reaction conditions. The scaled-up sample was characterized and showed good phase purity (see ESI) and was thus used for further experiments, and named MIL-100(Al), in contrast with the samples resulting from the small-scale synthesis optimization. However, it should be noted that higher centrifugation speeds were used for recovering this sample, which led to collection of smaller particles, as supported by TEM imaging (Fig. S IV-10). Therefore, a large amount of interparticle voids has also been formed in this sample. This is supported by a much more significant H3 type hysteresis at partial pressures close to unity on the nitrogen sorption isotherms (Fig. S IV-6), and the presence of porosity in the range of macropores on the BJH plots (Fig. S IV-7). However, the surface area of the obtained MOF samples was comparable to the sample from the small scale synthesis (Fig. S IV-8) and the ratio between *t*-plot calculated surface areas of micropores and external surface area remained constant (Fig. S IV-9), mainly because interparticle voids develop small surface areas.

4.3. Successful functionalization of Al-containing MIL-100 with EN

To perform functionalization with EN, the sample was activated in vacuum at 200°C and then reacted with ethylenediamine in refluxing anhydrous toluene. The sample was then isolated by centrifugation, washed with hexane and pentane and dried in air at 45°C to yield EN@MIL-100(Al). The obtained powder was characterized by PXRD (ESI, Fig. S IV-1), showing that the structure did not undergo collapse during the functionalization procedure, by opposition to MIL-100(Fe). Aluminum-based MIL-100, unlike its Fe analogue, is thus resistant enough to retain its structure upon reaction with EN. This shows that the choice of the metal composing the MOF, rather than the MOF's structure, is of critical importance for achieving efficient grafting of EN. Interestingly, a bimetallic MIL-100(Fe,Al) MOF (which preparation and detailed characterization of the bimetallic nature is described elsewhere),[281] characterized by a Fe/Al ratio of about 2/1 (determined by inductively coupled-plasma optical-emission spectroscopy (ICP-OES), see Table S IV-4), resists the same treatment with ethylenediamine, showing that Al stabilizes the structure, even when present in rather low concentrations in the MOF (see ESI for more details, Fig. S IV-1 and Fig. S IV-2). This observation is likely related to the higher strength of the Al–O bonds compared to Fe–O. Thermogravimetric analysis (TGA) (ESI, Fig. S IV-11) of EN@MIL-100(Al) showed a decomposition temperature very close to the one of pristine MIL-100(Al) (~430°C). A rather continuous weight loss, attributed to guest species (*i.e.* EN and solvent molecules), is taking place before decomposition.

The nitrogen sorption isotherms of EN@MIL-100(Al) after activation at 150°C (ESI, Fig. S IV-12, B.) revealed a BET surface area decrease from 1861 m^2/g for pristine MIL-100(Al) to 657 m^2/g upon functionalization (-64.7%), owing to the EN molecules partly occupying the volume of the pores. For the bimetallic MOF, a surface area decrease was also observed (ESI, Fig. S IV-12, C.) from 1029 m^2/g,

to 839 m²/g after functionalization (-18.5%). For MIL-100(Fe), the nitrogen sorption isotherms (ESI, Fig. S IV-12, A.), confirmed that the large surface-area MOF (2048 m²/g) completely collapsed, leading to a non-porous (3.98 m²/g) compound after contact with EN in toluene.

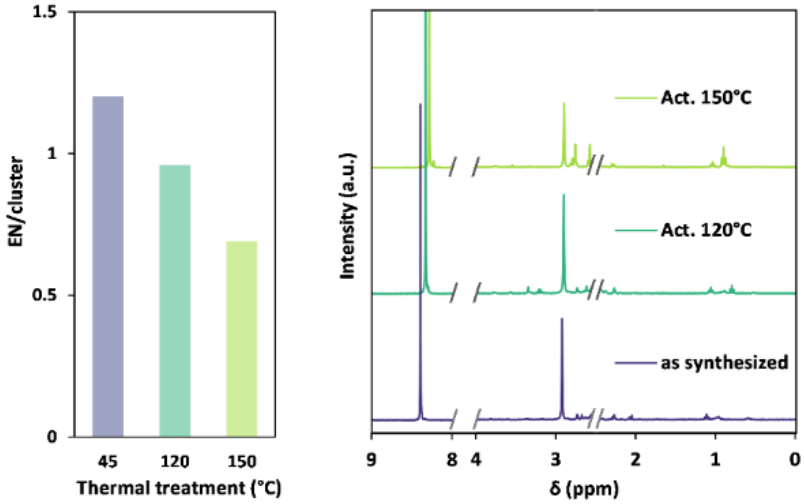

Figure IV-4. (Left) EN/cluster ratios calculated from integration of linker and ethylenediamine peaks in ^{1}H-NMR spectra of digested EN@MIL-100(Al) samples treated at different temperatures (45°C = as synthesized sample, 120°C and 150°C were heated under vacuum). (Right) Solution-state ^{1}H-NMR spectra of as-synthesized and activated EN@MIL-100(Al) digested samples.

The effectiveness of the grafting on MIL-100(Al) was evidenced by the FTIR spectrum (Figure IV-3), presenting characteristic absorption bands expected for ethylenediamine grafting, especially visible at 1370 cm^{-1}. The presence of EN in the MOF was further confirmed by solution-state ^{1}H NMR experiments on the digested MOF (details about ^{1}H NMR analysis and reference sample measurements can be found in the Experimental section and ESI, Fig. S IV-14). The spectrum of activated MIL-100(Al) presents a singlet at 8.14 ppm, corresponding to the aromatic signals of the trimesate linker, whereas the spectrum of digested EN@MIL-100(Al) shows the same peak (downshifted to 8.28 ppm, due to differences in D_2SO_4 concentration of the solution) and a supplementary singlet at 2.90 ppm, unambiguously

demonstrating the presence of ethylenediamine. The ratio of the integrals of the peaks of the aromatic protons of the linker and the protons of EN allowed us to determine the number of EN molecules per cluster (Figure IV-4; see also ESI for details on calculations based on the MOF's structure). The as-synthesized sample achieved 1.2 EN/cluster on average. A portion of the sample was heated under vacuum to remove physisorbed EN and was subsequently digested for ^{1}H NMR analysis. As expected, the amount of EN decreased somewhat when the sample was heated to 120°C, to reach 0.96 EN/cluster on average. Heating to 150°C however led to a decomposition of part of the EN present in the pores (see ESI, Fig. S IV-14, for detailed NMR spectra). Our results show that about one out of three Al sites is occupied by EN, which is in agreement with previous reports stating that only one Al per cluster can be coordinatively unsaturated by activation under vacuum,[221] and thus accept an EN molecule.

The FTIR spectra of the bimetallic MIL-100(Fe,Al) before and after functionalization with EN unfortunately do not display evident differences demonstrating the presence of ethylenediamine inside the MOF (Fig. S IV-2). Also, given the paramagnetic nature of the iron present in the MOF, characterization by digestion and ^{1}H-NMR analysis is not straightforward as this would require elimination of iron species prior to analysis. Therefore, the determination of the presence of EN in the bimetallic materials was done by combining results from ICP-OES and CHN elemental analyses (see Table S IV-4), as no N containing solvents were used throughout the synthesis procedures, enabling to hypothesize that all the nitrogen content originates from the presence of ethylenediamine. From those determinations, the N/metal content could be determined for as-synthesized samples, as well as after degassing under vacuum at 100°C. The EN/metal ratio is equal to 1.9 for the as-synthesized material and to 1.8 after heating at 100°C, indicating that about two out of three metal centers are coordinated to EN on average. However, it was not possible from these analyses to determine whether coordination occurs on either Fe or Al or on both metals. ICP analysis further showed that the Fe/Al ratio remained

constant, being equal to 2/1 before and after functionalization, showing that no metal leaching occurred during the reaction with EN. It is noteworthy that although after functionalization, the EN content of the bimetallic MOF is twice as high as for the monometallic one, the percentage of decrease in surface area for MIL-100(Al) is about 3.5 times higher than for MIL-100(Fe,Al). Such a huge difference cannot simply be explained by the difference of molar mass between both MOFs (586 g/mol for $Fe_2AlO(OH)BTC_2$ and 546 g/mol for $Al_3O(OH)(H_2O)BTC_2$). The explanation for this observation most likely lies in the fact that in the bimetallic MOF the ethylenediamine molecules occupy the mesoporous voids of the material, leaving the large surface area-developped by micropores mostly unaffected. This is supported by the decrease of the size of the hysteresis loop in the partial pressure range between 0.5 and 0.7 on the nitrogen sorption isotherm after functionalization (Fig. S IV-12, C.), as well as by the change of the pore size distribution (Fig. S IV-13, B.). In contrast, the pore size distribution of MIL-100(Al) does not change significantly after functionalization (Fig. S IV-13, A.), indicating that in this MOF the functionalization occurs homogeneously throughout the framework.

Thermogravimetric analyses were performed to probe the thermal stability of the MOFs before and after functionalization, and coupling to MS was used to determine the temperature at which EN leaves the framework of the functionalized materials (see Fig. S IV-11 and the corresponding note in the ESI for details). Concerning MIL-100(Fe), a completely different decomposition temperature was observed for the pristine MOF (~320°C) and the product obtained after reaction with ethylenediamine (~300°C). Such a difference is expected as the nature of both samples is different given the collapse of the MOF upon contact with EN. For the bimetallic and monometallic Al-based samples, the decomposition temperature remained unchanged upon functionalization, the bimetallic compounds having a decomposition temperature very close to that of monometallic MIL-100(Fe) (~320°C), whereas the Al-based MOFs have a higher decomposition temperature close to 430°C. Based on analysis of MS fragments with m/z values of

30, 42 and 43 (see ESI for detailed explanation), it seems that EN leaves the framework of EN@MIL-100(Al) around 290°C, well below the framework's decomposition temperature. For EN@MIL-100(Fe,Al), it seems that EN remains in the framework until decomposition (~320°C). Although the difference in observed temperatures at which EN leaves the MOFs could indicate stronger binding to Fe than to Al, these deductions are only based on a few fragments in the mass spectrum of ethylenediamine and must not be overinterpreted. Indeed, degradation of EN in the framework can occur well below the temperatures indicated by TGA-MS as shown by the solution NMR experiments on digested EN@MIL-100(Al) (*vide supra*).

Given that the monometallic Al-containing samples contain only non-paramagnetic nuclei, and that furthermore all those nuclei possess at least one NMR-active isotope, the grafting of EN could also be nicely evidenced by solid-state NMR CP-MAS experiments. ^{13}C spectra of MIL-100(Al) show signals around 170 and 130 ppm for the carboxylate and aromatic carbons, respectively.[221] Upon EN addition a separated signal around 38 ppm is clearly observed due to the aliphatic chain of the added ligand (Figure IV-5, **A**). Besides that, the ^{15}N solid state NMR spectrum (Figure IV-5, **B**) shows the presence of two signals of comparable intensities at 25 and 31 ppm, upshifted with respect to liquid (neat) EN (17.8 ppm, not shown). These results indicate that the two nitrogen atoms experience similar environment, in agreement with the results reported in the literature[288] and the EN grafting model we propose (see inset of Figure IV-5, **B**) with one Al-coordinated nitrogen atom and one free amine group. Signals of the ^{27}Al spectra of both pristine and functionalized MOFs (Fig. S IV-15) present a chemical shift around 0 ppm, similar to previously reported spectra of hydrated MIL-100(Al),[221] confirming that the metallic centers are six-coordinated. Furthermore, after functionalization with EN, the resulting signal possesses a more important downfield contribution, which can be explained by an increased p character of the Al–N bond of the metal center with the amine compared to the Al–O bonds with the oxo-, hydroxo- and carboxylate ligands.[289,290]

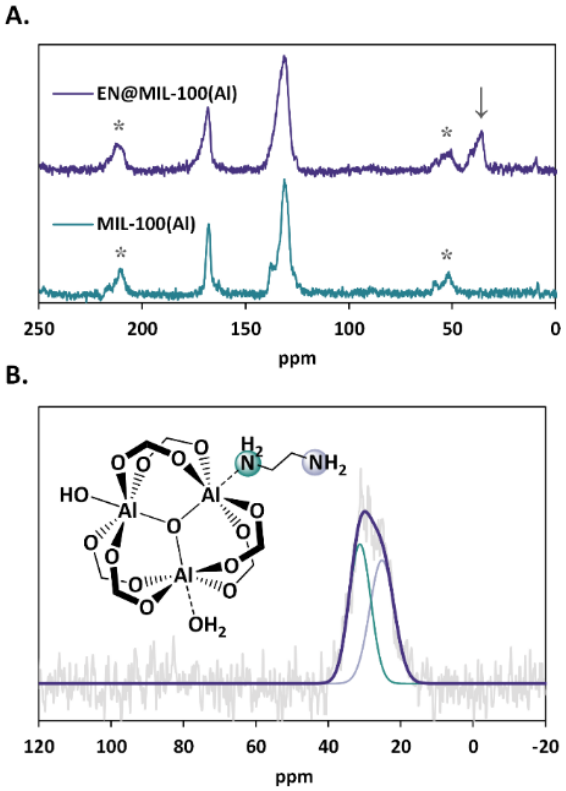

Figure IV-5. **A.** ^{13}C CPMAS NMR spectra of MIL-100(Al) after activation at 200°C and of as-synthesized EN@MIL-100(Al). **B.** ^{15}N CPMAS spectrum of EN@MIL-100(Al) with deconvolution of the signal. The inset is the determined structure of the functionalized cluster units of EN@MIL-100(Al). Asterisks indicate spinning sidebands and the arrow indicates the signal of the aliphatic chain of coordinated EN.

4.4. Availability of pendant amines

The possibility of performing post-functionalization of the pendant amine sites in the EN@MIL-100(Al) material was investigated through a fast and simple visual test. This was performed by using 8-thiomethyl-BODIPY (Figure IV-6, **A** and Fig. S IV-18 A.). This fluorescent molecule specifically reacts with primary amines, inducing the formation of linked 8-amino-BODIPY (Figure IV-6, **B**), shifting the emission maximum of the free dye from 525 nm (green) to 409-427 nm (blue), allowing to visually determine whether the reaction

occurred.[291,282] To do this, both pristine and ethylenediamine functionalized MIL-100(Al) were soaked in a dichloromethane solution of 8-thiomethyl-BODIPY and were then recovered by filtration. After this treatment, the pristine MOF showed a green fluorescence (Figure IV-6, **A**), which is typical of the unreacted BODIPY probe, indicating that the molecule was only non-specifically adsorbed onto the MOF's surface and/or in its pores. In contrast, the EN@MIL-100(Al) sample showed the specific blue fluorescence of the bonded BODIPY fluorophore (Figure IV-6, **B**), indicating that the post-functionalization reaction was performed successfully. It should be noted that this methodology was used only to assess the presence of pendant amine sites that are available for post-functionalization in the material, which could be present either on the MOF's external or internal surface, or both, but not to quantify them, as the BODIPY dye was not used in a stoichiometric amount. Although this test allows to visually evaluate the presence of amines, the fluorescence properties of the resulting solid samples deteriorate with time likely due to degradation of the fluorophore, which could be triggered by the acidic and/or basic nature of EN@MIL-100(Al) (*vide infra*), as BODIPY dyes can be decomposed in such media.[292]

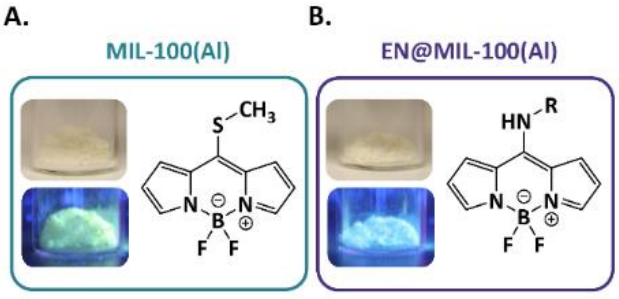

Figure IV-6. **A.** and **B.** Photographs under (upper) visible light and (lower) UV irradiation of (A) MIL-100(Al) and (B) EN@MIL-100(Al) after post-functionalization with 8-thiomethyl-BODIPY, with structures of the unreacted 8-thiomethyl-BODIPY and the 8-amino-BODIPY grafted upon reaction.

Therefore, the degree of availability of the amine functions for medium-sized molecules in the material's bulk was quantified by

reaction with ninhydrin (Fig. S IV-18 B.) in hot ethanol. Ninhydrin specifically reacts to form a blue dye, 2-(1,3-dioxoindan-2-yl)iminoindane-1,3-dione (Fig. S IV-18 C.), that is liberated in solution after its formation. The quantitative analysis of the dye content in the supernatant solution after centrifugal separation of the MOF allows determining the amount of amines that reacted with ninhydrin.[293] The UV-vis spectrum of the supernatant solution after reaction with ninhydrin revealed that reaction with primary amines occurred, as indicated by the typical absorption band at 580 nm (Fig. S IV-16). To ensure that the obtained results were not due to reaction with ethylenediamine leached in the hot ethanol solution, a blank test has also been performed. This test consisted of first soaking EN@MIL-100(Al) in boiling ethanol, followed by separation of the supernatant solution by centrifugation. In this case, after performing the ninhydrin test on the supernatant solution, no absorption band appeared at 580 nm (Fig. S IV-17), demonstrating that leaching of EN is negligible under the used conditions. Quantitative analysis of the ninhydrin test performed on EN@MIL-100(Al) however revealed that only 0.6 mmol of $–NH_2$ functions reacted per gram of MOF. This is less than the quantity of free amine functions determined by solution-state ^1H NMR on the digested EN@MIL-100(Al) sample (~ 1.65 $mmol.g^{-1}$, or one free $–NH_2$ per Al_3O trimer). This might be explained by the different possible diffusion pathways in MIL-100(Al), either through the larger hexagonal windows with a size of 8.6 Å or through smaller pentagonal windows of 5 Å (Fig. S IV-19 and Fig. S IV-20). Indeed, although ninhydrin, as well as 2-(1,3-dioxoindan-2-yl)iminoindane-1,3-dione are both small enough to diffuse through the larger windows, diffusion through the smaller ones is impossible, as shown in Fig. S IV-18 to Fig. S IV-21, especially taking into consideration that the pore openings are narrowed by the presence of EN coordinated to the Al_3O clusters. It is possible to calculate the proportion of ethylenediamine molecules that are present in the larger accessible mesopores compared to the amount of total EN. Those calculations (see ESI for details) give a proportion of available ethylenediamine molecules of 41%. This

nicely correlates with the 36% of amines detected in EN@MIL-100(Al) by the ninhydrin test (37.5% if considering that only 96% of the clusters are functionalized after thermal activation). This means that the detection efficiency of the amines by the ninhydrin test is about 87-91.5% of the free amines in the large pores. The few percent that are not detected can be ascribed to some adsorption of 2-(1,3-dioxoindan-2-yl)iminoindane-1,3-dione within the framework. Those results indicate that it is possible to selectively post-functionalize part of the EN molecules, localized in the diffusion path of the hexagonal windows, with large molecules, while leaving those in the small cages in their pristine state.

4.5. Brønsted acido-basicity of EN@MIL-100(Al)

It has previously been evidenced that MIL-100(Al) possesses a strong Brønsted acidity due to the presence of water coordinated to the aluminum.[294] We assumed that EN@MIL-100(Al) should possess both, Brønsted acidic sites due to the water molecules, and Brønsted basic sites due to the presence of $–NH_2$ functions. We decided to investigate this by a method inspired by the one of Hammett, which uses colored pH indicators to probe the strength of acid sites on colorless solids.[295] Our method relies on the use of bromothymol blue (BTB), which is fairly soluble in toluene. We used several solids which are known for their strong ($H_3PMo_{12}O_{40}$ and ZSM-5 zeolite) or medium (chromatography silica gel and UiO-66(Zr) MOF) Brønsted acidity, their strong basicity ($NaAlO_2$, Al_2O_3, MgO), as well as mixtures thereof (SiO_2/Al_2O_3 in various ratios) as reference materials (see ESI, Fig. S IV-22). In practice, the solids are immersed in the BTB solution and are repeatedly washed with toluene and alkanes before being dried and analyzed by diffuse reflectance UV-vis. The absorption spectra of the resulting powders is indicative of the surface Brønsted acidity of the materials, given by an absorption maximum around 550 nm for strong acids ($pKa < -0.66$), 425-450 nm for medium acids ($0.66 < pKa < 7.10$) and 620 nm for bases ($pKa > 7.10$), relatively to bromothymol blue,

resulting from the different protonation states of the indicator molecule (Figure IV-7, left).

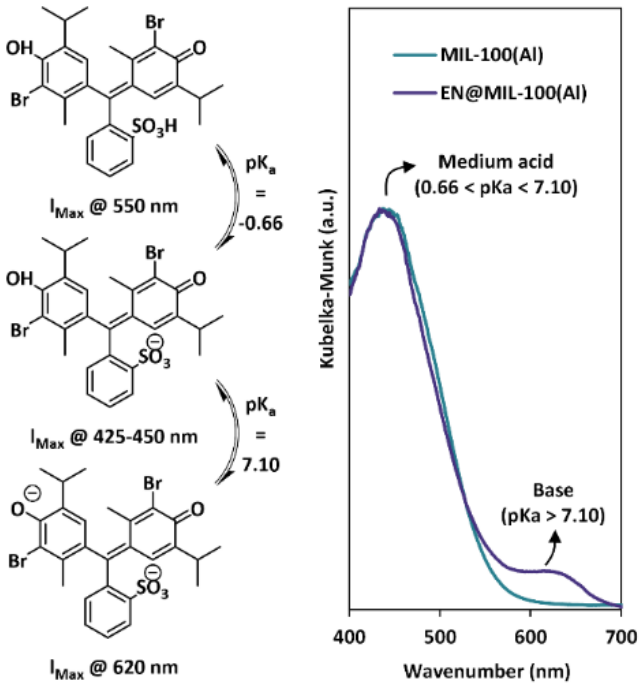

Figure IV-7. (Left) Structure of bromothymol blue under different protonation states. (Right) Diffuse-reflectance UV-vis spectra of BTB impregnated MIL-100(Al) and EN@MIL-100(Al).

This experiment shows that the Brønsted acidic sites in MIL-100(Al) are medium acids (pKa comprised between -0.66 and 7.10) and that acidic sites of similar strength are present in the ethylenediamine functionalized sample (Figure IV-7, right). The experiment also confirms that additionally to those acidic sites, EN@MIL-100(Al) possesses basic sites with a pKa > 7.10 due to the presence of amines, imparting both Brønsted acidity and basicity to this material. The crystallinity of the materials was checked after impregnation with bromothymol blue (see ESI, Fig. S IV-23). Interestingly, crystallinity was maintained for MIL-100(Al), whereas the long range order EN@MIL-100(Al) was clearly disrupted after impregnation. Such long range order disturbance has previously been

observed in MIL-100(Al) upon adsorption of other dyes such as methylene blue, Coomassie brilliant blue G-250 and rhodamine B.[296]

4.6. Carbon dioxide sorption

The adsorption of carbon dioxide in both pristine and functionalized MOFs was studied by means of gravimetric methods at a pressure of 1 atm and by low pressure adsorption isotherms as well as by volumetric methods at higher pressures. Gravimetric adsorption measurements at 1 atm were performed on a thermogravimetric system in which the samples were first heated at 100°C under helium atmosphere to remove physisorbed species but avoiding removing or damaging the grafted ethylenediamine. The samples were then cooled down to room temperature and three adsorption/desorption cycles were performed by switching the working gas from helium to CO_2. The obtained results are shown in the ESI (Fig. S IV-24). The results are indicative of the CO_2 sorption kinetics of the materials, as well as their sorption capacity. Concerning the pristine MOFs, MIL-100(Fe) is able to adsorb slightly more carbon dioxide than the aluminum-containing materials, which can be explained by its higher surface area and higher density of open-metal sites compared to the other materials. The iron-based MOF also reaches full capacity faster than the two other pristine MOFs, especially during the first adsorption cycle. Upon functionalization with EN, MIL-100(Fe) however loses its ability to adsorb CO_2, which was expected based on the amorphous nature of the material that was revealed by PXRD and the non-porous nature determined by nitrogen physisorption. EN@MIL-100(Al) adsorbs less CO_2 than its non-functionalized counterpart, which can be explained by its lower surface area (smaller free volume of the pores). The bimetallic MOF however retains most of its adsorption capacity after functionalization, allowing slightly more CO_2 to be adsorbed in EN@MIL-100(Fe,Al) than in EN@MIL-100(Al). This can be explained by the smaller loss of surface area of the bimetallic MOF upon functionalization compared to MIL-100(Al). For all the MOFs, a decrease of gravimetric uptake was observed after functionalization

with EN, which is in accordance with a previous report on functionalization of MIL-100(Cr) with ethylenediamine,[274] but contradictory with another report.[255]

The materials were further investigated by low-pressure gravimetric adsorption experiments (Fig. S IV-25). This was done after degassing the samples *ex-situ* at 100°C under vacuum and loading the samples in a TGA system which was hosted in a glovebox, allowing to avoid uptake of moist before the measurement. The samples were then subjected to gas fluxes with variable CO_2/Ar proportions, increasing the partial pressure of CO_2 stepwise. The sample weight was allowed to stabilize between each increase of CO_2 partial pressure by a 30 min equilibration time, after which the weight gain was recorded. Not surprisingly, the adsorption at the highest CO_2 partial pressure (P/P_0 = 0.8) followed the trends of the gravimetric adsorption experiments at 1 atm. More interestingly, the uptake in the lower partial pressure range is much steeper for EN@MIL-100(Al) than for all other materials. This indicates that this material has a much more marked affinity for CO_2, which can be explained by interaction of CO_2 with the amine moieties of the MOF. Surprisingly, this feature is absent in the bimetallic counterpart, EN@MIL-100(Fe,Al), indicating that in this material the amine functions cannot interact with CO_2 as efficiently. When normalizing the adsorbed quantity of CO_2 by the surface area of the materials (Fig. S IV-26), the bimetallic MOF seems to be the best performing of all non-functionalized MOFs. However, the quantity of adsorbed carbon dioxide by surface area lowers upon functionalization. After functionalization, EN@MIL-100(Al) absorbs about twice as much CO_2 per square meter than its non-functionalized counterpart at partial pressures above 0.25, and about three times more at low partial pressures ($P/P_0 < 0.1$), evidencing again the higher affinity of the functionalized Al-MOF for CO_2 upon functionalization with ethylenediamine.

Volumetric measurements were performed for all the MOFs displaying porosity (see ESI, Fig. S IV-27), after activation at either

200°C for non-functionalized materials or at 100°C for the MOFs functionalized with EN. As a general trend, the materials with higher surface areas adsorbed higher quantities of CO_2, the amount adsorbed increasing in the following order: EN@MIL-100(Al) [S_{BET} = 657 m²/g], EN@MIL-100(Fe,Al) [S_{BET} = 839 m²/g], MIL-100(Fe,Al) [S_{BET} = 1029 m²/g], MIL-100(Al) [S_{BET} = 1861 m²/g] and MIL-100(Fe) [S_{BET} = 2048 m²/g].

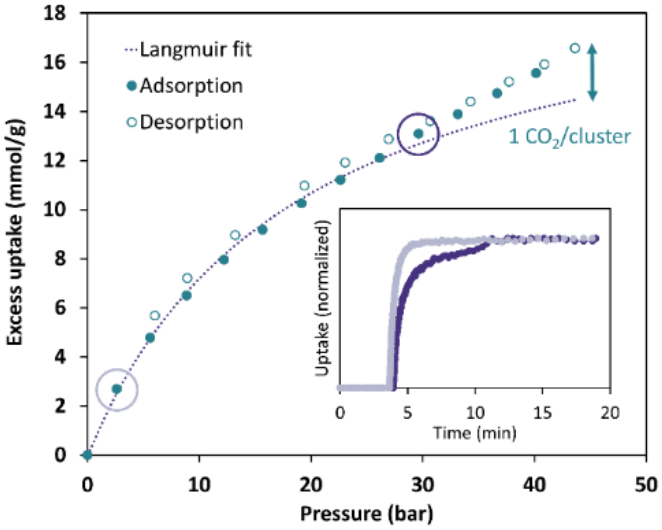

Figure IV-8. Experimental sorption isotherm of CO_2 in MIL-100(Al) together with Langmuir fit and (inset) difference of adsorption kinetics at the 1st and 9th adsorption points (circled on the isotherm), evidencing reaction with CO_2.

At pressures below 25 bar, all the materials show an adsorption behavior that follows typical Langmuir isotherms (Fig. S IV-27). However, it is noticeable that although MIL-100(Fe) follows the Langmuir equation, all the materials containing aluminum start to absorb an excess of CO_2 compared to what would be expected according to a Langmuir equation above a certain pressure (> 25 bar). It is noticeable that the more aluminum the samples contain, the more this deviation from the expected isotherm becomes large. Interestingly, the gas uptake at the pressure point at which the experimental value starts to become different from the expected one shows remarkably

slowed down kinetics compared to the ones of the lower pressure points (see Figure IV-8 for MIL-100(Al) and Fig. S IV-28 for other MOFs). Indeed, when following the Langmuir fit, equilibrium is usually reached in about 2 minutes, whereas during the unexpected increase in uptake, the stabilization takes between 7 and 15 minutes. Furthermore, those materials display a small hysteresis upon desorption (see ESI, Fig. S IV-29 and Figure IV-8 for MIL-100(Al)). Those observations clearly indicate that some other phenomenon than simple physisorption is occurring in the Al-containing materials. Such behavior is not observed in MIL-100(Fe) and was not reported for any other MIL-100(M) (M = any metal) structure before.[157,297] Calculations (Table S IV-2) show that the deviation from the expected uptake at high pressures is close to one CO_2 molecule per trinuclear cluster for MIL-100(Al) and EN@MIL-100(Al), and roughly half that quantity for MIL-100(Fe,Al) and EN@MIL-100(Fe,Al). This indicates that the presence of aluminum in the material is responsible for the observed effect. As coordinatively unsaturated metal sites are known to be one of the first filled sites during adsorption with coordinating gases like CO_2, and that this adsorption thus occurs at much lower pressures, we ruled out that Al open-metal sites are playing a role in the observed phenomenon. We thus hypothesized that species coordinated to Al are likely undergoing a reversible reaction (chemisorption) with CO_2 at high pressure. We ruled out ethylenediamine and water as the active species, as MIL-100(Al) and MIL-100(Fe,Al) do not contain EN and the presence of coordinated water in EN@MIL-100(Fe,Al) was ruled out by elemental analysis. The only common species to all the materials showing the unusual adsorption behavior is thus a hydroxyl moiety coordinated to Al. Based on this observation, it can be hypothesized that CO_2 insertion occurs between the oxygen and hydrogen atoms of the hydroxyl moiety (Figure IV-9). Such behavior can be promoted by the strong polarization of the Al–OH bonds, rendering the hydrogen atoms quite acidic. This mechanism is also in accordance with the fact that the difference between the observed excess uptake and the one expected based on the Langmuir fit is more important for the monometallic Al-

based materials than for the bimetallic ones. Indeed, the former contain one Al–OH moiety per cluster, whereas bimetallic Fe,Al materials probably contain a mixture of Al–OH and Fe–OH moieties. This explains why the amount of chemisorbed CO_2 is less than one molecule of carbon dioxide per trimeric cluster for the bimetallic MOFs. Further evidence concerning this adsorption mechanism could be gained from *in-situ* spectroscopic characterizations (FTIR, NMR, etc.) under high pressure of CO_2. However, those characterizations require specially dedicated equipment[298] and are thus outside the scope of this work.

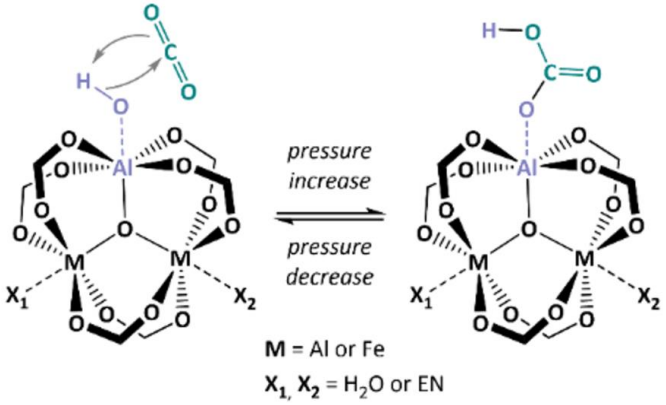

Figure IV-9. Scheme of the probable mechanism of CO_2 uptake at high pressure in Al-containing MIL-100 MOFs.

5. Conclusions

We performed functionalization of the metal sites of two distinct monometallic Fe and Al MOFs from the MIL-100 series with ethylenediamine. The second MOF, MIL-100(Al), was obtained under mild conditions as a hierarchically structured solid with micro- and mesopores, free of unreacted trimesic acid, through a new procedure. Our experiments showed that only MIL-100(Al) is retaining its crystallinity upon reaction with EN, whereas MIL-100(Fe) collapses. These results demonstrate that the choice of the metal composing the MOF's structure is of critical importance for the successful functionalization of the metal centers in MOFs, rather than the MOF

structure. The efficient incorporation of EN in the MOF was demonstrated by an original approach based on solution NMR, allowing to evidence and quantify the presence of the complete EN molecule, which is not possible by using elemental analysis. Solid-state NMR further confirmed that the grafted EN possesses one free $–NH_2$ that adds new functionality to the MOF. The stabilizing role of aluminum in the framework was further demonstrated by reacting EN with a mixed-metal MIL-100(Fe,Al) (Fe/Al = 2/1) MOF, which preserved its crystalline state.

The obtained materials are promising for post-functionalization through amine chemistry, as demonstrated by the successful reaction with 8-thiomethyl-BODIPY and ninhydrin. Thanks to the reaction with ninhydrin, we were able to demonstrate that the ethylenediamine molecules present in the large diffusion channels of EN@MIL-100(Al), accessible through hexagonal windows of 8.6 Å, can be selectively post-functionalized by molecules that are too large to diffuse through the smaller diffusion channels formed by the 5 Å-wide pentagonal windows. The amine moieties of the EN in the smaller mesopores (about 59% of the pendant amine sites), only accessible through the small pentagonal windows, can then remain in their pristine state, or could be transformed to a different functionality by reaction with a smaller molecule. EN@MIL-100(Al) could thus be used for developing bifunctional materials with a hierachized distribution of functionalities throughout the framework.

Interestingly, EN@MIL-100(Al) possesses both Brønsted acidic and basic sites, as demonstrated by a colorimetric approach based on bromothymol blue adsorption, opening the door to applications such as bifunctional acid/base catalysis. The ethylenediamine-functionalized MOFs show lower gravimetric and volumetric CO_2 uptakes than their pristine counterparts due to the space occupied by the EN molecules, but the functionalization of MIL-100(Al) by ethylenediamine is responsible for a higher affinity of the resulting material towards CO_2 at low partial pressures, as well as higher CO_2 adsorption per surface

area, which is promising for gas separation applications. Finally, we evidenced the unusual CO_2 adsorption behaviour of aluminum-containing MIL-100 MOFs and their EN-functionalized counterparts, revealing sorption isotherms with unexpected increase in excess uptake above 25 bar together with slowed down adsorption kinetics and a small hysteretic behavior during desorption, likely ascribed to formation of carbonate species, which, to the best of our knowledge, is unique among the MOFs of the MIL-100 family.

Further investigation of post-functionalization of aluminium- and iron-based MOFs of the MTN topology, such as MIL-101 derivatives, with ethylenediamine could also be promising. Indeed, they possess larger pores, leaving more available space upon functionalization, and their CUSs do not point towards the inside of the pores windows, unlike in MIL-100, diffusion problems would thus be less likely to occur upon appending EN.

CHAPTER V

Mild synthesis and water stability of rare-earth based MOF-76 series

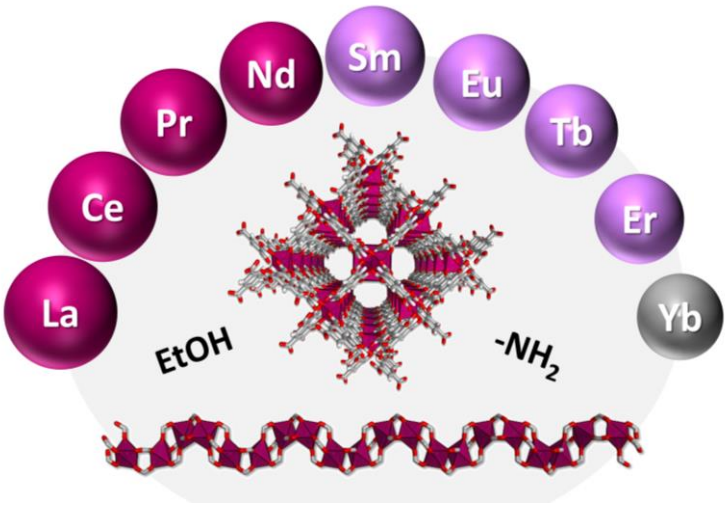

Chapter V – Mild synthesis and water stability of rare-earth based MOF-76 series

1. Abstract

Rare earth (RE) and lanthanide (Ln) based metal-organic frameworks (MOFs) are promising materials for diverse applications in the fields of catalysis and guest sorption as well as in optical devices. The trimesate (BTC^{3-}) linker-based MOF-76 (also known as REBTC) family is an example of such materials. However, to date the bulk synthesis of those MOFs has only been attempted under solvothermal conditions, mostly involving the use of toxic *N*,*N*-dimethylformamide (DMF) as solvent. Here we present a new convenient way to perform the synthesis of those MOFs using ethanol as the only solvent. This new procedure forms a gel intermediate, which decomposes to form microsized sea urchin-like aggregates of RE-BTC MOF crystals. The latter can be activated at temperatures well below the ones required for conventionally obtained RE-BTC MOFs. Furthermore, we investigated the reaction mechanism by *in-situ* NMR methods and show that the solvent, unreacted lanthanide precursor and the excess linker, which is selectively transformed into 3,5-bis(ethoxycarbonyl)benzoic acid, can easily be recovered for re-use. Interestingly, an investigation of the hydro(thermal) stability of the MOF-76 family across lanthanum and the lanthanide series showed improved stability of the materials with decreasing ionic radius. We also report the synthesis of the first amino-functionalized MOF-76, namely MOF-76(La)-NH_2, and its single crystal structure, and demonstrated that the presence of $–NH_2$ moieties on the linkers strongly increases the aqueous stability of the MOF. Finally, the materials were investigated for sorption of xenon by means of in situ powder X-ray diffraction.

2. Introduction

Rare earth-based MOFs (RE-MOFs), resulting from the assembly of lanthanides and carboxylate-type linkers, reveal good stability

towards heat and solvents,[299] as both the metals in the +III oxidation state and the carboxylate groups of typical linkers are considered to be hard Lewis acids and bases. Recently, many new MOF architectures based on lanthanide metals have been discovered (among which Ce^{IV}-based MOFs that are isostructural to previously studied Zr-based MOFs, such as UiO-66).[299] However, the strong metal-ligand interaction is also responsible for rapid precipitation of amorphous products. Therefore, RE-MOFs, as well as other high-valence metal-based carboxylate MOFs, are often synthesized under solvothermal conditions using high boiling point polar solvents.[300,301,302] Some typical solvents, such as *N*,*N*-dimethylformamide (DMF), are known to have a negative impact on health and environment.[303,304,305] DMF is also difficult to remove because of its strongly coordinating nature and high boiling point. This often requires solvent exchange, sometimes by long refluxing at high temperatures, or a thermal activation at very elevated temperatures (> 300°C).[34]

In this work, we present a new method to synthesize RE-MOFs (RE = La, Ce, Pr, Nd and mixtures of La with heavier Eu and Tb) involving benzene-1,3,5-tricarboxylate (trimesate, BTC^{3-}) linker.[137] These MOFs are the members of the MOF-76 (or REBTC) family,[76] whose structure is composed of lanthanide centres coordinated to six oxygen atoms from six different trimesate linkers, forming a 3-dimensionnal structure with 1D channels accessible to guest molecules (Figure V-1). Furthermore, the remaining coordination sites on the metal centres are occupied by solvent molecules that can be removed by simple heating under vacuum, allowing the creation of open-metal sites, of high interest in catalysis and gas sorption.[136] Here we study the possibility to use ethanol as the only solvent for performing the synthesis of RE-BTC MOFs, as this solvent has low toxicity and can easily be recycled.[69,306] The MOF formation mechanism, a possibility to obtain amine-functionalized MOF-76 derivatives, as well as the properties of the obtained materials (such as stability and guest adsorption) are also investigated in this work.

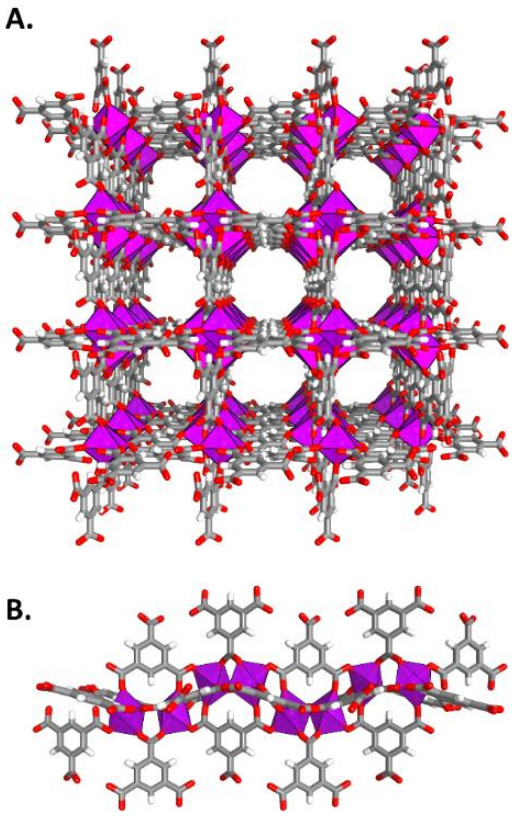

Figure V-1. Structure of RE-BTC MOF with the MOF-76 topology, showing the accessible 1D channels (A.), and the infinite RE coordination chains (B.). Colour chart: red: oxygen, grey: carbon, white: hydrogen, pink polyhedrons: Ln atoms.

3. Materials and methods

3.1. Instruments

Optical microscopy characterization was performed using a Euromex IS.1053-PLPOLRi polarizing microscope equipped with a Euromex VC 3036 camera. Calibration was realized using a 1 mm /100 (10 µm/division) calibration slide and images were collected using the ImageFocus 4 software.

Powder X-ray diffraction patterns were measured using a MAR345 diffractometer with X-rays generated either by a Rigaku ultraX 18S X-

ray generator (molybdenum anode, 0.71073 Å), with a monochromated beam (Xenocs FOX 3D mirrors) or an Incoatec Microfocus Source^{HIGHBRILLIANCE} (IμS^{HIGHBRILLIANCE}) Mo ELM47 operating at 50 kV and 1000 µA. The samples were prepared in glass capillaries (diameter: 0.7 mm). The raw data was integrated through the Fit2D software, using LaB_6 (measured in a 0.1 mm diameter capillary) as reference sample.

TGA measurements were performed on a Mettler Toledo TGA/DSC^{3+} system equipped with a sample robot. The used air flow was of 100 ml/min. An initial isotherm at 27°C was applied during 15 minutes before heating the sample to 900°C at a rate of 10 K/min.

Infrared spectra were recorded on a Bruker Alpha spectrometer equipped with a Platinum ATR module (diamond crystal) housed in an argon-filled glovebox in the 4000-370 cm^{-1} range with a resolution of 4 cm^{-1}.

Nitrogen sorption isotherms were measured at 77 K using a Micromeritics ASAP2020 equipment. All samples were activated at temperatures specified in the main text under dynamic vacuum for 10 h prior to analysis.

^{1}H-NMR spectra of products obtained from the linker syntheses were recorded in DMSO-d^6 at room temperature on a Bruker Avance II spectrometer equipped with a BBO 5 mm gradients-Z probe operating at 300 MHz for ^{1}H.

All NMR analyses for *in situ* follow-up of the MOF synthesis were recorded at room temperature (296 K) and 353 K on a Bruker Avance 500 operating at 11.7 T (Larmor frequencies of 500.13 MHz for ^{1}H, 125.76 MHz for ^{13}C and 70.65 MHz for ^{139}La). Experiments were run under TopSpin program (Bruker) using a BBO{^{1}H,X} probehead equipped with a *z*-gradient coil. Samples were prepared in CD_3CD_2OD. ^{1}H and ^{13}C chemical shifts were referenced to the residual $CD_3CD\mathbf{H}OD$ signal from the solvent (3.56 ppm for ^{1}H and 56.96 ppm for ^{13}C NMR spectra), respectively. ^{139}La NMR spectra were calibrated

using 0.01 M $LaCl_3$ in D_2O solution as external reference (δ = 0.00 ppm). Standard zg programs were employed for 1D NMR experiments. A Waltz-16 decoupling scheme with a pulse of 80 μsec was used for $^{13}C\{^1H\}$ NMR analyses. Sample spinning was deactivated during measurements.

3.2. Chemicals

Trimesic acid (98%) was purchased from Acros Organics. Denaturated ethanol (Technisolv, 99%), DMF (HPLC grade), dichloromethane (HiPerSolv, CHROMANORM) and hydrochloric acid (37%) were purchased from VWR Chemicals. Praseodymium(III,IV) oxide (99.9%) and 2,4,6-trimethylaniline (97%) were purchased from Acros. Cerium(III) acetate hydrate (99.9%) and terbium(III) nitrate hexahydrate (99.999%) were purchased from Aldrich. Lanthanum(III) carbonate was purchased from K&K Laboratories, Inc. Samarium(III) oxide (99.9%) was purchased from Koch-Light Laboratories Ltd. Neodymium oxide (99.9%), europium oxide (99.99%), erbium oxide (99.9%) and ytterbium oxide (99.9%) were purchased from Strategic Elements. Acetyl chloride (98%) was purchased from Alfa Aesar. Potassium permanganate crystals were purchased from J. T. Baker Chemicals N.V. (Holland). All chemicals were used as received.

3.3. Syntheses

Lanthanide chloride hydrates: To 3 eqs. of concentrated (37%) aqueous HCl was added 1 eq. of Ln in the form of $La_2(CO_3)_3$, $Ce(OAc)_3$ hydrate, Pr_6O_{11}, Nd_2O_3, Sm_2O_3, Eu_2O_3, Er_2O_3 or Yb_2O_3. The lanthanide source was reacted with the acid until a clear solution was obtained. Heating was applied when necessary to complete the dissolution, with accessory dropwise addition of concentrated HCl if needed. Then, excess acetone (technical grade) was added to precipitate the product. The crystalline solid was then recovered by filtration on a glass frit and washed with acetone. The salt was finally dried under vacuum (using a Schlenk line) and stored in a desiccator.

The reactions involved in the formation of the chlorides are the following:

$$Ln_2O_3 + 6\ HCl + x\ H_2O \rightarrow 2\ LnCl_3{\cdot}xH_2O + 3\ H_2O$$

$$Pr_6O_{11} + 22\ HCl + x\ H_2O \rightarrow 6\ PrCl_3{\cdot}xH_2O + 11\ H_2O + 2\ Cl_2$$

$$La_2(CO_3)_3 + 6\ HCl + x\ H_2O \rightarrow 2\ LaCl_3{\cdot}xH_2O + 3\ H_2O + 3\ CO_2$$

$$Ce(OAc)_3 + 3\ HCl + x\ H_2O \rightarrow CeCl_3{\cdot}xH_2O + 3\ AcOH$$

MOF syntheses: 30 ml of a 0.167M, 0.083M or 0.042M solution of trimesic acid (either in ethanol or in a 3:1 mixture of DMF:H_2O) was added to 30 ml of a solution of $LnCl_3$ in the same concentration and in the same solvent system. The resulting mixture was introduced in a 100 ml glass screw capped vial that was closed and introduced in an oven at 80°C, 45°C or left at room temperature without stirring for 14h30'. The obtained solid was recovered by filtration and washed with ethanol. Finally, the MOFs were dried at room temperature under vacuum. The yields were determined by weighing the compounds and subtracting the weight percentage of the solvent using the data of the thermogravimetric analyses. MOF-76(La)-NH_2 was synthesized in the same way by substituting trimesic acid by 2-aminotrimesic acid. Note: The lanthanum chloride and trimesic acid must be dissolved separately as trying to dissolve both reactants together leads to the formation of an insoluble precipitate.

N-mesitylacetamide was obtained through a previously described procedure.[307] In brief, 10.5 ml of 2,4,6-trimethylaniline were introduced under argon in a flame-dried 500 ml round-bottom flask equipped with a Teflon stir bar and a rubber septum. 100 ml CH_2Cl_2 was added to the flask and the mixture was cooled to 0°C (ice bath). 5.6 ml acetyl chloride were added dropwise by syringe, followed by 11 ml triethylamine. After 2 h of reaction, the mixture was filtered. The solid was then suspended in water and stirred for 30 min. The solid was then collected by filtration and was dried under vacuum. *2-aminobenzene-1,3,5-tricarboxylic acid* (2-aminotrimesic acid) was obtained through a previously described procedure.[307] In brief, 5 g of *N*-mesitylacetamide

and 165 ml of water were introduced in a 500 ml round bottom flask, followed by the portion wise addition of 0.55 g of sodium hydroxide. Then, 34 g of $KMnO_4$ were added in portions (~5 portions) over ~2 h under vigorous stirring. The flask was then equipped with a condenser and the solution was heated under stirring at 85°C for 72 h. The reaction mixture was then filtered through filter paper and the MnO_2 was rinsed with ~200 ml of hot water. The obtained filtrate was acidified with 40 ml of HCl and the mixture was refluxed overnight (100°C). The obtained white solid was then filtered and rinsed with ice-cold water and dried under vacuum. . ^{1}H NMR ($CDCl_3$, 300 MHz, δ): 6.93 ppm, s, 2H; 2.29 ppm, s, 3H; 2.25 ppm, s, 6H; 1.73 ppm, s, 3H.

Recycling of unreacted materials

1. *Separation of organic and inorganic materials*

The recycling test was performed on the filtrate of the large-scale synthesis of MOF-76(La). The filtrate was evaporated using a rotating evaporator in a 2L evaporation flask followed by treatment under high vacuum, upon which a foam formed in the flask. 250 mL of deionised water was then added to the dry foam, followed by filtration and washing with two times 100 mL water. The solid containing the organic part was dried by suction. To the filtrate, 200 mL of a 50g/L aqueous solution of Na_2CO_3 was then added to precipitate lanthanum carbonate. The precipitate was left in the solution overnight to allow the particles to grow sufficiently for enabling filtration. The next day, the lanthanum carbonate was filtrated over a filtration membrane (0.45 µm hydrophilic PVDF) and washed twice with water to yield shiny glitter-like crystals. The resulting solid was dried in an oven at 150°C for 2 h and allowed to cool down to room temperature to yield dried lanthanum carbonate.

2. *Treatment of the organic part*

About 10 g of the organic solid was added to 10 g of NaOH dissolved into 300 mL of water. This suspension was poured into a 500 mL glass screw-capped bottle which was then closed and heated in an oven at 80°C overnight. Then, and additional 5 g of NaOH was added

to the cloudy solution and the bottle was shaken vigorously for 2 minutes. The resulting mixture was then filtered over filter paper to obtain a clear transparent filtrate. To this filtrate, 40 mL of concentrated (37%) HCl was added dropwise by using an additions funnel under vigorous stirring. The clear solution became cloudy, and then transparent again (due to precipitation of H_3BTC and re-solubilisation by the heat released by the reaction). The solution was then allowed to cool into the fridge (4°C) to crystallize trimesic acid. The crystals were then filtered over a glass frit and the solid was dried in an oven at 80°C for about 2 h.

3. Treatment of the inorganic part

The dried lanthanum carbonate was transformed into lanthanum chloride by applying the same procedure as for the synthesis of lanthanide chloride hydrates from oxides and carbonates, by dissolution in hydrochloric acid and precipitation by acetone (see above).

4. Using recycled materials for re-synthesizing MOF-76(La)

The synthesis of MOF-76(La) from recycled materials was performed according to the same procedure in ethanol as for the synthesis from commercial reagents. However, the ethanol suspensions of both recycled reagents were slightly cloudy and were therefore filtered on a 0.45 µm PTFE membrane (syringe filter) before the La- and H_3BTC-containing solutions were mixed together.

4. Results and Discussion

4.1. Mild synthesis of RE MOF-76

4.1.1. Optimization of synthesis in ethanol for RE = La

To obtain RE MOF-76 under benign conditions, we hypothesized that trimesic acid and RE chlorides, owing to their good solubility in ethanol, would be able to form homogeneous mixtures from which the corresponding RE-BTC MOFs could be crystallized. We decided to use lanthanide chlorides as ethanol-soluble rare earth (RE) source instead of the equally soluble nitrates to avoid any oxidation reaction triggered

by the release of HNO_3.[308] To optimize the reaction parameters, lanthanum was used for its low cost, knowing that other REs behave similarly (see below for synthesis with other metals).[309,310] Stoichiometric amounts of both precursors were dissolved in ethanol and then solutions were mixed and introduced in screw-capped glass bottles, followed by heating in a pre-heated oven at 80°C. Different precursor concentrations for the final reaction mixture (0.167, 0.083 and 0.042 $mol.L^{-1}$) were tested in order to find optimal synthesis conditions. In each case, the solution formed a dense gel after approximately 30 minutes of heating. Upon standing in the oven for another hour, a precipitate appeared forming a supernatant solution, thus indicating the end of the reaction. The solid was recovered by filtration on a P4 glass frit (10 – 16µm), washed with ethanol and dried under vacuum.

The concentration of the precursors in the solution used for the synthesis had an important effect on the filterability of the materials. Indeed, when high concentrations (0.167 $mol.L^{-1}$) are used, the glass frit is quickly stoppered by the solid and filtration becomes very slow. At lower precursor concentrations the filtration proceeds very smoothly. The solid particles were studied by optical microscopy (Figure V-2**, A.**), finding in each case the product in a form of small sea urchin-like aggregates of needle-shaped crystals. The average size of these aggregates is relatively similar for all the obtained materials. However, the size of the needle-shaped crystals is larger and the size distribution broader when high concentrations of precursors are used. This makes the aggregates much more fragile, leading to plugging of the filter. Using lower concentrations of precursors (0.083 or 0.042 $mol.L^{-1}$) leads to materials that are easier to process, as the obtained aggregates are more robust, although it requires using more solvent. Although the crystal and aggregate sizes differ slightly with the used precursor concentrations, powder X-ray diffraction (PXRD) patterns (Figure V-2**, B.**) showed that in each case good quality crystalline MOF-76(La) samples are obtained.

A.

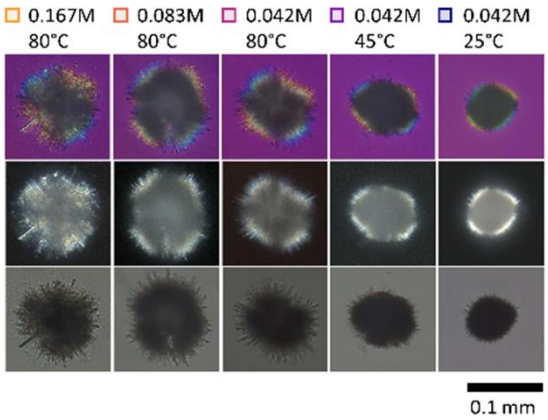

B.

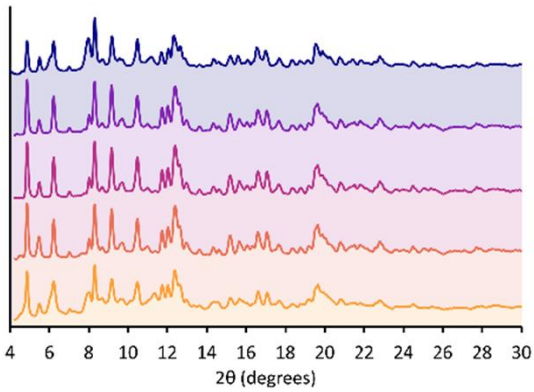

Figure V-2. (**A.**) Optical micrographs (from top to bottom: polarization with λ retardation plate and crossed polarizers; crossed polarizers; transmission) and (**B.**) PXRD patterns of La-BTC MOF obtained using different reaction temperatures and precursors concentrations.

The synthesis involving 0.042 M concentrations of reactants was repeated three times to check reproducibility, which was verified by PXRD and optical microscopy (data not shown). With the sample synthesized using the higher concentrations of precursors (0.167 M), some extra diffraction peaks appear (Figure V-2**, B.**). This could be due to the presence of residues that were not removed properly during the washing due to the difficult filtration of the particles. This hypothesis is further supported by the weight loss at decomposition of this sample

determined by TGA, which is *ca.* 8% higher than the theoretical value (Fig. S V-1). The weight loss of all the other La-BTC samples matches well the expected value. FTIR spectra (Figure V-3**., A.**) show peaks of carboxylic acids, in particular between 1650 and 1750 cm^{-1}, indicating that the impurity might be unreacted trimesic acid or secondary products (e.g. 3,5-bis(ethoxycarbonyl)benzoic acid, see below).

A.

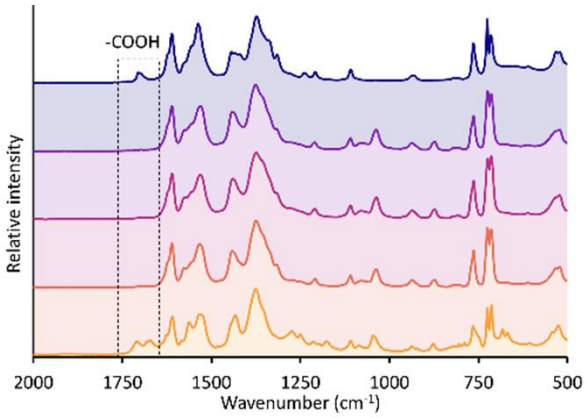

B.

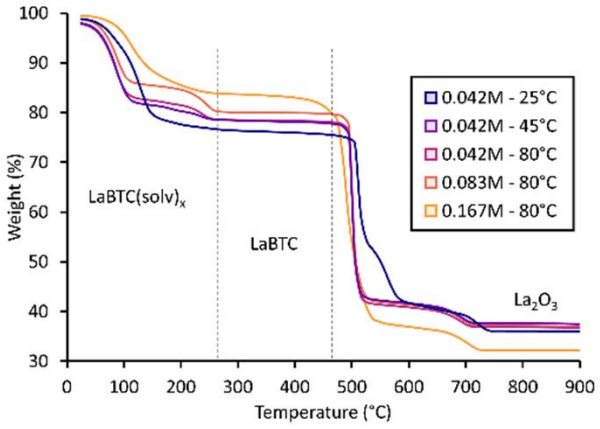

Figure V-3. (**A.**) FTIR spectra and (**B.**) thermogravimetric analyses (in air) of La-BTC MOF obtained using different reaction temperatures and precursors concentrations.

In an attempt to make the synthesis more energy-efficient, we decided to lower the reaction temperature to 45°C. In this case, crystalline La-BTC was also obtained, as shown by PXRD (Figure V-2**,**

B.). Optical microscopy showed that the obtained agglomerates are slightly smaller in size than the ones obtained at 80°C, the needle-shaped crystals are somewhat thinner (Figure V-2**, A.**), and FTIR spectra are identical to the one of the product obtained at 80°C (Figure V-3.**, A.**). Further lowering the reaction temperature to 25°C however did not lead to the formation of a gel after 30 minutes and resulted in a suspension rather than a well decanting precipitate even after standing overnight. After standing for two more days, a precipitate decanted and the particles were filtered through a P4 glass frit. Optical microscopy (Figure V-2**, A.**) revealed that the obtained particles also displayed a sea urchin-like shape. PXRD (Figure V-2**, B.**) and FTIR (Figure V-3.**, A.**) however indicated that the material obtained at 25°C contains a similar impurity to the sample synthesized at 80 °C from 0.167 M precursor solutions. This is evidenced by the presence of an absorption band at 1700 cm^{-1} in the FTIR spectrum, corresponding to the carboxylic acid, while the signals of physisorbed ethanol (in the 900 - 1100 cm^{-1} range) are missing in this sample, which could be due to more efficient drying.

Microscopic investigation shows that the temperature also has an influence on the size of the obtained aggregates, which become smaller, and thus more difficult to filter, when the reaction temperature decreases. The decomposition temperature of the materials (Fig. S V-1) is only slightly affected by the reaction temperature, and TGA curves of the obtained materials (Figure V-3.**, B.**) are very similar, except for the one obtained from 0.167 M precursor solutions and the one obtained at 25°C, both containing the same impurity. We identify the latter as the unreacted carboxylic acid, as evidenced by the PXRD patterns and FTIR spectra (Figure V-2., **B.** and Figure V-3.**, A.**) Finally, it seems that the temperature used for the synthesis has a small impact on the La-BTC yield, as slightly larger amounts of MOF are obtained at lower temperatures (Fig. S V-2, overall yield ~13%).

4.1.2. Synthesis for other RE metals

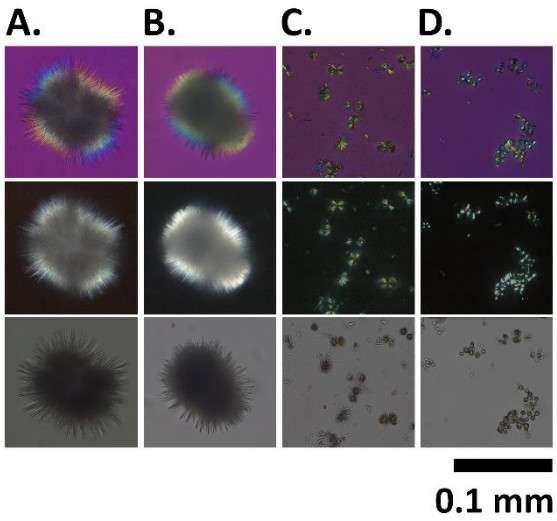

Figure V-4. Optical micrographs (from top to bottom: polarization with λ retardation plate and crossed polarizers; crossed polarizers; transmission) of MOF-76(RE) with RE = (**A.**) La, (**B.**) Ce, (**C.**) Pr and (**D.**) Nd obtained in EtOH.

Because the synthesis worked well with lanthanum, we investigated the possibility to synthesize RE-BTC MOFs of several other lanthanides. Ce, Pr, Nd, Sm, Eu, Er and Yb chlorides were used aiming to determine the influence of the size of the metal atom on the quality of the obtained product. The synthesis of two mixed-metal MOFs composed of lanthanum as cheap template doped with terbium or europium as luminescent centre ($La_{1-x}Ln_xBTC$, Ln = Tb or Eu, x = 0.05) was studied as well. In all cases, crystalline Ln-BTC MOFs were obtained as demonstrated by PXRD (Fig. S V-3), but the MOF-76 topology was only reached for the three largest lanthanides (i.e. Ce, Pr and Nd), as well as for the smallest, Yb (see summary in Figure V-5). A different crystalline phase, that could not be identified, was obtained for Sm, Eu and Nd. Noteworthy, the materials obtained with the smaller lanthanides (Eu, Er and Yb), were collected by centrifugation, as the obtained particles were too small for collection by conventional filtration. Investigation of the filtered MOFs by optical microscopy

(Figure V-4) shows that the size of the aggregates becomes smaller with decreasing lanthanide radius (i.e. Ce > Pr > Nd). Furthermore, during the synthesis, we observed that the formation and decomposition of the gel occurred faster with decreasing lanthanide radius, and when lanthanides from Sm to Yb were used, the precipitate formed very quickly, not allowing the observation of any intermediate gel phase.

In parallel, the syntheses with the same lanthanides were done using the classical DMF/H_2O solvent system in a 75/25 ratio. In this case, millimetre-sized single crystals of MOF-76 were isolated for all lanthanides except for lanthanum, see Fig. S V-4 and Figure V-5. For La-containing system, the obtained product was identified as the previously described non-porous hydrate LaBTC$(H_2O)_6$ (see the simulated pattern in Fig. S V-4).

FTIR spectra of the materials obtained in DMF (Fig. S V-5 and Fig. S V-6) contain an absorption band at 1650 cm^{-1}, typical for this solvent. This feature is not observed for the La-BTC material synthesized in DMF, since it was determined to be non-porous LaBTC$(H_2O)_6$, (see above) and thus its FTIR spectrum is completely different than for the other samples obtained in DMF/H_2O mixtures.

Characterization by thermogravimetric analysis under air shows that the materials obtained from ethanol have similar thermal stabilities to the ones obtained by the conventional methods in the DMF/water, as exemplified for MOF-76(Ln) with Ln = Ce and Pr (Fig. S V-7). However, when the synthesis is performed in the DMF mixture, the solvent is completely removed only at high temperatures (~350°C). Where ethanol was used, de-solvation readily occurs at about 200°C. This allows to activate (*i.e.* obtaining free coordination sites on the metal centres by heating under vacuum to remove coordinated solvents) the materials at much lower temperatures. To demonstrate this, the nitrogen sorption isotherms of the materials obtained from the ethanol synthesis were measured after activation at 200°C. The sorption isotherms are of very good quality, whereas measuring nitrogen sorption isotherms on materials obtained from synthesis in DMF after

activation at 200°C results in a adsorption/desorption curve hysteresis at low pressures, illustrated for MOF-76(Pr) in Fig. S V-8, the latter evidencing incomplete activation. Good quality isotherms for DMF-mediated materials could only be obtained after activation at 350°C.

Surface areas of the materials (Table V-1) were determined by using the BET equation from the data taken after an appropriate activation (at 200°C for materials synthesized in ethanol and 350°C for materials synthesized by the DMF mediated synthesis). All the materials have surface areas typical of MOF-76 structure (between 400 and 900 m^2/g).

Table V-1. Surface areas of MOF-76 samples obtained in ethanol and in DMF/H_2O, determined by nitrogen physisorption analysis. Samples prepared in ethanol were activated at 200°C and samples prepared in DMF/H_2O at 350°C.

Sample	Solvent system	BET surface area (m^2/g)
MOF-76(La)	EtOH	816
MOF-76(Ce)	EtOH	785
MOF-76(Ce)	DMF/H_2O	715
MOF-76(Pr)	EtOH	750
MOF-76(Pr)	DMF/H_2O	895
MOF-76(Nd)	EtOH	737
MOF-76(Nd)	DMF/H_2O	N/A
MOF-76(Sm)	DMF/H_2O	N/A
MOF-76(Eu)	DMF/H_2O	464
MOF-76(Yb)	EtOH	400
MOF-76(Yb)	DMF/H_2O	635
MOF-76(La,Eu)	EtOH	N/A
MOF-76(La,Tb)	EtOH	N/A

Finally, the mixed $La_{1-x}Eu_xBTC$ and $La_{1-x}Tb_xBTC$ MOFs show red and green luminescence, respectively, under UV irradiation (not shown). ICP-OES analysis of those two bimetallic MOFs shows that

the smallest lanthanides (i.e. Eu and Tb) are preferentially incorporated in the MOFs, as the Eu and Tb contents are higher in the final product than in the used reaction mixture (6.4 % and 6.1 % of the total metal content, respectively, instead of the engaged 5 %).

4.2. Study of MOF formation mechanism

To get a better understanding of the formation mechanism of La-BTC, the reaction in ethanol was monitored by liquid-state NMR and pH measurements. Although those techniques do not allow characterizing the formation of the solid phase, they enable the identification and monitoring of dissolved species that play an important role in the MOF's formation.

As the synthesis in ethanol leads to rather low yields, we decided to isolate secondary products for analysis, to make interpretation of the *in situ* data easier. This was performed by evaporating the filtrate after MOF synthesis. The obtained solid was washed with water to remove any water-soluble salts, and dried at room temperature. The obtained product was analysed by ^{1}H-NMR in DMSO-d^{6} and surprisingly, the spectrum did not show the presence of trimesic acid (Fig. S V-9). Instead, the analysis indicates that the di-ester of the linker, 3,5-bis(ethoxycarbonyl)benzoic acid, is remaining after the reaction. This can be explained by the formation of HCl during the MOF synthesis, according to the equation (1), which in turn catalyses an esterification reaction between trimesic acid and ethanol. However, the esterification only occurs on two carboxylic positions.

$$RECl_3 + H_3BTC \rightarrow RE\text{-}BTC + 3\ HCl \qquad (1)$$

In situ monitoring of the pH during the course of the reaction further confirmed the formation of HCl in the beginning, as the pH decreased quite drastically (Fig. S V-10). In situ ^{1}H-NMR showed the formation of the mono- and di-ethylester of trimesic acid a few hours after the reaction was started (Fig. S V-11), suggesting they form only after the jellification and thus formation of the MOF, which can already be isolated after two hours of reaction. Analysis of the ^{139}La spectra

before and after reaction indicates that lanthanum ions tend to coordinate to carboxylates over the course of the reaction, inducing a downfield shift of about 10 ppm (Fig. S V-12). (Ref.) The complexation of La to carboxylate explains why only the diester is obtained, as La^{3+} and BTC^{3-} are reacting in stoichiometric amounts, and therefore one carboxylate function, being coordinated to lanthanum, is not able to undergo esterification. The La remaining in solution is most likely coordinated to one carboxylate and two chlorides, with solvent molecules (water and/or ethanol) completing the coordination sphere.

4.3. Relative stabilities of RE MOF-76

4.3.1. Water stability

The stability of the synthesized MOF-76(RE) frameworks towards water, often overlooked in the literature, was evaluated by immersion of the powders in deionized water followed by filtration. The structural integrity of the samples was then evaluated by means of PXRD. Interestingly, the frameworks containing large rare-earth ions (i.e. La, Ce, Pr, Nd, Sm and Eu) all collapsed after short (less than 5 min) exposure to water at room temperature (data not shown). The frameworks containing smaller lanthanide ions (i.e. Er and Yb) however remained intact after immersion in water, showing that the smaller the lanthanide ion, the more the framework resists to water (data not shown, see hydrothermal tests, Fig. S V-13 and Fig. S V-14). High stability of MOF-76(Er) and MOF-76(Yb) has further been evidenced by PXRD analysis of samples immersed in boiling water for several days (Fig. S V-13 and Fig. S V-14), showing that both frameworks retained their structural integrity under those harsh conditions. These results indicate that smaller lanthanides are suitable for application in aqueous conditions. We attempted the synthesis of MOF-76(Er) in water by reaction between erbium sulfate and sodium trimesate but were only able to isolate a non-porous crystalline erbium trimesate hydrate (not shown). This indicates that the synthesis of MOF-76 in water is not an evidence, even when a water stable derivative is targeted. By opposition, the high sensitivity of the frameworks with

larger RE precludes their use in water-based applications, and framework decomposition could explain the previously observed decrease in conductivity of MOF-76 MOFs upon contact with moisture.[146] However, since the study of the whole lanthanide series goes beyond the scope of this work, we are not able to put a clear limit on the size at which destabilization by water occurs, but hypothesize that it sits somewhere between Gd and Ho (Figure V-5).

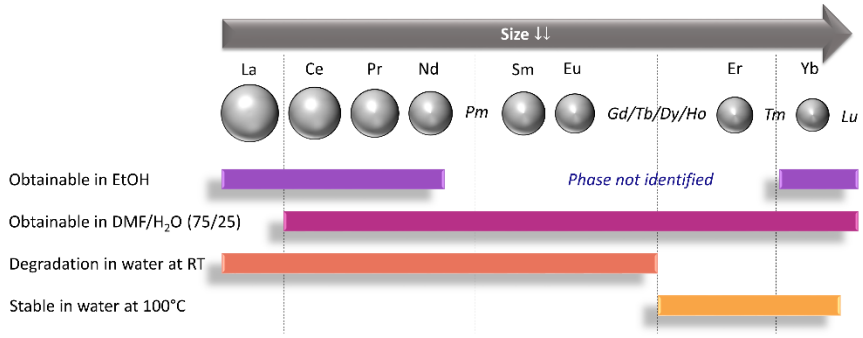

Figure V-5. Summary of RE MOF-76 synthesis conditions in ethanol and DMF/H_2O mixtures, and the stability in water for the series of rare-earth metals.

4.3.2. Improving water stability of RE MOF-76 through incorporation of the amino group

We investigated the influence of an amine functionality on the linkers towards water stability of the MOF-76 frameworks. This was done by using 2-aminotrimesate instead of non-functionalized trimesate in synthesis involving lanthanum, as its frameworks have the highest sensitivity to water, in both the ethanol and DMF/H_2O systems. In both cases, PXRD analysis of the product revealed the phase-pure MOF-76(La)-NH_2, even in the DMF/H_2O system in which the MOF without the amine groups could not be obtained. The presence of amino functions in the obtained MOF was clearly visible on the FTIR spectrum, as multiple new peaks not present on the spectra of MOF-76 samples, mainly between 1000-1500 cm^{-1} and 3000-3500 cm^{-1} (Fig. S V-15). Since the synthesis in DMF/H_2O leads to single crystals, we

were able to locate the amine functions inside the framework by means of single-crystal X-ray diffraction (Figure V-6). The structure shows that amines are located only on two of the three possible positions on the trimesate linkers, not pointing towards the lanthanide centers. Instead, the amine functions form hydrogen bonds with the carboxylate functions, which may help to stabilize the structure and render it more stable towards water. Furthermore, the presence of the amine function, by its electron affinity, makes the carboxylate a harder base and thus increases the MOF's stability. A similar increase of the water stability upon addition of an amino function on the linker has been observed in MIL-125(Ti)-NH_2, which is stable in water on the contrary to non-functionalized MIL-125(Ti).[311] In this paper, the increase in stability was explained by intramolecular hydrogen bonding between the hydrogen atom of the NH_2 group and an oxygen of the carboxylate group. The same phenomenon could also apply in the case of MOF-76- NH_2.

The textural properties of the MOF-76(La)-NH_2 sample obtained in both solvent systems was evaluated by means of nitrogen physisorption experiments, upon activation at 200°C for the sample obtained in EtOH and 350°C for the sample obtained in DMF/H_2O. For the sample obtained from DMF/H_2O, the surface area (S_{BET} = 754 m²/g and $S_{Langmuir}$ = 995 m²/g) was similar to the one of non-functionalized MOF-76(La) obtained in ethanol. The surface area of MOF-76(La)-NH_2 obtained in ethanol was however somewhat lower (S_{BET} = 380 m²/g and $S_{Langmuir}$ = 502 m²/g). These results indicate that the porous network remains accessible even in the presence of amine functions occupying a part of the space inside the pores, in agreement with the crystal structure. Interestingly, the obtained framework shows a blue fluorescence, which is due to the presence of the 2-aminotrimesate linker coordinated to the metal (see photography in Fig. S V-16). The water stability of the obtained amino-functionalized MOF has been assessed by the same methodology as for the non-functionalized MOFs (see above), and satisfactorily, the framework integrity was preserved upon contact with water, as shown by PXRD,

demonstrating that the framework's resistance to water can efficiently be increased by addition of amine functions on the linker. To rule out that the difference in observed water stability could be due to differences in framework flexibility, variable-temperature PXRD patterns of MOF-76(La) and MOF-76(La)-NH_2 were recorded (Fig. S V-17 and Fig. S V-18), as the removal of solvents usually results in flexible behavior of MOF-76 frameworks.[136] However, the evolution of PXRD patterns with temperature were very similar for both MOFs, showing that the presence of an amine function in the framework did not result in any change of flexibility, and demonstrating that the framework flexibility and water stability are not related for those MOFs.

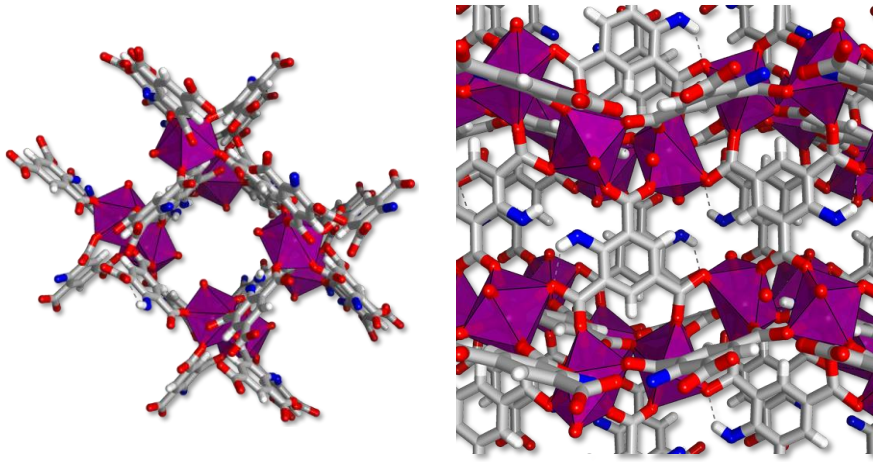

A. **B.**

Figure V-6. Structure of MOF-76(La)-NH_2 determined by single-crystal XRD. (A.) Opening of the porous channels and (B.) detail of the position of the amine functions. La atoms are represented by purple polyhedrons, carbon, oxygen, nitrogen and hydrogen are represented in grey, red, blue and white respectively. Solvent molecules inside the pores and disorder have been removed for clarity. Crystallographic data can be found in Table S V-1.

4.4. Scale-up and recycling of unreacted materials

We evaluated the possibility to scale up the ethanol-mediated synthesis of the La-BTC MOF by increasing the reactor capacity to 2500 ml and using 1500 ml of precursor solution. The reaction was performed using precursor concentrations of 0.042 $mol.L^{-1}$ and heating at 80°C. The obtained material showed good filterability on a porosity 4 fritted glass filter and homogeneous aggregate shape and size (Fig. S V-19), and the crystallinity and phase purity of the compound was demonstrated by PXRD (Fig. S V-20). This scale-up procedure was repeated twice, in a reproducible manner (data not shown). Nitrogen sorption was performed on the product (Fig. S V-21) and the BET surface area was determined to be 816 m^2/g.

Since the reaction yield is not very high, but reproducible (*i.e.* the yield was similar to the one obtained for the smaller scale synthesis; i.e. here 16% *vs.* 13% for the small scale), we evaluated the possibility to recycle the unreacted materials by making a second batch. For this purpose, the filtrate resulting from the MOF synthesis was evaporated under reduced pressure, allowing recovering the ethanol. The residue was dried under vacuum, and the obtained foamy liquid was further dried under vacuum overnight, yielding a solid powder. Separation of the lanthanum salt and organic products was achieved through addition of some aqueous HCl to the evaporation residue and thoroughly shaking the resulting suspension to solubilize all the Ln^{3+}. The solution was then filtered and the solid residue and filtrate were treated separately, as described below.

A concentrated aqueous solution of sodium carbonate was added to the filtrate in order to precipitate lanthanum carbonate according to the equation (2), which was recovered by filtration and washed with water. The lanthanum carbonate could then be transformed again into the corresponding chloride by treating with HCl according to the equation (3) and subsequent precipitation by addition of acetone. The FTIR spectrum of the recycled lanthanum chloride matches well with that of the starting $LaCl_3 \cdot 7H_2O$ (Fig. S V-22). Alternatively, the

obtained lanthanum carbonate could be calcined in air at 900°C to yield La_2O_3 without any traces of residual organic species, and transformed to the corresponding chloride according to the same procedure.

$$2\ La^{3+}_{(aq.)} + 3\ CO_3^{2-}{}_{(aq.)} \rightarrow La_2(CO_3)_{3\ (s)} \quad (2)$$

$$La_2(CO_3)_{3\ (s)} + 6\ HCl_{\ (aq.)} \rightarrow 2\ LaCl_{3\ (aq.)} + 3\ H_2O + 3\ CO_{2\ (g)} \quad (3)$$

To recover the linker, the solid residue was washed with water and dried under vacuum. This allowed obtaining NMR-pure diethyl 1,3,5-benzenetricarboxylic acid that could be converted back into trimesic acid by saponification through heating in an aqueous sodium hydroxide solution, followed by acidification with dilute hydrochloric acid.

$$HBTCEt_{2\ (s)} + 2\ NaOH_{\ (aq.)} \rightarrow HBTCNa_{2\ (aq.)} + 2\ EtOH \quad (4)$$

$$HBTCNa_{2\ (aq.)} + 2\ HCl_{\ (aq.)} \rightarrow H_3BTC_{\ (s)} + 2\ NaCl_{\ (aq.)} \quad (3)$$

The obtained recycled materials could successfully be reused to obtain La-BTC in ethanol, as shown by FTIR spectra (Fig. S V-23).

4.5. Xenon adsorption

In order to evaluate the adsorption of xenon in MOF-76(La), we used *in situ* PXRD. Xe is particularly well suited for this purpose as its X-ray atomic scattering factor is very high. MOF-76(La) obtained by the ethanol-mediated synthesis was loaded in a glass capillary connected to a home-made gas-loading system. The temperature of the sample was controlled with Oxford Cryostream 700.

Before the experiment, the sample was outgassed overnight at 100°C. The capillary was then cooled down to 160 K, and a blank experiment was performed by heating the sample under vacuum by 10 K steps until 400 K to assess any structural changes of the MOF in the absence of xenon (Figure V-7). The structure was maintained when cooling down from 400 K to 160 K, but upon heating, a structural change surprisingly occurred near room temperature.

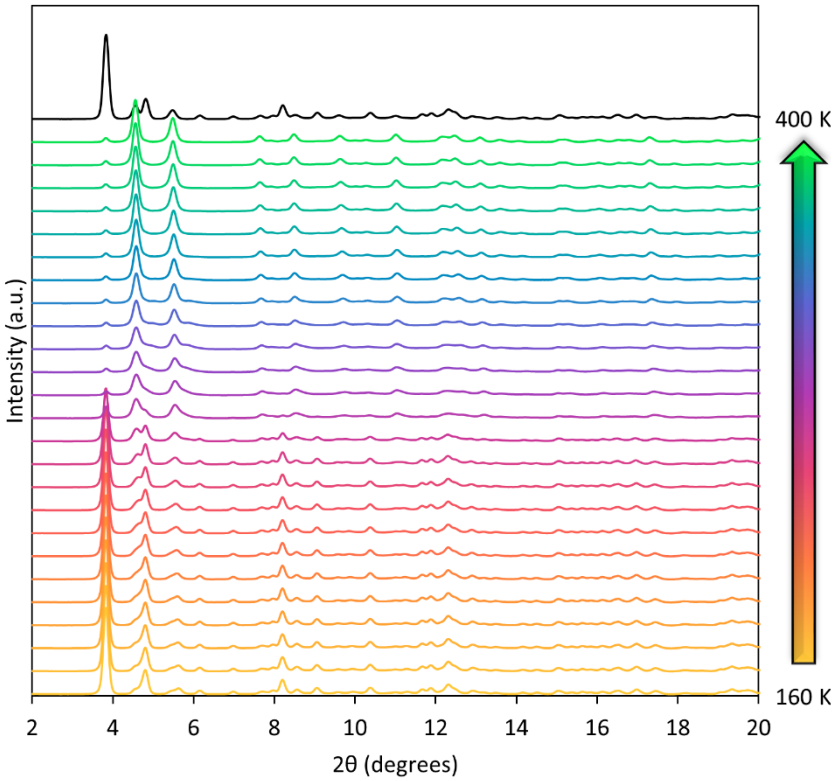

5.

Figure V-7. Variable temperature PXRD patterns of MOF-76(La) under vacuum. The black line represents the sample after overnight heating under vacuum at 400 K. The sample was then cooled down to 160 K and ramped up by 10 K steps (from yellow to green).

After this cooling/heating cycle under vacuum, the sample was cooled down to 160 K again, and dosed with 1.10 bar of xenon. And isobars were then characterized by increasing the temperature, at 10 K steps up to 400 K (Figure V-8). At low temperature, X-ray absorption likely accounts for weaker intensities of the diffraction peaks. Overall, the sample remains crystalline over the whole temperature range and the intensity of the diffraction peaks increases with increasing temperature, due to lower loading of Xe inside the structure. A nice gradual change in diffraction patterns can be observed during the whole ramping process, indicating that Xe is gradually leaving the structure. The fact that all peak intensities do not change in the same proportion

indicates that xenon occupy a pore within the MOF structure. Interestingly, at 400 K the initial diffraction pattern (i.e. the one of the MOF after activation) is obtained again, indicating that the structural transformations of the MOF under vacuum and under 1.10 bar Xe loading are completely different.

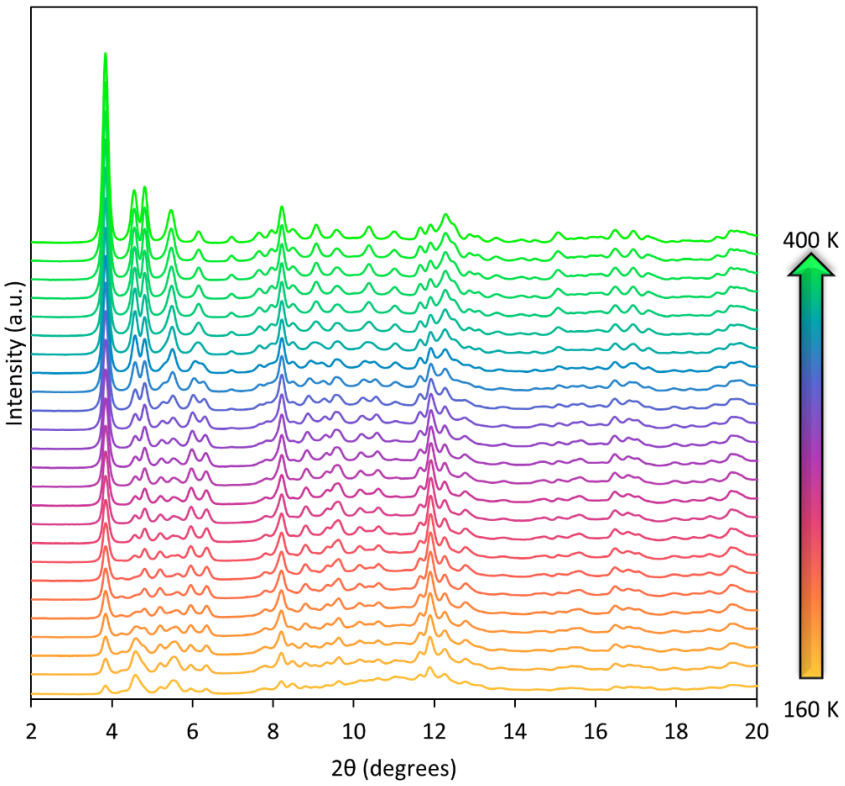

Figure V-8. Variable temperature PXRD patterns of MOF-76(La) under 1.10 bar of xenon, from 160K (yellow) to 400 K (green).

Furthermore, there is no clear shift of diffraction peaks during the desorption process under xenon, and differences are mainly due to variations in peaks intensities, indicating that the structure remains rigid and difference between patterns is only due to the presence of Xe within the pores. The data collected under vacuum and in Xe should be interpreted in terms of structural models, but this requires a substantial work we are still planning to do in the future.

6. Conclusions

A new synthetic route to RE MOF-76 MOFs in mild conditions in ethanol solution was developed. The synthesis is based on the good solubility of lanthanide chlorides and trimesic acid used as metal and linker sources, respectively, and avoids using toxic and environmentally unfriendly DMF as solvent. The synthesis leads to the formation of micro-sized sea urchin-like aggregates of needle-shaped crystals, the size of which can be controlled by the concentrations of the precursors and the reaction temperature, which can be as low as 45°C and still yield high quality materials. Ideal filterability of the materials is achieved only when the concentration of precursors is maintained below a certain limit.

The synthesis is easy to apply to different types of lanthanides, including La, Ce, Pr and Nd, as well as mixed-metal systems, allowing obtaining for example luminescent materials by including smaller ions like Eu or Tb. The nature of the used metal defines the MOF's formation rate, which increases with decreasing radius of the RE ion, and affects the size of the obtained aggregates. Furthermore, the obtained materials require lower activation temperatures than those obtained by conventional solvothermal syntheses in DMF. We also demonstrated that the procedure is easy to scale-up and that the solvent as well as the unreacted lanthanide precursor can be efficiently recycled. On the other side, the linker that is not converted to the MOF during the reaction is transformed into 3,5-bis(ethoxycarbonyl)benzoic acid that can also easily be recycled into trimesic acid for re-use.

The stability of the MOFs towards water has been assessed, showing increasing stability with decreasing RE radius and exceptional stability even upon prolonged heating in boiling water for MOF-76(Er) and MOF-76(Yb). We also showed that the water stability can efficiently be increased by adding amine functions to the linkers, as evidenced by the synthesis of water-stable MOF-76(La)-NH_2. Finally, we showed that MOF-76(La) undergoes an interesting structural

transition with temperature, and is able to adsorb xenon, as monitored by *in situ* XRPD.

CHAPTER VI

Synthesis, structure and thermal stability of a mesoporous titanium(III) amine containing MOF with improved hydrogen sorption properties

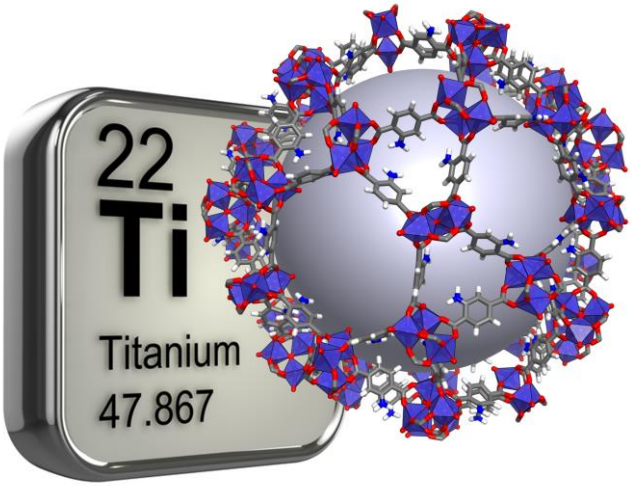

Chapter VI – Synthesis, structure and thermal stability of a mesoporous titanium(III) amine containing MOF with improved hydrogen sorption properties

1. Abstract

The first mesoporous bimetallic Ti^{III}/Al metal-organic framework (MOF) containing amine functionalities on its linkers has been selectively obtained by converting the cheap commercially available $(TiCl_3)_3AlCl_3$ into $Ti_{3-x}Al_xCl_3(THF)_3$ and reacting this complex with 2-aminoterephthalic acid in DMF under soft solvothermal conditions. This compound is structurally related to the previously described NH_2-MIL-101(M) (M = Cr, Al and Fe) MOFs. Thermal gravimetric analyses and *in situ* PXRD measurements demonstrated that this highly air-sensitive Ti^{III}-containing MOF is structurally stable up to 200°C. Nuclear magnetic resonance (NMR) spectroscopy, elemental and inductively-coupled plasma (ICP) analyses revealed that NH_2-MIL-101(Ti^{III}) contains trinuclear $Ti_3(\mu_3\text{-}O)Cl(DMF)_2(RCOO)_6$ clusters with strongly bound DMF molecules, and a small amount of aluminum. Sorption experiments reveal a higher affinity of this MOF for hydrogen compared to the previously described monometallic unfunctionalized MIL-101(Ti^{III}) MOF.

2. Introduction

Amidst the vast variety of existing MOFs, the ones with the so-called MTN topology are particularly interesting. The topology of those frameworks is derived from that of the zeolite Socony Mobil Thirthy-Nine (ZSM-39)[152] and consists of the assembly of two types of large interconnected mesopores that are accessible through hexagonal and pentagonal windows (Figure VI-1, A and B). The vast majority of those MOFs (although a few exceptions are known)[312] are built from trinuclear M_3-μ_3-oxo clusters bearing six carboxylate functions from the organic linkers and additional anions (F^-, OH^-, Cl^-, etc.) for charge

balancing when needed, together with solvent molecules to complete the coordination spheres of the metal centers (Figure VI-1, C). The linkers interconnect four metal cluster units to form microporous supertetrahedra of which they form either edges or faces, depending on whether they are ditopic or tritopic (i.e. linkers having two or three carboxylate functions),[313] respectively. The most representative members of this series of MOFs are MIL-101(M) and MIL-100(M), built respectively from terephthalate (BDC^{2-}) or trimesate (BTC^{3-}) linkers (Figure VI-1, D and E) and containing chromium,[147,314] iron[177,315] or aluminum[160,82,316] as metal centers. Several reports also mention the use of vanadium,[317,318] indium,[319] manganese,[320] scandium[321] or, more recently, titanium(IV) [322] or the combination of several metals (e.g. Ni^{2+}, Co^{2+}, Zn^{2+}, Ti^{4+} or even lanthanides)[186,187,281] for the construction of such frameworks.

Although titanium(IV) carboxylate-based MOFs are of interest because of the strong Ti-O bonds, they are also very difficult to form because of the strong Lewis acidity (and hence reactivity and oxophilicity) of Ti^{IV} complexes.[323,324] Titanium(IV)-based MOFs are formed by polynuclear clusters and low nuclearity is not easily achieved. Ti^{IV}_3-(μ_3-O) clusters were only reported for COK-69 and MIL-100(Ti), the former having tilted TiO_6 octahedra (the central μ_3-O is slightly above the plane defined by the three Ti atoms),[325] and the latter can be obtained only in very specific conditions that we were not able to reproduce in the lab despite many attempts.[185,326] Therefore, we decided to investigate new pathways towards the formation of Ti^{III}-based MOFs with the MTN topology (in the initial hope to transform them into Ti^{IV} MOFs upon controlled oxidation), as Ti^{III} is less reactive and more prone to form crystalline MOFs with low nuclearity clusters. Indeed, its reactivity is similar to that of Fe^{III}, and quite different from that of Al^{III}, so the formation of clusters is favored over the growth of chains.

However, there are very few reports of MTN MOFs containing titanium in the +III oxidation state,[33,327,328] or more generally reports

concerning the incorporation of Ti^{III} in metal-organic frameworks,[325,329,330] although Ti^{3+} open metal centers in other type of materials are known to be efficient sites for hydrogen sorption, catalysis or other applications.[331,332,333,334]

Mason et al. obtained the first Ti^{III}-based MOF, MIL-101(Ti^{III}) (Figure VI-1, C), in 2015 by using a solvothermal approach consisting of heating H_2BDC and $TiCl_3$ in a 10:1 mixture of DMF and ethanol.[33] The obtained purple solid was shown to be crystallographically pure MIL-101(Ti^{III}) having the chemical formula $Ti_3O(OEt)(BDC)_3(DMF)_2$, DMF being partly exchangeable by THF. This MOF was not only the first reported Ti^{III}-based one, but was also the first ever described compound containing carboxylate-bridged titanium-oxo clusters of the $Ti_3O(O_2CR)_6L_3$ type (Figure VI-1, A). Activation of MIL-101(Ti^{III}) by washing with THF followed by heating at 150°C allowed to remove coordinated solvent molecules from one out of three Ti centres, creating open-metal sites, whereas washing the MOF with methanol or ethanol instead of THF led to decomposition of the framework. Furthermore, the activated MOF showed high and irreversible reactivity with oxygen by forming peroxide and superoxide species, evidencing its particular sensitivity.

After this first investigation, the area of Ti^{III}-based MOFs remained largely unexplored, likely due to their air-sensitive nature. However, quite recently, Antonio et al. developed a procedure based on the *in-situ* generation of $TiCl_3$ as precursor for the synthesis of such compounds.[327] This procedure was first used to synthesize MIL-101(Ti^{III}), by electrochemically reducing $TiCl_4$, which is cheaper and available in higher purity grades than commercial $TiCl_3$. This was carried out in a mixture of DMF and ethanol in the presence of terephthalic acid and NBu_4PF_6 as electrolyte. The obtained solution with the freshly generated Ti^{3+} was then solvothermally treated at 120°C without any intermediate purification to yield the desired MOF. In their study, the authors also extended their synthetic approach to various other MOFs with the MTN topology having tritopic and extended linkers. In this

way, they were able to obtain MIL-100(Ti^{III}) (Figure VI-1, E), MIL-101(Ti^{III})-BPDC (Figure VI-1, F) and MIL-100(Ti^{III})-TATB (Figure VI-1, G) (BPDC = 4,4'-biphenyldicarboxylate; TATB = 4,4',4''-[1,3,5]triazine-2,4,6-triyl-tris-benzoate).

Interestingly, the MOFs obtained by this electrochemical-mediated approach were compared with products obtained solvothermally from commercial $TiCl_3$ in the absence of NBu_4PF_6. In addition to a higher crystallinity and porosity, X-ray photoelectron spectroscopy analysis indicated that the electrochemically obtained MOFs contain F^- as charge counterbalancing anions, whereas the solvothermally obtained ones seemed to contain Cl^-. This latter observation, based on results of a surface analysis, is in disagreement with the report of Mason et al.[33] who used a very similar procedure to obtain their MIL-101(Ti^{III}) with an ethoxide charge balancing anion. To the best of our knowledge, up to now, there have been no reports on Ti^{III}-MOFs that contain functionalities within their linkers. Adding such functionalities could not only have an important impact on the properties of the resulting MOFs for various applications in fields such as gas adsorption or catalysis,[265,335] but it could also open the door for further post-functionalization of the materials to modify their properties.[207,336,337] For those reasons, we have decided to focus on the development of NH_2-MIL-101(Ti^{III}) (Figure VI-1, H.), a derivative of MIL-101(Ti^{III}) with amine functions on its linkers.

The MOF described in this work contains a small amount of aluminum, from the titanium (III) precursor used for the synthesis, and is thus a bimetallic MOF. Interestingly, only one previous literature report concerns the synthesis of Ti-based bimetallic MOFs with the MTN (MIL-100 (Figure VI-1, E.) or PCN-333 topology (another name for MIL-100-TATB, Figure VI-1, G.)), containing scandium as a second metal.[184] However, the previously reported strategy relied on the exchange of the very expensive Sc^{3+} in the pre-synthesized monometallic Sc-based MOFs by Ti^{3+}. Our bimetallic

NH_2-MIL-101(Ti^{III}, Al) MOF is obtained by a much cheaper and facile, one-pot synthetic strategy.

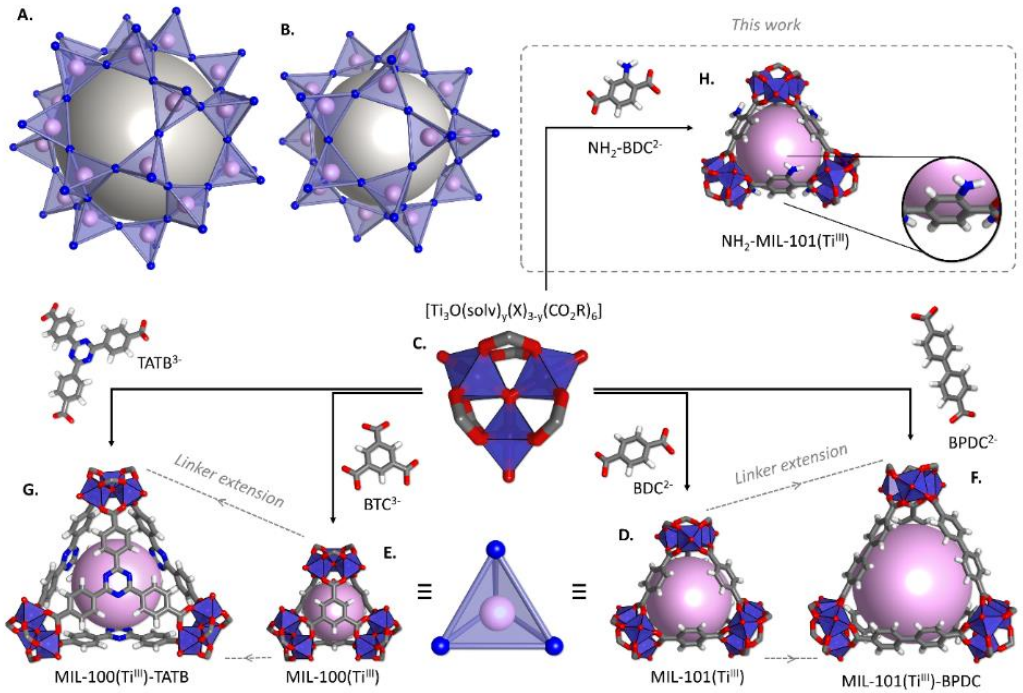

Figure VI-1. (**A.** and **B.**) Assembly of the supertetrahedra into large and small mesoporous cages forming MOFs with MTN topology. The structure of microporous supertetraedra in previously described Ti^{III}-based MOFs with MTN topology containing the (**C.**) $[Ti_3O(solv)_y(X)_{3-y}(CO_2R)_6]$ cluster based on (**D.**) BDC^{2-}, (**E.**) BTC^{3-} linkers or their extended versions, (**F.**) $BPDC^{2-}$ and (**G.**) $TATB^{3-}$. (**H.**) The supertetrahedron of the new MOF described in this work, NH_2-MIL-101(Ti^{III}) is represented in the inset, with an enlargement around the amine function. Color code: deep blue = Ti; red = O, grey = C; marine blue = N; white = H; large pink spheres = micropores formed by the supertetrahedra.

3. Materials and methods

Chemicals and syntheses

$(TiCl_3)_3AlCl_3$ (76.0-78.5% $TiCl_3$) and acetyl chloride (98 %) were purchased from Alfa Aesar. Dry toluene (99.85%, Extra dry, AcroSeal®), 4-bromoacetophenone (98 %), potassium pyrosulfate (98 %), *n*-BuLi (1.6 M in hexanes) and 2,4,6-trimethylaniline (97 %) were purchased from Acros Organics. Dry THF (≥ 99.9%, with 250 ppm BHT as inhibitor), aluminum chloride (99.9%) and 2-aminoterephthalic acid (99%) were purchased from Sigma Aldrich. DMF (HiPerSolv, CHROMANORM®), DCM (HiPerSolv, CHROMANORM®), sulfuric acid (96 %), chloroform (HiPerSolv, CHROMANORM®), concentrated hydrochloric acid (37 %), glacial acetic acid (ACS reagent grade), ethanol (technical grade) were purchased from VWR. The used acetone was of technical grade. Triethylamine (99.7 %) was purchased from Fisher Chemicals. $CDCl_3$, NaOD (40% w/w in D_2O, ≥ 99.00%) and D_2O were purchased from Eurisotop. Carbon dioxide (Alphagaz 1) was purchased from Air Liquide. Potassium permanganate crystals were purchased from J. T. Baker Chemicals N.V. (Holland).

Synthesis of $Ti_{3-x}Al_xCl_3(THF)_3$

$TiCl_3(THF)_3$ was synthesized from $(TiCl_3)_3AlCl_3$ according to a reported procedure.[338] In brief: in a glovebox, 20 g of $(TiCl_3)_3AlCl_3$ was loaded in a 250 mL custom-made Schlenk flask equipped with a glass-frit filter (see Fig. S VI-1) containing a magnetic stirring bar and the flask was closed with a rubber septum. Outside the glovebox, maintaining the flask under argon atmosphere (using a Schlenk line), 10 mL of dry toluene was added to the flask, which was subsequently cooled down to -63°C using a $CHCl_3$/liquid nitrogen mixture. 200 mL of dry THF was then added to the mixture, which was subsequently stirred at room temperature for one hour, allowing the formation of a pale blue solid. The product was then isolated by filtration under vacuum and the solid was washed several times with degassed (by argon bubbling) hexane and dried under vacuum to yield pale blue

crystalline $TiCl_3(THF)_3$. The analysis of the obtained solid by ICP-OES revealed some residual aluminum, the compound can be formulated as $Ti_{0.93}Al_{0.07}Cl_3(THF)_3$ (see supporting info).

Synthesis of NH_2-MIL-101 (Ti^{III}, Al)

A yellow solution containing 0.126 (or 0.63) g of 2-aminoterephthalic acid in 15 (or 75) mL of DMF was introduced in a 500 mL GL32 glass bottle equipped with a magnetic stirring bar. A B29/32 rubber septum from which the collar had been previously cut off (see Fig. S VI-2, A.) was then used to close the bottle and the solution was degassed by passing argon through it with the help of a long needle. Separately, a dark blue solution containing 0.556 (or 2.78) g of $Ti_{0.93}Al_{0.07}Cl_3(THF)_3$ (weighed in a glovebox, see preparation above) in 15 (or 75) mL of degassed (argon bubbling) DMF was prepared using Schlenk techniques. This Ti^{III}-containing solution was then added to the linker solution *via cannula* under stirring, yielding a dark blue solution. A heat resistant (180°C) screw cap with flat interior (see Fig. S VI-2, A.) was then fitted on the glass bottle to secure the rubber septum. The glass bottle was then introduced in a preheated oven at 130°C to allow crystallization of the MOF during 18h (without stirring). The solution was then allowed to cool down to room temperature and the septum was removed carefully (*Attention! Internal pressure is possible at this stage and the rubber septum might pop off the bottle! It is recommended to insert a needle into the septum just after removal of the screw cap in order to remove excess pressure*). The solution was then filtered over a nylon membrane under a continuous flux of argon (see experimental setup in Fig. S VI-2, B.), to separate the brown MOF from the dark blue solution. The product was then washed several times with degassed (by argon bubbling) DMF and acetone until a clear filtrate was obtained. Special care was taken at this stage to never allow the product to dry completely or passing air through it (oxidation by air resulting in a color change of the MOF from chocolate to yellow). After a final washing with acetone, the still slightly wet product (the solvent in the pores allows to exclude oxygen) was quickly transferred

to a round bottom flask with a large (B29/32) neck that was fitted to a glass stopcock and the product was then put under vacuum. This last step must be performed quickly as the product may not dry in the air, otherwise quick oxidation and degradation of the MOF occurs. The MOF was then dried under vacuum and heated at 130°C for about 10 min to give NH_2-MIL-101(Ti^{III}, Al) as a dark brown (chocolate) powder that can be stored in an argon-filled glovebox. *Alternatively, the filtration step might be performed in a dedicated glovebox, but as DMF dissolves most types of plastic (and can therefore cause damage to the transparent windows of gloveboxes) this is not recommended and is at the risk of the experimentalist.*

Activation of NH_2-MIL-101(Ti^{III}, Al) in boiling DCM

Inside an argon-filled glovebox, about 1 gram of as-synthesized NH_2-MIL-101(Ti^{III}, Al) was loaded in a large glass 100 mL test tube with a ground glass joint, together with a magnetic stirring bar. The glass tube was then closed with a rubber septum and removed from the glovebox. On a Schlenk line, about 40 mL of CH_2Cl_2 (DCM) degassed by Ar bubbling was added to the solid. The tube was immerged in a beaker containing hot water (~50 °C) and stirring was started. The DCM was allowed to boil during 5 to 10 min, after which the beaker with hot water was removed and stirring was stopped to allow decantation of the solid. The supernatant was then removed *via cannula*. Fresh degassed DCM was then added for a second washing. This procedure was repeated five times. After the fifth washing and removal of DCM, the product was dried under vacuum and then transferred to a glovebox for storage prior to further analyses.

Synthesis of MIL-101(Al)-NH_2

Crystallographically pure MIL-101(Al)-NH_2 was obtained through a slightly modified procedure taken from the literature.[339] In brief, a solution of 0.63 g 2-aminoterephthalic acid in 75 mL of DMF was heated to 130°C in a 500 mL round-bottom flask equipped with a magnetic stirrer. Then, a clear solution containing 1.81 g of previously dissolved aluminum chloride hexahydrate in 75 mL of DMF (slow

dissolution) was added dropwise with the help of an addition funnel over a period of one hour. The mixture was then stirred further at 130°C for 14h. The yellow precipitate was recovered through centrifugation and washed several times with DMF and acetone until a clear supernatant was obtained. The MOF was recovered as a yellow powder upon drying in a vacuum oven at 60°C for about 1 hour. To avoid any degradation from moisture, the MOF was stored in an argon-filled glovebox.

Synthesis of complementary linkers

1,3,5-tris(carboxyphenyl)benzene was synthesized according to a previously described procedure.[340] In brief, 3.04 g of 4-bromoacetophenone and 4.09 g of potassium pyrosulfate were finely ground with a mortar and pestle and were subsequently introduced in a 100 mL round-bottom flask equipped with a magnetic stirring bar. 0.2 mL of concentrated sulfuric acid (96 %) was then added dropwise under stirring. The reaction mixture was heated at 180 °C during 16 h using an oil bath. After cooling down the reaction mixture to room temperature, 25 mL of ethanol was added and the mixture refluxed for two hours. The solid was then filtered off and washed two times with ethanol. The solid was subsequently introduced in a 100 mL round bottom flask, and refluxed in water for one hour, followed by filtration and two washings with water. The product was finally recrystallized in chloroform to yield the 1,3,5-tris(4-carboxyphenyl)benzene intermediate. 0.84 of the obtained 1,3,5-tris(4-carboxyphenyl)benzene were then introduced in a dry three-neck flask equipped with an entrance and exit for CO_2 and a rubber septum. 100 mL of dry THF were added to the reaction medium, which was cooled down to -78 °C (acetone/dry ice bath) under stirring. 2.35 mL of a 1.6 M solution of *n*-BuLi in hexanes were then added dropwise through the rubber septum and reacted further for 5 minutes. Gaseous CO_2 was then bubbled through the reaction medium to precipitate the product and the reaction was quenched by addition of 20 mL of a 50/50 mixture of acetic acid and water. Concentrated (37 %) hydrochloric acid was added slowly

until no more product precipitated. The obtained powder was recrystallized in hot acetic acid and dried at 120 °C under vacuum. The final linker was obtained in 50 % yield. ^{1}H-NMR ($CDCl_3$, 300 MHz, δ): 7.69 ppm, s, 3H; 7.63-7.52 ppm, m, 12 H.

N-mesitylacetamide was obtained through a previously described procedure.[307] In brief, 10.5 ml of 2,4,6-trimethylaniline were introduced under argon in a flame-dried 500 ml round-bottom flask equipped with a Teflon stir bar and a rubber septum. 100 ml CH_2Cl_2 was added to the flask and the mixture was cooled down to 0°C (ice bath). 5.6 ml acetyl chloride was added dropwise by syringe, followed by 11 ml triethylamine. After 2 h of reaction, the mixture was filtered. The solid was then suspended in water and stirred for 30 min. The solid was then collected by filtration and was dried under vacuum. *2-aminobenzene-1,3,5-tricarboxylic acid* (2-aminotrimesic acid, H_3BTCNH_2) was also obtained through a previously described procedure.[307] In brief, 5 g of the obtained *N*-mesitylacetamide and 165 ml of water were introduced in a 500 ml round bottom flask, followed by the portion wise addition of 0.55 g sodium hydroxide. Then, 34 g of $KMnO_4$ were added in portions (~5 portions) over ~2 h under vigorous stirring. The flask was then equipped with a condenser and the solution was heated under stirring at 85°C for 72 h. The reaction mixture was then filtered through filter paper and the MnO_2 was rinsed with ~200 ml of hot water. The obtained filtrate was acidified with 40 ml of HCl and the mixture was refluxed overnight (100°C). The obtained white solid was then filtered and rinsed with ice-cold water. ^{1}H NMR ($CDCl_3$, 300 MHz, δ): 6.93 ppm, s, 2H; 2.29 ppm, s, 3H; 2.25 ppm, s, 6H; 1.73 ppm, s, 3H.

Analytical

Inductively-coupled plasma optical emission spectroscopy (ICP-OES) and chlorine analyses (Schöniger flask method) were performed by Medac Ltd.

PXRD patterns were measured in glass capillaries (0.7 mm diameter, Hilgenberg GmbH) that were filled with the samples in a glovebox and sealed with grease. Before analysis, the capillaries were

cut and instantly placed into molten wax on goniometric heads and the measurements were performed immediately after preparation to avoid air from entering. The analysis was performed using a MAR345 image plate detector and an Incoatec Microfocus Source^{HIGHBRILLIANCE} (IμS^{HIGHBRILLIANCE}) Mo ELM47 operating at 50 kV and 1000 μA. The samples were exposed to X-rays for 5 minutes during which the capillary with the sample was rotated by 180°. Diffraction data was integrated by the Fit2D software (using data from a 0.1 mm diameter capillary filled with LaB_6 as calibrant). Variable-temperature PXRD (VT-PXRD) was performed by heating the sample-containing capillary with a Leister LE MINI SENSOR KIT hot air blower (Leister Technologies Benelux B.V.). The air blower was calibrated by a thermocouple housed in a capillary; the determined error on sample temperature is ±5°C. Alternatively, PXRD measurements were collected on a STOE STADI P Combi diffractometer using $CuK_{\alpha 1}$ radiation (40 kV, 40 mA) (graphite primary monochromator). The diffracted beam was recorded on a DECTRIS MYTHEN 1K strip detector. Samples were loaded in 0.7 mm diameter capillaries, aligned to the geometric center of the diffractometer and measured in transmission, with independent 2-theta movement.

FTIR spectra were measured with a Bruker Alpha spectrometer equipped with a Platinum ATR sample holder (diamond crystal, single bounce) housed in an argon-filled glovebox.

Nitrogen physisorption measurements were performed on an ASAP2020 device from Micromeritics at 77 K. The sample tube was filled inside a glovebox to avoid degradation.

TGA measurements were performed using a Netszch STA 449 F3 TGA/DSC equipped with a stainless steel oven hosted in an argon-filled glovebox. Conventional TGA was run with a heating speed of 10 K/min under argon atmosphere until 500°C, followed by air/argon (reactive/protective gas) from 500°C to 900°C.

^{1}H-NMR spectra were recorded at room temperature (296 K) on a Bruker Avance 500 spectrometer operating at 500.13 MHz using a

BBFO {^{1}H, X} probehead equipped with a *z*-gradient coil. The measurements were performed using the standard Bruker zg pulse program. Acquisition time was fixed to 1.6 s, number of scans to 16 and relaxation delay was 30 s. About 5 mg of activated MOF were weighed in a glovebox and introduced in a 4 mL screw-capped vial. Outside the glovebox, 0.2 mL of concentrated NaOD was added to the sample, followed by 1.0 mL of D_2O (allowing air to enter the vial to oxidize the paramagnetic Ti^{III} to Ti^{IV}). The suspension was then shaken, heated with a heat gun and sonicated until a white suspension, formed by dissolved organic species and sodium salts together with solid titanium oxides/hydroxides, was obtained. The suspension was filtered using a PTFE syringe filter (0.45 µm) to obtain a clear solution. 0.6 mL of the obtained solution was used for NMR determination. Reference solutions of "digested" formic acid and DMF (spectra not shown) were obtained by the same procedure.

Hydrogen sorption isotherms were measured on a Micromeritics ASAP2020 device, according to Application Note 136 of the manufacturer (www.micromeritics.com). A degassing temperature different from that in the application note (100°C instead of 300°C) was used to avoid sample degradation. Measurements were performed at 77 K in the pressure range between 0 and 620 mbar with Alphagaz 1 grade hydrogen from Air Liquide.

4. Results and Discussion

4.1. Synthesis of NH_2-MIL-101(Ti^{III}) and attempts with other linkers

Most Ti^{III} complexes are quite expensive precursors and therefore unsuitable for synthesizing large amounts of Ti^{III}-based MOFs. Therefore, the cheap commercially available $(TiCl_3)_3AlCl_3$ was investigated as metal source for synthesizing Ti^{III}-containing NH_2-MIL-101(M) MOFs (M = Ti and/or Al). The synthesis was performed by making two solutions of each of the precursors (metal and linker) in DMF as only solvent, which easily dissolves all the reactants.

Those were then mixed together under argon and the resulting solution was subsequently heated in a closed glass vial at 130°C, well below the boiling point of DMF. Care was taken to do so by excluding air from entering (see experimental part and Fig. S VI-2), as Ti^{III} easily oxidizes. Unfortunately, attempts when directly using the bimetallic $(TiCl_3)_3AlCl_3$ precursor resulted in a very fine powder that was unrecoverable through filtration, and readily oxidized in air. In the same reaction conditions, using pure $AlCl_3$, we obtained an amorphous material, as revealed by powder X-ray diffraction (PXRD) (not shown), that could only be isolated by centrifugation. As we expected that Al was responsible of the small particle size obtained when using $(TiCl_3)_3AlCl_3$, we reacted this bimetallic precursor with THF to form a light blue solid, likely $TiCl_3(THF)_3$, which is insoluble in alkanes, allowing to easily eliminate the soluble $AlCl_3$ through simple filtration, according to [338]. Although the obtained $TiCl_3(THF)_3$ still contained some residual aluminum, as determined by ICP analysis (the obtained complex was determined as being $Ti_{0.93}Al_{0.07}Cl_3(THF)_3$, see Table S VI-3), we were able to obtain crystallographically pure Ti^{III}-containing NH_2-MIL-101 from this precursor (Fig. S VI-3 and Figure VI-2). We performed this successful synthesis twice, in a reproducible manner. The product's crystal structure has been assessed by PXRD, showing that it is isostructural to other MIL-101 MOFs (Figure VI-3 and Fig. S VI-3), and its infrared spectrum showed the characteristic features of NH_2-MIL-101 frameworks, as well as the absence of reactants in the obtained MOF (Fig. S VI-4). ICP-OES analysis (Table S VI-6) revealed that the obtained MOF is bimetallic in nature, having a Ti/Al ratio of 85/15, which indicates that Al is preferentially incorporated in the framework compared to Ti^{III}, as the precursor contains a 93/7 Ti/Al ratio. This is in accordance with the fact that the filtrate after synthesis was blue in color, indicating that some Ti^{III} used for the synthesis was not incorporated in the MOF. The obtained MOF is thus named NH_2-MIL-101(Ti^{III}, Al) further in this work.

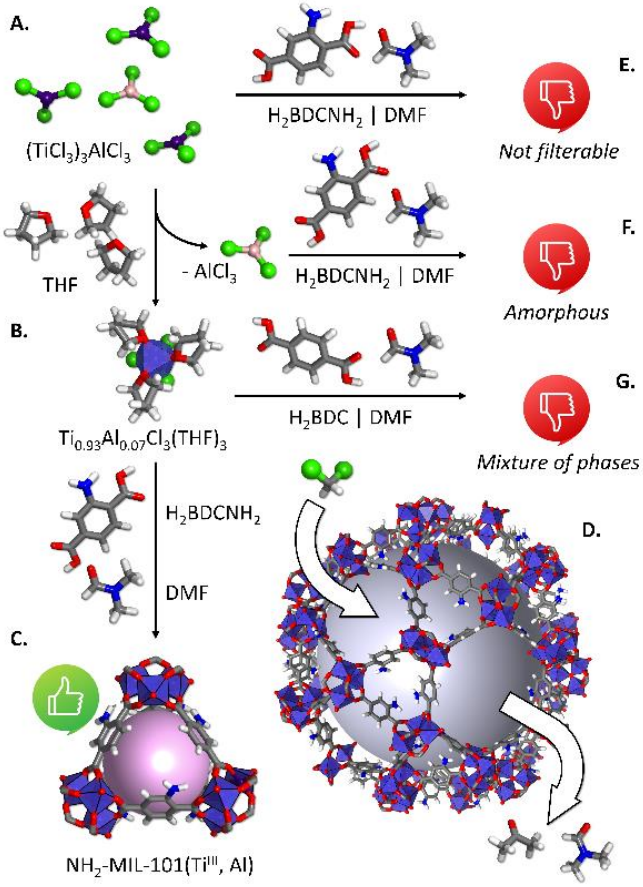

Figure VI-2. Conversion of (**A.**) $(TiCl_3)_3AlCl_3$ into (**B.**) $Ti_{0.93}Al_{0.07}Cl_3(THF)_3$ complex and its reaction with 4-aminoterephthalic acid in DMF at 130°C to yield (**C.**) NH_2-MIL-101(Ti^{III}, Al), from which (**D.**) physisorbed DMF and acetone was exchanged for DCM. Attempts to obtain similar MOFs in DMF at 130°C by either engaging (**E.**) $(TiCl_3)_3AlCl_3$ or (**F.**) $AlCl_3$ as metal sources or (**G.**) non-functionalized terephthalic acid as linker source did not yield the desired material.

It is noteworthy that using terephthalic acid instead of 4-aminoterephthalic acid as linker source resulted in a mixture of crystalline phases including MIL-101(Ti^{III}) (Fig. S VI-5), evidencing that the presence of an amine function is essential for selectively obtaining the desired topology under the used conditions. Interestingly, one of the phases in this latter attempt seems isostructural to MOF-235 (Fig. S VI-5, A.), which has been reported only with a limited number

of metals, including Fe [341] and Al for which it has been described only with an amine function on the linker.[54] In addition, the way of performing the mixing is of importance for the outcome of the reaction. This was demonstrated in the case of the reaction with $AlCl_3$ as precursor, for which pure NH_2-MIL-101(Al) could be obtained by slowly adding a solution of 4-aminoterephthalic acid to a *preheated* solution of $AlCl_3$ (Fig. S VI-6), but not by heating a cold solution of both reactants. This is intrinsically linked to the formation mechanism of NH_2-MIL-101(Al), which is discussed in one of our review articles.[342] The slow addition of the aluminum chloride solution to the preheated solvent mixture, which is a small but important modification compared to the previously described syntheses, even allowed obtaining an NH_2-MIL-101(Al) MOF with the highest surface area yet described for this MOF (S_{BET} = 3440 m^2/g, Table VI-1 and Table S VI-2). Amorphous materials were also obtained when using tritopic linker precursors such as trimesic acid (H_3BTC) or 1,3,5-tris(carboxyphenyl)benzene (H_3BTB), or in the presence of water (Fig. S VI-5, B. and C.). Interestingly, the use of 2-aminotrimesic acid (H_3BTCNH_2) as trimeric linker allowed obtaining a MOF with the MTN topology (MIL-100), although the important broadening of the peaks in the PXRD pattern could indicate the presence of a large number of defects or small crystallites (Fig. S VI-5, D.). This last synthesis further indicates that the presence of an amine function seems to facilitate the synthesis of MOFs with the MTN topology using $TiCl_3(THF)_3$ as precursor. However, owing to the difficulty of analyzing defects,[243] this last MOF has not been analyzed further, due to the extreme sensitivity of the product towards air. All the tested synthetic parameters and outcome of the reactions are given in Table S VI-1.

4.2. Thermal stability and porosity

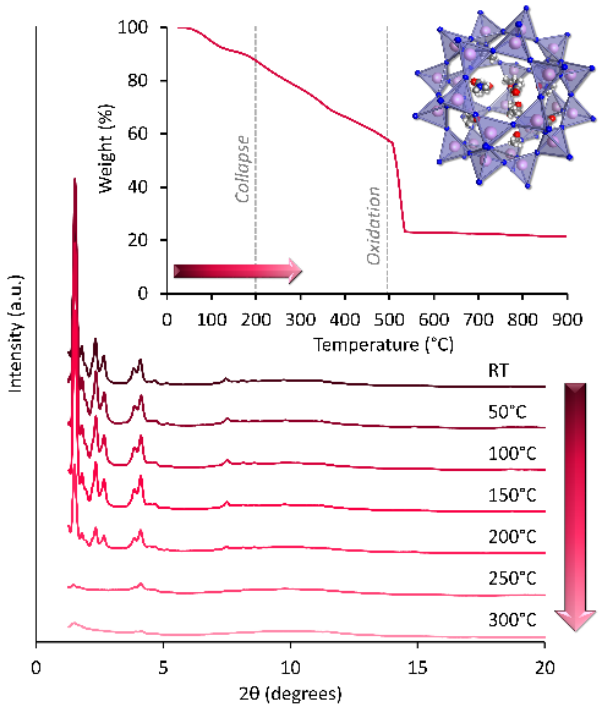

Figure VI-3. Variable-temperature PXRD patterns and (insets) thermal gravimetric analysis of as-synthesized NH_2-MIL-101(Ti^{III}, Al). TGA was recorded with a heating speed of 10 $K.min^{-1}$ under argon until 500°C, followed by oxidation under air from 500°C to 900°C (indicated by the "*Oxidation*" dashed line on the TGA curves). The scheme shows the large mesopore of the MOF with acetone and DMF molecules.

The thermal stability of NH_2-MIL-101(Ti^{III}, Al) was evaluated by means of thermogravimetric analysis by heating the sample at 10 $K.min^{-1}$ under argon from room temperature to 500°C, and under air from 500°C to 900°C to be able to calculate theoretical weight losses after calcination. PXRD analysis of the oxidation product was performed to confirm that TiO_2, as a mixture of essentially rutile with small amounts of anatase (see Fig. S VI-7) was the final combustion residue, together with some Al_2O_3, which is not visible on the PXRD pattern either because of the small proportion or tiny crystallite size in the combustion residue or because it is obtained as an amorphous phase

or due to the microabsorption effect. The theoretical TiO_2/Al_2O_3 ratio should be 92/8, according to the ICP-determined proportion of both metals in the MOF (Ti/Al = 2.54/0.46, see Table S VI-6). The TGA results (Figure VI-3 A., inset) highlight a constant weight loss over the complete temperature range under argon with no well-defined plateau, indicating that removal of solvents is overlapping with framework decomposition.

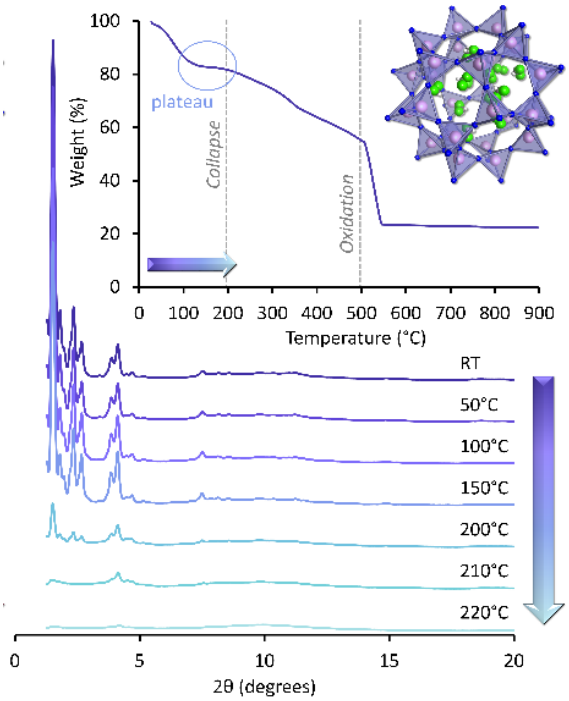

5.

Figure VI-4. Variable-temperature PXRD patterns and (insets) thermal gravimetric analysis of DCM-exchanged NH_2-MIL-101(Ti^{III}, Al). TGA was recorded with a heating speed of 10 $K.min^{-1}$ under argon until 500°C, followed by oxidation under air from 500°C to 900°C (indicated by the "*Oxidation*" dashed line on the TGA curves). The scheme show the large mesopore of the MOF with DCM molecules.

The MOF's decomposition temperature was therefore determined by *in situ* variable-temperature PXRD (VT-PXRD). From those experiments (Figure VI-3, A.), it appeared that the framework remains stable at least up to 150°C, after which decomposition occurs, as shown by the

intensity decrease of diffraction peaks from 200°C, to yield an amorphous compound at higher temperatures. This quite low observed thermal stability, compared to that of some other NH_2-MIL-101(M) MOFs (see Table VI-1) could be due to the removal of residual solvents with high surface tension (i.e. residual DMF from the synthesis), which causes the framework to collapse. To remove any remaining DMF from the pores, the as-synthesized MOF was activated by refluxing five times in degassed boiling dichloromethane (DCM) (see experimental part), which is a solvent having a low surface tension.[3] FTIR indicated that this procedure enabled successful exchange of the solvent molecules (Fig. S VI-4). VT-PXRD was then performed on the DCM-activated MOF to evaluate changes in thermal stability (Figure VI-3, B.). However, the overall stability remained unchanged, as diffraction peaks started to vanish away at 200°C, yielding an amorphous material at 210°C. The observed thermal stability is lower than those previously observed for this type of materials with other metals (Table VI-1), but is higher than the one of NH_2-MIL-101(Al), that we determined experimentally to be around 150°C through VT-PXRD (Fig. S VI-6). It should be noted that for NH_2-MIL-101(Al) this decomposition temperature is much lower than 370-500°C that has been reported even in most recent literature (see Table VI-1) but whose determination was based on TGA data only. This indicates that TGA might overestimate the structural thermal stability of this type of MOFs, as this analysis only reflects the temperature at which the linker combustion occurs.[82,343] Noteworthy, in both cases (as-synthesized and DCM-activated MOF), the color of the powder changed from chocolate to caramel after framework decomposition. The main change on the TGA curve of the DCM-activated MOF compared to the as-synthesized material is reflected by the plateau after solvent removal around 150°C, indicating facilitated solvent removal from this sample and the stability of the sample with emptied pores until 200°C. Furthermore, the intensities of the diffraction peaks of the activated material (Figure VI-3 and Fig. S VI-8) are higher than for the as-synthesized one, indicating

better crystallinity. Therefore, the DCM-activated sample was used for further experiments.

Table VI-1. Decomposition temperatures and surface areas of various reported MIL-101(M) and NH_2-MIL-101(M) MOFs, together with those of NH_2-MIL-101(Ti^{III}, Al) described in this work.

MOF	Decomposition temperature (°C)		Surface area ($m^2 \cdot g^{-1}$)		Reference
	TGA	VT-PXRD	BET	Langmuir	
MIL-101(Cr)	n/a	n/a	2800-4230	n/a	[314]
	~350	n/a	2134	n/a	[344]
NH_2-MIL-101(Cr)	250	n/a	2070	n/a	[345]
MIL-101(Fe)	n/a	n/a	2123	n/a	[346]
	n/a	n/a	1420	n/a	[347]
NH_2-MIL-101(Fe)	n/a	n/a	2572	n/a	[346]
MIL-101(V)	300	n/a	3600	5700	[318]
MIL-101(Sc)	450	n/a	155-640	n/a	[348]
NH_2-MIL-101(Sc)	300*	n/a	n/a*	n/a*	[347]
NH_2-MIL-101(Al)	n/a	~150	3440	4799	*This work*
	n/a	n/a	2074	n/a	[346]
	> 377	n/a	2100	n/a	[82]
	> 500	n/a	2530	n/a	[343]
MIL-101(Ti^{III})	n/a	n/a	2970	3890-4440	[33]
	n/a	n/a	3285	4360	[327]
NH_2-MIL-101(Ti^{III}, Al)	n/a	200	2024-2146	2792-2966	*This work*

* Cannot be activated, structural transformation to NH_2-MIL-88(Sc) upon heating.

The accessible surface area of NH_2-MIL-101(Ti^{III}, Al) was probed by nitrogen physisorption at 77 K after activation of the sample under vacuum at 100°C and 150°C (Fig. S VI-9). During thermal activation at those two temperatures, the sample lost 26.0 % and 28.8 % of its

initial weight, respectively (for calculations, see Table S VI-4). The results show that thermal activation at 100°C led to a BET surface area of 2024 $m^2.g^{-1}$ ($S_{Langmuir}$: 2792 $m^2.g^{-1}$) whereas increasing the activation temperature to 150°C increased the BET surface area to 2146 $m^2.g^{-1}$ ($S_{Langmuir}$: 2966 $m^2.g^{-1}$). The determined specific surface areas are in a similar range as those previously reported for similar MOFs based on other metals (Table VI-1). FTIR analysis performed on the samples after nitrogen physisorption shows that the activation procedure efficiently removed DCM from the MOF's pores (Fig. S VI-4).

5.1. Determination of cluster structure

To determine the presence of organic species coordinating to the metal clusters of the thermally activated MOF, some amount of sample was digested in a $NaOD/D_2O$ mixture and the obtained solution analyzed by ^{1}H-NMR. The spectra (Fig. S VI-10) showed the characteristic signals of the aromatic protons of 2-aminoterephthalate (7.3, 6.9 and 6.8 ppm), together with two singlets at 8.1 ppm and 1.9 ppm. Those singlets are attributed to sodium formate and dimethylamine, which are both products of the hydrolysis of DMF in NaOD.[349] Since the integration of both signals gives a ratio close to 6 ($NH(C\mathbf{H}_3)_2/\mathbf{H}COO^-$), it was deduced that those signals originated from DMF present inside the framework prior to digestion. It should be noted that the ratio of both integrals is always slightly inferior to 6, which can be explained by the high volatility of dimethylamine. Quantification based on the integration of those signals, and especially the one of the non-volatile sodium formate, compared to the signal of the 2-aminoterephthalate linker allowed to determine that after activation slightly less than two molecules of DMF were present per trinuclear cluster (Table S VI-5). Those results indicate very strong affinity between the DMF molecules used for the synthesis and the titanium metal centers. However, as the number of DMF molecules per cluster determined by ^{1}H-NMR seemed to decrease when the MOF was activated at 150°C (1.4 DMF/cluster) instead of 100°C (1.7 DMF/cluster), it seems that thermal activation can at least remove some

of the coordinated solvent, leading to the formation of coordinatively unsaturated metal centers (Figure VI-5, B.).

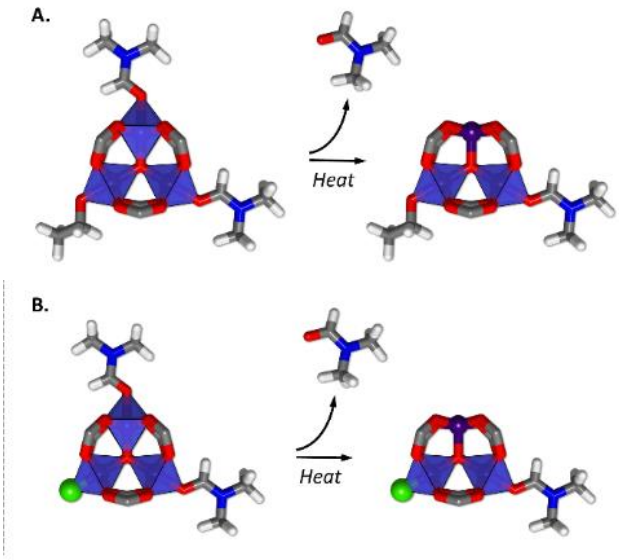

Figure VI-5. (**A.**) Structure of $Ti_3O(EtO)(DMF)_2(COOR)_6$ cluster composing MIL-101(Ti^{III}) and activation mechanism as proposed by Mason et al. (part of the DMF can be replaced by THF).[33] (**B.**) Structure of $Ti_3OCl(DMF)_2(COOR)_6$ cluster of NH_2-MIL-101(Ti^{III}) obtained in this work and its activation. Color code: deep blue = Ti; red = O, grey = C; marine blue = N; white = H; green = Cl.

As no other species were detected by ^{1}H-NMR, we excluded the presence of organic anions balancing the residual positive charge of the clusters. Based on the results of ^{1}H-NMR, ICP analysis and Cl analysis by the Schöniger flask method (Table S VI-6), we concluded that the composition of the activated MOF is $Ti_{2.54}Al_{0.46}OCl(DMF)_{1.7}(BDCNH_2)_3$. The charge balancing anion on the clusters is thus chloride, unlike for the MIL-101(Ti^{III}) MOF obtained by Mason et al., in which an ethoxide anion ensures the neutrality of the clusters (Figure VI-5, A.), that can be explained by the absence of ethanol in the reaction medium for our synthesis.[33] Given the significant amount of Ti^{III} compared to Al in the framework, it is reasonable to assume that some of the clusters composing the MOF are monometallic

and of the $Ti_3O(Cl)(DMF)_2(COOR)_6$ type (Figure VI-5, B.), whereas some clusters are of the $Ti_2AlO(Cl)(DMF)_2(COOR)_6$ type. However, it should be noted that the presence of clusters with a higher number of aluminum atoms (i.e. $TiAl_2O$, or Al_3O) in the framework cannot be excluded based on the available data. The verification of this hypothesis requires highly specialized techniques, and would be very challenging due to the complex structure, high sensitivity of the MOF towards air, and the paramagnetic nature of Ti^{III}, and is therefore outside the scope of this work.

Thermogravimetric analysis of the sample after nitrogen physisorption analysis (Fig. S VI-11) was performed to further confirm the above conclusions. Based on the determined structure, a weight loss of 73.1% is expected upon transformation of the framework into TiO_2 and Al_2O_3. The experimental weight loss of the activated MOF after combustion is very close to the theoretical value and thus confirms our findings. Furthermore, the slightly higher weight loss on combustion for the DCM-washed sample activated at 100°C (73.11%) compared to the same sample activated at 150°C (72.68%) further indicates that higher activation temperatures allow for an increased removal of the coordinated DMF.

5.2. Hydrogen sorption

The hydrogen sorption isotherm of NH_2-MIL-101(Ti^{III}, Al) at 77 K was recorded after activation at 100°C. Interestingly, the uptake is quite steep at low pressures, especially when compared to H_2 sorption in MIL-101(Ti^{III}) as previously described by Mason et al.[33] This steep uptake might be indicative of interaction between the coordinatively unsaturated Ti^{III} centers of the MOF and hydrogen, likely through interaction of the Kubas type.[350] Remarkably, when normalized to the surface area, the uptake capacity of NH_2-MIL-101(Ti^{III}, Al) is nearly twice as high as for MIL-101(Ti^{III}), which further confirms that stronger interactions exist for this bimetallic amine-containing MOF. This is particularly interesting as normally the hydrogen uptake in porous

materials is mainly dependent on the surface area, according to Chahine's rule.[351]

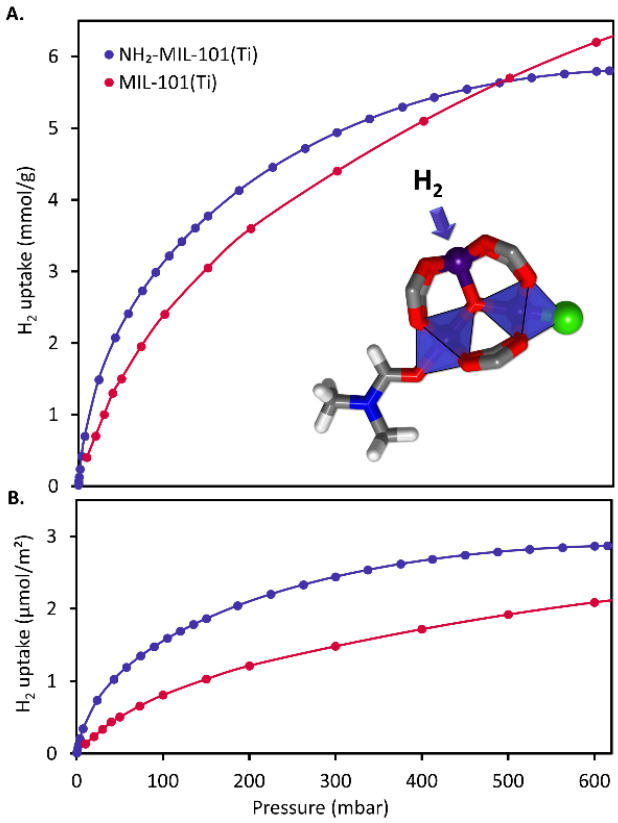

Figure VI-6. Hydrogen adsorption isotherms (77 K) of MIL-101(Ti^{III}) reported by Mason et al.[33] (S_{BET} = 2970 m²/g) and NH_2-MIL-101(Ti^{III}, Al) from this work (2024 m²/g), expressed in (**A.**) mmol H_2/g and (**B.**) relative to the BET surface area (µmol/m²). The inset shows the Ti^{III} open-metal site on which H_2 is likely to interact.

This improved adsorption performance might indicate that tuning the nature of the functionalities on the MOF's linkers might be an effective way of tuning the hydrogen sorption properties of Ti^{III}-based MOFs, in a similar way as to previous observations made for various MOFs based on other metals.[352] The gravimetric hydrogen sorption at 0.6 bar is of approximately 1.1 wt %. This is in the same order of magnitude than the previously reported values for MIL-101(Cr), for which high-

pressure isotherms were reported, with the advantage that Ti does not present the same toxicity concerns as Cr.[353]

6. Conclusions

We developed a synthesis strategy for obtaining bimetallic NH_2-MIL-101(Ti^{III}, Al) in a reproducible manner, by reacting $Ti_{0.93}Al_{0.07}Cl_3(THF)_3$ with 4-aminoterephthalic acid in DMF at 130°C, through a direct one pot synthesis strategy. All other reaction conditions screened with changes in used linkers or metals sources all yielded amorphous materials or structures that did not correspond to the MTN topology, or to low crystallinity materials. The thermal stability of this air sensitive MOF was determined to be around 200°C by means of thermogravimetric analysis and variable temperature PXRD. ^{1}H-NMR and chloride determination by the Schöniger flask method revealed that the new MOF is composed of clusters having a Cl^- charge neutralizing anion, of the $Ti_3OCl(DMF)_2(O_2CR)_6$ type, from which less than one DMF molecule can be thermally removed to create Ti^{III} open metal sites. Surprisingly, the obtained NH_2-MIL-101(Ti^{III}, Al) has better affinity for hydrogen than the previously described MIL-101(Ti^{III}) material, indicating that linker functionalization can have a positive impact on the H_2 sorption properties of Ti^{III}-based MOFs. We anticipate that the properties of Ti^{III}-containing NH_2-MIL-101(Ti^{III}, Al) could further be modulated through linker post-synthetic modification through amine chemistry, similarly to previous work on NH_2-MIL-101(M) structures based on other metals, or by varying the nature and amount of the second metal. For example, the amount of Al could be increased to render the MOF less prone to degradation in the presence of oxygen.

CHAPTER VII

Mechanochemical defect engineering of HKUST-1 and impact of the resulting defects on carbon dioxide sorption and catalytic cyclopropanation

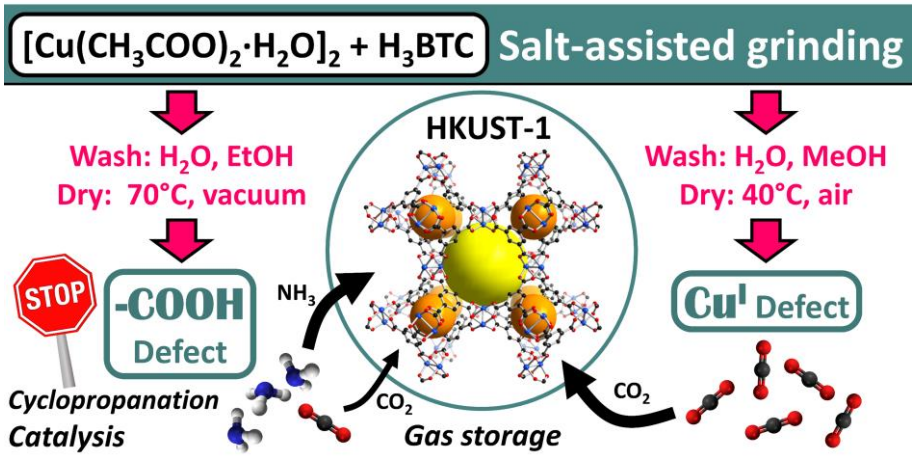

This Chapter is inspired by the following publication:

Steenhaut, T.; Grégoire, N.; Barozzino-Consiglio, G.; Filinchuk Y.; Hermans, S. *Mechanochemical defect engineering of HKUST-1 and impact of the resulting defects on carbon dioxide sorption and catalytic cyclopropanation*, RSC Advances., **2020**, *10*, 34, 19822-19831, doi: 10.1039/c9ra10412g.

Chapter VII - Mechanochemical defect engineering of HKUST-1 and impact of the resulting defects on carbon dioxide sorption and catalytic cyclopropanation

1. Introduction

In this chapter, we focus on the introduction of defects in one of the most studied MOFs, namely HKUST-1.[124] This material is based on copper(II) paddlewheel units that are connected together by the benzene-1,3,5-tricarboxylate ligand (BTC^{3-}), which is the deprotonated form of trimesic acid (H_3BTC) (Figure VII-1).[354]

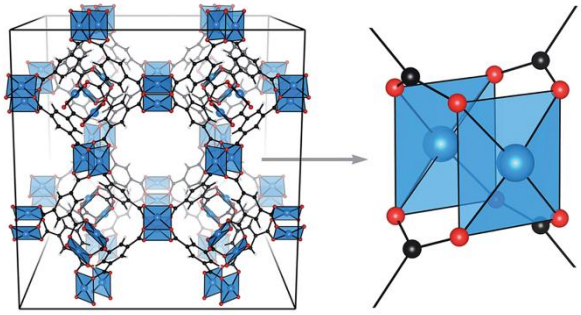

Figure VII-1. 3D structural model of HKUST-1 (left) and zoom on Cu-Cu paddlewheel unit (right). Copper atoms are depicted in blue, oxygen in red and carbon in black. Reproduced from Ref. 354 with permission from the Royal Society of Chemistry.

Being one of the most popular MOFs covered in the literature over the past few years, HKUST-1 has been extensively studied and some aspects dealing with defects inside its structure, either formed during the synthesis or upon exposure to moisture[355] or solvents, have already been addressed. For example, the formation of defects in solvothermally obtained HKUST-1 by adding isophthalate as defective linker was studied by Zhang *et al.*[356] Investigation through microscopic techniques were also performed to identify and localize inherent defect

sites in this MOF.[357,358] Strategies to overcome and reconstruct structural defects in HKUST-1 were also described.[359,44,360]

In this work, we aim at introducing defects into the structure of HKUST-1 without addition of defective linkers, but by modifying the synthesis conditions (Figure VII-2). The defects will be characterized and their impact on the gas sorption and catalytic properties of the material evaluated. For this purpose, we used recently developed mechanochemical synthesis strategies, namely liquid-assisted grinding (LAG) using a small amount of ethanol[361 and] salt-assisted grinding (SAG).[362] Mechanochemical synthesis of MOFs gives high yields of material and is therefore considered as a possible production method at industrial scale.[363] The latter technique, SAG, was recently shown to be a convenient way to introduce mesoporosity into HKUST-1, leading to hierarchized solids. This approach consists in milling the precursors of the MOF, namely copper (II) acetate monohydrate and trimesic acid, in the presence of a given amount of salt, giving rise to the inclusion of very small salt particles, which are removable from the MOFs by simple washing. We used post-synthetic treatment procedures different from those described earlier.[362] Our procedures consist in treating the MOFs with alcohols, which did not yield hierarchized porosity but allowed us to introduce in a controllable manner two types of structural defects. We determined the nature of these defects to be free carboxylic acid groups of the partially protonated ligand and reduced copper (I) sites, respectively. We systematically evaluated the carbon dioxide sorption properties of the materials to determine the influence of the defects on the interaction with this gas. We also tested all the obtained MOFs in the cyclopropanation of styrene with ethyl diazoacetate, as it was previously shown that HKUST-1 is able to efficiently catalyse this reaction.[364]

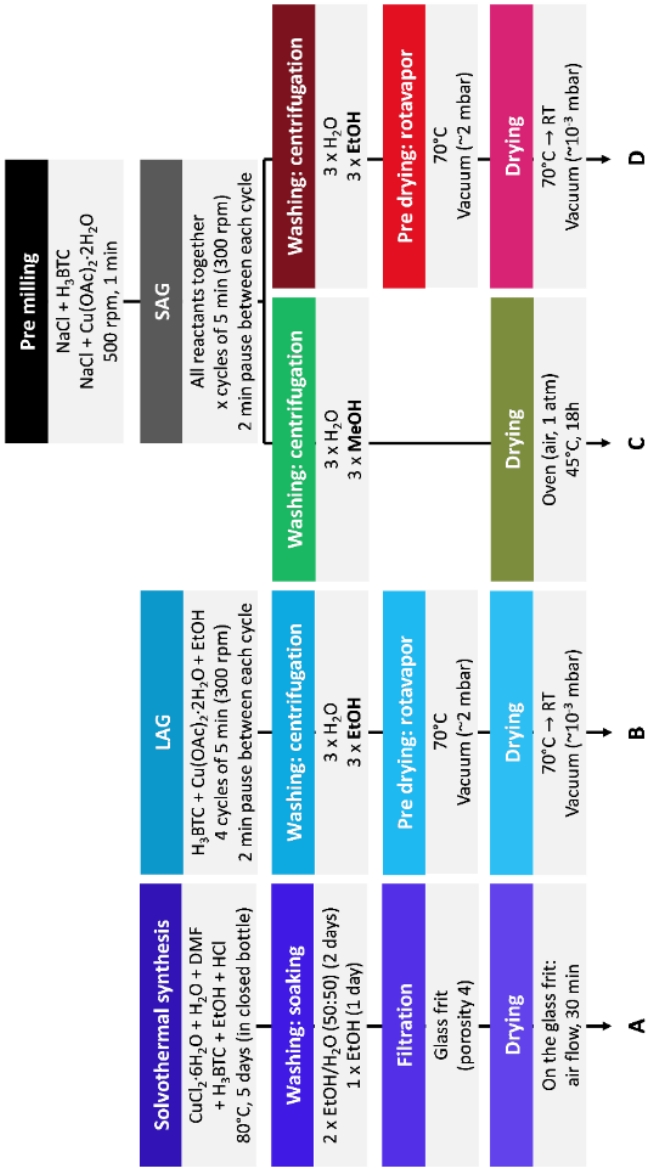

Figure VII-2. Scheme of the synthesis of HKUST-1 samples via the different preparation routes envisaged in this work: (A) solvothermal procedure to obtain single crystals, (B) liquid-assisted grinding (LAG) and salt assisted-grinding (SAG) with post-synthetic treatments using (C) methanol and (D) ethanol.

2. Materials and methods

Instrumental

Powder X-ray diffraction patterns were measured using a MAR345 diffractometer with X-rays generated by a Rigaku ultraX 18S X-ray generator (molybdenum anode, 0.71073 Å), with a monochromated beam (Xenocs FOX 3D mirror). The samples were prepared in glass capillaries (diameter: 0.7 mm). The raw data was integrated through the Fit2D software, using LaB_6 (measured in a 0.1 mm diameter capillary) as a reference sample.

Nitrogen sorption isotherms were measured at 77K using a Micromeritics ASAP2020 equipment. All samples were activated at 150°C under dynamic vacuum for 10 h prior to analysis.

Infrared spectra were recorded on a Bruker Alpha spectrometer equipped with a Platinum ATR module (diamond crystal) housed in an argon-filled glovebox in the 4000-370 cm^{-1} range with a resolution of 4 cm^{-1}.

TGA measurements were performed on a Mettler Toledo TGA/DSC^{3+} system equipped with a sample robot. The used air flow was set at 100 ml/min. An initial isotherm at 27°C was applied during 15 minutes before heating the sample to 900°C at a rate of 10 °C/min.

NH_3-TPD was used to evaluate the acidity of the HKUST SAG EtOH materials. A Hiden Catlab reactor combined with a QGA Hiden quadrupole mass spectrometer was used to perform these experiments. Samples were pretreated under Ar (40 ml/min, 5.0 AirLiquide) at 200 °C during 90 minutes. NH_3 adsorption was performed at 70 °C during 1 hour by flowing a mixture of Argon (20 ml/min) and 5% NH_3 in He (20 ml/min) through the sample. The MOF was then flushed in Ar (40 ml/min) during 90 minutes and then the NH_3 desorption measurement was performed under Ar (40 ml/min) from 70 to 300°C (heating rate of 10 °C/min).

XPS analyses were carried out with a SSI-X-probe (SSX 100/206) photoelectron spectrometer from Surface Science Instruments, equipped with a monochromatized microfocus Al X-ray source. The samples were prepared by sticking onto a double-face adhesive tape fixed onto small brass sample holders that were placed on an insulating ceramic carousel (Macor). An electron flood gun (8 keV) combined with a nickel grid were used to avoid charge effects. The CasaXPS software (Casa Software Ltd.) was used to perform the data treatment, using a Shirley type baseline and fixing the value of C1s peak to 284.6 eV. The samples obtained through ball-milling were analyzed as obtained, whereas the single crystals were ground prior to analysis. The high vacuum (~10^{-8} Torr) used in the analysis chamber made the samples change colour from light to dark blue, indicating *in-situ* activation.

GC analyses were performed under helium flow (38.9 ml/min) using a SHIMADZU GC2010 equipped with a Varian *FactorFour* VF-5ms (30Mx0.25MM ID DF=0.25, part number CP8944) capillary column. The initial temperature of the oven was 50.0°C (0.2 min equilibration time), which was raised at 5.0°C/min to 100.0°C for elution (the column was then heated to 300.0°C at 50.0°C/min to ensure complete removal of any residue in the column). The temperature of the injection port was set at 250.0°C.

^{1}H-NMR spectra were recorded at room temperature (296 K) on a Bruker Avance II 300 spectrometer operating at 300.1 MHz for ^{1}H. Experiments were run under TopSpin program (3.2 version, Bruker) using a BBFO {^{1}H, X} probehead equipped with a z-gradient coil. ^{1}H chemical shifts were referenced to the signal of the aromatic H of 1,3,5-trimethylbenzene (6.07 ppm) that was used as internal standard. For a proper quantification, T_1 of styrene was determined (see ESI) and the recycle delay (d1) time was set at 30s (T_1 = 5 x d1) for the measurements to ensure that integration of the peaks yielded correct quantitative values (with an error of ±1%).

Gravimetric carbon dioxide sorption experiments were realized using a Mettler Toledo TGA/DSC^{3+} system equipped with a sample robot. The samples were pretreated under He atmosphere (100 ml/min), by heating to 200°C (10 K/min), followed by a 2h isotherm and cooling to 27°C (10 K/min). The samples were then further purged with He for 30 min at 27°C, before being subjected to 3 adsorption desorption cycles with CO_2 (100 ml/min, on adsorption) and He (100 ml/min, on desorption). Carbon dioxide (N27; $H_2O \leq 10$ ppm, $O_2 \leq 1000$ ppm, $N_2 \leq 4000$ ppm) and helium (Alphagaz 1, $\geq 99.999\%$; $H_2O \leq 3$ ppm, $O_2 \leq 2$ ppm, $C_nH_m \leq 0.5$ ppm) were supplied from Air Liquide.

Optical microscopy characterization was performed using a Euromex IS.1053-PLPOLRi polarizing microscope equipped with a Euromex VC 3036 camera. Calibration was realized using a 1mm/100 (10µm/division) calibration slide and images were collected using the ImageFocus 4 software.

Chemicals

Trimesic acid (98%) was purchased from Acros Organics. The used sodium chloride was food grade. Copper (II) acetate monohydrate (>99%, AnalaR) was purchased from the British Drug Houses Ltd. Denaturated ethanol (Technisolv, 99%), methanol (HiPerSolv, CHROMANORM), dimethylformamide (HiPerSolv, CHROMANORM), dichloromethane (HiPerSolv, CHROMANORM) and HCl 37% (AnalaR, NORMAPUR) were purchased from VWR Chemicals. Copper (II) chloride hexahydrate (min. 99%) was purchased from Riedel-de Haën. Ethyl diazoacetate (contains ≥13% dichloromethane) was purchased from Sigma-Aldrich. Styrene (99.5%) and trimethoxybenzene (99%) were purchased from Acros Organics. $CDCl_3$ (D>99.8%, H_2O<0.01%) was purchased from Euriso-top. Styrene was distilled under reduced pressure to eliminate stabilizers before use. All other chemicals were used as received.

Syntheses

Single crystals: Single crystals of HKUST-1 were obtained by adding a clear solution containing 1.47 g of copper (II) chloride hexahydrate and 2.33 ml of *N*,*N*-dimethylformamide in 200 ml of deionized water to a clear solution containing 2.10 g of trimesic acid and 0.21 ml HCl 37% in 200 ml of denaturated ethanol. The obtained clear mixture was then introduced in a 500 ml glass bottle closed with a screw cap and was left to crystallize in a laboratory oven at 80°C for 5 days. The obtained crystals were recovered by filtration from the still warm solution and were soaked 2 times in a 50:50 volume mixture of ethanol and water for 2 days, then were soaked one more day in ethanol. The crystals were then filtered out from the washing solution and allowed to dry at room temperature for 30 min before being stored in a closed glass vial.

Ball-milling was performed with a Fritsch Pulverisette 7 premium line apparatus. All experiments were carried out in stainless-steel milling bowls of 45 ml (Fristch^{TM} 50.9750.00), and three stainless-steel balls of 10 mm (Fritsch^{TM} 55.0100.09) were used for each synthesis.

Washings by centrifugation were performed using 45 ml plastic centrifugation tubes using a Heraeus biofuge stratos instrument running at 5500 rpm for a duration of 3 minutes.

LAG sample (see Figure VII-2)*:* 0.59 g (3 eqs.) of copper (II) acetate monohydrate and 0.41 g (2 eqs.) of trimesic acid were introduced into a milling jar together with 1 ml of ethanol. The mixture was subjected to milling at 300 rpm for 20 min (4 cycles of 5 min with 2 minutes pause). The sample was washed with 3 x 45 ml H_2O and 3 x 45 ml EtOH and was then dried under vacuum at 70°C using a rotary evaporator, followed by cooling under dynamic vacuum using a Schlenk line.

SAG samples (see Figure VII-2)*:* A first mixture of 0.59 g (3 eqs.) of copper (II) acetate monohydrate and 0.2 g of NaCl and a second mixture 0.41 g (2 eqs.) of trimesic acid and 0.2 g of NaCl were pre-

milled at 500 rpm for 1 min in two individual milling jars. Then, the two mixtures were gathered together and further milled at 300 rpm for a given amount of time (5, 10 or 20 minutes depending on the sample) in cycles of 5 min with 2 min pause. The ethanol-treated samples were washed with 3 x 45 ml H_2O and 3 x 45 ml EtOH and were then dried under vacuum at 70°C using a rotary evaporator, followed by cooling under dynamic vacuum using a Schlenk line. The methanol-treated samples were washed with 3 x 45 ml H_2O and 3 x 45 ml MeOH followed by drying in an oven at 45°C and ambient pressure for 18h.

Catalytic tests

Note: stirring and heating of the reaction mixtures for the catalytic tests was achieved by using a Heidolph Hei-Tec magnetic stirrer. The rotation speed accuracy was of ± 2%. The stirrer was equipped with an external Pt 1000 temperature probe ensuring a temperature accuracy of ±1°C. Heating was achieved by using a stirred oil bath coated with aluminium foil to insulate the bath, allowing to easily attain the activation temperature of 150°C.

Cyclopropanation reactions were carried-out in a 50 ml three-neck round-bottom flask equipped with a condenser and a glass stopcock connected to a Schlenk line. An ellipsoid shaped magnetic stirring bar was introduced into the flask (all the experiments were run at 300 rpm). 36 mg of the MOF sample was introduced in the experimental setup and heating to 150°C under dynamic vacuum for 1 h was applied to activate the catalyst. The flask was allowed to cool down to room temperature (25°C) and the volume was refilled with argon. 224 mg of 1,3,5-trimethoxybenzene (internal standard, 1.33 mmol) in 3 ml of $CDCl_3$ was then introduced into the setup. 0.46 ml (4 mmol) of styrene was added to the stirred mixture. The reaction was initiated by the dropwise addition of EDA (containing ≥13% dichloromethane) diluted in 7 ml of $CDCl_3$ over two hours using a syringe pump. After complete addition of the EDA, the reaction mixture was allowed to react for another 1h. 1 ml was then sampled from the reaction mixture and the catalyst was separated by filtration on custom-made filter columns made from

Pasteur pipettes filled with silica (± 20 mm) that was retained through a small cotton wool plug. The filter was eluted by adding 1 ml of $CDCl_3$ and 0.5 ml of the filtrate was used for ^{1}H-NMR analysis.

3. Results and Discussion

3.1. Crystal structure and thermal properties

The crystal structure of all the synthesized MOF materials was verified by PXRD on the as-synthesized powders. All the obtained compounds show powder patterns revealing the presence of HKUST-1 as single phase (Fig. S VII-1). Some peak broadening as well as well as a non-flat baseline (possibly caused by some amorphous phase) can be observed for the materials synthesized by the SAG method compared to the LAG and single crystal samples. This, as well as differences in relative intensities of the peaks at 4.38° and 5.32°,[365] is indicative of the presence of a significant amount of structural defects in those materials.

Nitrogen sorption isotherms were measured for all the synthesized compounds. The single crystal sample shows a well-defined I(a) type isotherm, characteristic of microporous compounds,[154] which is expected based on the crystal structure of HKUST-1 (Figure VII-3a). The materials synthesized by the mechanochemical approaches also show a steep uptake at very low P/P_0 values, typical of microporous solids. However, for those materials, hysteresis loops of the H4 type are also observed, which can be ascribed to the presence of intergrain spaces formed by the aggregation of small crystallites (Figure VII-3a-c).

Importantly, the calculated Brunauer-Emmett-Teller (BET) surface areas of the samples vary largely according to the parameters used for the synthesis as well as the applied washing and drying procedures (Figure VII-3d-f). The highest surface area is obtained for the HKUST-1 single crystals (1881 m^2/g), directly followed by the sample made by LAG (1739 m^2/g).

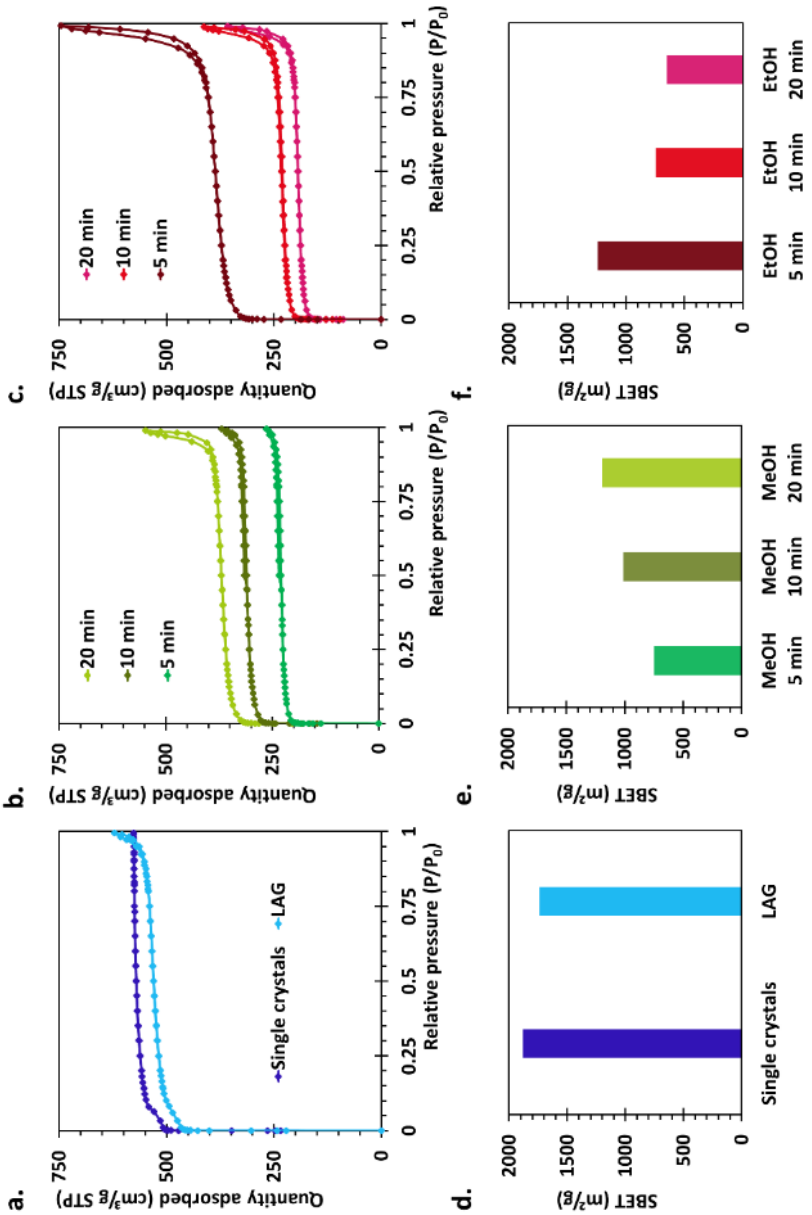

Figure VII-3. Nitrogen sorption isotherms of (a) single crystals and LAG samples, (b) SAG samples washed with MeOH, (c) SAG samples washed with EtOH and (d-f) corresponding calculated Brunauer-Emmett-Teller surface areas.

The surface areas of the samples obtained by the SAG procedure decreases with increasing milling time when the post-synthetic treatment with ethanol is applied, which could be explained by degradation of the crystal structure under prolonged high-energy milling. However, the samples series washed with methanol and dried in an oven show the opposite tendency: the surface area increases with increasing milling time. This indicates that the structure rearranges upon removal of the sodium chloride particles trapped in the cavities formed during the mechanochemical synthesis, and that this rearrangement is dependent on the applied post-synthetic treatment.

3.2. Identification of defect sites

The FTIR spectra of the materials all show the typical vibration frequencies expected for the chemical bonds in HKUST-1 as described in earlier reports, the main features being ν_{as} and ν_{sym} of carboxylates that are present at 1649 and 1451 cm^{-1} respectively.[44,366,367,368] In the as-synthesized samples, ν C-O bands assigned to primary alcohols also appear at 1106 and 1042 cm^{-1} (Fig. S VII-2). Those disappear after thermal activation of the samples under vacuum at 150°C, showing that this procedure is effective to desorb residual coordinated methanol and ethanol molecules. Furthermore, differences in the IR spectra appear between the various series of samples, indicating the formation of different types of defects, depending on the used synthetic procedure and applied post-synthetic treatment.

An absorption band characteristic of C=O stretching of free carboxylic acids is observed at around 1710 cm^{-1} both for the MOFs obtained by SAG and in the form of single crystals, whereas this feature is not present in the one synthesized by LAG (Figure VII-4). Interestingly, the intensity of this signal is quite weak for the samples treated with MeOH as well as for the single crystals. On the opposite, the samples that underwent the EtOH post-synthetic treatment show a significantly more intense absorption band that increases with increasing milling time used for the synthesis of the materials. The presence of -COOH functions in those samples is further confirmed by

the presence of absorption bands around 1193 cm^{-1} (C-O stretching) and 1232 cm^{-1} (OH bending), typical of non-coordinated carboxylic acids.[369] Furthermore, a shift of the ν_{as} band towards lower wavenumbers, from 1649 cm^{-1} to 1647, 1645 and 1643 cm^{-1} for the 5, 10 and 20 min milled samples, respectively, accompanies the increase of signals related to carboxylic acids. The O-H stretchings, that are usually comprised between 3200 and 2600 cm^{-1} are however absent of the spectra (and therefore this region of the spectra is not shown on Figure VII-4), which could be explained by the dilution of the functionalities in the sample, as well as the lower sensitivity of ATR-IR in this region compared to transmission FTIR.

The acidity of the EtOH treated samples obtained by SAG was investigated by ammonia temperature-programmed desorption (NH_3-TPD) experiments (Fig. S VII-3). The obtained curves show the presence of two overlapped desorption peaks, one at about 150°C and the other, less intense, at ~200°C. The same experiment was performed on the sample obtained by LAG which showed only one desorption peak at 150°C. The peak at 150°C can be assigned to desorption of NH_3 coordinated to the copper sites of the MOF. The presence of a second peak at higher temperatures for the EtOH treated samples means that a second, more acidic, site is present, which is in this case attributed to the presence of -COOH moieties in the materials. This peak is especially visible for the sample obtained after 20 min of milling, which correlates with the most intense -COOH bands in the FTIR spectra.

The presence of free carboxylic acid moieties in the EtOH washed samples, especially for the 20 min EtOH material, is further supported by the weight losses observed in the TGA curves (Fig. S VII-4), which show an excess weight loss during the decomposition (61.2%, 61.5% and 68.8% for 5, 10 and 20 min milled samples respectively) compared to the value calculated for a perfect Cu_3BTC_2 formula without any defects (60.5%), considering a CuO residue. This means that the organic linker/metal ratio is higher than the one expected from the 2:3 stoichiometric ratio.

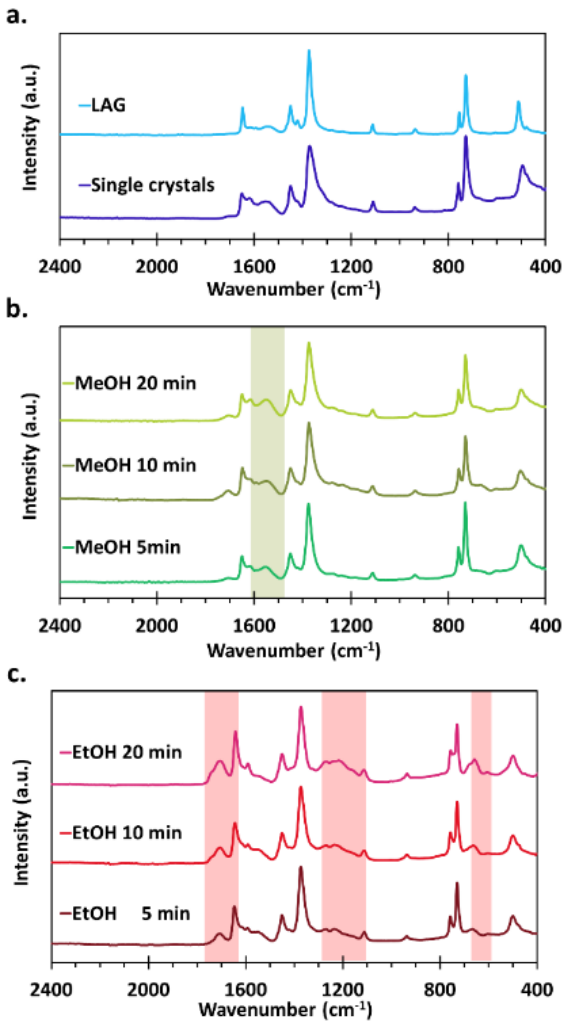

Figure VII-4. FTIR spectra of the HKUST-1 materials obtained through the different synthesis pathways: (a) single crystals and LAG samples, (b) SAG samples washed with MeOH, (c) SAG samples washed with EtOH. The zones highlighted in colour indicate the absorption bands that are the most affected by the presence of Cu^{I} (green) and -COOH (red) defects.

This observed excess of organic linker is in perfect agreement with the presence of free -COOH moieties. Moreover, the thermal stability of the EtOH treated SAG samples increases with the amount of present carboxylic acidic sites (Fig. S VII-4). The thermal stability of the

HKUST-1 materials was compared to starting copper acetate and trimesic acid and showed that the acetate has a lower decomposition temperature (289°C) than HKUST-1 (between 300 and 350°C, depending on the sample) which itself is less stable than trimesic acid (T_{dec} = 408°C). This indicates that the observed increase of thermal stability is indeed due to the presence of excess, partially protonated, carboxylate ligand in the materials.

For the MeOH treated SAG samples, as well as for the single crystals, the FTIR spectra show the appearance of an absorption band at 1616 cm^{-1}. This quite intense band does not appear in the spectra of the EtOH treated SAG samples and is of negligible intensity in the case of the LAG sample. Based on its position, this absorption band can be ascribed to a ν_{as} of carboxylate. However, as stated previously, the antisymmetric stretching band of the carboxylates in typical HKUST-1 materials is located at 1649 cm^{-1}. It has been established since a long time that the positions of the symmetric and antisymmetric stretching bands of carboxylates in inorganic compounds depend on the nature of the coordination mode of the $-COO^-$ moiety.[370] Thus, from the FTIR spectra, it seems that a different type of metal-to-ligand coordination is present in the MeOH treated samples.

XPS measurements were performed to further investigate the defects present within the different samples. It was observed that they all contain copper in the +I and +II oxidation state at the surface, see Fig. S VII-5 for more details. Although Cu^{II} readily reduces into Cu^{I} during XPS measurements,[371] the analysis of all the samples under strictly identical conditions allows for a reasonable comparison between the different materials. It was observed that the MeOH treated samples display a much higher Cu^{I}/Cu^{II} ratio than all other samples. This can be explained by reduction of Cu^{II} into Cu^{I} by methanol during the prolonged drying at 45°C used for the post-synthetic treatment. Furthermore, this ratio increases with increasing milling time (Fig. S VII-5). From this, it is concluded that Cu^{I}, associated with a change in coordination of the carboxylate moieties, is the main type of defect

present in the MeOH treated materials and that the amount of such defects increases with the milling time used during the mechanochemical synthesis. From the FTIR spectra, it is expected that the same type of defects are present in the single crystals. However, those were ground prior to XPS analysis, exposing the bulk composition, whereas the XPS spectra of all other samples are representative of the external surface of the as-obtained powders.

The presence of Cu^{I} defect sites in the MeOH treated and single crystal materials is further confirmed by the weight losses observed during their thermal decomposition (Fig. S VII-4), which, on the contrary to the EtOH treated samples, are lower than the expected value for Cu_3BTC_2. This observation means that an excess of Cu is present in the materials, which is in agreement with the existence of Cu^{I}. Furthermore, this weight loss decreases with increasing milling time and associated Cu^{I} content revealed by XPS. Interestingly, the loss observed during the decomposition of the single crystals (58.4°C) indicate that they contain an amount of Cu^{I} that is intermediate between that of the 10 min (~60.6°C) and 20 min (57.5°C) milled samples. The thermal stabilities of the MeOH treated and single crystal samples, similar to that of the MOF obtained by LAG, are lower than for the EtOH treated SAG materials. It should be noted that from TGA analysis, the as obtained single crystals have an apparent higher thermal stability (360°C), which is due to the large size of the crystallites (~100-400 µm, see optical microscopy characterization in the SI). This thermal stability is greatly lowered to 320°C by reducing the particle size by gentle grinding in an agate mortar prior to analysis (Fig. S VII-4), enabling a more accurate comparison with the small sized particles resulting from the mechanochemical syntheses.

Finally, although possessing the second highest surface area of all the materials, the MOF obtained through the LAG procedure seems to be the one that possesses the least amount of structural defects. The flatness of the background of the PXRD pattern, the absence of absorption bands associated to -COOH in the FTIR spectrum or Cu^{I}

defects detected by XPS, its weight loss during decomposition that is close to the expected value for Cu_3BTC_2 as well as its decomposition temperature are all features that support the low defect content of this MOF. Furthermore, the XPS data show that the surface composition of this sample is nicely located in between that of the two SAG sample series (Fig. S VII-5).

3.3. Carbon dioxide sorption properties

Although of no industrial interest because of the water sensitivity of HKUST-1, and because industrial CO_2 exhausts always contain water, carbon dioxide sorption capacities of the different materials were evaluated by using a thermogravimetric analyser in order to determine the influence of defects on the performances, from a fundamental perspective. This type of measurement allows obtaining an evaluation of the gravimetric sorption by using a minimum amount of sample. The samples were activated thermally *in situ* at 200°C under a helium flow before three CO_2 adsorption/desorption cycles that were performed at 27°C. Appropriate corrections were applied for each measurement (see details in the SI) and the obtained results are presented in Figure VII-5.

The CO_2 that is initially adsorbed by the materials during the first loading is not completely released after 30 min of purging with He: about 2 to 3% weight CO_2 remains adsorbed on the samples. This can be expected since the desorption kinetics is slower than the adsorption kinetics. Furthermore, the adsorption curves display two distinct regions, the first one showing a very steep uptake, likely related to the filling of a preferential CO_2 sorption site (probably the desolvated copper sites). The second adsorption step is much slower and is related to occupation of less favourable adsorption sites, likely in the cavities of the MOF's pores.

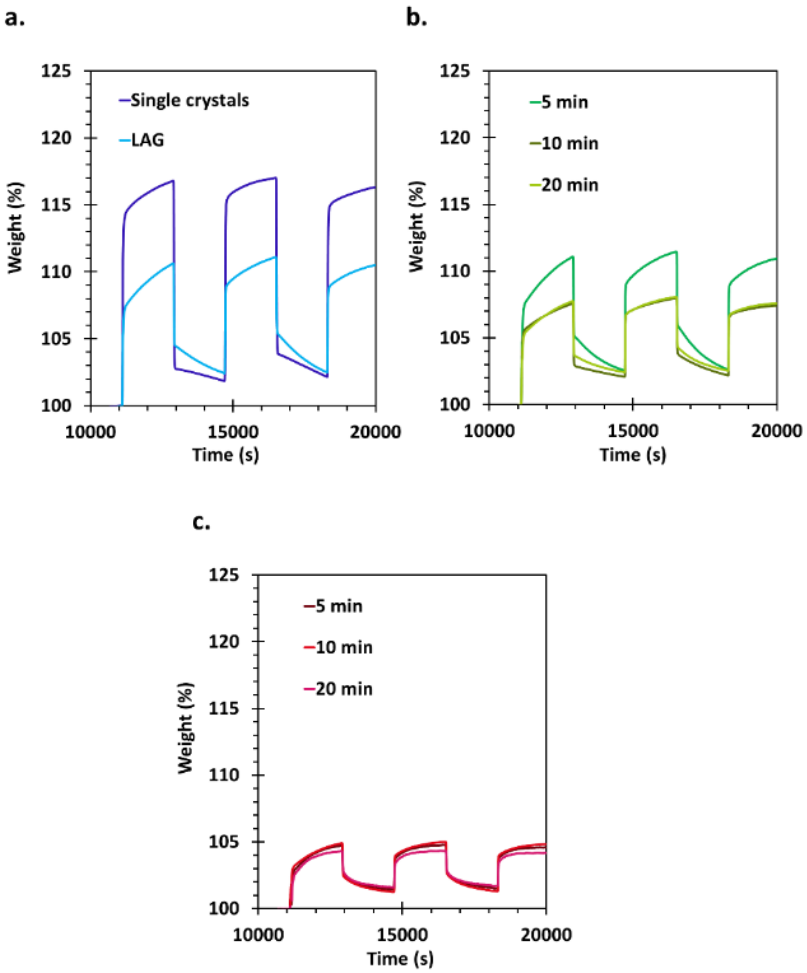

Figure VII-5. Gravimetric CO_2 sorption cycles realized using TGA with (a) single crystals and LAG material, (b) SAG samples washed with methanol and dried at 45°C and (c) SAG samples washed with ethanol and dried under vacuum. Errors on the measurements are estimated to be ±1 wt.% (see ESI for details on corrections and reproducibility).

The best performing material for gas sorption are the single crystals, which are able to adsorb about 17% weight of CO_2. This is much higher than the values reported previously under similar conditions for HKUST-1 materials[372], and even in comparison with other porous materials measured under similar conditions (see Table S VII-1). Only MOFs of the MOF-74 type and MOFs functionalized with

amines, which are known to exhibit very good affinity for CO_2, possess higher uptake values. Surprisingly, the LAG material, having a surface area only about 7.5% smaller than the single crystals, showed an adsorption of only 10% weight of CO_2. The adsorption capacity of the 5 min MeOH SAG sample is very similar to that observed for the LAG material, although its surface area is much lower. However, the 10 and 20 min MeOH samples adsorb a lower amount of CO_2 whereas they possess higher surface areas.

Importantly, the presence of -COOH defects in the EtOH treated samples has a very negative effect on the CO_2 sorption of the materials, allowing the sorption of only 5% weight CO_2. This can be attributed to the Brønsted acidity of these MOFs, which is not favourable for the adsorption of carbon dioxide that is an acidic gas. The obtained results demonstrate that the CO_2 sorption capacity of HKUST-1 is largely governed by the type and amount of defects in the MOF rather than by its surface area.

3.4. Catalytic cyclopropanation

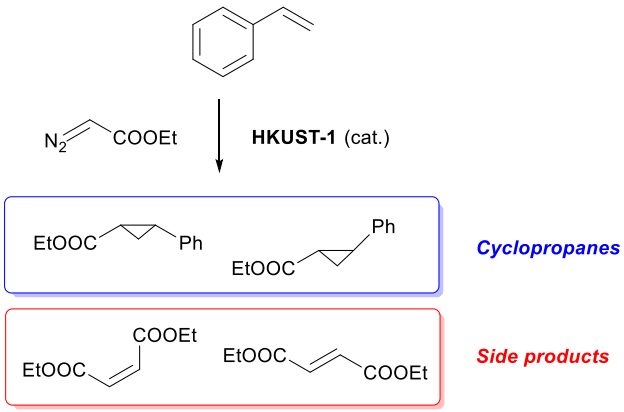

Scheme VII-1. Cyclopropanation reaction of styrene with EDA catalysed by HKUST-1.

The materials were tested for their ability to catalyze the cyclopropanation reaction of styrene with ethyl diazoacetate (EDA) (Scheme VII-1) to evaluate the impact of the number and type of defects on the catalytic activity. The LAG sample was used as reference

catalyst and kinetic follow-up by gas chromatography (GC) of the reaction in dichloromethane showed that EDA was totally converted in less than 30 minutes (Fig. S VII-6). The GC experiment also showed the formation of significant amounts of side products: diethyl fumarate and diethyl maleate. Further experiments were therefore run by adding the EDA dropwise over 2 hours to a solution of styrene containing the catalyst by using a syringe pump. In this way, the concentration of EDA in the reaction mixture was kept as low as possible, lowering the formation of unwanted side products. The solvent was shifted from dichloromethane to $CDCl_3$, which has similar properties to CH_2Cl_2, and 1,3,5-trimethoxybenzene was added as internal standard to enable reaction follow-up by ^{1}H-NMR. All the reactions were stopped one hour after complete addition of the EDA to the reaction mixture. The catalysts were all activated under vacuum at 150°C prior to the catalytic tests, although this step could have been skipped as exposure to small halogenoalkanes, like CH_2Cl_2 and $CDCl_3$, can achieve activation of HKUST-1 *in situ*.[373]

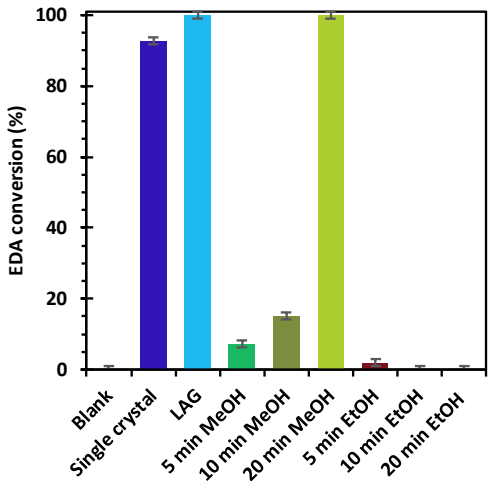

Figure VII-6. Ethyl diazoacetate conversions after the reaction with styrene in the presence of the different HKUST-1 materials as catalysts.

The EDA conversion and selectivity of all the catalysts are summarized in Figure VII-6, Figure VII-7 and Table S VII-2. A blank

test was run without catalyst and showed no conversion of the reactants after 3 hours. On the contrary, the LAG sample showed 100% EDA conversion. The EtOH treated SAG samples, on the one hand, showed very poor (5 min milled sample) or no conversion at all. This indicates that the presence of acidic defects in the MOF drastically inhibits the catalytic activity of HKUST-1 towards cyclopropanation of styrene with EDA. On the other hand, the methanol treated samples showed better EDA conversion, which increases with the amount of Cu^{I} defects at the surface of the sample, reaching 100% conversion for the 20 min milled sample. The conversion observed when using the single crystals as catalyst (92.6%) is comprised between that of the MeOH treated SAG samples that were obtained by milling for 10 min (15.2%) and 20 min (100%). This is in striking agreement with the previous conclusion that the single crystals possess the same type of defects as the MeOH treated samples and that the amount of those defects is comprised between that of the 10 and 20 min milled materials.

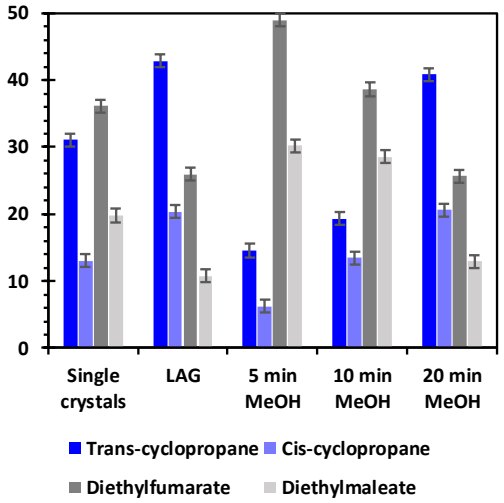

Figure VII-7. Selectivity of the cyclopropanation reaction of EDA with styrene obtained by using the different HKUST-1 materials as catalysts.

Furthermore, the selectivity of the single crystal and methanol washed catalysts show that the formation of cyclopropanes is favoured when the amount of Cu^{I} defects increases, whereas a low amount of

defects, such as in the 5 min MeOH sample favour the formation of dimethylfumarate and –maleate side-products. The LAG sample, which presents the least defects, shows similar conversion and selectivity than the 20 min MeOH material, which is the best performing one in its category. Interestingly, the XPS analyses (Fig. S VII-5) indicate that the 20 min EtOH and 5 min MeOH treated SAG samples, which are both the worst performing materials of their series, possess a surface composition quite similar to that of the material obtained by LAG, which is the best performing of all tested MOFs. On the contrary, the 5 min EtOH and 20 min MeOH materials have a surface composition largely differing from that of the LAG MOF but are both the best performing catalysts of their series. This observation shows that the course of the catalytic reaction is not governed by the surface of the MOF but rather by its bulk composition.

Overall, the outcome of the experiments show that acidic defects in the form of free -COOH functions in HKUST-1 poison the catalytic activity towards cyclopropanation. On the other hand, the activity of the MeOH treated SAG samples and the single crystals, also showing the presence of small amounts of free -COOH functions, increases with increasing Cu^{I} concentration. This indicates that Cu^{I} defects can counteract the poisoning effect of carboxylic acid. The LAG sample, which shows nearly no defects, seems to possess the best activity and conversion toward cyclopropanes, although being close to the ones obtained for the Cu^{I} rich 20 min MeOH sample in the conditions used for the experiments. In this perspective, it seems that the defectless Cu^{II} sites are the most active towards the cyclopropanation reaction.

4. Conclusions

We demonstrated that mechanochemical synthesis of HKUST-1 by salt-assisted grinding induces the formation of high amounts of defects in the structure of this MOF. Importantly, the type and amount of defects is dependent on the applied post-synthetic treatment and the duration of the milling. We showed that washing with water and ethanol followed by drying under vacuum at 70°C mainly results in the presence

of free -COOH non-coordinated functions in the MOF, whereas treatment with water and methanol followed by gentle heating at 45°C for 18h results in partial reduction of the Cu^{II} sites into Cu^{I}. We also evidenced that large (~100-400 µm) single crystals of HKUST-1 obtained in this work also possess a large amount of similar Cu^{I} defects. Surprisingly, liquid-assisted grinding (LAG) appears to be the strategy resulting in the material with the lowest amount of structural defects. This encourages the use of LAG for making HKUST-1, as it also results in high synthetic yields. Those conclusions were drawn through thorough characterization of the materials by vibrational spectroscopy (FTIR), XPS, TGA and NH_3 temperature-programmed desorption experiments. We also showed that CO_2 adsorption by HKUST-1 seems to be the most efficient when using materials with low amounts of structural defects. Acidic -COOH sites in the materials result in poor adsorption of CO_2 but strongly increases affinity of the materials for NH_3. However, even in the presence of some Cu^{I} defects, HKUST-1 in the form of large single crystals show the highest gravimetric carbon dioxide uptake, evidencing an influence of the texture and size of the MOF particles on its performance. Finally, we showed that the presence of -COOH defect sites in HKUST-1, despite increasing the thermal stability of the material, strongly poisons the catalytic activity of this MOF towards the cyclopropanation of styrene with ethyl diazoacetate. The presence of high amounts of Cu^{I} seems to partly counteract this poisoning effect. However, the absence of carboxylic acid sites in the LAG-obtained material leads to the highest conversion as well as the best selectivity towards the desired cyclopropanes, even with low amounts of Cu^{I}, indicating that the pristine Cu^{II} sites are the most catalytically active ones.

CHAPTER VIII

General Conclusions and Perspectives

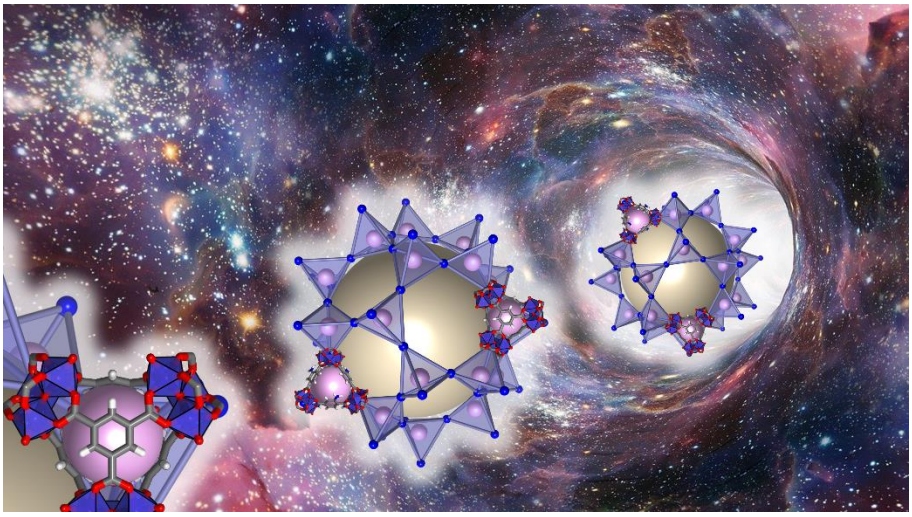

Chapter VIII - General Conclusions and Perspectives

1. Conclusions

The green synthesis of MIL-100(Fe) has been optimized by synthesizing alkali (Li^+, Na^+, K^+, Rb^+ and Cs^+) trimesates as precursor salts. Those salts and their hydrates were characterized by thermal analysis, and their structures solved by combination of single-crystal and variable-temperature synchrotron X-ray diffraction. Systematic investigation of the synthesis of MIL-100(Fe) from aqueous solution of those salts with iron(II) sulphate revealed that a maximum in surface area is obtained across the alkali series when Na_3BTC is used. An iron(II) intermediate could successfully be isolated under inert atmosphere and its structure solved by means of single crystal X-ray diffraction. It was demonstrated that the formation of this Fe_3BTC_2 intermediate is essential to the subsequent formation of MIL-100(Fe), and that the presence of air oxygen as oxidant, as well as water as solvent, are necessary for the formation of the desired MOF. The effect of different sodium carboxylate salts as crystallization modulators on the textural properties of the obtained MIL-100(Fe) was also evaluated. Aromatic modulators were incorporated in the final MOFs, whereas aliphatic modulators were not. Furthermore, the use of sodium 2-aminocaproate as modulator yielded a MIL-100(Fe) MOF with increased surface area. The samples obtained through the green synthesis strategy with or without modulators surprisingly demonstrated better Au^{III} removal capacities than previously described for non-functionalized MIL-100(Fe). This behaviour could be ascribed to the presence of hydroxide charge balancing anions and Fe^{II} in the MOF, increasing its reduction potential and favouring the formation of Au^0 nanoparticles.

The improved synthesis strategy of MIL-100(Fe) allows the reaction to proceed under slightly acidic conditions, in contrast to the previously described aqueous green syntheses of this MOF. This was

shown to be essential to allow for controlled incorporation of doping metals through direct synthesis. A large variety of transition and p-block metals could be incorporated into bimetallic MIL-100(Fe,M) through this strategy. Iron was incorporated preferentially over metals in the +II oxidation state whereas metals in higher oxidation states were incorporated preferentially over iron, leading to a difference in bulk and surface compositions of doping metals. Lanthanides could also be incorporated into MIL-100(Fe,Ln). It was shown in this latter case that efficient stirring was a pre-requisite to formation of good quality samples. Furthermore, metals from the middle of the lanthanide series, such as terbium and europium, could be incorporated in high amounts in the MOF (up to 20% of the metal content). For other lanthanides, a secondary phase of a lanthanide trimesate hydrate was formed when doping amounts even as low as 10% were used. In complement to classical AAS and ICP analyses, we developed a strategy for determining the amount of doping metal in the samples by Rietveld refinement on the PXRD patterns of oxides obtained after calcination (residues obtained upon TGA analysis) of the MOFs.

The coordinatively-unsaturated metal sites of monometallic and MIL-100 MOFs based on iron and aluminium were exploited for post-synthetic functionalization with ethylenediamine. It was shown that MIL-100(Fe) collapsed under the conditions used for the functionalization, whereas MIL-100(Al) and bimetallic MIL-100(Fe,Al) containing an Fe/Al ratio of 2/1 could withstand this treatment. The efficient functionalization of MIL-100(Al) with ethylenediamine was confirmed through liquid-state and solution state NMR, demonstrating that one out of three Al-sites per Al_3O cluster could be attached to one amino function of the ethylenediamine molecule, leaving one pendant amine site, introducing basicity to the material. This second amine site could efficiently be post-functionalized with a fluorescent BODIPY derivative, and reaction with ninhydrin showed that selective post-functionalization of the $–NH_2$ functions inside the large mesopores could be performed while leaving the functions inside the small mesopores intact, by selecting molecules

with appropriate diameters for selective diffusion through the large hexagonal channels of the MOF. EN@MIL-100(Al) showed increased affinity for CO_2 at low pressures, compared to the other materials, and all the Al-containing MOFs showed an unexpected but interesting increase in adsorbed CO_2 above 20 bar of pressure compared to the expected values based on Langmuir isotherms. This increase was tentatively explained by insertion of CO_2 in the Al-O-H bonds to form a carbonic acid species.

Frameworks with the MOF-76 topology based on different rare-earth metals were obtained through a new synthetic strategy involving ethanol as the only solvent, avoiding the use of toxic DMF. *In situ* experiments allowed to determine that the reaction forms HCl which in turns catalyses the partial esterification of trimesic acid, leading to rather low yields. Although the yields were not satisfactory, especially compared to classical methods in DMF where yields are close to 100%, recycling of unreacted materials for launching a second batch of MOF was possible. The synthesis could be performed successfully at temperatures as low as 45°C with lanthanum, light lanthanides (Ce, Pr and Nd) as well as with the heavier ones (represented by Yb as only example). MOF-76(Ln) with lanthanides from the middle of the series could however not be obtained through this approach. The stability of the MOF-76 series towards water has been evaluated, showing that it increases with decreasing radius of the metal cation. Similar increase in stability with decreasing ionic radius might exist for other lanthanide MOFs. The stability towards water could efficiently be improved by using trimesate linkers bearing an amine function, and the structure of NH_2-MOF-76(La), which shows intense blue fluorescence owing to the linker, has been solved by single crystal XRD. Finally, *in situ* powder diffraction experiments on MOF-76(La) showed that this framework undergoes interesting structural changes upon changes in temperature under vacuum, whereas under 1.1 bar of xenon no structural changes were observed, but progressive pore filling strongly impacts the PXRD patterns.

We investigated the possibility of synthesizing MOFs with the mtn topology based on Ti^{3+} by using the cheap $(TiCl_3)_3AlCl_3$ reactant and transforming it into $TiCl_3(THF)_3$ as precursor. We successfully obtained NH_2-MIL-101(Ti^{3+}), extending the currently rather limited family of MOFs (with the mtn topology) based on Ti^{3+} and creating the first member of this family having functionalities (amines) on its linkers. By applying the same synthesis conditions with other derivatives of terephthalate or (extended) trimesate linkers, no crystalline MOF with this interesting topology could be obtained. The synthesis of the aluminium derivative has also been improved compared to reported procedures, resulting in NH_2-MIL-101(Al) with the highest surface area reported yet. By using variable-temperature PXRD, we demonstrated that NH_2-MIL-101(Al) possesses a lower thermal stability than previously reported based on TGA data only. The thermal stability of NH_2-MIL-101(Ti^{3+}) was shown to be similar to that of the aluminium derivative (~150°C). The cluster structure of NH_2-MIL-101(Ti^{3+}) has been elucidated by combination of liquid state NMR and elemental analysis, showing that chloride is present as charge balancing anion on one Ti centre and, and that two strongly coordinated DMF molecules, which can only be partly removed by thermal activation under vacuum, complete the coordination sphere of the two other Ti atoms. Activated NH_2-MIL-101(Ti^{3+}) also shows slightly improved hydrogen sorption at low pressure and -196°C compared to the previously reported MIL-101(Ti^{3+}).

Defects induced in HKUST-1, which was used as model framework in this work, by salt-assisted mechanochemical synthesis followed by two types of post-synthetic treatments, either with ethanol or methanol were characterized through means of PXRD, FTIR and XPS. It was shown that the amount of defects induced in the framework depends on the milling time for the synthesis, whereas the type of defect depends on the post-synthetic treatment. Washing with water and ethanol followed by drying under vacuum at 70°C induced the formation of free carboxylic acid functions resulting from excess linker defects, whereas washing with methanol followed by drying at 45°C

under ambient pressure results in partial reduction of Cu^{II} into Cu^{I} defective sites. The last type of defects was also observed in single crystal samples that were synthesized by solvothermal reaction. By comparison, synthesis by liquid-assisted grinding in the presence of some ethanol resulted in the material with the least defects. The obtained HKUST-1 samples were tested for adsorption of CO_2, and the materials with the smallest amounts of defects were the most efficient from all the samples obtained by mechanochemical means. The presence of carboxylic acid defects in the MOF resulted in decreased affinity for CO_2 but increased affinity towards ammonia, as revealed by NH_3-TPD experiments. The presence of Cu^{I} defects had a lower impact on affinity for CO_2, as the single crystals containing this type of defects show the highest uptake of carbon dioxide. The materials were also evaluated as catalyst for the cyclopropanation of styrene with ethyldiazoacetate. It was shown that –COOH defects strongly poison the catalyst whereas high amounts of Cu^{I} defects inside the materials could counteract this poisoning effect. The sample obtained by liquid-assisted grinding, that does not produce Cu^{I} defects, showed the best catalytic performances, both in conversion and selectivity towards cyclopropanes, indicating that Cu^{II} sites are the most catalytically active for this reaction.

Taking a broader view, we can state that the sustainability of the synthesis conditions for obtaining monometallic MIL-100(Fe), bimetallic MIL-100(Fe,M) and MOF-76 MOFs have been improved regarding the choice of solvents and their impact on the environment, as well as lowering the energy requirements (lower reaction temperatures) compared to conventionally used preparation methods. However, improvements can still be done regarding the (space time) yields of both syntheses to enable industrial scale fabrication through the developed methods. We showed that, providing suitable adaptation to the whole reaction system, green synthesis conditions without the need of many (corrosive and/or toxic) additives and modulators, and benign starting metallic reactants, can be achieved even for the most complex MOFs, previously obtained under harsh conditions. We expect

that such improvements can be achieved for most existing MOFs, although the whole reaction system might need to be changed and that, unfortunately, the changes to apply to the synthetic parameters are very dependent on the targeted MOF structure and composition (type of metal and eventual presence and nature of functions on the linkers). It has been demonstrated that facile post-synthetic modification with ethylenediamine on the metal sites of MIL-100(Al) leads to interesting new properties and opens new ways to post-functionalization. Improvement of the water-stability of MOFs containing the trimesate linker might be achieved through the use of 2-aminotrimesate, similarly to the case of MOF-76, although the use of the (non-commercial) functionalized linker increases the cost of synthesis. Furthermore, we evidenced that the use of alcohols as greener synthesis solvents, despite decreasing the energy for MOF activation compared to the use of high-boiling point solvents, might lead to partial esterification of the linkers during synthesis, reducing yields. This yield-lowering mechanism might occur during the synthesis of any MOF based on carboxylate linkers when performed in alcohols and particular attention should be paid to avoid this esterification process that is decreasing yields.

The introduction of metals in "exotic" oxidation states (such as Ti^{3+}) in known MOF structures can lead to unexpected properties and different activation mechanisms than the ones commonly admitted for MOFs based on "routinely used" metal centres. This evidences that modification of known MOFs (through complete or partial substitution of metal centres, linkers and/or charge balancing anions) might lead to completely different properties, and is worth pursuing. We finally demonstrated that particular attention should be paid to the analysis and determination of the type of defects in MOFs, having an important impact on the properties of simple model MOFs, and likely having similar impact on more complex structures such as MIL-100. However, this work has shown that the determination of the types of defects even in the simplest structures is not straightforward, implies the need for many types of analytical methods, and that even in this case a clear view of all defects cannot always be obtained in a qualitative manner, and

quantification of such sites is even trickier. Further developments are thus needed to understand the composition of MOFs at the microscopic scale and properties should not be linked blindly to their crystal structure.

2. Perspectives

The synthetic efforts made during this thesis work have afforded many interesting, phase pure, porous and well characterized MOF samples. Those new compounds might find numerous applications in catalysis or gas sorption for example, under their current state or after further post-synthetic modification.

Regarding the green synthesis of MIL-100(Fe), further efforts may be applied to scale-up the synthesis to kilogram- or pilot scale, as in the lab we successfully managed to scale-up this synthesis for obtaining tens of grams from a single batch. The main improvement that is still possible would be regarding the concentrations of the solutions used for the synthesis, as increasing them could allow for reducing reactor size and reducing amounts of aqueous waste that needs to be treated. This, together with active injection of air (or pure oxygen), would enable to increase the space time yield to render the synthesis suitable for industrialization. Further efforts could also be put on understanding the reaction mechanism regarding the oxidative transformation of the Fe_3BTC_2 intermediate into MIL-100(Fe). This might be achieved through isotopic labelling of oxygen for example, or by characterizing the oxidation state of the iron over the course of the reaction (*in situ* monitoring) through specialized techniques such as Mössbauer spectroscopy, EXAFS, SAXS or pair distribution function analysis for example. Such characterization, along with electron microscopy, could also help in further understanding the mechanism of gold loading and reduction inside MIL-100(Fe).

The bimetallic MIL-100(Fe,M) MOFs that were obtained are ideal candidates for catalysis. Appropriate reactions that could be catalysed depend on the nature of the doping metal. Lewis acid catalysis could be

tested for samples doped with metals in stable high oxidation states (e.g. Al^{3+}, Cr^{3+}, lanthanides). Oxidation or reduction reactions would be appropriate with redox active doping metals (e.g. Mn, Co, V), and photocatalysis could even be an option for MIL-100(Fe,Ti). When evaluating catalytic applications of those MOFs, the study of their stability under the used conditions should also be performed, not only by evaluation of the stability of the framework through PXRD and textural analyses, but also through determination of metal leaching. From a fundamental point of view, understanding the spatial distribution of metals in the bimetallic MOFs is also a very challenging point that still needs to be addressed. For this purpose, the bimetallic MIL-100(Fe,Eu) would be an ideal candidate, to tackle questions concerning coordination of both metals, and especially of europium, through means of ^{57}Fe and ^{151}Eu Mössbauer spectroscopy. The samples with doping metals in oxidation state +II could also be good candidates for the adsorption of gases, thanks to their larger density of CUSs. Samples doped with heavy metals (e.g. MIL-100(Fe,Cd)) could be good candidates for the adsorption and removal of (toxic) molecules with soft basic functions (e.g. H_2S or thiols), although the toxicity of the doping metal itself would be of concern.

The green synthesis of MIL-100(Fe) could be further extended to the production of samples containing functionalities on the linkers. On the contrary to MIL-101, for which many types of linker functionalities have been described, MIL-100 is, to the best of our knowledge, always synthesized from non-functionalized trimesic acid. Some efforts in this direction have been performed during this thesis, although the obtained results are not presented in this dissertation. We were able to obtain mixed-linker MIL-100(Fe) samples constructed from trimesate and 2-aminotrimesate linkers. Preliminary results suggest that increasing the amount of 2-aminotrimesate decreases the MOF's formation rate, resulting in smaller particles. However, the availability of the amine functions in the obtained materials could not be evidenced (yet) and needs further investigation.

Concerning functionalization of open-metal sites on MIL-100 MOFs with ethylenediamine, the selective post-functionalization of the "large" and "small" mesopores of the framework could be exploited to develop materials with hierarchically distributed functionalities. Such materials, if well designed, could enable the creation of two distinct types of "pockets" with different active sites for catalysis for example, were consecutive reactions could happen. The functionalization of bimetallic MIL-100 samples should also be investigated further, as two metals are likely to interact differently with the functions of the molecules used for functionalization, and hence modifications could be performed selectively on one metal while leaving the other intact. Some preliminary work concerning this point, not presented in this manuscript, has also been performed. For this purpose, a bimetallic MIL-100(Ti,Zn) sample has been synthesized, and functionalization has been attempted with ethanolamine hydrobromide by direct melting (avoiding the use of solvents for functionalization). The MOF used for this investigation has been chosen because all elements have NMR active nuclei, enabling to use solid-state NMR for understanding the activation and functionalization processes, as well as the distribution of both metals and added functionalities throughout the framework. Functionalization of CUSs could also be performed with more sustainable molecules, eventually creating enantioselective sites, for example by using amino acids.

The adsorption of carbon dioxide under high pressure in Al-containing MIL-100 materials is also worth further fundamental investigation to confirm the hypothesis of an insertion mechanism in the hydroxyl groups. This could be performed through means of *in situ* FTIR and/or solid-state NMR experiments under CO_2 pressure, requiring specialized equipment.

The rare-earth based MOF-76 samples could be used to evaluate their performances towards catalytic applications, and especially to compare them to the ones of bimetallic MIL-100(Fe,RE) samples for determining the importance of the rare-earth size, the types of cluster

and detecting eventual synergistic effects with iron in catalysis. The yield of the "green" synthesis of MOF-76 derivatives in ethanol could be significantly improved by the use of a proton trap (e.g. triethylamine) during the synthesis to avoid the esterification of the linker by the formed HCl. However, this could have a major influence on the crystallization rate, therefore on the size and shape of the obtained particles. Further optimization in this direction is mandatory to envisage scaling-up the synthesis for industrialisation of those MOFs by synthesis in ethanol. The positive effect of amino functions on the linkers of NH_2-MOF-76 on its stability towards water might indicate that substituting trimesate by 2-aminotrimesate could also be used for increasing the water stability of other MOFs. Partial or complete substitution with 2-aminotrimesate could thus also be used for increasing the water stability of MIL-100 samples for even more demanding applications. Finally, the fluorescent properties of MOF-76 derivatives might be interesting for further investigations. Those fluorescent properties could be achieved by metal (e.g. Eu^{3+} and Tb^{3+} for fluorescence in the red and green region of the visible spectrum respectively) and linker (for fluorescence in the blue region) doping, while using a heavy lanthanide as template to increase the stability of the resulting frameworks towards water. Furthermore, the MOF-76 MOFs could be evaluated for catalytic applications (mainly Lewis acid catalysis), and their performances compared to that of bimetallic MIL-100(Fe,Ln) containing the same lanthanide metal centres. Regarding the evaluation of those MOFs for catalytic applications, a particular attention should be paid to the presence of defects, which should ideally be characterized by EXAFS or pair distribution function analysis to correlate structure with activity.

Concerning the development of Ti^{3+} containing MOFs with the mtn topology, it is clear that much is still to be discovered. Several trials, that are not presented in this thesis, were performed to oxidize the Ti^{3+} centres of NH_2-MIL-101(Ti^{III}) into Ti^{4+}, however this systematically led to structural collapse of the framework. The possibility to switch between oxidation states +III to +IV and vice versa

would allow easier storage of this type of materials and their (re)use for different types of applications, including (photo)catalysis. One strategy that could be envisaged to maintain Ti^{3+} CUSs in the MOF while improving the air-resistance of the MOF would be to synthesize bimetallic frameworks, that contain only a small amount of Ti^{3+} (typically with a maximum of one Ti per cluster). The second metal should be redox-inactive (e.g. Al^{3+}) and would ensure the structural integrity of the framework upon exposure to air. The presence of amine sites on NH_2-MIL-101(Ti) could also be useful for post-functionalization, although much care must be taken to avoid oxidation of the metal centres. Furthermore, the amine sites could be useful to envisage the use of this MOF for CO_2 adsorption, although the high sensitivity of this MOF towards oxygen would not enable its use in real-life applications.

Although in this work we limited ourselves to the "model" MOF HKUST-1 for this purpose, we evidenced that structural defects in MOFs have a tremendous impact on their gas sorption and catalytic properties. This highlights that for further applications with more complex structures, like MIL-100 and MIL-101 derivatives, such defects must be considered. However, the high structural complexity of those MOFs renders the characterization of defects sites even more complicated than for HKUST-1. Based on our results concerning the impact of defects, we could expect that for MIL-100 and MIL-101 derivatives, not only the linker and metal making up the MOF are of importance for their properties, but also the charge-balancing anion (which can be F^-, Cl^-, OH^-, EtO^-, etc.). The influence of this charge balancing anion on the MOF's properties is largely overlooked in the literature, and we would like to underline the need for systematically identifying its nature, as it could have similar impact on the properties as structural defects.

Despite MOFs have been discovered a long time ago, much is yet to be done and understood, especially for the most complex structures. Although industrial applications slowly start to emerge, much work still

needs to be done regarding the improvement of the sustainability and scaling-up of the syntheses. We expect that screening reaction conditions towards the discovery of new MOFs, which are currently performed mostly under demanding conditions, will be realized in a more sustainable fashion in the future as it has been demonstrated that less demanding conditions allow obtaining interesting topologies too. Furthermore, by creating softer reaction conditions, the fundamental study of MOF formation would be facilitated, enabling to envisage the design of new synthetic methods based on new knowledge that could be gathered during these mechanistic studies.

Appendices

1. Table of contents of Appendices

Appendices to Chapter II

Appendices to Chapter V

2. Supporting information to Chapter II

Fig. S II-1 A. TGA plot of Li_3BTC under air (gas flow: 100ml/min; heating rate: 10°C/min)

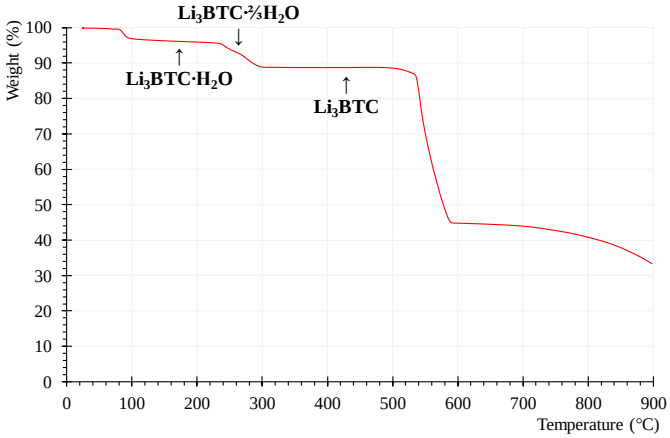

Fig. S II-1 B. TGA plot of Li_3BTC under nitrogen (gas flow: 100ml/min; heating rate: 10°C/min)

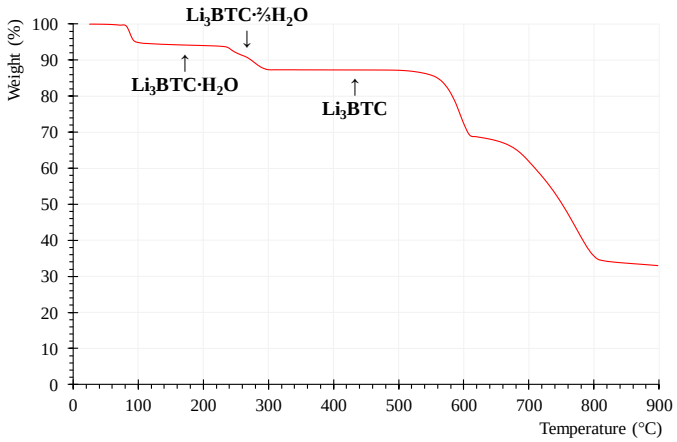

Fig. S II-2 A. TGA plot of Na_3BTC under air (gas flow: 100ml/min; heating rate: 10°C/min)

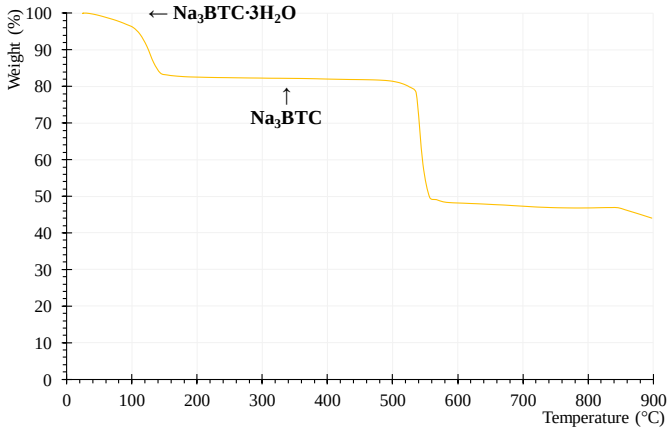

Fig. S II-2 B. TGA plot of Na_3BTC under nitrogen (gas flow: 100ml/min; heating rate: 10°C/min)

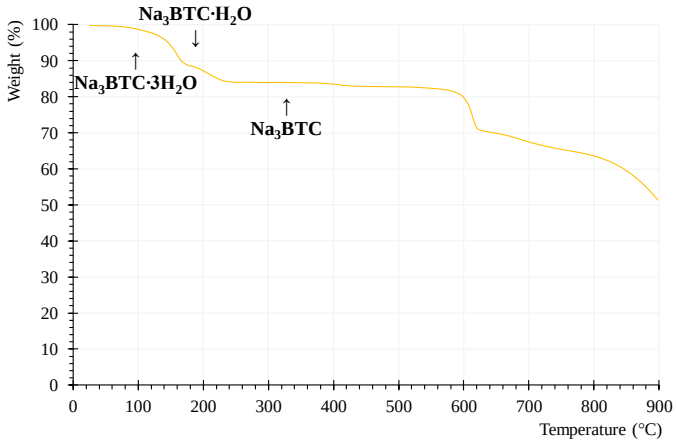

Fig. S II-3 A. TGA plot of K_3BTC under air (gas flow: 100ml/min; heating rate: 10°C/min)

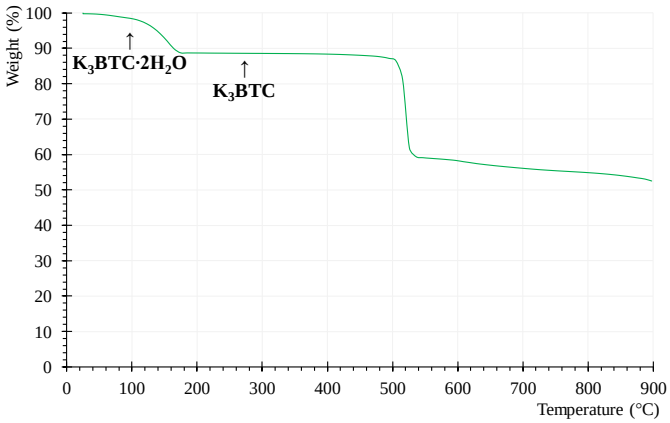

Fig. S II-3 B. TGA plot of K_3BTC under nitrogen (gas flow: 100ml/min; heating rate: 10°C/min)

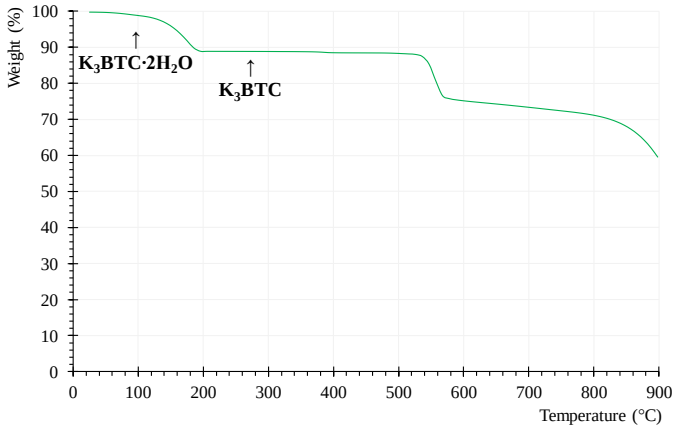

Fig. S II-4 A. TGA plot of Rb_3BTC under air (gas flow: 100ml/min; heating rate: 10°C/min)

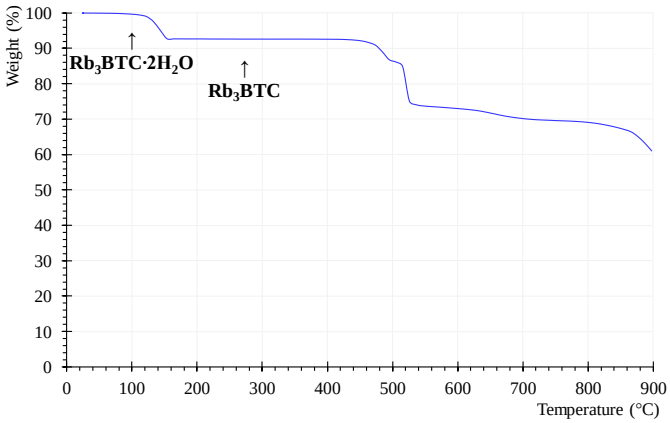

Fig. S II-4 B. TGA plot of Rb_3BTC under nitrogen (gas flow: 100ml/min; heating rate: 10°C/min)

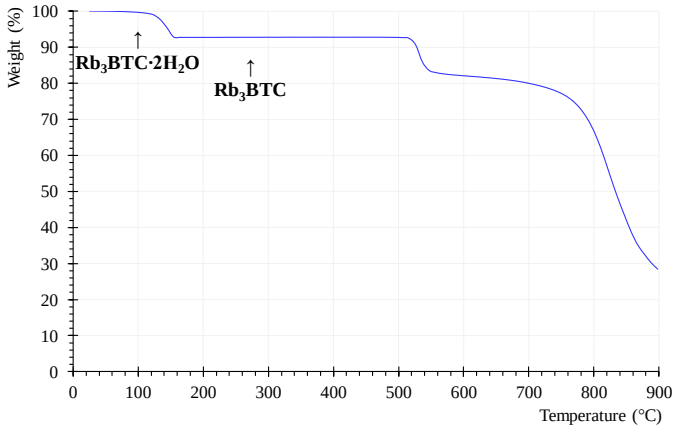

Fig. S II-5 A. TGA plot of Cs_3BTC under air (gas flow: 100ml/min; heating rate: 10°C/min)

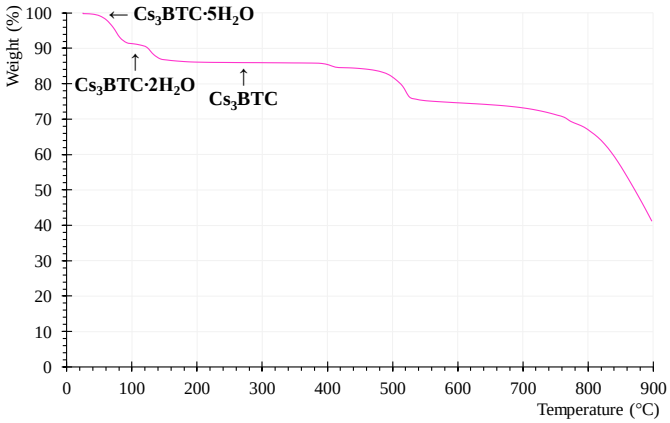

Fig. S II-5 B. TGA plot of Cs_3BTC under nitrogen (gas flow: 100ml/min; heating rate: 10°C/min)

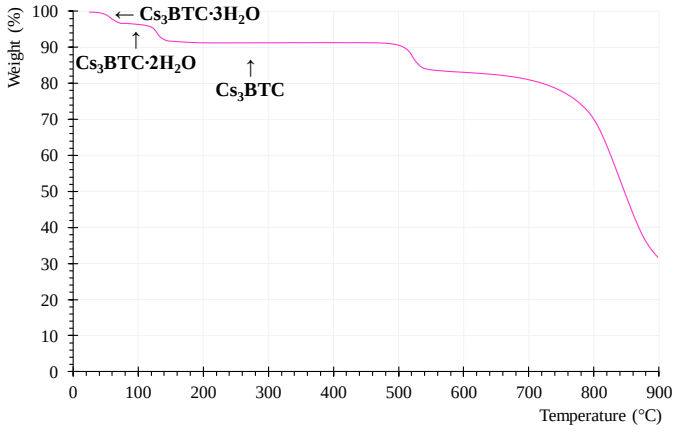

Fig. S II-6. Detail of Raman spectra of $Li_3BTC \cdot H_2O$ and Li_3BTC.

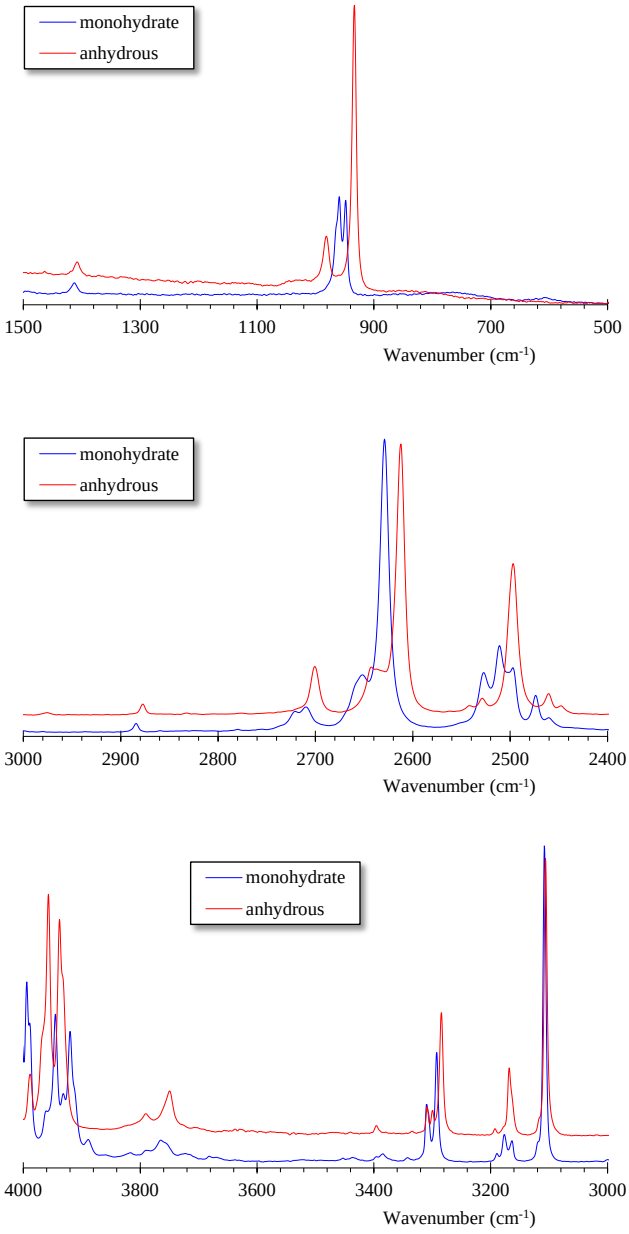

Fig. S II-7. Detail of variable temperature Raman spectra of hydrated sodium trimesate.

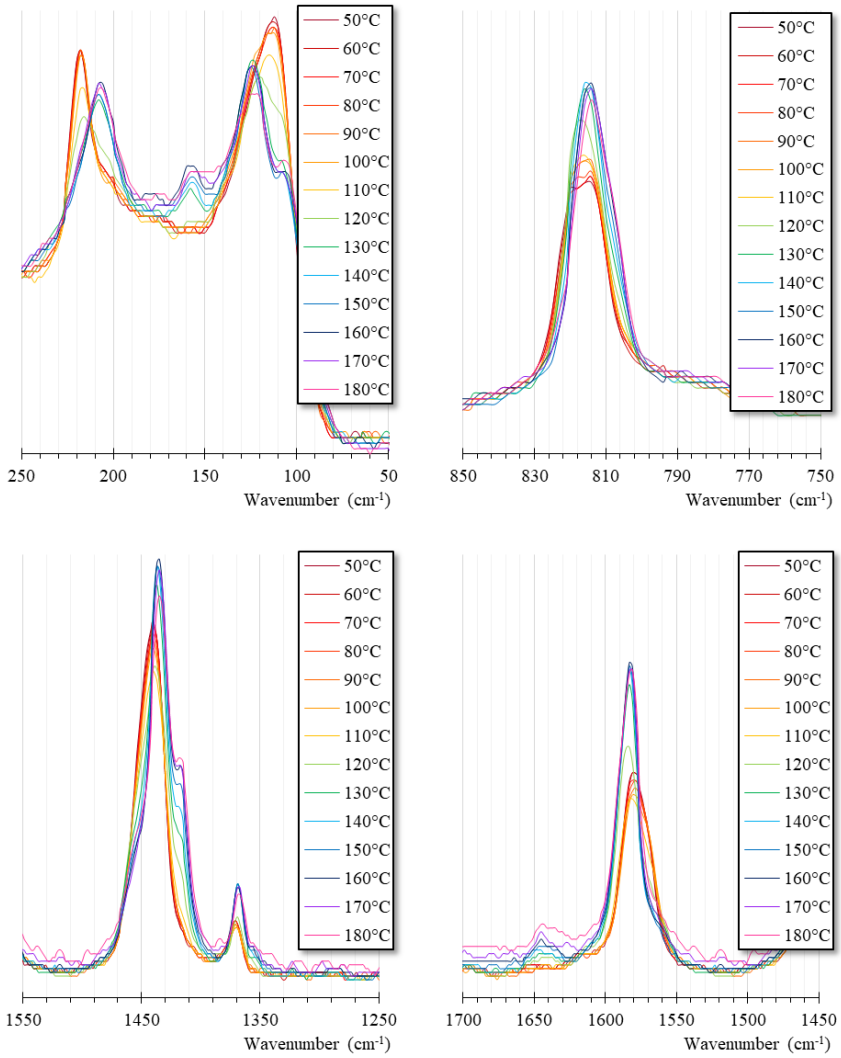

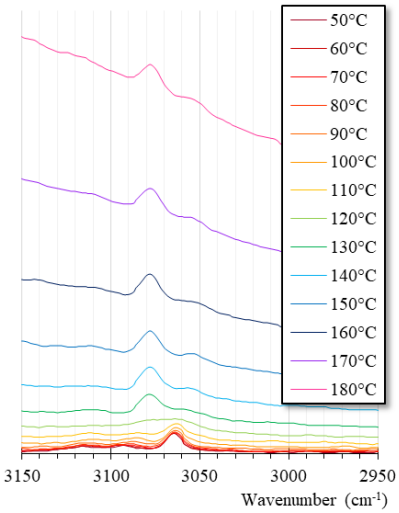

Fig. S II-8. Detail of variable temperature Raman spectra of hydrated rubidium trimesate.

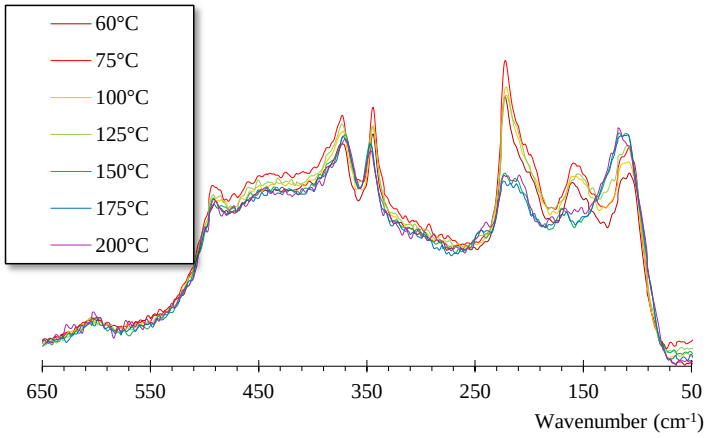

Fig. S II-9. Nitrogen sorption isotherms (77K) (top) and BJH transform plots (bottom) of MIL-100(Fe) obtained in acidic (red curve) and basic medium (blue curve). BET calculated surface areas are 2012 m^2/g and 1542 m^2/g respectively.

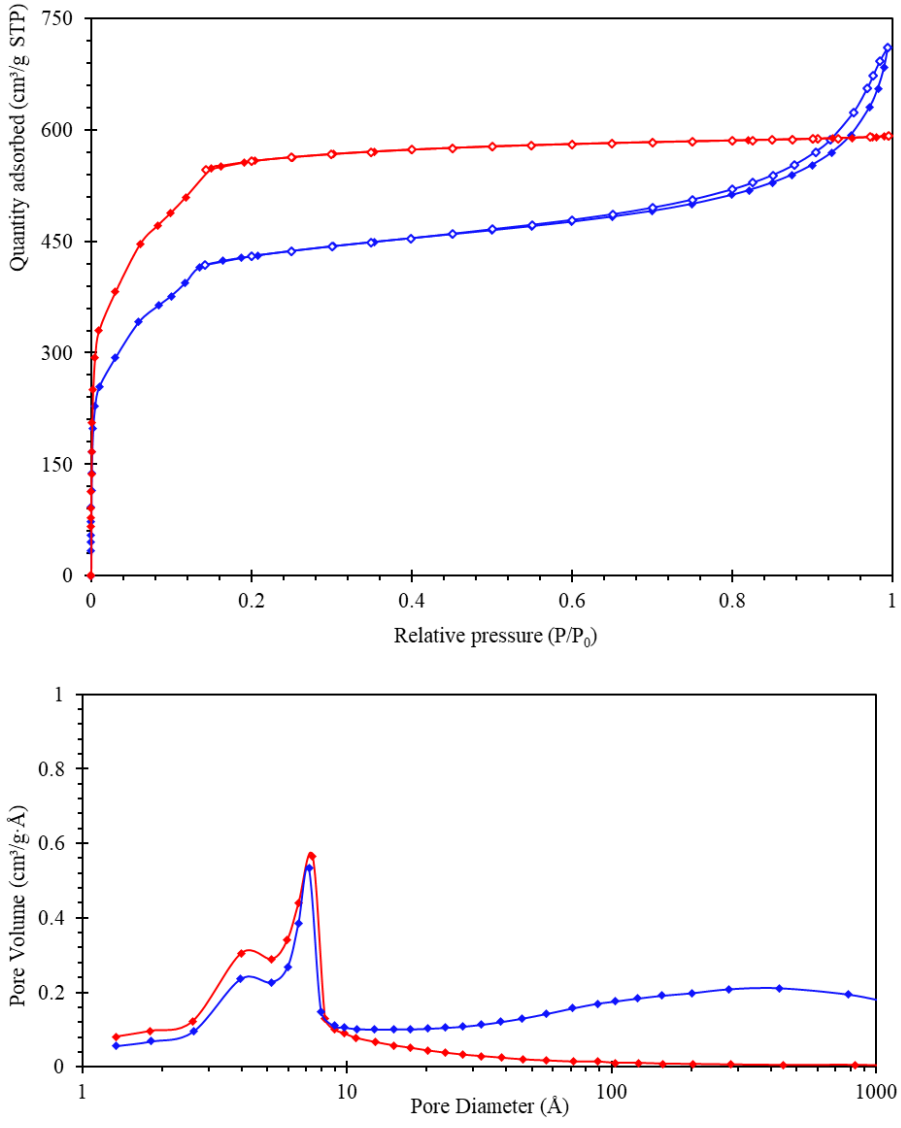

Fig. S II-10. Laboratory measured PXRD patterns of MIL-100(Fe) obtained in acidic and basic conditions.

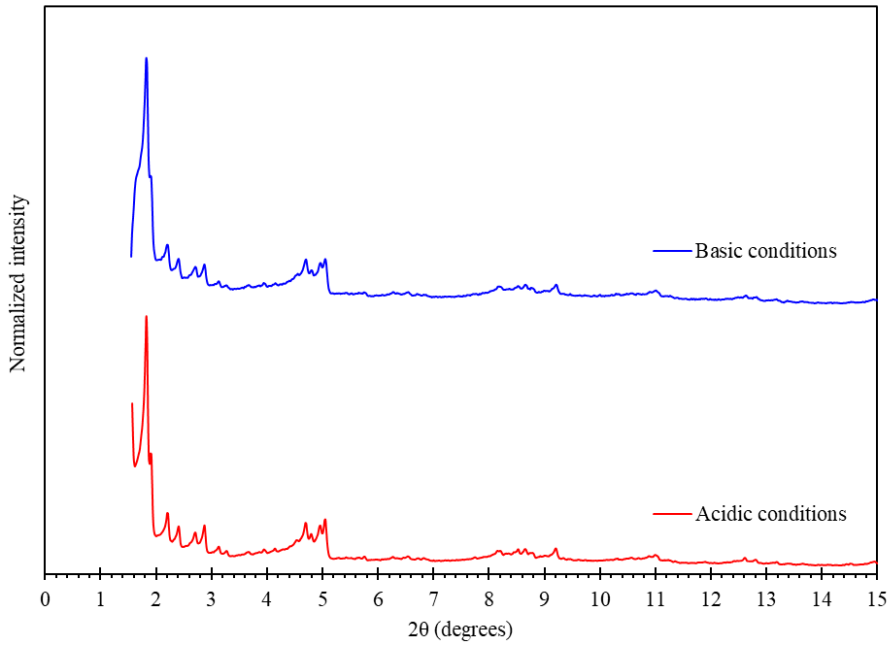

Fig. S II-11. PXRD patterns of MIL-100(Fe) samples obtained from different alkali trimesate precursors.

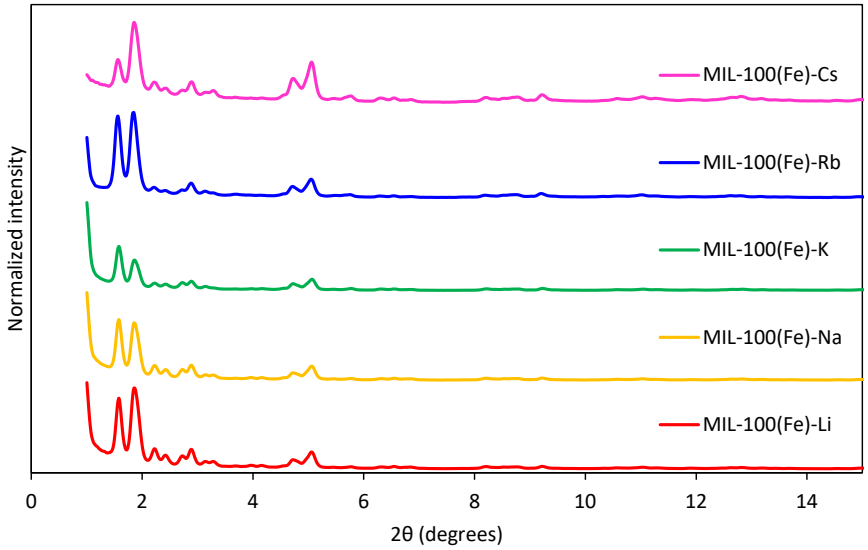

Table S II-1. Calculated BET and Langmuir surface areas of MIL-100(Fe) obtained using various alkali trimesates as precursors.

Sample name	Precursor	S_{BET} ($m^2\ g^{-1}$)	$S_{Langmuir}$ ($m^2\ g^{-1}$)
MIL-100(Fe)-Li	$Li_3BTC{\cdot}H_2O$	2060	2857
MIL-100(Fe)-Na	$Na_3BTC{\cdot}3H_2O$	2173	3006
MIL-100(Fe)-K	K_3BTC	1935	2683
MIL-100(Fe)-Rb	Rb_3BTC	1813	2482
MIL-100(Fe)-Cs	Cs_3BTC	1553	2133

Fig. S II-12. PXRD patterns of isolated Fe_3BTC_2 intermediate and products obtained by various oxidation tests with Br_2, H_2O_2 and I_2 as oxidants in water or hexane as solvents, as well as in vapour form.

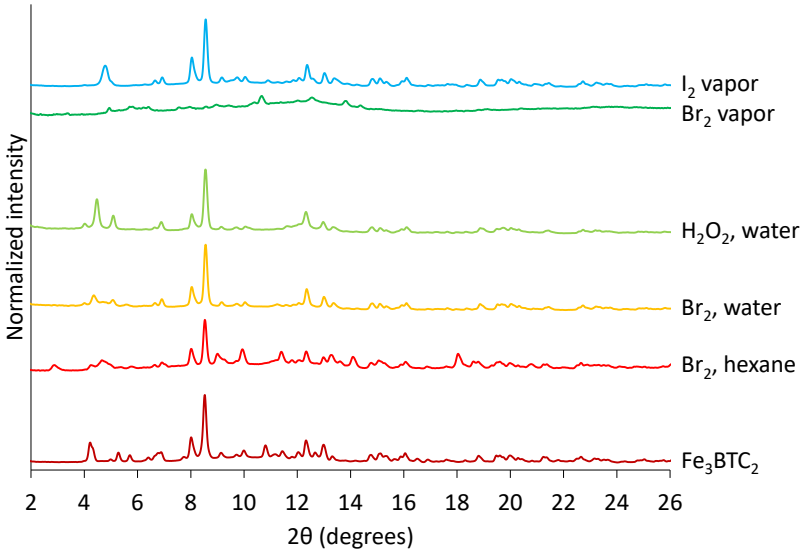

Fig. S II-13. PXRD pattern of the Fe_3BTC_2 intermediate after stirring in ethanol in the presence of air for 4 hours, showing no transformation to MIL-100(Fe).

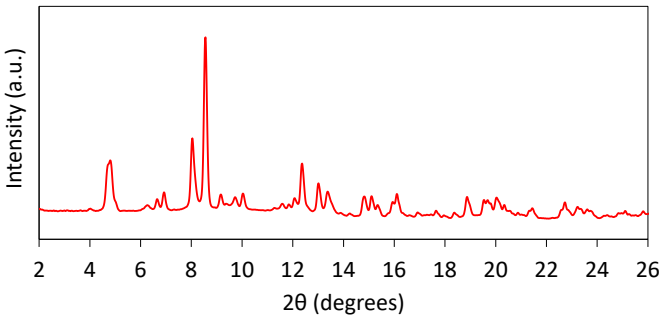

Fig. S II-14. Nitrogen physisorption isotherms (77 K) of MIL-100(Fe) samples obtained using different crystallization modulators.

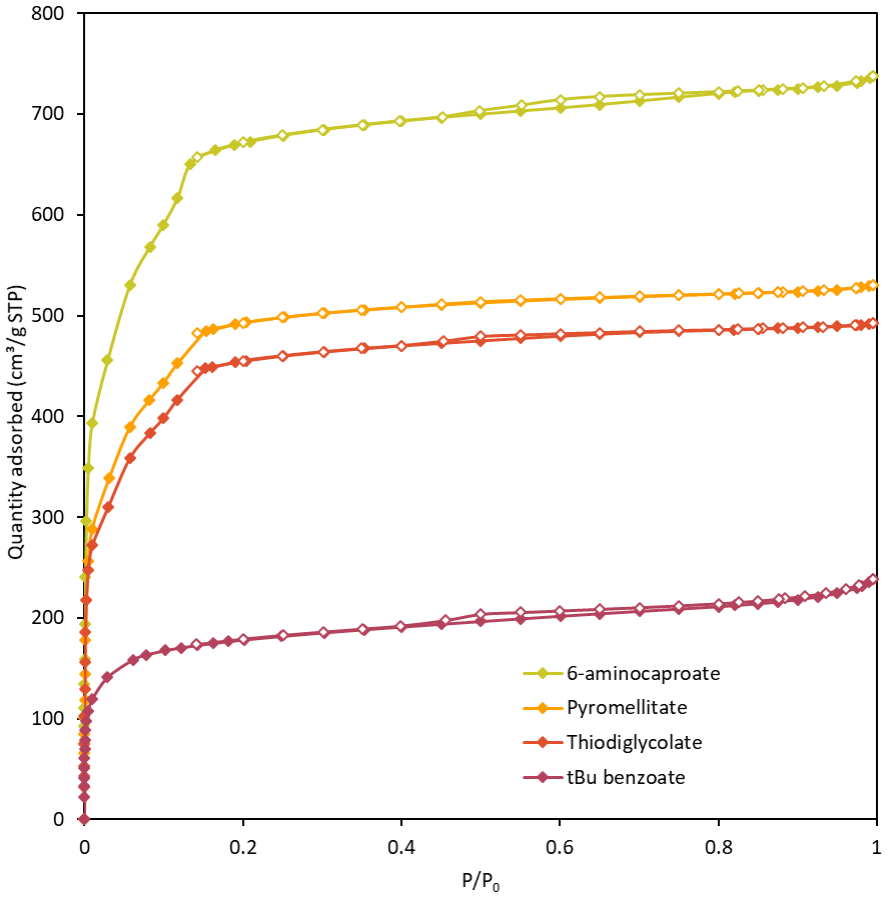

Fig. S II-15. FTIR spectra of MIL-100(Fe) samples obtained using different crystallization modulators. Asterisks indicate IR signals that are observed only for the MIL-100(Fe)-*t*BuBenz sample but not for the ones obtained with other modulators.

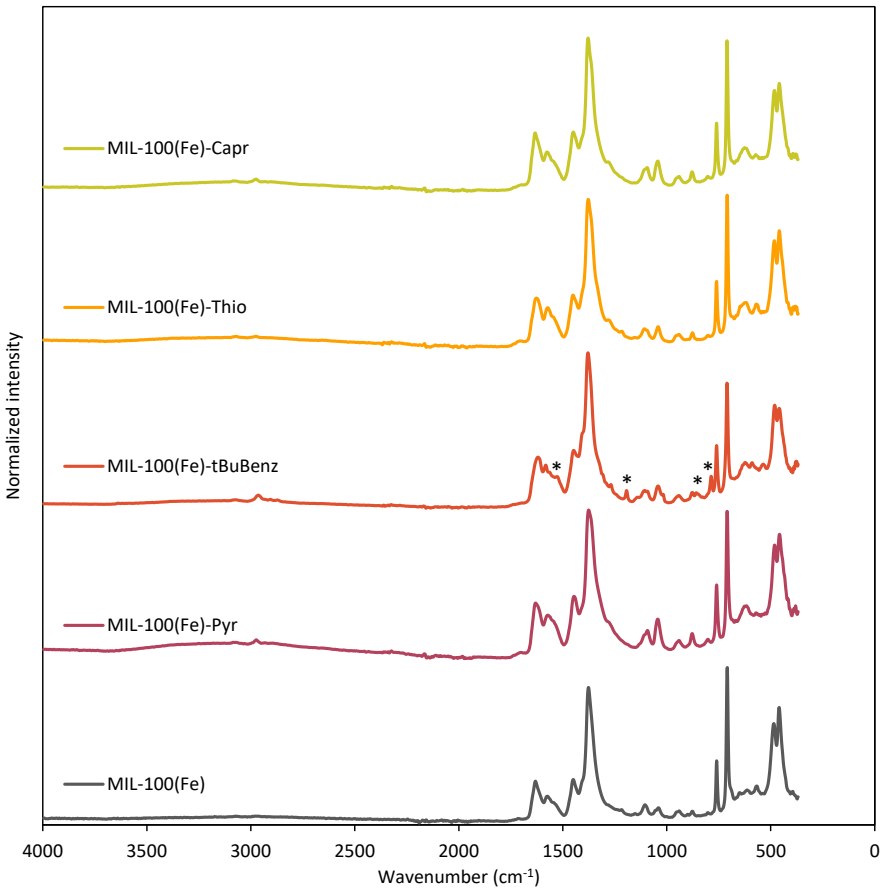

Fig. S II-16. PXRD patterns of MIL-100(Fe) samples obtained using different crystallization modulators and MIL-100(Fe)-Cl after 18 h 20 min gold loading experiment. The diffraction peaks of Au^0 are highlighted in yellow.

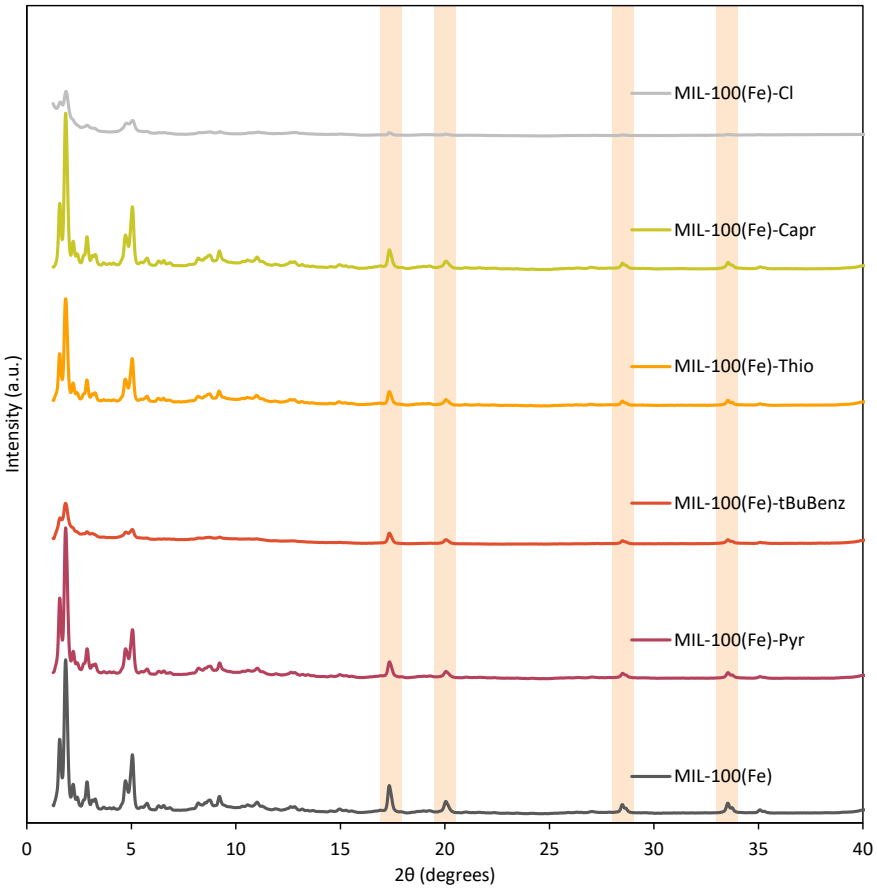

Fig. S II-17. PXRD pattern of the precipitated gold obtained from reaction of $FeSO_4$ and $KAuCl_4$ in water.

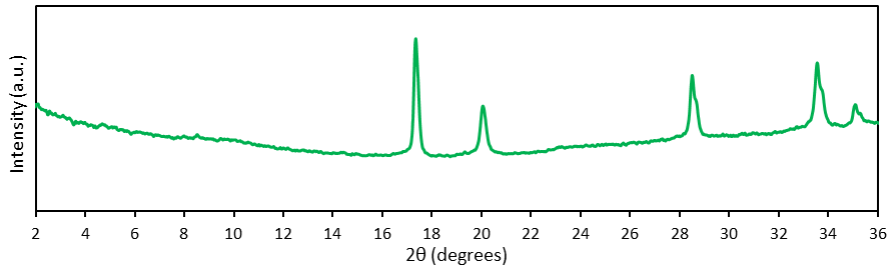

Table S II-2. Results of ICP and chlorine analysis on MIL-100(Fe)-Cl.

Element	**MM**	**Quantity**	
	g.mol^{-1}	mass % [measured]	at. % (on Fe + Cl) [calc.]
Fe	55.85	7.91	77
Cl	35.45	1.5	23

3. Supporting information to Chapter III

The supporting info of this Chapter has been published online (New J. Chem., 2020, *44*, 10, 3847-3855) and is accessible through the following doi: 10.1039/D0NJ00257G.

4. Supporting information to Chapter IV

The supporting info of this Chapter has been published online (Inorg. Chem., 2021, *60*, 21, 16666-166677) and is accessible through the following doi: 10.1021/acs.inorgchem.1c02568.

5. Supporting information to Chapter V

Fig. S V-1. Thermogravimetric analyses of LaBTC samples obtained in ethanol with different precursor concentrations and reactions temperatures. Upper left: TGA curves; Right: experimental and theoretical weight losses, together with the weight loss at decomposition of LaBTC$(H_2O)_6$ (synthesis in DMF/H_2O); Lower left: decomposition temperatures.

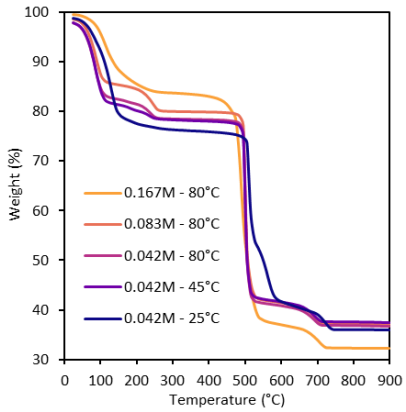

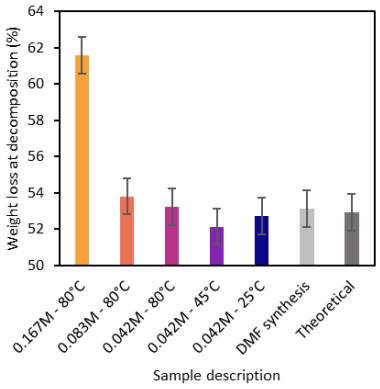

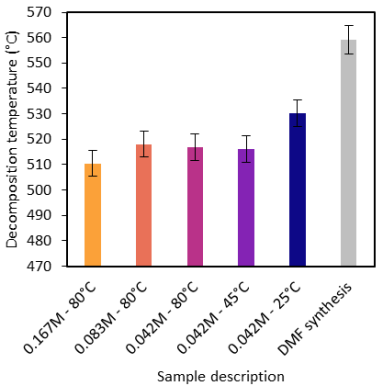

Fig. S V-2. Yields of LaBTC in ethanol synthesis using different precursor concentrations and reaction temperatures.

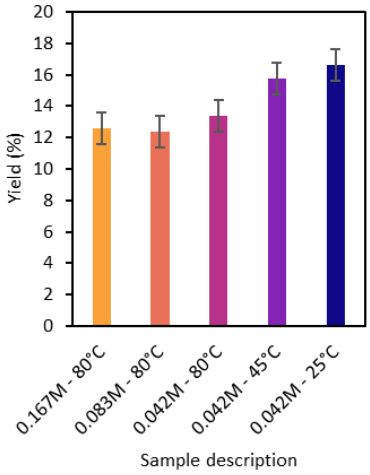

Fig. S V-3. PXRD patterns of MOF samples obtained in ethanolic solution with 0.042 M precursor concentrations at 80°C for several RE metals. Only La, Ce, Pr, Nd and Yb present the MOF-76 topology.

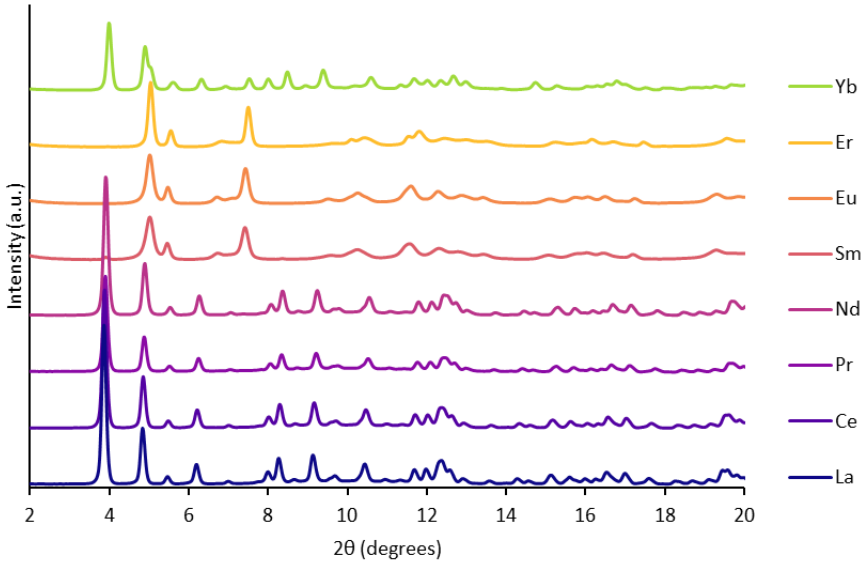

Fig. S V-4. PXRD patterns of MOF samples obtained in DMF/H_2O (75/25) solution with 0.042 M precursor concentrations at 80°C for several RE metals. The MOF-76 topology is obtained for all lanthanide metals, but not for La.

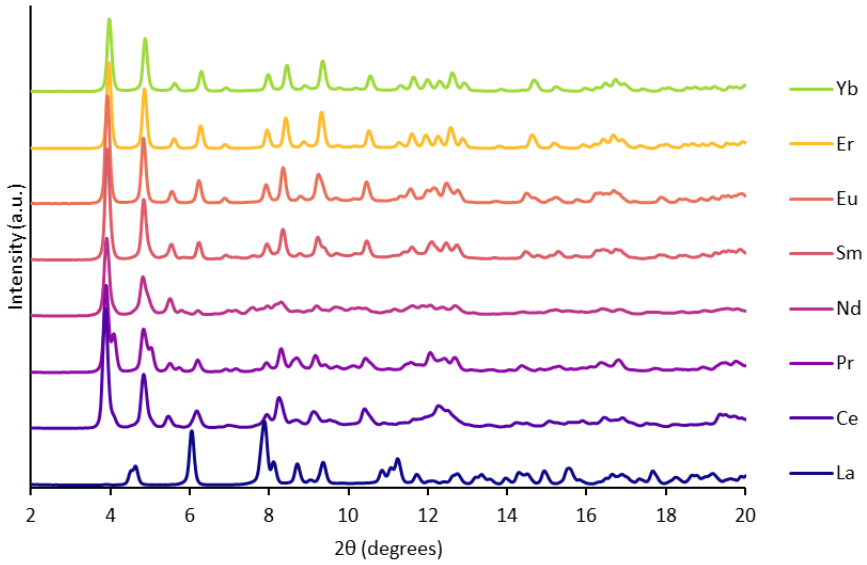

Simulated powder pattern of $LaBTC(H_2O)_6$ [CCDC Refcode: KEBSOA]

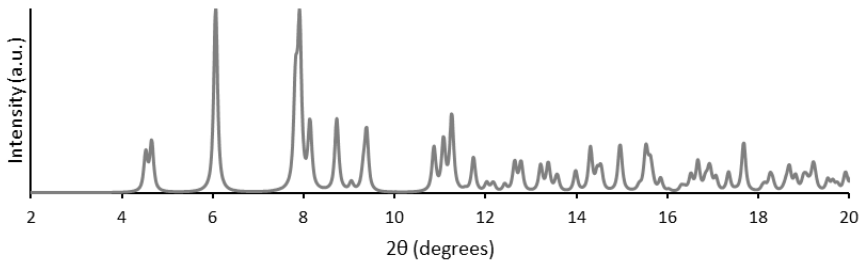

Fig. S V-5. FTIR spectra of LnBTC samples obtained in ethanol (YbBTC was not measured).

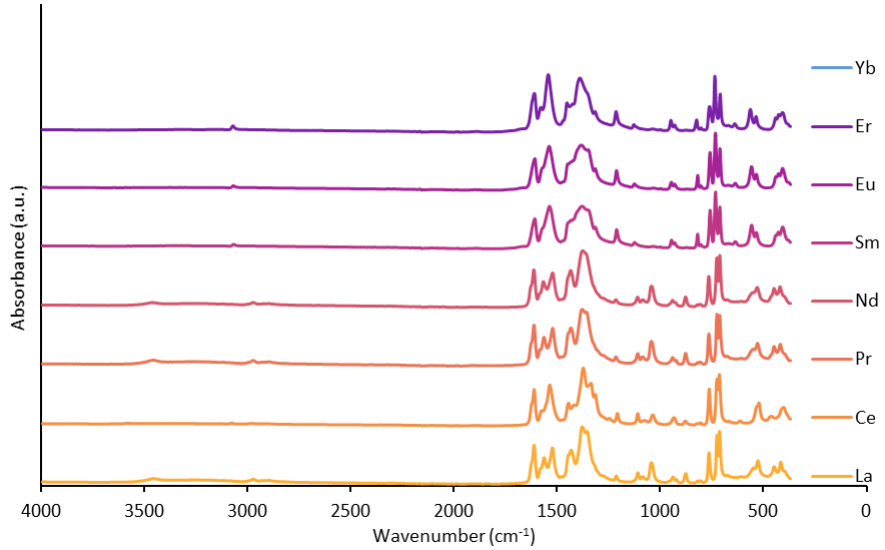

Fig. S V-6. FTIR spectra of LnBTC samples obtained in DMF/water.

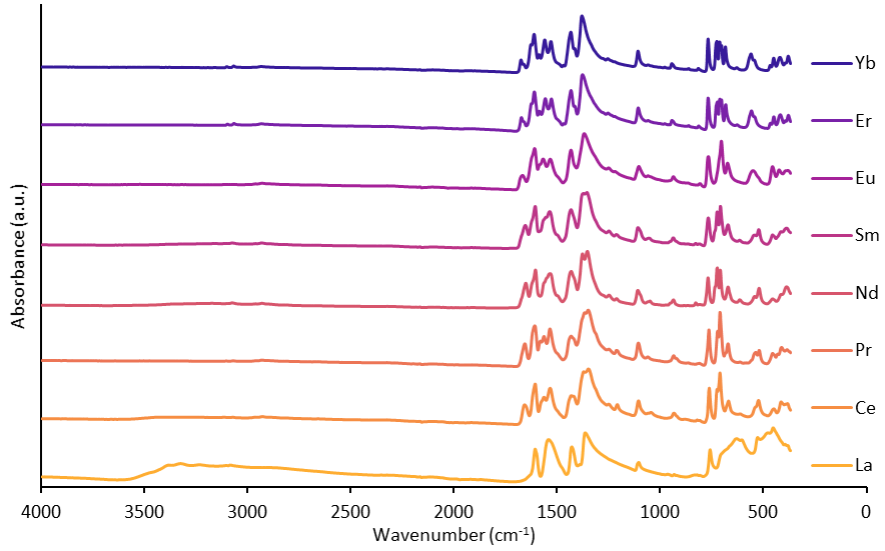

Fig. S V-7. Thermogravimetric analyses (under air) of MOF-76(Ln) (Ln = Ce and Pr) obtained in ethanol and DMF/water mixtures.

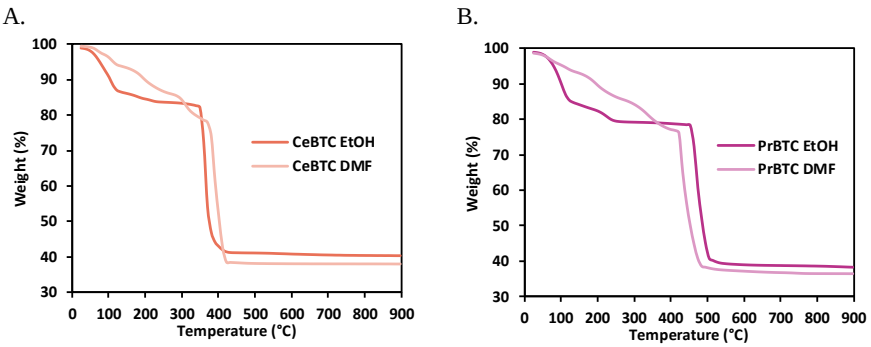

Fig. S V-8. Nitrogen sorption isotherms of MOF-76(Pr) obtained in ethanol and DMF/water mixture upon activation at 200°C and 350°C.

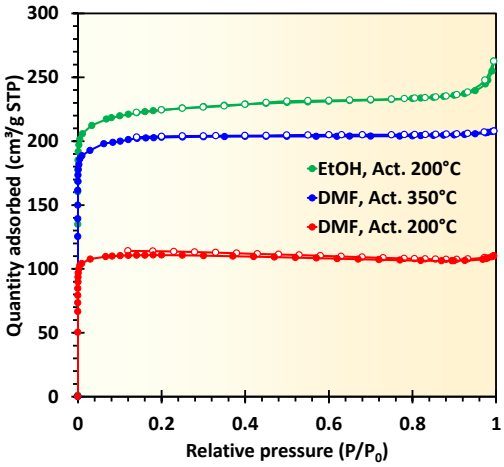

Fig. S V-9. ^{1}H-NMR spectra of trimesic acid, the organic residue obtained after separation of lanthanum of the unreacted material from the LaBTC synthesis and 1,3,5-triethyltrimesate ester. The residual signal of DMSO-d^{5} (2.5 ppm, quintuplet) and the signal of water (3.33 ppm, broad singlet) are omitted for clarity.

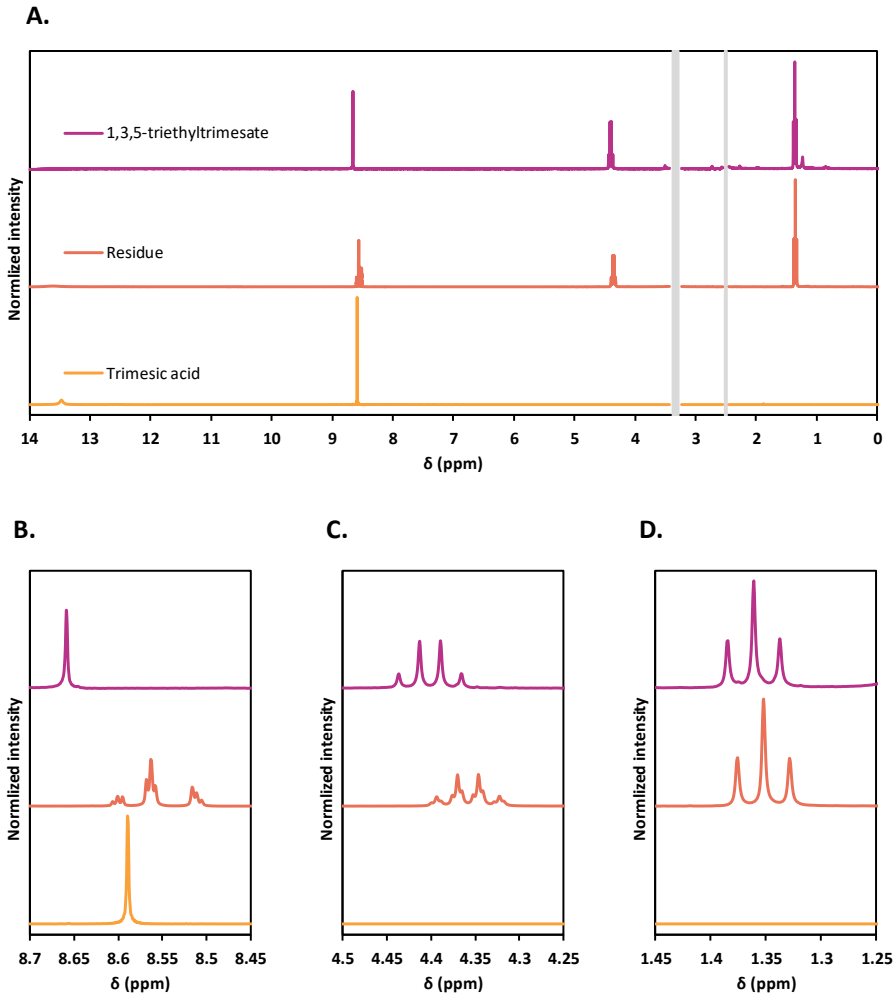

Fig. S V-10. pH follow-up of the synthesis of MOF-76(La) at 80°C. The electrode of the pH meter was calibrated in aqueous solution (hence the negative values).

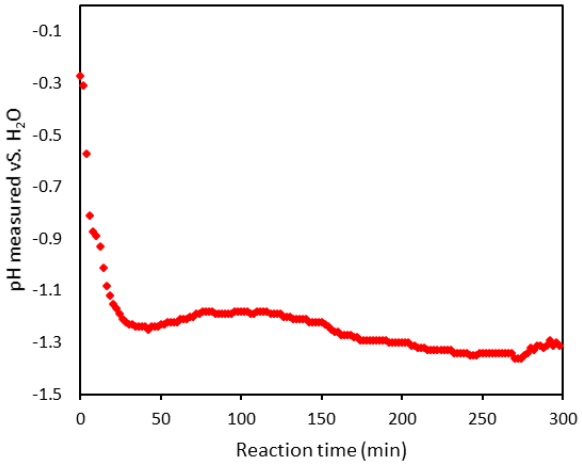

Fig. S V-11. In situ ^{1}H-NMR spectra of the synthesis of MOF-76(La) in EtOD at 80°C, showing the formation of the mono- and di-ester with time.

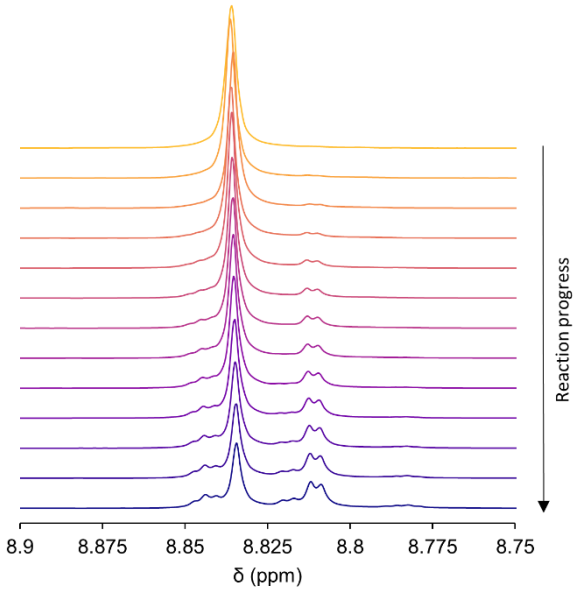

Fig. S V-12. In situ ^{139}La-NMR spectra of the synthesis of MOF-76(La) in EtOD at 80°C, evidencing the coordination of La to carboxylate.

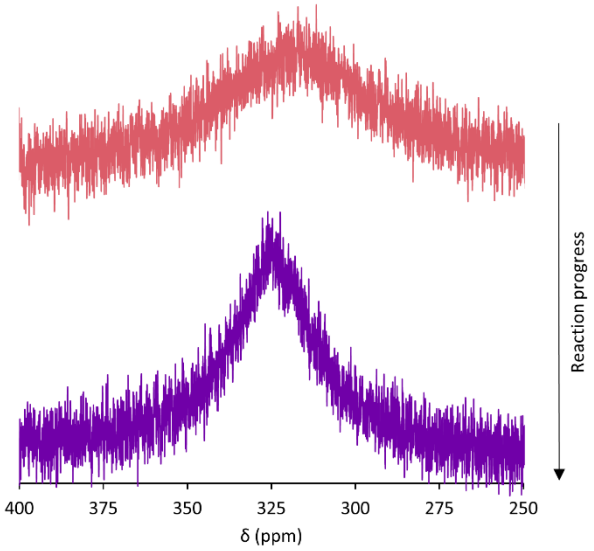

Fig. S V-13. PXRD pattern of MOF-76(Er) upon exposure to water at 100°C for 3 days.

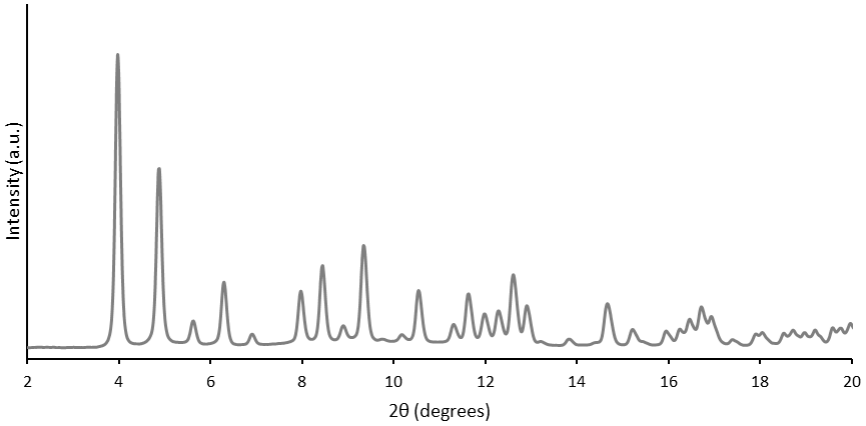

Fig. S V-14. PXRD pattern of MOF-76(Yb) upon exposure to water at 100°C for 3 days.

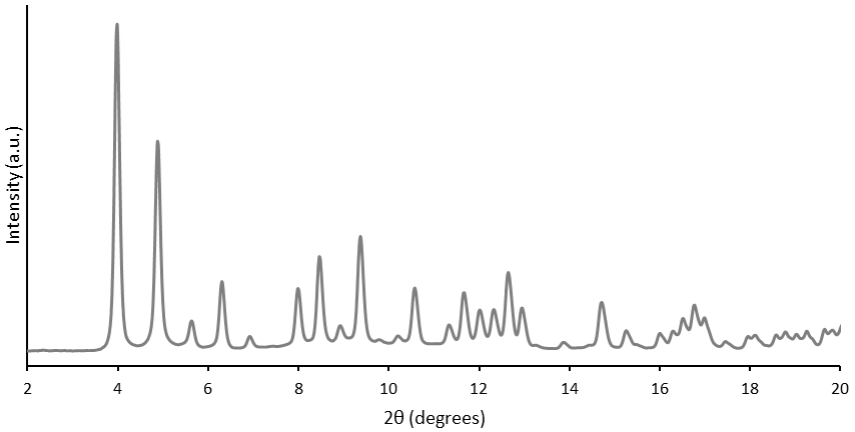

Fig. S V-15. FTIR spectrum of as-synthesized MOF-76(La)-NH_2.

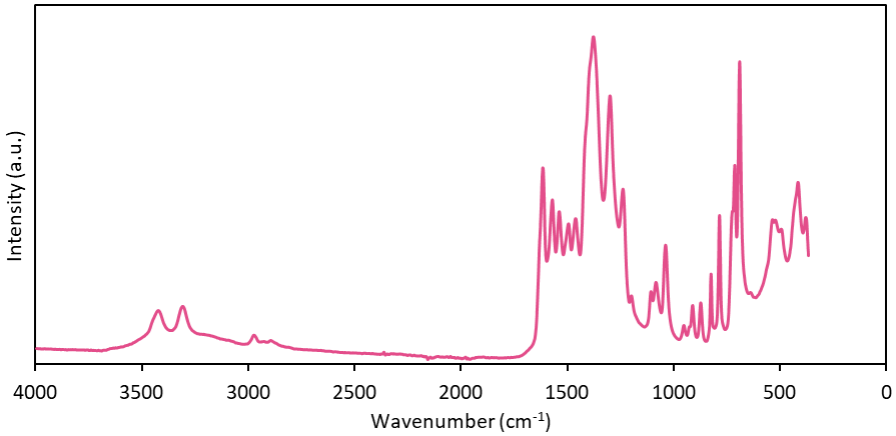

Fig. S V-16. Photography of MOF-76(La)-NH_2 sample under UV irradiation.

Table S V-1. Crystallographic data for the MOF-76(La)-NH_2 structure.

Empirical formula	C11.12 H8.95 La N1.71 O7
Formula weight	417.42
Temperature	298(2) K
Wavelength	0.71073 Å
Crystal system	Tetragonal
Space group	$P4_12_12$
Unit cell dimensions	a = 14.80431(18) Å
	b = 14.80431(18) Å
	c = 14.3104(3) Å
Volume	3136.37(10) $Å^3$
Z	8
Density (calculated)	1.768 g/cm^3
Absorption coefficient	2.753 mm^{-1}
F(000)	1605
Crystal size	0.20 x 0.05 x 0.04 mm^3
Theta range for data collection	3.077 to 26.182°.
Reflections collected	10439
Independent reflections	3136 [R(int) = 0.0261]
Completeness to θ = 25.242°	99.6 %
Absorption correction	Semi-empirical from equivalents
Max. and min. transmission	1.00000 and 0.94665
Refinement method	Full-matrix least-squares on F^2
Data / restraints / parameters	3136 / 334 / 280
Goodness-of-fit on F^2	1.074
Final R indices [I>2sigma(I)]	R_1 = 0.0274, wR_2 = 0.0680
R indices (all data)	R_1 = 0.0287, wR_2 = 0.0686
Absolute structure parameter	0.45(4)
Δρ max min	0.576 and -0.407 $e.Å^{-3}$

Fig. S V-17. Variable-temperature PXRD pattern of MOF-76(La) obtained in ethanol.

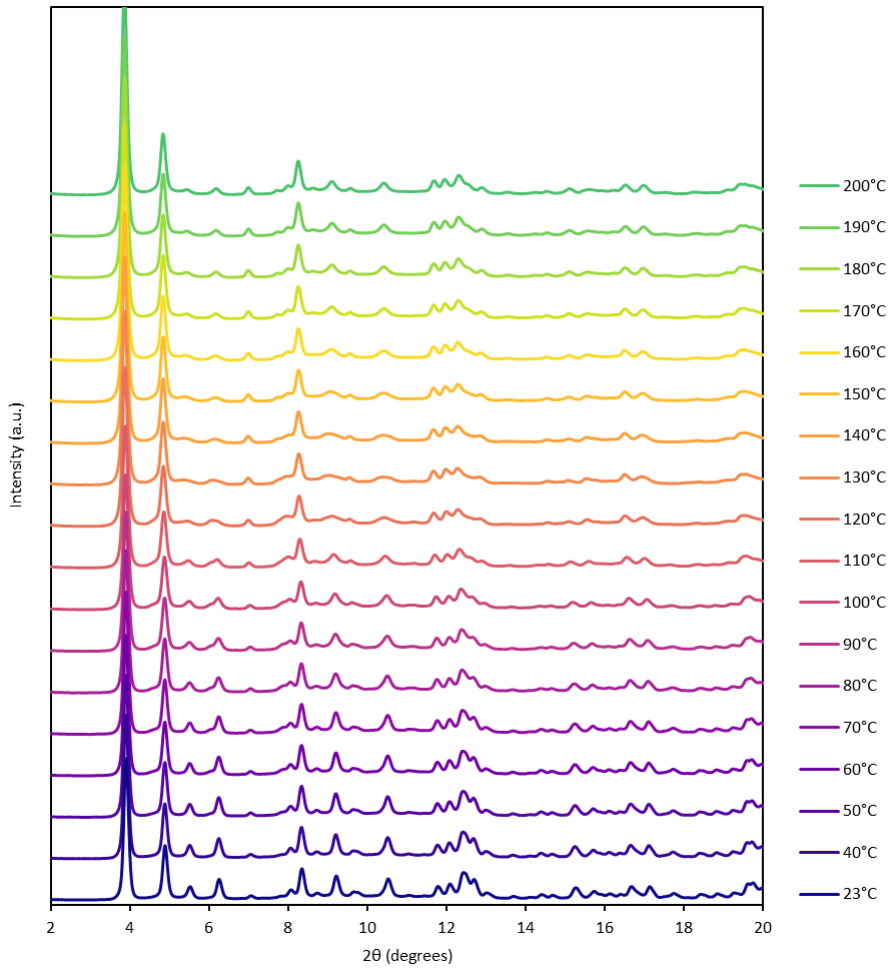

Fig. S V-18. Variable-temperature PXRD pattern of MOF-76(La)-NH_2 obtained in ethanol.

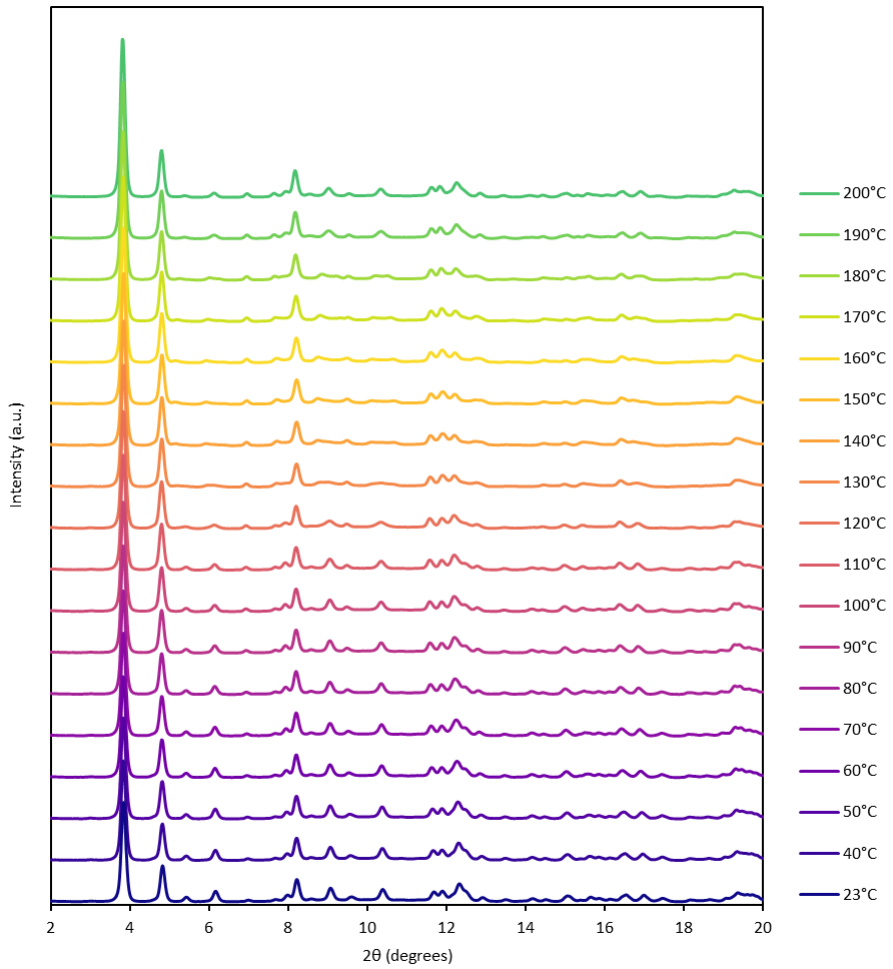

Fig. S V-19. Optical micrographs of MOF-76(La) sample obtained after scale up of the reaction in a 2.5 L reactor, using 0.042M concentration of precursors at 80°C. A. and D. Crossed polarizers, B. and E. transmission, C. and F. polarization with λ retardation plate and crossed polarizers.

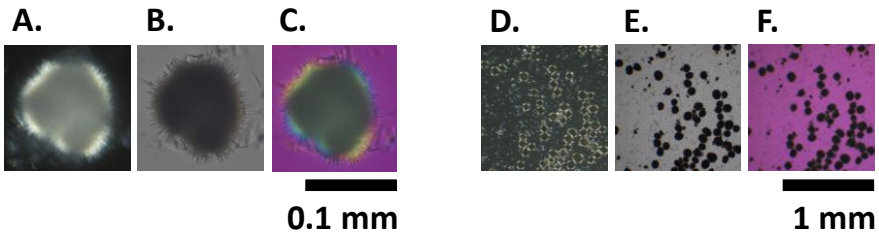

Fig. S V-20. PXRD patterns of MOF-76(La) sample obtained on a small-scale synthesis (100 ml reactor) and after a scale-up (2500 ml reactor).

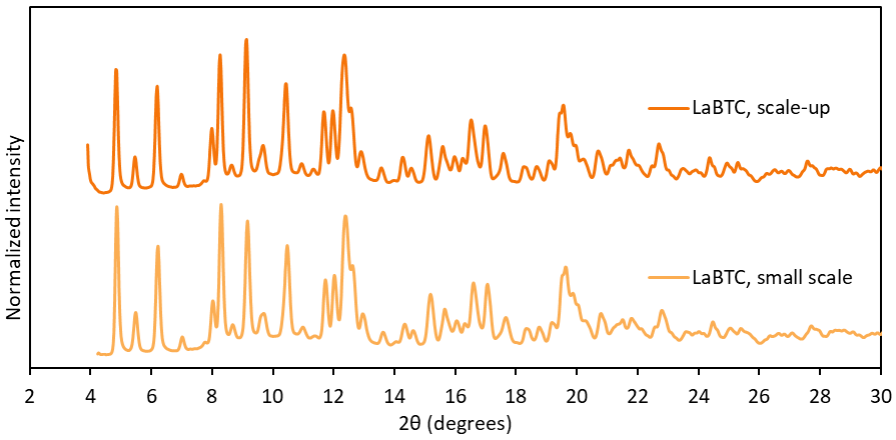

Fig. S V-21. Nitrogen sorption isotherm (77K) of the scaled-up MOF-76(La) sample obtained in ethanol.

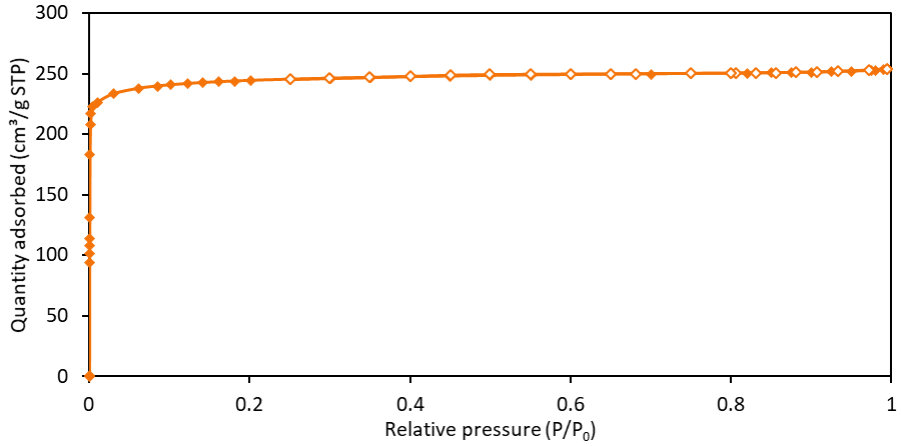

Fig. S V-22. FTIR spectra of some of the lanthanide(III) chloride hydrates (Ln = La, Ce, Pr and Sm) as obtained from their oxides, acetate or carbonate, and FTIR spectrum of the recycled lanthanum(III) chloride isolated from the filtrate of the scaled-up MOF-76(La) MOF synthesis.

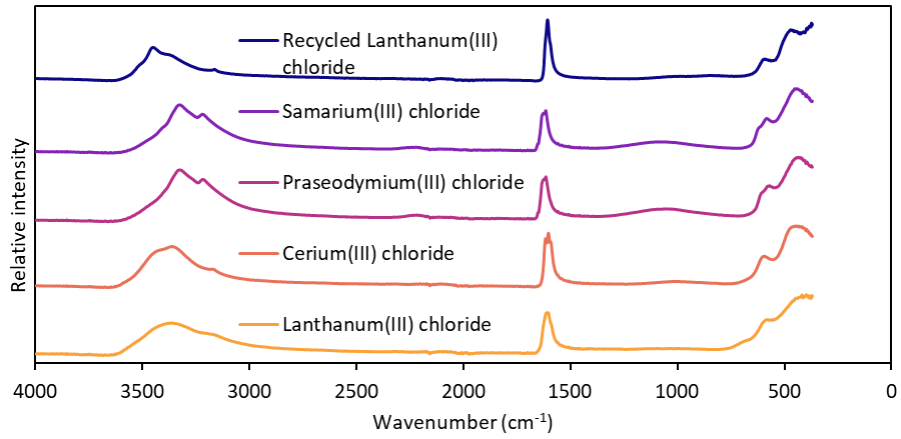

Fig. S V-23. FTIR spectra of (lower, grey) MOF-76(La) obtained in ethanol and (upper, pink) sample obtained from recycled materials.

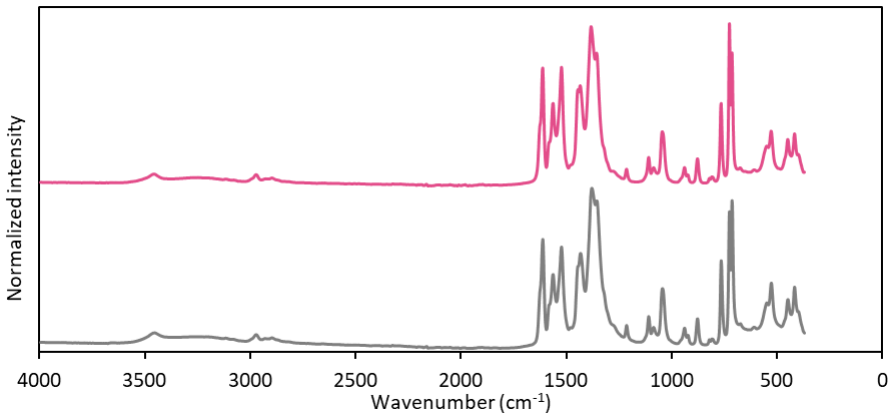

6. Supporting information to Chapter VI

The supporting info of this Chapter has been deposited online (ChemRxiv) and is accessible through the following doi: 10.26434/chemrxiv-2021-8rdgv.

7. Supporting information to Chapter VII

The supporting info of this Chapter has been published online (RSC Advances., 2020, *10*, 34, 19822-19831) and is accessible through the following doi: 10.1039/c9ra10412g.

Publications and scientific Communications

1. Articles published in peer-review journals

1.1.

Desmecht, A.; **Steenhaut, T.**; Pennetreau, F.; Hermans, S.; Riant, O. *Synthesis and Catalytic Applications of Multi-Walled Carbon Nanotube-Polyamidoamine Dendrimer Hybrids*, Chemistry: A European Journal, **2018**, *24*, 12992-13001, doi: 10.1002/chem.201802301.

1.2.

Iakunkov, A. ; Klechikov, A. ; Sun, J. ; **Steenhaut, T.**; Hermans, S.; Filinchuk, Y.; Talyzin, A. *Gravimetric tank method to evaluate material-enhanced hydrogen storage by physisorbing materials*, Physical Chemistry Chemical Physics, **2018**, *20*, 44, 27983-27991, doi: 10.1039/c8cp05241g.

1.3.

Steenhaut, T.; Hermans, S.; Filinchuk, Y. *Green synthesis of a large series of bimetallic MIL-100(Fe) MOFs*, New Journal of Chemistry, **2020**, *44*, 3847-3855, doi: 10.1039/d0nj00257g / ***journal back cover***.

1.4.

Steenhaut, T.; Grégoire, N., Barozzino-Consiglio, G., Filinchuk. Y. ; Hermans, S. *Mechanochemical defect engineering of HKUST-1 and impact of the resulting defects on carbon dioxide sorption and catalytic cyclopropanation*, RSC Advances, **2020**, *10*, 34, 19822-1931, doi: 10.1039/c9ra10412g.

1.5.

Hassen, S.; Chebbi, H.; Arfaoui, Y.; Robeyns, K. ; **Steenhaut, T.** ; Hermans, S. ; Filinchuk, Y. *Spectroscopic and structural studies,*

thermal characterization, optical properties and theoretical investigation of 2-aminobenzimidazolium tetrachlorocobaltate(II), Spectrochimica Acta Part A: Molecular and Biomolecular Spectroscopy, **2020**, *240*, 118612, doi:10.1016/j.saa.2020.118612.

1.6.

Steenhaut, T.; Filinchuk, Y.; Hermans, S. *Aluminium-based MIL-100(Al) and MIL-101(Al) metal-organic frameworks, derivative materials and composites: synthesis, structure, properties and applications*, Journal of Materials Chemistry A, **2021**, *9*, 38, 21483-21509, doi: 10.1039/D1TA04444C / ***26 page review / Journal front cover***.

1.7.

Steenhaut, T.; Fusaro, L.; Robeyns, K.; Lacour, S.; Li, X.; Mahy, J. ; Louppe, V. ; Grégoire, N. ; Barozzino-Consiglio, G. ; Statsyns, J.-F. ; Aprile ; C. ; Filinchuk, Y., Hermans, S. *Functionalization of mono- and bimetallic MIL-100(Al,Fe) MOFs by ethylenediamine: postfunctionalization, Brønsted acido-basicity, and unusual CO_2 sorption behaviour*, Inorganic Chemistry, **2021**, *60*, 21, 16666-16677, doi: 10.1021/acs.inorgchem.1c02568.

2. Submitted articles

2.1.

Benzaqui, M.; Wahiduzzaman, M.; Zhao, H.; Hasan, Md R.; **Steenhaut T.**; Saad, A.; Marrot, J., Normand P.; Grenèche, J.-M.; Heymans N.; De Weireld, G.; Tissot, A.; Shepard, W.; Filinchuk, Y.; Hermans, S.; Carn, F.; Manlankowska, M.; Téllez, C.; Coronas, J.; Maurin, G.; Steunou, N.; Serre, C. *A Robust Eco-compatible Microporous Iron Coordination Polymer for CO_2 capture*, Submitted to Journal of Materials Chemistry A.

2.2.

Golub, I. E.; Heere, M.; Gounaris, V.; Li, X.; **Steenhaut, T.**; Wang, J.; Robeyns, K.; Li, H.-W.; Dovgaliuk, I.; Ikeda, K.; Hautier, G.; Filinchuk, Y. *Structural insight into solid-state Mg-ion conductor in magnesium borohydride – ethylenediamine system*, Submitted to Chemical Communications.

2.3.

Steenhaut, T.; Lacour, S.; Barozzino-Consiglio, G.; Robeyns, R.; Crits, R.; Hermans, S.; Filinchuk, Y. *Synthesis, structure and thermal stability of a mesoporous titanium(III) amine containing MOF with improved hydrogen sorption properties*, Pre-published online on ChemRxiv^{TM} (doi: 10.26434/chemrxiv-2021-8rdgv), to be submitted to Inorg. Chem.

3. Presentations meetings and conferences

3.1.

Steenhaut, T.; Hermans, S.; Filinchuk, Y. *How we use metal substitutions in MOFs (HKUST-1 and MIL-100)*, Meeting of the FNRS contact group for Synchrotron Radiation, **25/04/2019**, Louvain-la-Neuve, Belgium / oral.

3.2.

Steenhaut, T.; Filinchuk, Y.; Hermans, S. *Easy synthesis of complex bimetallic Metal-Organic Frameworks*, IMCN Ph.D. Student's Day 2019, **29/05/2019**, Louvain-la-Neuve, Belgium / poster.

3.3.

Steenhaut, T.; Louppe, V.; Grégoire, N.; Hermans, S. ; Filinchuk, Y. *Metal doping in Metal-Organic Frameworks to improve hydrogen sorption*, Gordon Research Conference (GRC) on Hydrogen-Metal Systems, **30/06/2019-05/07/2019**, Castelldefels, Spain / poster.

3.4.

Wang, J.; Golub, I.; **Steenhaut, T.**; Li, H.-W.; Filinchuk, Y. *High yield selective synthesis of $Na_2B_{12}H_{12}$ with autoclave method*, Kyushu University Energy Week, **27/01/2020-31/01/2020**, Fukuoka, Japan / poster.

3.5.

Steenhaut, T.; Filinchuk. Y.; Hermans, S. *Metal and ligand doping in highly porous Metal-Organic Frameworks*, IMCN Ph. D. Students' Day 2021, **21/05/2021**, Louvain-la-Neuve, Belgium / videoclip / best videoclip award.

References

1 S. R. Batten, N. R. Champness, X.-M. Chen, J. Garcia-Martinez, S. Kitagawa, L. Öhrström, M. O'Keeffe, M. Paik Suh and J. Reedijk, *Pure Appl. Chem.*, 2013, **85**, 1715–1724.

2 M. J. Kalmutzki, N. Hanikel and O. M. Yaghi, *Sci. Adv.*, 2018, **4**, eaat9180.

3 E. Barea, C. Montoro and J. A. R. Navarro, *Chem. Soc. Rev.*, 2014, **43**, 5419–5430.

4 J. Li, X. Wang, G. Zhao, C. Chen, Z. Chai, A. Alsaedi, T. Hayat and X. Wang, *Chem. Soc. Rev.*, 2018, **47**, 2322–2356.

5 S. Ramanayaka, M. Vithanage, A. Sarmah, T. An, K. H. Kim and Y. S. Ok, *RSC Adv.*, 2019, **9**, 34359–34376.

6 L. Rani, J. Kaushal, A. L. Srivastav and P. Mahajan, *Environ. Sci. Pollut. Res.*, , DOI:10.1007/s11356-020-10738-8.

7 Z. Hu, Y. Wang, B. B. Shah and D. Zhao, *Adv. Sustain. Syst.*, 2019, **3**, 1800080.

8 T. Ghanbari, F. Abnisa and W. M. A. Wan Daud, *Sci. Total Environ.*, 2020, **707**, 135090.

9 N. Gargiulo, A. Peluso and D. Caputo, *Processes*, 2020, **8**, 1–21.

10 H. Wang, Q. L. Zhu, R. Zou and Q. Xu, *Chem*, 2017, **2**, 52–80.

11 R. Zhao, Z. Liang, R. Zou and Q. Xu, *Joule*, 2018, **2**, 2235–2259.

12 C. C. Hou and Q. Xu, *Adv. Energy Mater.*, 2019, **9**, 1801307.

13 X. Zhang, A. Chen, M. Zhong, Z. Zhang, X. Zhang, Z. Zhou and X.-H. Bu, *Electrochem. Energy Rev.*, 2019, **2**, 29–104.

14 A. Ahmed, S. Seth, J. Purewal, A. G. Wong-Foy, M. Veenstra, A. J. Matzger and D. J. Siegel, *Nat. Commun.*, , DOI:10.1038/s41467-019-09365-w.

15 L. Wang, M. Zheng and Z. Xie, *J. Mater. Chem. B*, 2018, **6**, 707–717.

16 Y. Sun, L. Zheng, Y. Yang, X. Qian, T. Fu, X. Li, Z. Yang, H. Yan, C. Cui and W. Tan, *Nano-Micro Lett.*, 2020, **12**, 103.

17 W.-T. Koo, J.-S. Jang and I.-D. Kim, *Chem*, 2019, **5**, 1938–1963.

18 H. Y. Li, S. N. Zhao, S. Q. Zang and J. Li, *Chem. Soc. Rev.*, 2020, **49**, 6364–6401.

19 D. J. Tranchemontagne, J. L. Mendoza-Cortés, M. O'Keeffe and O. M. Yaghi, *Chem. Soc. Rev.*, 2009, **38**, 1257–1283.

20 S. Abednatanzi, P. G. Derakhshandeh, H. Depauw, F.-X. Coudert, H. Vrielinck, P. Van Der Voort and K. Leus, *Chem. Soc. Rev.*, 2019, **48**, 2535–2565.

21 L. J. Wang, H. Deng, H. Furukawa, F. Ga, K. E. Cordova, D. Peri and O. M. Yaghi, *Inorg. Chem.*, 2014, **53**, 5881–5883.

22 W. Lu, Z. Wei, Z. Gu, T. Liu, J. Park, J. Park, J. Tian, M. Zhang, Q. Zhang, T. Gentle, M. Bosch and H.-C. Zhou, *Chem. Soc. Rev.*, 2014, **43**, 5561–5593.

23 S. M. Moosavi, A. Nandy, K. M. Jablonka, D. Ongari, J. P. Janet, P. G. Boyd, Y. Lee, B. Smit and H. J. Kulik, *Nat. Commun.*, 2020, **11**, 4068.

24 P. Li, N. A. Vermeulen, C. D. Malliakas, D. A. Gómez-gualdrón, A. J. Howarth, B. L. Mehdi, A. Dohnalkova, N. D. Browning, M. O. Keeffe and O. K. Farha, *Science (80-.).*, 2017, **356**, 624–627.

25 W. Xuan, C. Zhu, Y. Liu and Y. Cui, *Chem. Soc. Rev.*, 2012, **41**, 1677–1695.

26 M. Eddaoudi, J. Kim, N. Rosi, D. Vodak, J. Wachter, M. O. Keeffe and O. M. Yaghi, *Science (80-.).*, 2002, **295**, 469–472.

27 P. Horcajada, H. Chevreau, D. Heurtaux, F. Benyettou, F. Salles, T. Devic, A. Garcia-marquez, C. Yu, H. Lavrard, C. L. Dutson, E. Magnier, G. Maurin, E. Elkaïm and C. Serre, *Chem. Comm.*, 2014, **50**, 6872–6874.

28 B. Chen, M. Eddaoudi, S. T. Hyde, M. O'Keeffe and O. M. Yaghi, *Science (80-.).*, 2001, **291**, 1021–1023.

29 M. Ding, X. Cai and H.-L. Jiang, *Chem. Sci.*, 2019, **10**, 10209–10230.

30 Z. Wang, A. Bilegsaikhan, R. T. Jerozal, T. A. Pitt and P. J. Milner, *ACS Appl. Mater. Interfaces*, 2021, **13**, 17517–17531.

31 X. Liu, X. Wang and F. Kapteijn, *Chem. Rev.*, 2020, **120**, 8303–8377.

32 J. E. Mondloch, O. Karagiaridi, O. K. Farha and J. T. Hupp, *CrystEngComm*, 2013, **15**, 9258–9264.

33 J. A. Mason, L. E. Darago, W. W. Lukens and J. R. Long, *Inorg. Chem.*, 2015, **54**, 10096–10104.

34 X. Zhang, Z. Chen, X. Liu, S. L. Hanna, X. Wang, R. Taheri-Ledari, A. Maleki, P. Li and O. K. Farha, *Chem. Soc. Rev.*, 2020, **49**, 7406–7427.

35 B. Liu, A. G. Wong-Foy and A. J. Matzger, *Chem. Commun.*, 2013, **49**, 1419–1421.

36 J. Espín, L. Garzón-Tovar, A. Carné-Sánchez, I. Imaz and D. Maspoch, *ACS Appl. Mater. Interfaces*, 2018, **10**, 9555–9562.

37 Ü. Kökçam-Demir, A. Goldman, L. Esrafili, M. Gharib, A. Morsali, O. Weingart and C. Janiak, *Chem. Soc. Rev.*, 2020, **49**, 2751–2798.

38 J. Ma, A. P. Kalenak, A. G. Wong-Foy and A. J. Matzger, *Angew. Chemie - Int. Ed.*, 2017, **56**, 14618–14621.

39 J. N. Hall and P. Bollini, *React. Chem. Eng.*, 2019, **4**, 207–222.

40 Y. S. Wei, M. Zhang, R. Zou and Q. Xu, *Chem. Rev.*, 2020, **120**, 12089–12174.

41 T. Pham, K. A. Forrest, D. M. Franz, Z. Guo, B. Chen and B. Space, *Phys. Chem. Chem. Phys.*, 2017, **19**, 18587–18602.

42 A. K. Cheetham, T. D. Bennett, F.-X. Coudert and A. L. Goodwin, *Dalt. Trans.*, 2015, **45**, 4113–4126.

43 X. Chen, Y. Lyu, Z. Wang, X. Qiao, B. C. Gates and D. Yang, *ACS Catal.*, 2020, **10**, 2906–2914.

44 K. Müller, N. Vankova, L. Schöttner, T. Heine and L. Heinke, *Chem. Sci.*, 2019, **10**, 153–160.

45 P. S. Petkov, G. N. Vayssilov, J. Liu, O. Shekhah, Y. Wang, C. Wöll and T. Heine, *ChemPhysChem*, 2012, **13**, 2025–2029.

46 S. Chong, G. Thiele and J. Kim, *Nat. Commun.*, 2017, **8**, 1539.

47 J. Wang, L. Liu, C. Chen, X. Dong, Q. Wang, L. Alfilfil, M. R.

AlAlouni, K. Yao, J. Huang, D. Zhangab and Y. Han, *J. Mater. Chem. A*, 2020, **8**, 4464–4472.

48 W. Xiang, Y. Zhang, Y. Chen, C. Liu and X. T, *J. Mater. Chem. A*, 2020, **8**, 21526–21546.

49 I. A. Lázaro, N. Almora-Barrios, S. Tatay and C. Martí-Gastaldo, *Chem. Rev.*, 2021, **12**, 2586–2593.

50 W. Liang, L. Li, J. Hou, N. D. Shepherd, T. D. Bennett, M. D. Alessandro and V. Chen, *Chem. Sci.*, 2018, **9**, 3508–3516.

51 Y. Lee, J. Kim and W. Ahn, *Korean J. Chem. Eng.*, 2013, **30**, 1667–1680.

52 N. Stock and S. Biswas, *Chem. Rev.*, 2012, **112**, 933–969.

53 E. Biemmi, S. Christian, N. Stock and T. Bein, *Microporous Mesoporous Mater.*, 2009, **117**, 111–117.

54 M. G. Goesten, E. Stavitski, J. Juan-Alcañiz, A. Martiñez-Joaristi, A. V. Petukhov, F. Kapteijn and J. Gascon, *Catal. Today*, 2013, **205**, 120–127.

55 M. Haouas, C. Volkringer, T. Loiseau, G. Férey and F. Taulelle, *Chem. Mater.*, 2012, **24**, 2462–2471.

56 J. Vehrenberg, M. Vepsäläinen, D. S. Macedo, M. Rubio-Martinez, N. A. S. Webster and M. Wessling, *Microporous Mesoporous Mater.*, 2020, **303**, 110218.

57 S. Wang, H. Reinsch, N. Heymans, G. De, G. Maurin, S. Wang, H. Reinsch, N. Heymans, M. Wahiduzzaman, C. Martineau-corcos, G. De Weireld, G. Maurin and C. Serre, *Matter*, 2020, **2**, 440–450.

58 J. C. Warner, A. S. Cannon and K. M. Dye, *Environ. Impact Assess. Rev.*, 2004, **24**, 775–799.

59 T. Friščić, C. Mottillo and H. M. Titi, *Angew. Chemie - Int. Ed.*, 2019, **59**, 1018–1029.

60 T. Stolar and K. Užarević, *CrystEngComm*, 2020, **22**, 4511–4525.

61 C.-A. Tao and J.-F. Wang, *Crystals*, 2021, **11**, 15.

62 J. Klinowski, F. A. A. Paz, P. Silvab and J. Rocha, *Dalt. Trans.*,

2011, **40**, 321–330.

63 I. Thomas-hillman, A. Laybourn, C. Dodds and S. W. Kingman, *J. Mater. Chem. A*, 2018, **6**, 11564–11581.

64 D. J. Tranchemontagne, J. R. Hunt and O. M. Yaghi, *Tetrahedron*, 2008, **64**, 8553–8557.

65 V. A. Dubskikh, A. A. Lysova, D. G. Samsonenko, D. N. Dybtsev and V. P. Fedin, *CrystEngComm*, 2020, **22**, 6295–6301.

66 M. Kalaj, K. E. Prosser and S. M. Cohen, *Dalt. Trans.*, 2020, **49**, 8841–8845.

67 D. M. Venturi, F. Campana, F. Marmottini, F. Costantino and L. Vaccaro, *ACS Sustain. Chem. Eng.*, 2020, **8**, 17154–17164.

68 J. Zhang, G. B. White, M. D. Ryan, A. J. Hunt and M. J. Katz, *ACS Sustain. Chem. Eng.*, 2016, **4**, 7186–7192.

69 C. Capello, U. Fischer and K. Hungerbühler, *Green Chem.*, 2007, **9**, 927–934.

70 S. Kumar, S. Jain, M. Nehra, N. Dilbaghi, G. Marrazza and K. Kim, *Coord. Chem. Rev.*, 2020, **420**, 213407.

71 M. Sánchez-Sánchez, N. Getachew, K. Díaz, M. Díaz-García, Y. Chebudeb and I. Díaza, *Green Chem.*, 2015, **17**, 1500–1509.

72 L. Wang, J. Li, L. Cheng, Y. Song, P. Zeng and X. Wen, *J. Mater. Chem. A*, 2021, **9**, 14868–14876.

73 X. Li, Y. Mao, K. Leng, G. Ye, Y. Sun and W. Xu, *Mater. Lett.*, 2017, **197**, 192–195.

74 M. E. Dmello, N. G. Sundaram, A. Singh, A. K. Singh and S. B. Kalidindi, *Chem. Comm.*, 2019, **55**, 349–352.

75 S. Mandal, S. Natarajan, P. Mani and A. Pankajakshan, *Adv. Funct. Mater.*, 2020, **31**, 2006291.

76 N. L. Rosi, J. Kim, M. Eddaoudi, B. Chen, M. O'Keeffe and O. M. Yaghi, *J. Am. Chem. Soc.*, 2005, **127**, 1504–1518.

77 Z. Yin, S. Wan, J. Yang, M. Kurmoo and M. Zeng, *Coord. Chem. Rev.*, 2019, **378**, 500–512.

78 M. Lalonde, W. Bury, O. Karagiaridi, Z. Brown, J. T. Hupp and O. K. Farha, *J. Mater. Chem. A*, 2013, **1**, 5453–5468.

79 A. M. Hamisu, A. Ariffin and A. C. Wibowo, *Inorganica Chim. Acta*, 2020, **511**, 119801.

80 N. M. Padial, B. Lerma-Berlanga, N. Almora-Barrios, J. Castells-Gil, I. da Silva, M. de la Mata, S. I. Molina, J. Hernández-Saz, A. E. Platero-Prats, S. Tatay and C. Martí-Gastaldo, *J. Am. Chem. Soc.*, 2020, **142**, 6638–6648.

81 S. Bernt, V. Guillerm, C. Serre and N. Stock, *Chem. Comm.*, 2011, **47**, 2838–2840.

82 P. Serra-Crespo, E. V. Ramos-Fernandez, J. Gascon and F. Kapteijn, *Chem. Mater.*, 2011, **23**, 2565–2572.

83 A. Chołuj, N. I. Nikishkin and M. J. Chmielewski, *Chem. Commun.*, 2017, **53**, 10196–10199.

84 V. Pascanu, G. González Miera, A. K. Inge and B. Martín-Matute, *J. Am. Chem. Soc.*, 2019, **141**, 7223–7234.

85 S. Kumar, B. Mohan, Z. Tao, H. You and P. Ren, *Catal. Sci. Technol.*, 2021, **11**, 5734–5771.

86 P. García-García, M. Müller and A. Corma, *Chem. Sci.*, 2014, **5**, 2979–3007.

87 W. Gong, Y. Liu, H. Li and Y. Cui, *Coord. Chem. Rev.*, 2020, **420**, 213400.

88 J. Canivet, M. Vandichel and D. Farrusseng, *Dalt. Trans.*, 2016, **45**, 4090–4099.

89 J. Chen, R. Liu, H. Gao, L. Chen and D. Ye, *J. Mater. Chem. A*, 2014, **2**, 7205–7213.

90 F. G. Cirujano, N. Martín, G. Fu, C. Jia and D. De Vos, *Catal. Sci. Technol.*, 2020, **10**, 1796–1802.

91 S. Smolders, K. A. Lomachenko, B. Bueken, A. Struyf, A. L. Bugaev, C. Atzori, N. Stock, C. Lamberti, M. B. J. Roeffaers and D. E. De Vos, *ChemPhysChem*, 2018, **19**, 373–378.

92 Z. Sharifzadeh, K. Berijani and A. Morsali, *Coord. Chem. Rev.*, 2021, **445**, 214083.

93 B. A. Johnson and S. Ott, *Chem. Sci.*, 2020, **11**, 7468–7478.

94 H. Li, K. Wang, Y. Sun, C. T. Lollar, J. Li and H. C. Zhou,

Mater. Today, 2018, **21**, 108–121.

95 R. Lin, S. Xiang, W. Zhou and B. Chen, *Chem*, 2020, **6**, 337–363.

96 E. Borfecchia, S. Maurelli, D. Gianolio, E. Groppo, M. Chiesa, F. Bonino and C. Lamberti, *J. Phys. Chem. C*, 2012, **116**, 19839–19850.

97 D. Ongari, D. Tiana, S. J. Stoneburner, L. Gagliardi and B. Smit, *J. Phys. Chem. C*, 2017, **121**, 15135–15144.

98 J. R. Álvarez, E. Sánchez-González, E. Pérez, E. Schneider-Revueltas, A. Martínez, A. Tejeda-Cruz, A. Islas-Jácome, E. González-Zamora and I. A. Ibarra, *Dalt. Trans.*, 2017, **46**, 9192–9200.

99 M. Ding, R. W. Flaig, H. Jiang and O. M. Yaghi, *Chem. Soc. Rev.*, 2019, **48**, 2783–2828.

100 R. W. Flaig, T. M. O. Popp, A. M. Fracaroli, E. A. Kapustin, M. J. Kalmutzki, R. M. Altamimi, F. Fathieh, J. A. Reimer and O. M. Yaghi, *J. Am. Chem. Soc.*, 2017, **139**, 12125–12128.

101 Q. Yan, Y. Lin, C. Kong and L. Chen, *Chem. Commun.*, 2013, **49**, 6873–6875.

102 T. Ghanbari, F. Abnisa and W. M. A. Wan Daud, *Sci. Total Environ.*, 2020, **707**, 135090.

103 S. E. M. Elhenawy, M. Khraisheh, F. AlMomani and G. Walker, *Catalysts*, 2020, **10**, 1293.

104 J. Lin, T. T. T. Nguyen, R. Vaidhyanathan, J. Burner, J. M. Taylor, H. Durekova, F. Akhtar, R. K. Mah, O. Ghaffari-nik, S. Marx, N. Fylstra, S. S. Iremonger, K. W. Dawson, P. Sarkar, P. Hovington, A. Rajendran, T. K. Woo and G. K. H. Shimizu, *Science (80-.).*, 2021, **374**, 1464–1469.

105 G. Ozin, CALF-20: A carbon capture success story, https://www.advancedsciencenews.com/calf-20-a-carbon-capture-success-story/, (accessed 20 February 2022).

106 Lafarge, Project CO2MENT, https://www.lafarge.ca/en/project-co2ment, (accessed 20 February 2022).

107 R. Moradi and K. M. Groth, *Int. J. Hydrogen Energy*, 2019, **44**,

12254–12269.

108 A. Ahmed, S. Seth, J. Purewal, A. G. Wong-Foy, M. Veenstra, A. J. Matzger and D. J. Siegel, *Nat. Commun.*, 2019, **10**, 1568.

109 R. Balderas-Xicohténcatl, M. Schlichtenmayer and M. Hirscher, *Energy Technol.*, 2018, **6**, 578–582.

110 K. Sumida, J. Her, M. Dinca, L. J. Murray, J. M. Schloss, C. J. Pierce, B. A. Thompson, S. A. Fitzgerald, C. M. Brown and R. Long, *J. Phys. Chem. C*, 2011, **115**, 8414–8421.

111 S. Kang, L. Klebanoff, A. Baker, D. F. Cowgill, J. Lee, M. H. Nielsen, K. Ray and Y. Liu, *Int. J. Hydrogen Energy*, 2018, **43**, 14507–14519.

112 S. P. Shet, S. S. Priya, K. Sudhakar and M. Tahir, *Int. J. Hydrogen Energy*, 2021, **46**, 11782–11803.

113 A. Maleki, B. Hayati, M. Naghizadeh and S. W. Joo, *J. Ind. Eng. Chem.*, 2015, **28**, 211–216.

114 L. Zhao, M. R. Azhar, X. Li, X. Duan, H. Sun, S. Wang and X. Fang, *J. Colloid Interface Sci.*, 2019, **542**, 421–428.

115 D. T. Sun, N. Gasilova, S. Yang, E. Oveisi and W. L. Queen, *J. Am. Chem. Soc.*, 2018, **140**, 16697–16703.

116 V. K.-M. Au, *Front. Chem.*, 2020, **8**, 708.

117 S. Nazri, M. Khajeh, A. R. Oveisi, R. Luque, E. Rodríguez-Castellón and M. Ghaffari-Moghaddam, *Sep. Purif. Technol.*, 2021, **259**, 118197.

118 G. Xu, Z. An, K. Xu, Q. Liu, R. Das and H. Zhao, *Coord. Chem. Rev.*, 2021, **427**, 213554.

119 M. I. Severino, E. Gkaniatsou, F. Nouar, M. L. Pinto and C. Serre, *Faraday Discuss.*, 2021, **231**, 326–341.

120 W. P. R. Deleu, I. Stassen, D. Jonckheere, R. Ameloot and D. E. De Vos, *J. Mater. Chem. A*, 2016, **4**, 9519–9525.

121 V. F. Cheong and P. Y. Moh, *Mater. Sci. Technol.*, 2018, **34**, 1025–1045.

122 W. Liang, W. Zhou, C. Qian and Y. Zhao, *Mater. Today*, 2021, **47**, 170–186.

123 A. Dhakshinamoorthy, M. Alvaro, P. Horcajada, E. Gibson, M. Vishnuvarthan, A. Vimont, J. Grene, C. Serre and M. Daturi, *ACS Catal.*, 2012, **2**, 2060–2065.

124 S. S. Chui, S. M. Lo, J. P. H. Charmant, A. G. Orpen and I. D. Williams, *Science (80-.).*, 1999, **283**, 1148–1151.

125 L. J. Murray, M. Dinca, J. Yano, S. Chavan, S. Bordiga, C. M. Brown and J. R. Long, *J. Am. Chem. Soc.*, 2010, **132**, 7856–7857.

126 M. Kramer, U. Schwarz and S. Kaskel, *J. Mater. Chem.*, 2006, **16**, 2245–2248.

127 L. Xie, S. Liu, C. Gao, R. Cao, J. Cao, C. Sun and Z. Su, *Inorg. Chem.*, 2007, **46**, 7782–7788.

128 P. Maniam and N. Stock, *Inorg. Chem.*, 2011, **50**, 5085–5097.

129 J. I. Feldblyum, M. Liu, D. W. Gidley and A. J. Matzger, *J. Am. Chem. Soc.*, 2011, **133**, 18257–18263.

130 O. Kozachuk, K. Yusenko, H. Noei, Y. Wang, S. Walleck, T. Glaser and R. A. Fischer, *Chem. Comm.*, 2011, **47**, 8509–8511.

131 Z. Zhang, L. Zhang, L. Wojtas, M. Eddaoudi and M. J. Zaworotko, *J. Am. Chem. Soc.*, 2012, **134**, 928–933.

132 J. Hu, H. Yu, W. Dai, X. Yan, X. Hu and H. Huang, *RSC Adv.*, 2014, **4**, 35124–35130.

133 W. R. Heinz, T. Kratky, M. Drees, A. Wimmer, O. Tomanec, S. Günther, M. Schuster and R. A. Fische, *Dalt. Trans.*, 2019, **48**, 12031–12039.

134 W. Zhang, Z. Chen, M. Al-Naji, P. Guo, S. Cwik, O. Halbherr, Y. Wang, M. Muhler, N. Wilde, R. Gläser and R. A. Fischer, *Dalt. Trans.*, 2016, **45**, 14883–14887.

135 M. Almási, V. Zelenák, J. Kuchár, S. Bourrelly and P. L. Llewellyn, *Colloids Surfaces A Physicochem. Eng. Asp.*, 2016, **496**, 114–124.

136 J. Ethiraj, F. Bonino, J. G. Vitillo, K. A. Lomachenko, C. Lamberti, H. Reinsch, K. P. Lillerud and S. Bordiga, *ChemSusChem*, 2016, **9**, 713–719.

137 W. Mu, X. Huang, R. Zhong, W. Xia, J. Liu and R. Zou, *CrystEngComm*, 2015, **17**, 1637–1645.

138 S. A. Cotton, *Comptes Rendus Chim.*, 2005, **8**, 129–145.

139 B. Chen, Y. Yang, F. Zapata, G. Lin, G. Qian and E. B. Lobkovsky, *Adv. Mater.*, 2007, **19**, 1693–1696.

140 X. Lian and B. Yan, *RSC Adv.*, 2016, **6**, 11570–11576.

141 M. Almáši and V. Zeleňák, Single-crystal-to-single-crystal phenomena in novel Lutetium(III) metal-organic framework, https://photon-science.desy.de/annual_report/files/2012/20122088.pdf, (accessed 23 February 2022).

142 A. V Mayeuski, D. Y. Poloneeva, E. A. Toshcheva, A. V. Bardakova, A. V. Shuruhina, A. V. Emeline and D. W. Bahnemann, *J. Lumin.*, 2021, **235**, 117970.

143 W. Yang, Z.-Q. Bai, W.-Q. Shi, L.-Y. Yuan, T. Tian, Z.-F. Chai, H. Wang and Z.-M. Sun, *Chem. Commun.*, 2013, 10415–10417.

144 Y. Yang, L. Zhao, M. Sun, P. Wei, G. Li and Y. Li, *Dye. Pigment.*, 2020, **180**, 108444.

145 V. Zeleňák, M. Almáši, A. Zeleňáková, P. Hrubovčák, R. Tarasenko, S. Bourelly and P. Llewellyn, *Sci. Rep.*, 2019, **9**, 15572.

146 A. Garg, M. Almási, D. R. Paul, E. Poonia, J. R. Luthra and A. Sharma, *Front. Energy Res.*, 2021, **8**, 340.

147 G. Férey, C. Serre, C. Mellot-Draznieks, F. Millange, S. Surblé, J. Dutour and I. Margiolaki, *Angew. Chemie - Int. Ed.*, 2004, **43**, 6296–6301.

148 C. Férey, C. Mellot-Draznieks, C. Serre, F. Millange, J. Dutour, S. Surblé and I. Margiolaki, *Science (80-.).*, 2005, **309**, 2040–2042.

149 M. Y. Zorainy, M. G. Alalm, S. Kaliaguine and D. C. Boffito, *J. Mater. Chem. A*, 2021, **9**, 22159–22217.

150 A. J. Howarth, A. W. Peters, N. A. Vermeulen, T. C. Wang, J. T. Hupp and O. K. Farha, *Chem. Mater.*, 2017, **29**, 26–39.

151 Ü. Kökçam-Demir, A. Goldman, L. Esrafili, M. Gharib, A. Morsali, O. Weingart and C. Janiak, *Chem. Soc. Rev.*, 2020, **49**, 2751–2798.

152 J. L. Schlenker, F. G. Dwyer, E. E. Jenkins, W. J. Rohrbaugh, G. T. Kokotailo and W. M. Meier, *Nature*, 1981, **294**, 340–342.

153 T. K. Trung, N. A. Ramsahye, P. Trens, N. Tanchoux, C. Serre, F. Fajula and G. Férey, *Microporous Mesoporous Mater.*, 2010, **134**, 134–140.

154 M. Thommes, K. Kaneko, A. V. Neimark, J. P. Olivier, F. Rodriguez-Reinoso, J. Rouquerol and K. S. W. Sing, *Pure Appl. Chem.*, 2015, **87**, 1051–1069.

155 T. Hidalgo, M. Giménez-Marqués, E. Bellido, J. Avila, M. C. Asensio, F. Salles, M. V. Lozano, M. Guillevic, R. Simón-Vázquez, A. González-Fernández, C. Serre, M. J. Alonso and P. Horcajada, *Sci. Rep.*, 2017, **7**, 43099.

156 E. Bellido, M. Guillevic, T. Hidalgo, M. J. Santander-Ortega, C. Serre and P. Horcajada, *Langmuir*, 2014, **30**, 5911–5920.

157 L. Hamon, N. Heymans, P. L. Llewellyn, V. Guillerm, A. Ghoufi, S. Vaesen, G. Maurin, C. Serre, G. De Weireld and G. D. Pirngruber, *Dalt. Trans.*, 2012, **41**, 4052–4059.

158 Q. R. Fang, T. A. Makal, M. D. Young and H. C. Zhou, *Comments Inorg. Chem.*, 2010, **31**, 165–195.

159 L. Feng, K.-Y. Wang, X.-L. Lv, T.-H. Yan and H.-C. Zhou, *Natl. Sci. Rev.*, , DOI:10.1093/nsr/nwz170.

160 C. Volkringer, D. Popov, T. Loiseau, G. Férey, M. Burghammer, C. Riekel, M. Haouas and F. Taulelle, *Chem. Mater.*, 2009, **21**, 5695–5697.

161 N. A. Khan, J. S. Lee, J. Jeon, C. H. Jun and S. H. Jhung, *Microporous Mesoporous Mater.*, 2012, **152**, 235–239.

162 M. Vinu, W. C. Lin, D. S. Raja, J. L. Han and C. H. Lin, *Polymers (Basel).*, , DOI:10.3390/polym9100498.

163 A. García Márquez, A. Demessence, A. E. Platero-Prats, D. Heurtaux, P. Horcajada, C. Serre, J. S. Chang, G. Férey, V. A. De La Peña-O'Shea, C. Boissière, D. Grosso and C. Sanchez,

Eur. J. Inorg. Chem., 2012, **100**, 5165–5174.

164 Y. Fu, K. Li, M. Batmunkh, H. Yu, S. Donne, B. Jia and T. Ma, *ACS Appl. Mater. Interfaces*, 2020, **12**, 44830–44839.

165 J. Yang, J. Wang, S. Deng and J. Li, *Chem. Commun.*, 2016, **52**, 725–728.

166 B. Seoane, A. Dikhtiarenko, A. Mayoral, C. Tellez, J. Coronas, F. Kapteijn and J. Gascon, *CrystEngComm*, 2015, **17**, 1693–1700.

167 M. Qiu, Q. Guan and W. Li, *Cryst. Growth Des.*, 2016, **16**, 3639–3646.

168 W. Xia, X. Zhang, L. Xu, Y. Wang, J. Lin and R. Zou, *RSC Adv.*, 2013, **3**, 11007–11013.

169 Y. Fang, Z. Yang, H. Li and X. Liu, *Environ. Sci. Pollut. Res.*, 2020, **27**, 4703–4724.

170 L. Han, H. Qi, D. Zhang, G. Ye, W. Zhou, C. Hou, W. Xu and Y. Sun, *New J. Chem.*, 2017, **41**, 13504–13509.

171 K. Guesh, C. Caiuby, Á. Mayoral, M. Díaz-García, I. Díaz and M. Sanchez-Sanchez, *Cryst. Growth Des.*, 2017, **17**, 1806–1813.

172 H. Tian, J. Peng, Q. Du, X. Hui and H. He, *Dalt. Trans.*, 2018, **47**, 3417–3424.

173 B. Barth, M. Mendt, A. Pöppl and M. Hartmann, *Microporous Mesoporous Mater.*, 2015, **216**, 97–110.

174 Y. Feng, C. Wang, F. Ke, J. Zang and J. Zhu, *Nanomaterials*, , DOI:10.3390/nano8060446.

175 F. Moreau, J. Marrot, F. Banse, C. Serre and A. Tissot, *J. Mater. Chem. C*, , DOI:10.1039/d0tc03756g.

176 M. Haouas, C. Volkringer, T. Loiseau, G. Férey and F. Taulelle, *J. Phys. Chem. C*, 2011, **115**, 17934–17944.

177 J. W. Yoon, Y. K. Seo, Y. K. Hwang, J. S. Chang, H. Leclerc, S. Wuttke, P. Bazin, A. Vimont, M. Daturi, E. Bloch, P. L. Llewellyn, C. Serre, P. Horcajada, J. M. Grenèche, A. E. Rodrigues and G. Férey, *Angew. Chemie - Int. Ed.*, 2010, **49**, 5949–5952.

178 C. P. Cabello, P. Rumori and G. T. Palomino, *Microporous Mesoporous Mater.*, 2014, **190**, 234–239.

179 L. Mitchell, P. Williamson, B. Ehrlichovμ, A. E. Anderson, V. R. Seymour, S. E. Ashbrook, N. Acerbi, L. M. Daniels, R. I. Walton, M. L. Clarke and P. A. Wright, *Chem. Eur. J.*, 2014, **100**, 17185–17197.

180 C. P. Cabello, G. Gómez-pozuelo and M. Opanasenko, *Chempluschem*, 2016, **81**, 828–835.

181 M. N. Timofeeva, V. N. Panchenko, N. A. Khan, Z. Hasan, I. P. Prosvirin, S. V. Tsybulya and S. H. Jhung, *Appl. Catal. A Gen.*, 2017, **529**, 167–174.

182 G. Gema, P. Cabello and M. Opanasenko, *Chempluschem*, 2017, **82**, 152–159.

183 W. Zhang, Y. Shi, C. Li, Q. Zhao and X. Li, *Catal. Lett.*, 2016, **146**, 1956–1964.

184 L. Zou, D. Feng, T.-F. Liu, Y.-P. Chen, S. Yuan, K. Wang, X. Wang, S. Fordhama and H.-C. Zhou, *Chem. Sci.*, 2016, **7**, 1063–1069.

185 J. Castells-gil, N. M. Padial, N. Almora-Barrios, I. Da Silva, D. Mateo, J. Albero, H. García and C. Martí-Gastaldo, *Chem. Sci.*, 2019, **10**, 4313–4321.

186 M. Giménez-Marqués, A. Santiago-Portillo, S. Navalón, M. Álvaro, V. Briois, F. Nouar, H. Garcia and C. Serre, *J. Mater. Chem. A*, 2019, **7**, 20285–20292.

187 J. Castells-Gil, N. M. Padial, N. Almora-Barrios, R. Gil-San-Millán, M. Romero-Ángel, V. Torres, I. da Silva, B. C. J. Vieira, J. C. Waerenborgh, J. Jagiello, J. A. R. Navarro, S. Tatay and C. Martí-Gastaldo, *Chem*, 2020, **6**, 3118–3131.

188 J. Fonseca, T. Gong, L. Jiaoa and H.-L. Jiang, *J. Mater. Chem. A*, 2021, **9**, 10562–10611.

189 F. Gándara and T. D. Bennett, *IUCrJ*, 2014, **1**, 563–570.

190 J. Martí-Rujas, *Dalt. Trans.*, 2020, **49**, 13897–13916.

191 C. Volkringer, D. Popov, T. Loiseau, N. Guillou, G. Ferey, M. Haouas, F. Taulelle, C. Mellot-Draznieks, M. Burghammer and

C. Riekel, *Nat. Mater.*, 2007, **6**, 760–764.

192 J. Bedia, V. Muelas-Ramos, M. Peñas-Garzón, A. Gómez-Avilés, J. J. Rodríguez and C. Belver, *Catalysts*, 2019, **9**, 52.

193 A. A. Yakovenko, Z. Wei, M. Wriedt, J.-R. Li, G. J. Halder and H. Zhou, *Cryst. Growth Des.*, 2014, **14**, 5397–5407.

194 T. A. Vu, G. H. Le, C. D. Dao, L. Q. Dang, K. T. Nguyen, P. T. Dang, H. T. K. Tran, Q. T. Duong, T. V. Nguyen and G. D. Lee, *RSC Adv.*, 2014, **4**, 41185–41194.

195 P. S. Rahimabadi, M. Khodaei and K. R. Koswattage, *X-ray Spectrom.*, 2020, **49**, 348–373.

196 S. J. I. Shearan, J. Jacobsen, F. Costantino, R. D. Amato, D. Novikov, N. Stock, E. Andreoli and M. Taddei, *Chem. - A Eur. J.*, 2021, **27**, 6579–6592.

197 T. M. McDonald, E. D. Bloch and J. R. Long, *Chem. Commun.*, 2015, **51**, 4985–4988.

198 I. A. Lázaro, *Eur. J. Inorg. Chem.*, 2020, 4284–4294.

199 X. Mu, Y. Chen, E. Lester and T. Wu, *Microporous Mesoporous Mater.*, 2018, **270**, 249–257.

200 H. Seifi, T. Gholami, S. Seifi, S. M. Ghoreishi and M. Salavati-Niasari, *J. Anal. Appl. Pyrolysis*, 2020, **149**, 104840.

201 B. Mu and K. S. Walton, *J. Phys. Chem. C*, 2011, **115**, 22748–22754.

202 C. Healy, K. M. Patil, B. H. Wilson, L. Hermanspahn, N. C. Harvey-Reid, B. I. Howard, C. Kleinjan, J. Kolien, F. Payet, S. G. Telfer, P. E. Kruger and T. D. Bennett, *Coord. Chem. Rev.*, 2020, **419**, 213388.

203 M. Lacalamita, G. Ventruti, G. Della Ventura, F. Radica, D. Mauro and E. Schingaro, *Minerals*, 2021, **11**, 392.

204 K. I. Hadjiivanov, D. A. Panayotov, M. Y. Mihaylov, E. Z. Ivanova, K. K. Chakarova, S. M. Andonova and N. L. Drenchev, *Chem. Rev.*, 2021, **121**, 1286–1424.

205 J. Ren, N. M. Musyoka, H. W. Langmi, J. Walker, M. Mathe and S. Liao, *Polyhedron*, 2018, **153**, 205–212.

206 O. Karagiaridi, N. A. Vermeulen, R. C. Klet, T. C. Wang, P. Z. Moghadam, S. S. Al-juaid, J. F. Stoddart, J. T. Hupp and O. K. Farha, *Inorg. Chem.*, 2015, **54**, 1785–1790.

207 S. M. Cohen, *Chem. Rev.*, 2012, **112**, 970–1000.

208 H. G. T. Nguyen, L. Mao, A. W. Peters, C. O. Audu, Z. J. Brown, O. K. Farha, J. T. Hupp and S. T. Nguyen, *Catal. Sci. Technol.*, 2015, **5**, 4444–4451.

209 A. Klinkebiel, N. Reimer, M. Lammert, N. Stock and U. Lüning, *Chem. Commun.*, 2014, **50**, 9306–9308.

210 R. Febrian, J. P. Roddy, C. H. Chang, C. T. Devall and P. J. Bracher, *ACS Omega*, 2021, **6**, 14727–14733.

211 T. K. Ky, V. N. Le, V. C. Nguyen, M. Song, D. Kim, K. S. Yoo, B. J. Park and J. Kim, *J. Ind. Eng. Chem.*, 2020, **86**, 178–185.

212 H. A. Hamzah, T. S. Crickmore, D. Rixson and A. D. Burrows, *Dalt. Trans.*, 2018, **47**, 14491–14496.

213 M. Servalli, M. Ranocchiari and J. A. Van Bokhoven, *Chem. Comm.*, 2012, **48**, 1904–1906.

214 T. Rundlöf, M. Mathiasson, S. Bekiroglu, B. Hakkarainen, T. Bowden and T. Arvidsson, *J. Pharm. Biomed. Anal.*, 2010, **52**, 645–651.

215 W. C. Cooper, A. Chilukoorie, S. Polam, D. Scott and F. Wiseman, *J. Phys. Org. Chem.*, 2017, **30**, e3701.

216 M. G. Goesten, P. C. M. M. Magusin, E. A. Pidko, B. Mezari, E. J. M. Hensen, F. Kapteijn and J. Gascon, *Inorg. Chem.*, 2014, **53**, 882–887.

217 M. Haouas, *Materials (Basel).*, 2018, **11**, 1416.

218 C. Gerardin, M. Haouas, C. Lorentz and F. Taulelle, *Magn. Reson. Chem.*, 2000, **38**, 429–435.

219 H. C. Hoffmann, M. Debowski, P. Müller, S. Paasch, I. Senkovska, S. Kaskel and E. Brunner, *Materials (Basel).*, 2012, **5**, 2537–2572.

220 B. E. G. Lucier, S. Chen and Y. Huang, *Acc. Chem. Res.*, 2018, **51**, 319–330.

221 M. Haouas, C. Volkringer, T. Loiseau, G. Férey and F. Taulelle, *J. Phys. Chem. C*, 2011, **115**, 17934–17944.

222 K. Chen, *Int. J. Mol. Sci.*, 2020, **21**, 5666.

223 V. A. Wirnkor, E. C. Ebere and V. E. Ngozi, *Anal. Methods Environ. Chem. J.*, 2019, **2**, 13–30.

224 G. L. Donati, R. S. Amais and C. B. Williams, *J. Anal. At. Spectrom.*, 2017, **32**, 1283–1296.

225 M. Aceto, O. Abollino, M. Concetta Bruzzoniti, E. Mentasti, C. Sarzanini and M. Malandrino, *Food Addit. Contam.*, 2002, **19**, 126–133.

226 W. Schöninger, *Mikrochim. Acta*, 1955, **43**, 123–129.

227 É. M. M. Flores, J. S. Barin, M. F. Mesko and G. Knapp, *Spectrochim. Acta Part B At. Spectrosc.*, 2007, **62**, 1051–1064.

228 S. Brunauer, P. H. Emmett and E. Teller, *J. Am. Chem. Soc.*, 1938, **60**, 309–319.

229 I. Langmuir, *J. Am. Chem. Soc.*, 1918, **40**, 1361–1403.

230 E. P. Barrett, L. G. Joyner and P. P. Halenda, *J. Am. Chem. Soc.*, 1951, **73**, 373–380.

231 K. S. Walton and R. Q. Snurr, *J. Am. Chem. Soc.*, 2007, **129**, 8552–8556.

232 K. C. Kim, T. Yoon and Y. Bae, *Microporous Mesoporous Mater.*, 2016, **224**, 294–301.

233 B. Streppel and M. Hirscher, *Phys. Chem. Chem. Phys.*, 2011, **13**, 3220–3222.

234 I. Saita, L. Li, K. Saito and T. Akiyama, *Mater. Trans.*, 2002, **43**, 1100–1104.

235 T. P. Blach and E. M. Gray, *J. Alloys Compd.*, 2007, **446**–**447**, 692–697.

236 A. Ahmed, Y. Liu, J. Purewal, L. D. Tran, A. G. Wong-Foy, M. Veenstra, A. J. Matzger and D. J. Siegel, *Energy Environ. Sci.*, 2017, **10**, 2459–2471.

237 S. Brandani, E. Mangano and L. Sarkisov, *Adsorption*, 2016, **22**, 261–276.

238 H. Isochema, www.hidenisochema.com, https://hidenisochema.com/hiden-products/imi-htp/, (accessed 18 December 2021).

239 A. Nuhnen and C. Janiak, *Dalt. Trans.*, 2020, **49**, 10295–10307.

240 J. Wang, E. Mangano, S. Brandani and D. M. Ruthven, *Adsorption*, 2021, **27**, 295–318.

241 D. O. Ojwang, J. Grins and G. Svensson, *Microporous Mesoporous Mater.*, 2018, **272**, 70–78.

242 J. Multia, A. Khayyami, J. Heiska and M. Karppinen, *J. Vac. Sci. Technol. A*, 2020, **38**, 052406.

243 T. Steenhaut, N. Grégoire, G. Barozzino-Consiglio, Y. Filinchuk and S. Hermans, *RSC Adv.*, 2020, **10**, 19822–19831.

244 T. Steenhaut, L. Fusaro, K. Robeyns, S. Lacour, X. Li, J. G. Mahy, V. Louppe, N. Grégoire, G. Barozzino-Consiglio, J.-F. Statsyns, C. Aprile, Y. Filinchuk and S. Hermans, *Submitted*.

245 W. R. Lee, H. Jo, L.-M. Yang, H. Lee, D. W. Ryu, K. S. Lim, J. H. Song, D. Y. Min, S. S. Han, J. G. Seo, Y. K. Park, D. Moon and C. S. Hong, *Chem. Sci.*, 2015, **6**, 3697–3705.

246 S. Huang, K. Yang, X. Liu, H. Pan, H. Zhang and S. Yang, *RSC Adv.*, 2017, **7**, 5621–5627.

247 Y.-R. Chen, K.-H. Liou, D.-Y. Kang, J.-J. Chen and L.-C. Lin, *Langmuir*, 2018, **34**, 4180–4187.

248 D. Kim, H. Kim and D. Cho, *Catal. Commun.*, 2016, **73**, 69–73.

249 Y. Shi, C. Li, X. Liu, H. Zhang, Q. Zhao and X. Li, *Integr. Ferroelectr.*, 2017, **181**, 14–25.

250 P. L. Llewellyn, S. Bourrelly, C. Serre, A. Vimont, M. Daturi, L. Hamon, G. De Weireld, J.-S. Chang, D. Hong, Y. K. Hwang, S. H. Jhung and G. Férey, *Langmuir*, 2008, **24**, 7245–7250.

251 C. K. Brozek and M. Dinca, *J. Am. Chem. Soc.*, 2013, **135**, 12886–12891.

252 S. Wongsakulphasatch, F. Nouar, J. Rodriguez, L. Scott, C. Le Guillouzer, T. Devic, P. Horcajada, P. L. Llewellyn, A. Vimont, G. Clet, M. Daturi and C. Serre, *Chem. Commun.*, 2015, **51**,

10194–10197.

253 A. Dhakshinamoorthy, A. M. Asiric and H. Garcia, *Catal. Sci. Technol.*, 2016, **6**, 5238–5261.

254 R. D. Shannon, *Acta Cryst. A*, 1976, **32**, 751–767.

255 C. P. Cabello, G. Berlier, G. Magnacca, P. Rumori and G. T. Palomino, *CrystEngComm*, 2015, **17**, 430–437.

256 H. Tian, J. Peng, Q. Du, X. Hui and H. He, *Dalt. Trans.*, 2018, **47**, 3417–3424.

257 M. Sánchez-sánchez, N. Getachew, M. Díaz-garcía, Y. Chebude and I. Díaz, *Green Chem.*, 2015, **17**, 1500–1509.

258 L. Hamon, N. Heymans, P. L. Llewellyn, V. Guillerm, A. Ghoufi, S. Vaesen, G. Maurin, C. Serre, G. De Weireld and G. D. Pirngruber, *Dalt. Trans.*, 2012, **41**, 4052–4059.

259 B. Šopotrajanov, V. Stefov, M. Žugić and V. M. Petruševski, *J. Mol. Struct.*, 1999, **482**–**483**, 109–113.

260 B. Y. R. D. Shannon, M. H, N. H. Baur, O. H. Gibbs, M. Eu and V. Cu, *Acta Cryst.*, 1976, **A 32**, 751–767.

261 R. Kishor and A. K. Ghoshal, *Ind. Eng. Chem. Res.*, 2017, **56**, 6078–6087.

262 H. H. Wang, W. J. Shi, L. Hou, G. P. Li, Z. Zhu and Y. Y. Wang, *Chem. - A Eur. J.*, 2015, **21**, 16525–16531.

263 R. Vaidhyanathan, S. S. Iremonger, K. W. Dawson and G. K. H. Shimizu, *Chem. Commun.*, 2009, 5230–5232.

264 W. Ma, L. Xu, Z. Li, Y. Sun, Y. Bai and H. Liu, *Nanoscale*, 2016, **8**, 10908–10912.

265 Y. Lin, C. Kong and L. Chen, *RSC Adv.*, 2016, **6**, 32598–32614.

266 C. Montoro, E. García, S. Calero, M. A. Pérez-Fernández, A. L. López, E. Barea and J. A. R. Navarro, *J. Mater. Chem.*, 2012, **22**, 10155–10158.

267 N. Wang, A. Mundstock, Y. Liu, A. Huang and J. Caro, *Chem. Eng. Sci.*, 2015, **124**, 27–36.

268 R. Zhong, X. Yu, W. Meng, S. Han, J. Liu, Y. Ye, C. Sun, G. Chen and R. Zou, *Chem. Eng. Sci.*, 2018, **184**, 85–92.

269 J. S. Yeon, W. R. Lee, N. W. Kim, H. Jo, H. Lee, J. H. Song, K. S. Lim, D. W. Kang, J. G. Seo, D. Moon, B. Wiers and C. S. Hong, *J. Mater. Chem. A*, 2015, **3**, 19177–19185.

270 S. Choi, T. Watanabe, T. H. Bae, D. S. Sholl and C. W. Jones, *J. Phys. Chem. Lett.*, 2012, **3**, 1136–1141.

271 Z. Q. Bai, L. Y. Yuan, L. Zhu, Z. R. Liu, S. Q. Chu, L. R. Zheng, J. Zhang, Z. F. Chai and W. Q. Shi, *J. Mater. Chem. A*, 2015, **3**, 525–534.

272 T. M. McDonald, J. A. Mason, X. Kong, E. D. Bloch, D. Gygi, A. Dani, V. Crocellà, F. Giordanino, S. O. Odoh, W. S. Drisdell, B. Vlaisavljevich, A. L. Dzubak, R. Poloni, S. K. Schnell, N. Planas, K. Lee, T. Pascal, L. F. Wan, D. Prendergast, J. B. Neaton, B. Smit, J. B. Kortright, L. Gagliardi, S. Bordiga, J. A. Reimer and J. R. Long, *Nature*, 2015, **519**, 303–308.

273 R. L. Siegelman, T. M. McDonald, M. I. Gonzalez, J. D. Martell, P. J. Milner, J. A. Mason, A. H. Berger, A. S. Bhown and J. R. Long, *J. Am. Chem. Soc.*, 2017, **139**, 10526–10538.

274 L. Wang, F. Zhang, C. Wang, Y. Li, J. Yang, L. Li and J. Li, *Sep. Purif. Technol.*, 2020, **235**, 116219.

275 H. Sepehrmansouri, M. Zarei and M. Ali, *Mol. Catal.*, 2020, **481**, 110303.

276 R. Pertiwi, R. Oozeerally, D. L. Burnett, T. W. Chamberlain, N. Cherkasov, M. Walker, R. J. Kashtiban, Y. K. Krisnandi, V. Degirmenci and R. I. Walton, *Catalysts*, , DOI:10.3390/catal9050437.

277 L. Bartlett and P. A. Vesilind, *Environ. Eng. Policy*, 1998, **1**, 81–86.

278 P. Horcajada, S. Surble, C. Serre, D. Hong, Y. Seo, J. Chang and J. Grene, *Chem. Comm.*, 2007, **100**, 2820–2822.

279 C. R. Morcombe and K. W. Zilm, *J. Magn. Reson.*, 2003, **162**, 479–486.

280 P. Bertani, J. Raya and B. Bechinger, *Solid State Nucl. Magn. Reson.*, 2014, **61**–**62**, 15–18.

281 T. Steenhaut, S. Hermans and Y. Filinchuk, *New J. Chem.*, 2020,

44, 3847–3855.

282 D. Kim, D. Ma, M. Kim, Y. Jung, N. H. Kim, C. Lee, S. W. Cho, S. Park, Y. Huh, J. Jung and K. H. Ahn, *J. Fluoresc.*, 2017, **27**, 2231–2238.

283 H. Zhang, J. Wen, Y. Fang, S. Zhang and G. Zeng, *J. Colloid Interface Sci.*, 2019, **551**, 155–163.

284 S. Mutyala, S. M. Yakout, S. S. Ibrahim, M. Jonnalagadda and H. Mitta, *New J. Chem.*, 2019, **43**, 9725–9731.

285 M. Benzaqui, R. S. Pillai, A. Sabetghadam, V. Benoit, P. Normand, J. Marrot, N. Menguy, D. Montero, W. Shepard, A. Tissot, C. Martineau-Corcos, C. Sicard, M. Mihaylov, F. Carn, I. Beurroies, P. L. Llewellyn, G. De Weireld, K. Hadjiivanov, J. Gascon, F. Kapteijn, G. Maurin, N. Steunou and C. Serre, *Chem. Mater.*, 2017, **29**, 10326–10338.

286 T. Loiseau, C. Volkringer, M. Haouas, F. Taulelle and G. Férey, *Comptes Rendus Chim.*, 2015, **18**, 1350–1369.

287 J. Koo, I. C. Hwang, X. Yu, S. Saha, Y. Kim and K. Kim, *Chem. Sci.*, 2017, **8**, 6799–6803.

288 J. Jaźwiński, B. Kamieński and A. Sadlej, *Magn. Reson. Chem.*, 2013, **51**, 788–794.

289 C. Martineau, F. Taulelle and M. Haouas, in *The Chemistry of Organoaluminum Compounds (PATAI'S Chemistry of Functional Groups)*, eds. L. Micouin, I. Marek and Z. Rappoport, John Wiley & Sons, Ltd., Chichester, 2016, pp. 1–51.

290 M. E. Smith, *Appl. Magn. Reson.*, 1993, **4**, 1–64.

291 D. Kim, K. Yamamoto and K. H. Ahn, *Tetrahedron*, 2012, **68**, 5279–5282.

292 Y. S. Marfin, S. D. Usoltsev and E. V. Rumyantsev, *BODIPY Dye. - A Privil. Mol. Scaffold with Tunable Prop.*, , DOI:10.5772/intechopen.80498.

293 E. Soto-Cantu, R. Cueto, J. Koch and P. S. Russo, *Langmuir*, 2012, **28**, 5562–5569.

294 C. Volkringer, H. Leclerc, J. C. Lavalley, T. Loiseau, G. Férey,

M. Daturi and A. Vimont, *J. Phys. Chem. C*, 2012, **116**, 5710–5719.

295 S. J. Lyle, R. W. Flaig, K. E. Cordova and O. M. Yaghi, *J. Chem. Educ.*, 2018, **95**, 1512–1519.

296 J. Cai, X. Mao and W. G. Song, *Mater. Chem. Front.*, 2018, **2**, 1389–1396.

297 P. Billemont, N. Heymans, P. Normand and G. De Weireld, *Adsorption*, 2017, **23**, 225–237.

298 V. J. Witherspoon, J. Xu and J. A. Reimer, *Chem. Rev.*, 2018, **118**, 10033–10048.

299 Y. Zhang, S. Liu, Z. Zhao, Z. Wang, R. Zhang, L. Liu and Z.-B. Han, *Inorg. Chem. Front.*, 2021, **8**, 590–619.

300 Y. R. Lee, J. Kim and W. S. Ahn, *Korean J. Chem. Eng.*, 2013, **30**, 1667–1680.

301 Y. Sun and H. C. Zhou, *Sci. Technol. Adv. Mater.*, , DOI:10.1088/1468-6996/16/5/054202.

302 C. P. Raptopoulou, *Materials (Basel).*, 2021, **14**, 1–32.

303 T. H. Kim and S. G. Kim, *Saf. Health Work*, 2011, **2**, 97–104.

304 Y. Lei, S. Xiao, S. Chen, H. Zhang, H. Li and Y. Lu, *Exp. Ther. Med.*, 2017, **14**, 5659–5663.

305 B. O. Jang, G. H. Choi, H. Y. Jang, S. Ahn, J. K. Choi, S. Kim, K. Lee, E. S. Jang, J. W. Kim and S. H. Jeong, *J. Korean Med. Sci.*, 2020, **35**, 1–6.

306 F. P. Byrne, S. Jin, G. Paggiola, T. H. M. Petchey, J. H. Clark, T. J. Farmer, A. J. Hunt, C. Robert McElroy and J. Sherwood, *Sustain. Chem. Process.*, 2016, **4**, 1–24.

307 H. N. Rubin and M. M. Reynolds, *Inorg. Chem.*, 2017, **56**, 5266–5274.

308 M. Thiemann, E. Scheibler and K. W. Wiegand, *Ullmann's Encycl. Ind. Chem.*, 2000, **24**, 178.

309 T. Behrsing, G. B. Deacon and P. C. Junk, *The chemistry of rare earth metals, compounds, and corrosion inhibitors*, Woodhead Publishing Limited, 2014.

310 S. Cotton, *Lanthanide and Actinide Chemistry*, 2006.

311 S. Kim, J. Kim, H. Kim, H. Cho and W.-S. Ahn, *Catal. Today*, 2013, **204**, 85–93.

312 Q. Fang, G. Zhu, M. Xue, J. Sun, Y. Wei, S. Qui and R. Xu, *Angew. Chemie - Int. Ed.*, 2005, **44**, 3845–3848.

313 W. Lu, Z. Wei, Z. Y. Gu, T. F. Liu, J. Park, J. Park, J. Tian, M. Zhang, Q. Zhang, T. Gentle, M. Bosch and H. C. Zhou, *Chem. Soc. Rev.*, 2014, **43**, 5561–5593.

314 P. L. Llewellyn, S. Bourrelly, C. Serre, A. Vimont, M. Daturi, L. Hamon, G. De Weireld, J. Chang, D. Hong, Y. K. Hwang and S. H. Jhung, 2008, 7245–7250.

315 A. D. S. Barbosa, D. Julião, D. M. Fernandes, A. F. Peixoto, C. Freire, B. de Castro, C. M. Granadeiro, S. S. Balula and L. Cunha-Silva, *Polyhedron*, 2017, **127**, 464–470.

316 T. Steenhaut, Y. Filinchuk and S. Hermans, *J. Mater. Chem. A*, 2021, **9**, 21483–21509.

317 A. Lieb, H. Leclerc, T. Devic, C. Serre, I. Margiolaki, F. Mahjoubi, J. S. Lee, A. Vimont, M. Daturi and J. S. Chang, *Microporous Mesoporous Mater.*, 2012, **157**, 18–23.

318 F. Carson, J. Su, A. E. Platero-Prats, W. Wan, Y. Yun, L. Samain and X. Zou, *Cryst. Growth Des.*, 2013, **13**, 5036–5044.

319 Z. Dou, J. Cai, Y. Cui, J. Yu, T. Xia, Y. Yang and G. Qian, *Zeitschrift fur Anorg. und Allg. Chemie*, 2015, **641**, 792–796.

320 H. Reinsch and N. Stock, *CrystEngComm*, 2013, **15**, 544–550.

321 L. Mitchell, B. Gonzalez-Santiago, J. P. S. Mowat, M. E. Gunn, P. Williamson, N. Acerbi, M. L. Clarke and P. A. Wright, *Catal. Sci. Technol.*, 2013, **3**, 606–617.

322 J. Castells-Gil, N. M. Padial, N. Almora-Barrios, I. Da Silva, D. Mateo, J. Albero, H. García and C. Martí-Gastaldo, *Chem. Sci.*, 2019, **10**, 4313–4321.

323 H. Assi, G. Mouchaham, N. Steunou, T. Devic and C. Serre, *Chem. Soc. Rev.*, 2017, **46**, 3431–3452.

324 H. L. Nguyen, *New J. Chem.*, 2017, **41**, 14030–14043.

325 B. Bueken, F. Vermoortele, D. E. P. Vanpoucke, H. Reinsch, C. C. Tsou, P. Valvekens, T. De Baerdemaeker, R. Ameloot, C. E. A. Kirschhock, V. Van Speybroeck, J. M. Mayer and D. De Vos, *Angew. Chemie - Int. Ed.*, 2015, **54**, 13912–13917.

326 S. Lacour, UCLouvain Master thesis 'Functionalization of open-metal sites in stable MOFs through the use of small post-functionalized anchor molecules', 2020.

327 A. M. Antonio, J. Rosenthal and E. D. Bloch, *J. Am. Chem. Soc.*, 2019, **141**, 11383–11387.

328 C. K. Brozek and M. Dincă, *J. Am. Chem. Soc.*, 2013, **135**, 12886–12891.

329 L. Zou, D. Feng, T. F. Liu, Y. P. Chen, S. Yuan, K. Wang, X. Wang, S. Fordham and H. C. Zhou, *Chem. Sci.*, 2016, **7**, 1063–1069.

330 P. Ji, Y. Song, T. Drake, S. S. Veroneau, Z. Lin, X. Pan and W. Lin, *J. Am. Chem. Soc.*, 2018, **140**, 433–440.

331 S. Kang, L. E. Klebanoff, A. A. Baker, D. F. Cowgill, V. Stavila, J. R. I. Lee, M. H. Nielsen, K. G. Ray, Y. Liu and B. C. Wood, *Int. J. Hydrogen Energy*, 2018, **43**, 14507–14519.

332 N. Liu, M. Xu, Y. Yang, S. Zhang, J. Zhang, W. Wang, L. Zheng, S. Hong and M. Wei, *ACS Catal.*, 2019, **9**, 2707–2717.

333 X. Yang, J. Qu, L. Wang and J. Luo, *RSC Adv.*, 2021, **11**, 24144–24155.

334 Y. Qing, Y. Li, W. Li and H. Yao, *J. Mater. Chem. C*, 2021, **9**, 1205–1214.

335 C. Xu, R. Fang, R. Luque, L. Chen and Y. Li, *Coord. Chem. Rev.*, 2019, **388**, 268–292.

336 S. Wu, L. Chen, B. Yin and Y. Li, *Chem. Commun.*, 2015, **51**, 9884–9887.

337 M. Kalaj and S. M. Cohen, *ACS Cent. Sci.*, 2020, **6**, 1046–1057.

338 N. A. Jones, S. T. Liddle, C. Wilson and P. L. Arnold, *Organometallics*, 2007, **26**, 755–757.

339 F. L. Morel, M. Ranocchiari and J. A. Van Bokhoven, *Ind. Eng.*

Chem. Res., 2014, **53**, 9120–9127.

340 U. Rana, S. Mondal, J. Sannigrahi, P. K. Sukul, M. A. Amin, S. Majumdarb and S. Malik, *J. Mater. Chem. C*, 2014, **2**, 3382–3389.

341 J. H. Yoon, S. B. Choi, Y. J. Oh, M. J. Seo, Y. H. Jhon, T. B. Lee, D. Kim, S. H. Choi and J. Kim, *Catal. Today*, 2007, **120**, 324–329.

342 T. Steenhaut, Y. Filinchuk and S. Hermans, *J. Mater. Chem. A*, 2021, **9**, 21483–21509.

343 M. Babar, M. Mubashir, A. Mukhtar, S. Saqib, S. Ullah, M. A. Bustam and P. L. Show, *Environ. Pollut.*, 2021, **279**, 116924.

344 M. L. Chen, S. Y. Zhou, Z. Xu, L. Ding and Y. H. Cheng, *Molecules*, , DOI:10.3390/molecules24203718.

345 A. D. Burrows, D. Jiang, L. L. Keenan, A. D. Burrows and K. J. Edler, *Chem. Comm.*, 2012, **48**, 12053–12055.

346 A. A. Taha, L. Huang, S. Ramakrishna and Y. Liu, *J. Water Process Eng.*, 2020, **33**, 101004.

347 R. Karimi Alavijeh and K. Akhbari, *Inorg. Chem.*, 2020, **59**, 3570–3578.

348 B. G. Santiago and A, *Synthesis and properties of scandium carboxylate metal-organic frameworks*, University of St Andrews, 2015.

349 E. Buncel and E. A. Symons, *J. CHem. Soc. D*, 1970, 164–165.

350 C. V. J. Skipper, A. Hamaed, D. M. Antonelli and N. Kaltsoyannis, *Dalt. Trans.*, 2012, **41**, 8515–8523.

351 M. Murialdo, N. J. Weadock, Y. Liu, C. C. Ahn, S. E. Baker, K. Landskron and B. Fultz, *ACS Omega*, 2019, **4**, 444–448.

352 H. Deng, C. J. Doonan, H. Furukawa, R. B. Ferreira, J. Towne, C. B. Knobler, B. Wang and O. M. Yaghi, *Science (80-.).*, 2010, **327**, 846–850.

353 M. Latroche, S. Surblé, C. Serre, C. Mellot-Draznieks, P. L. Llewellyn, J.-H. Lee, J. Chang, S. H. Jhung and G. Férey, *Ange*, 2006, **45**, 8227–8231.

354 C. H. Hendon and A. Walsh, *Chem. Sci.*, 2015, **6**, 3674-.

355 M. Todaro, G. Buscarino, L. Sciortino, A. Alessi, F. Messina, M. Taddei, M. Ranocchiari, M. Cannas and F. M. Gelardi, *J. Phys. Chem. C*, 2016, **120**, 12879–12889.

356 W. Zhang, M. Kauer, P. Guo, S. Kunze, S. Cwik, M. Muhler, Y. Wang, K. Epp, G. Kieslich and R. A. Fischer, *Eur. J. Inorg. Chem.*, 2017, **2017**, 925–931.

357 M. Shöâeè, J. R. Agger, M. W. Anderson and M. P. Attfield, *CrystEngComm*, 2008, **10**, 646–648.

358 R. Ameloot, F. Vermoortele, J. Hofkens, F. C. De Schryver, D. E. De Vos and M. B. J. Roeffaers, *Angew. Chemie - Int. Ed.*, 2013, **52**, 401–405.

359 G. Majano, O. Martin, M. Hammes, S. Smeets, C. Baerlocher and J. Pérez-Ramírez, *Adv. Funct. Mater.*, 2014, **24**, 3855–3865.

360 T. Wang, H. Zhu, Q. Zeng and D. Liu, *Adv. Mater. Interfaces*, 2019, **6**, 1–27.

361 T. Stolar, L. Batzdorf, S. Lukin, D. Žilić, C. Motillo, T. Friščić, F. Emmerling, I. Halasz and K. Užarević, *Inorg. Chem.*, 2017, **56**, 6599–6608.

362 J. Yang, X. Feng, G. Lu, Y. Li, C. Mao, Z. Wen and W. Yuan, *Dalt. Trans.*, 2018, **47**, 5065–5071.

363 M. Klimakow, P. Klobes, A. F. Thünemann, K. Rademann and F. Emmerling, *Chem. Mater.*, 2010, **22**, 5216–5221.

364 A. Corma, M. Iglesias, F. X. Llabrés i Xamena and F. Sánchez, *Chem. - A Eur. J.*, 2010, **16**, 9789–9795.

365 H. V. Doan, A. Sartbaeva, J. C. Eloi, S. A. Davis and V. P. Ting, *Sci. Rep.*, 2019, **9**, 1–9.

366 S. Loera-Serna, L. L. Núñez, J. Flores, R. López-Simeon and H. I. Beltrán, *RSC Adv.*, 2013, **3**, 10962–10972.

367 J. B. DeCoste, G. W. Peterson, B. J. Schindler, K. L. Killops, M. A. Broweb and J. J. Mahle, *J. Mater. Chem. A*, 2013, **1**, 11922–11932.

368 T. Toyao, K. Liang, K. Okada, R. Ricco, M. J. Styles, Y.

Tokudome, Y. Horiuchi, A. J. Hill, M. Takahashi, M. Matsuoka and P. Falcaro, *Inorg. Chem. Front.*, 2015, **2**, 434–441.

369 Y. K. Seo, G. Hundal, I. T. Jang, Y. K. Hwang, C. H. Jun and J. S. Chang, *Microporous Mesoporous Mater.*, 2009, **119**, 331–337.

370 G. B. Deacon and R. J. Phillips, *Coord. Chem. Rev.*, 1980, **33**, 227–250.

371 Y. Liu, P. Bailey, T. C. Q. Noakes, G. E. Thompson, P. Skeleton and M. R. Alexander, *Surf. Interface Anal.*, 2004, **36**, 339–346.

372 Y. Chen, X. Mu, E. Lester and T. Wu, *Prog. Nat. Sci. Mater. Int.*, 2018, **28**, 584–589.

373 H. K. Kim, W. S. Yun, M. Kim, J. Y. Kim, Y. Bae and J. Lee, **222**, 1–8.